CZECH TECHNICAL UNIVERSITY IN
PRAGUE

Faculty of Nuclear Sciences and Physical
Engineering

Physics Department

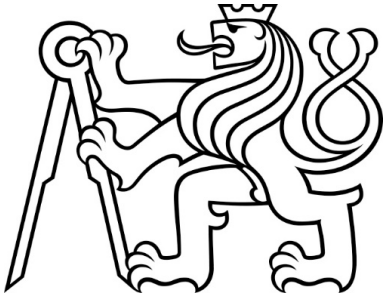

Doctoral Thesis

Study of Heavy Flavor at the STAR Experiment

Ing. Miroslav Šimko

Supervisor: Doc. Mgr. Jaroslav Bielčík, Ph.D.

Supervisor specialist: RNDr. Jana Bielčíková, Ph.D.

Prague, 2021

ČESKÉ VYSOKÉ UČENÍ TECHNICKÉ

V PRAZE

Fakulta jaderná a fyzikálně inženýrská

Katedra fyziky

Disertační práce

Studium těžkých vůní na experimentu STAR

Ing. Miroslav Šimko

Školitel: Doc. Mgr. Jaroslav Bielčík, Ph.D.

Školitel specialista: RNDr. Jana Bielčíková, Ph.D.

Praha, 2021

Bibliographic Entry

Author:	**Ing. Miroslav Šimko**
	Czech Technical University in Prague
	Faculty of Nuclear Sciences and Physical Engineering
	Physics Department
Title of the doctoral thesis:	Study of Heavy Flavor at the STAR Experiment
Specialization:	Nuclear Engineering
Supervisor:	**Doc. Mgr. Jaroslav Bielčík, Ph.D.**
	Faculty of Nuclear Sciences and Physical Engineering
	of the Czech Technical University in Prague
Supervisor Specialist:	**RNDr. Jana Bielčíková, Ph.D.**
	Nuclear Physics Institute of the Czech Academy of Sciences
Academic year:	2020/2021
Number of pages:	170
Key words:	Lambda_c, coalescence, STAR, RHIC, HFT

Bibliografický záznam

Author:	**Ing. Miroslav Šimko**
	České vysoké učení technicé v Praze
	Fakulta jaderná a fyzikálně inženýrská
	Katedra fyziky
Název práce:	Studium těžkých vůní na experimentu STAR
Obor:	Jaderné inženýrství
Školitel:	**Doc. Mgr. Jaroslav Bielčík, Ph.D.**
	Fakulta jaderná a fyzikálně inženýrská
	českého vysokého učení technického v Praze
Školitel specialista:	**RNDr. Jana Bielčíková, Ph.D.**
	Ústav jaderné fyziky akademie věd České republiky, v.v.i.
Akademický rok:	2020/2021
Počet stran:	170
Klíčová slova:	Lambda_c, koalescence, STAR, RHIC, HFT

English abstract

This work focuses on the analysis of Λ_c which is the lightest baryon containing a charm quark. As such, the Λ_c presents a unique probe to study the behavior of charm quarks in the hot and dense QCD medium created in ultra-relativistic heavy-ion collisions. Together with the measurement of the D^0 meson, we can study modes of charm quark hadronization and bring additional insights into the quark coalescense process in the strongly coupled quark-gluon plasma. Λ_c baryons have an extremely short lifetime ($c\tau \sim 60\,\mu m$) which makes the reconstruction experimentally challenging. The novel detector Heavy Flavor Tracker, installed at the STAR experiment between the years 2014–2016, has shown high efficiency and an unparalleled pointing resolution that can facilitate the Λ_c reconstruction in heavy-ion collisions. In this thesis, we describe the first reconstruction of the Λ_c baryons via hadronic decays in Au+Au collisions and, moreover, the first such measurement differentiated in transverse momentum and the number of participants in heavy-ion collisions. The measured yield shows that the Λ_c make a sizeable contribution to the total charm yield in Au+Au collisions. Moreover, the Λ_c/D^0 yield ratio is significantly larger in Au+Au collisions, compared to simulated p+p collisions, and is consistent with theoretical calculations that include charm-quark coalescence.

Český abstrakt

Cílem této práce je analýza baryonu Λ_c, což je nejlehčí baryon, který obsahuje půvabný (c) kvark. Jako takový představují Λ_c unikátní nástroj pro studování vlastností silně interagující hmoty, jež se produkuje ve srážkách ultrarelativistických těžkých iontů. Spolu s měřením mezonu D^0 může analýza Λ_c přinést nové poznatky o procesu hadronizace c kvarku a objasnit, zda je hlavním způsobem pro hadronizaci c kvarku v kvark gluonovém plazmatu t.zv. koalescence. Λ_c mají nicméně velice krátkou střední dobu rozpadu ($c\tau \sim 60\,\mu m$), kvůli čemuž je jejich analýza velice náročná. Mezi lety 2014–2016 byl ale nainstalován přesný dráhový detektor Heavy Flavor Tracker (HFT), který má zatím ve světě ojedinělé rozlišení, takže umožňuje měření baryonů Λ_c i ve srážkách těžkých iontů při energii srážky na jeden nukleon–nukleonový pár $\sqrt{s_{NN}} = 200\,GeV$. V této práci popisujeme první přímou rekonstrukci Λ_c v hadronovém rozpadovém kanálu ve srážkách Au+Au. Změřený výtěžek ukazuje, že Λ_c se výrazně podílí na celkovém výtěžku půvabného kvarku ve srážkách Au+Au. Dále je poměr výtěžků Λ_c/D^0 výrazně vyšší ve srážkách Au+Au než v ekvivalentních simulacích srážek p+p, což je konzistentní výsledek s teoretickými předpověďmi, které obsahují koalescenci půvabného kvarku.

Acknowledgement

This thesis would not be finished without the help and support of many people that are impossible to name in a single page, but I would like to, none-the-less, acknowledge several people that, I feel, mostly contributed to the work, presented in this document, and who deserve a big thanks. First and foremost I would like to thank Jaro and Jana Bielčíkovi for their continuing and unwavering support during the entire course of my studies. Be it with with life and professional advice, good leadership, motivation, and last but not least, financial support. My doctoral studies were some of the best years of my life and I cannot imagine that they would be the same without my two supervisors. Moreover, several calamities were avoided only thanks to Jaro Bielčík and his support for all of which he will have my gratitude for the rest of my life.

I would also like to thank my dear friends at Lawrence Berkeley National Laboratory, Xin Dong, Mustafa Mustafa, and Sooraj Radhakrishnan who helped jumpstarting my journey into science and programming with good advice and leadership by example. I will always aspire to uphold the work standards and integrity I have learnt at Berkeley.

Another big thanks goes to Zhangbu Xu and Les Bland from Brookhaven National Laboratory. Zhangbu Xu helped me with the introduction into the works of the ZDC detector and STAR in general. Later, he also helped me with support and good leadership, thanks to which the ZDC continued to work smoothly for all these years. Without the advice and supervision of Les Bland, the ZDC PMT test and upgrade would not be possible and STAR functions in part thanks to him.

With regards to the text in this thesis, a big thanks goes to Filip Křížek from NPI CAS who helped with the corrections of several chapters. A lot of work went into these corrections and I appreciate it.

Lastly, I would like to thank all the STAR collaborators, several of whom I consider life-long friends and who made this journey such a blast.

Thank you all!

Author's Contribution

Throughout my Ph.D. studies, I was a member of the Solenoidal Tracker at RHIC (STAR) collaboration. As such, I was able to perform two service tasks on two of the STAR subdetectors and the analysis of the Λ_c baryon on STAR data, recorded in 2014 and 2016 from Relativistic Heavy-Ion Collider (RHIC) Au+Au collisions at full energy ($\sqrt{s_{\mathrm{NN}}} = 200\,\mathrm{GeV}$). In this chapter, I describe my contribution to the STAR collaboration that led to the results, presented in this thesis.

Service tasks

During the course of my Ph.D. studies, I had two major service tasks on the hardware and software of the Solenoidal Tracker at RHIC (STAR) experiment: One was on the slow simulator on the Heavy Flavor Tracker (HFT — for more detail see Section 3.5) which was installed at STAR in the years 2014–2016. The other one is the maintenance of the STAR Zero Degree Calorimeters (ZDC — for more detail see Section 3.6).

HFT–Pixel Slow Simulator Evaluation

Simulations are an integral part of every analysis on high-energy experiments. My task was to evaluate the slow simulator for the Pixel (PXL) detector of the HFT. Part of this work was performed during my stay at Lawrence Berkeley National Laboratory (LBNL) for 6 months in 2013–2014. The HFT [1–3] is a state-of-the-art silicon vertex detector out of which the two innermost layers consist of the novel MAPS-technology based Pixel detector which provides a yet unparalleled tracking resolution that can facilitate the reconstruction of the

relatively short-lived heavy-flavor hadrons via their decay products, e.g. the Λ_c which was never measured in heavy-ion collisions before.

The point of a Slow simulator is to generate the output of the detector on the level of a single pixel, whereas the fast simulator operates on the level of a hit, i.e. an already reconstructed cluster of pixels. The slow simulator is mainly used in the, so called, embedding in which the detector signal of a particle is simulated, using GEANT [4] and then embedded into a real measured event which is then reconstructed in the same manner as a real collision. This is used at STAR to evaluate detector efficiencies of particle tracks.

My task was to simulate hits of particles in the detector and then compare them to real measured particles. This comparison was done for cosmic particles and, later, for Au+Au collisions at the center-of-mass energy per nucleon $\sqrt{s_{\mathrm{NN}}} = 200\,\mathrm{GeV}$ from 2014. The particles were divided into bins by angle and then the sizes of the clusters and compared to the simulation output.

This work was later continued by Jakub Kvapil, to whom I served as an advisor. His results, presented in [5], were not only differentiated in angle, but also by particle species, identified by the Time Projection Chamber (TPC). More on the HFT slow simulator can be found in Section 3.5.

Zero Degree Calorimeter (ZDC)

The ZDC is an integral part of the STAR–trigger system and it serves as an important tool for monitoring the instant luminosity at RHIC. It consists [6, 7] of two identical sides, both placed in the RHIC tunnel, behind the first deflecting magnets. Each side consists of 3 towers made of a tungsten absorber, scintillator volume and a photomultiplier tube. Behind the first tower, there is the Shower-Maximum Detector (SMD) which adds spatial information to the ZDC.

In the years 2015–2019, I was personally responsible for the smooth operation of the ZDC system, partially on-site at BNL and remotely as an on-call expert. The RHIC runs from this period are listed in Table 1. Part of the duty is also the preparation of the detector before each run and its calibration (see Section 3.6.1). In 2018, as a part of maintenance,

Table 1: Table of runs where the author was present as a ZDC on-call expert.

Year	Species	$\sqrt{s_{\mathrm{NN}}}$ (GeV)
2015	polarized p+p	200.4
	polarized p+Au	202.4
	polarized p+Al	202.5
2016	Au+Au	200.0
	d+Au	200.7
	d+Au	62.4
	d+Au	19.7
	d+Au	39.0
2017	polarized p+p	499.8
	Au+Au	54.4
2018	^{96}Zr+^{96}Zr	200.0
	^{96}Ru+^{96}Ru	200.0
	Au+Au	27.0
	Au+Au fixed target	3.0
	Au+Au fixed target	7.2
2019	Au+Au	9.8
	Au+Au	7.3
	Au+Au fixed target	7.3
	Au+Au	3.85
	Au+Au fixed target	3.85
	Au+Au	4.59
	Au+Au fixed target	4.59
	Au+Au fixed target	31.2
	Au+Au	100

several photomultilier tubes (PMT) were exchanged for ones with better performance. As an upcycling project, we refurbished and tested old PMTs from the currently phased-out Broad

RAnge Hadron Magnetic Spectrometers (Brahms) experiment. This effort is described in more detail in Section 3.6.2. This year, as a part of a plan to increase the reliability and stability of the detector, a new high-voltage power supply is going to be installed at the ZDC and deployed with a new slow-controls system for remote control of the source. Moreover, as there was no prior documentation on how to operate the detector, we created a manual [8] for maintenance of the ZDC together with Lukáš Kramárik and Jan Vaněk who continue as ZDC on-call experts. More on this effort is described in Section 3.6.

Λ_c analysis

The main topic of my research and this thesis is the analysis of the Λ_c baryon at the STAR experiment at RHIC. Other than my supervisors, this analysis has been done in a close collaboration with a number of people from LBNL; most notably Sooraj Radhakrishnan, Guannan Xie, Xin Dong, Jochen Thaeder, Mustafa Mustafa, and Michael Lomnitz. Much of this work was done during my stays as an affiliate at LBNL in 2015 (2 months), 2016 (1 month), and 2018 (2 months). As a result of the collaboration with LBNL, the Λ_c analysis was published in the article J. Adam et al., *"First Measurement of Λ_c Baryon Production in Au+Au Collisions at $\sqrt{s_{NN}} = 200$ GeV"*, Phys. Rev. Lett. **124**, 172301 (2020) [9] where I was present as one of the primary authors of the analysis, I participated also in other activities that led to publication of the results, such Heavy Flavor PWG aproval process, GPC review, collaboration review, and communication with reviewers of the PRL.

Within the Λ_c analysis, my tasks were to perform an independent check of the Λ_c reconstruction and the difference between the of ${\Lambda_c}^+$ baryon and its antibaryon $\overline{\Lambda_c}^-$. I also notably developed the mixed-event combinatorial-background subtraction method for the Λ_c analysis and provided it in the general STAR open-heavy-flavor-analysis code [10].

List of Figures

List of Tables

Contents

List of Abbreviations

β ..... Fraction of the speed of light in vacuum, page 67

ϵ ..... Efficiency, page 98

ϵ_{HFT} ..... Heavy-Flavor Tracker matching efficiency, page 110

ϵ_{PID} ..... Efficiency of particle identification, page 110

ϵ_{TOF} ..... Time-Of-Flight detector matching efficiency, page 113

ϵ_{TPC} ..... Time-Projection Chamber tracking efficiency, page 110

$\epsilon_{1/\beta}$ ..... Efficiency of the $1/\beta$ cut in TOF, page 116

$\epsilon_{n\sigma}$ ..... Efficiency of the $n\sigma_{\mathrm{d}E/\mathrm{d}x}$ cut in the TPC, page 116

η ..... Pseudorapidity, page 62

η_{B} ..... Baryon-chemical potential, page 21

c ..... charm quark, page 9

e^{+} ..... positron, page 15

e^{-} ..... electron, page 15

ϕ ..... Azimuthal angle (in a perpendicular plane to the beam pipe), page 62

$\sigma_{\mathrm{d}E/\mathrm{d}x}$ ..... Width of the $\mathrm{d}E/\mathrm{d}x$ distribution, page 90

τ ..... Average lifetime, page 9

ν ..... neutrino, page 16

π ..... pion, page 15

τ ..... tauon, page 16

A ..... Nucleon number, page 53

c ..... Speed of light in vacuum, page 9

D_s ..... Spatial diffusion coefficient, page 35

E ..... Energy, page 21

e ..... Elementary charge, page 16

m ..... Mass (or rest mass), page 21

N_{coll} ..... Number of binary collisions, page 39

N_{part} ..... Number of participants, page 10

n_{q} ..... number of valence quarks in a hadron, page 29

T ..... Temperature, page 21

T_{ch} ..... Temperature of chemical freeze-out, page 23

T_{fo} ..... Temperature of kinetic freeze-out, page 23

v_1 ..... Direct flow, page 27

v_2 ..... Elliptic flow, page 27

v_3 ..... Triangular flow, page 27

v_r ..... Radial distance of the primary vertex from the center of the TPC, page 90

v_x ..... Position of the primary vertex along the x-axis, page 90

v_y ..... Position of the primary vertex along the y-axis, page 90

v_z ..... Position of the primary vertex along the z-axis, page 90

x ..... Horizontal axis in STAR, perpendicular to the beam pipe, page 63

y ..... Vertical axis in STAR, also rapidity, page 63

z ..... Horizontal axis in STAR along the beam pipe, page 62

Λ_{QCD} ..... Typical QCD scale, infrared cutoff for perturbative QCD, page 19

B ..... Number of background candidates, page 97

N_{Event} ..... Number of events, page 98

S ..... Number of signal candidates, page 97

p_{T} ..... Momentum in the transverse plane to the beam pipe, page 10

R_{AA} ..... Nuclear modification factor, page 24

$\sqrt{s_{\mathrm{NN}}}$ ..... Center-of-mass energy per nucleon-nucleon collision, page 9

AGS ..... Alternating-Gradient Synchrotron, page 14

ALICE ..... A Large-Ion-Collider Experiment, page 50

AMPT ..... A Multi-Phase Transport, page 43

AtR ..... AGS-to-RHIC transfer line, page 58

BDT ..... Boosted Decision Trees, page 98

BNL ..... Brookhaven National Laboratory, page 9

BR ..... Branching Ratio, page 137

Brahms ..... Broad RAnge Hadron Magnetic Spectrometers, page 82

CBM ..... Compressed Baryonic Matter, page 67

CERN ..... European Organization for Nuclear Research (derived from Conseil Européen pour la Recherche Nucléaire), page 16

CMOS ..... Complementary Metal-Oxide-Semiconductor, page 71

CR ..... Color reconnection, page 145

DCA ..... Distance of Closest Approach, page 70

DIGMAPS ..... MAPS Digitizer, page 74

DNP ..... Double-Neutron Peak, page 80

EBIS ..... Electron Beam Ion Source, page 58

eTOF ..... endcap-Time-Of-Flight detector, page 67

FAIR ..... Facility for Antiproton and Ion Research, page 22

FCS ..... Forward Calorimeter System, page 86

FEE ..... Front-End Electronics, page 71

FST ..... Forward Silicon Tracker, page 86

FTS ..... Forward Tracking System, page 86

FTT ..... Forward sTGC Tracker, page 86

GMT ..... GEM Chambers to Monitor the TPC Tracking Calibrations, page 60

HFT ..... Heavy-Flavor Tracker, page 9

HRG ..... Hadron-Resonance Gas, page 34

HTL ..... Hard Thermal Loop approximation, page 44

HV ..... High Voltage, page 80

IST ..... Intermediate Silicon Tracker, page 68

ITS ..... Inner-Tracking System, page 55

LBNL ..... Lawrence Berkeley National Laboratory, page ix

LEP ..... Large Electron-Positron collider, page 16

LHC ..... Large Hadron Collider, page 9

lQCD ..... lattice–QCD, page 22

MAPS ..... Monolythic-Active-Pixel Sensor, page 10

MB ..... Minimum Bias, page 128

MC ..... Monte Carlo, page 110

MIP ..... Minimum-Ionizing Particle, page 75

MRPC ..... Multi-gap Resistive Plate Chamber, page 65

MWPC ..... Multi-Wire Proportional Chamber, page 63

NCQ scaling ..... Number-of-Constituent-Quarks scaling, page 30

NDF ..... Number of Degrees of Freedom, page 145

nPDF ..... Nuclear Parton-Distribution Function, page 39

PC ..... Poly-Carbonate, page 66

PCA ..... Point of Closest Approach, page 93

PDF ..... Parton-Distribution Function, page 39

PHSD ..... Parton-Hadron-String Dynamics, page 44

PID ..... Particle IDentification, page 61

pQCD ..... Perturbative ChromoDynamics, page 34

PV ..... Primary Vertex, page 67

PXL ..... Pixel Detector, page 68

QCD ..... Quantum ChromoDynamics, page 17

QGP ..... Quark-Gluon Plasma, page 10

RHIC ..... Relativistic Heavy Ion Collider, page 9

SLAC ..... Stanford Linear Accelerator Laboratory, page 14

SM ..... Standard Model, page 13

SNP ..... Single-Neutron Peak, page 80

SPS ..... Super Proton-antiproton Synchrotron, page 17

sQGP ..... strongly-coupled Quark-Gluon Plasma, page 9

SST/SSD ..... Silicon Strip Tracker/Detector, page 68

STAR ..... Solenoidal Tracker At RHIC, page 9

TAMU ..... Texas A&M University, page 44

TOF ..... Time-Of-Flight Detector, page 61

TPC ..... Time-Projection Chamber, page 60

UPC ..... Ultra-Peripheral Collision, page 79

VDP ..... Vertex of Daughter Pairs, page 93

VPD ..... Vertex Position Detector, page 66

ZDC ..... Zero-Degree Calorimeter, page 10

ZdcX ..... ZDC-crossing rate, page 114

Introduction

High-energy physics and, in particular, the study of high-energy heavy-ion–ion collisions are currently at the cutting edge of human research. These collisions can be facilitated at large accelerators such as Relativistic Heavy-Ion Collider (RHIC) located at Brookhaven National Laboratory (BNL) and the Large Hadron Collider (LHC). These facilities can achieve the center-of-mass energy per nucleon-nucleon collision $\sqrt{s_{\mathrm{NN}}}$ of hundreds of GeV or even TeV. One of the main objectives of this research is the study of properties of the new hot and dense state of matter – the strongly-coupled quark-gluon plasma (sQGP) that is created in heavy-ion collisions [11].

Due to their relatively large mass, charm (or c) quarks make excellent probes into the behavior of sQGP. At RHIC energies (up to $\sqrt{s_{\mathrm{NN}}} = 200\,\mathrm{GeV}$), the charm quarks are only generated in the initial stages of the heavy-ion collisions and their number is conserved through strong interaction. Therefore, it remains constant during the evolution-time scale of the collision. Open-charm hadrons are such that have a non-zero number of valence charm quarks c minus anti-charm quarks $\bar{\mathrm{c}}$. Λ_{c} is the lightest open-charm baryon and as such, together with the measurement of the D mesons, can bring crucial insight into the hadronization process of the charm quark. However, the reconstruction of these baryons is experimentally challenging due to their low lifetime (when multiplied by the speed of light, $c\tau \sim 60\,\mu\mathrm{m}$).

In the years 2014–2016, the experiment Solenoidal Tracker At RHIC (STAR) installed a crucial upgrade, dedicated to the study of heavy flavor — a new vertex detector called the Heavy-Flavor-Tracker (HFT). One of its main objectives, as stated in the Proposal [2],

was the measurement of the Λ_c baryon. This detector utilized the Monolythic-Active-Pixel Sensor (MAPS) technology for the first time in a collider experiment. The unprecedented granularity of the HFT improved reconstruction of open-charm hadrons in a transformative way and enabled the Λ_c to be measured for the first time in Au+Au collisions.

This publication is dedicated to the study of open charm production in ultra-relativistic heavy-ion collisions at the STAR experiment. The author's analysis focuses on the Λ_c baryon which has never been measured before in Au+Au collisions before and has a potential to uncover some key properties of the sQGP. This is also the first measurement of the Λ_c differentiated in the transverse momentum p_T and the number of participants N_{part} in heavy-ion collisions.

Outline

The purpose of this thesis is for the reader to find an extended description of the results published in J. Adam et al., *"First Measurement of Λ_c Baryon Production in Au+Au Collisions at $\sqrt{s_{NN}} = 200\ GeV$"*, Phys. Rev. Lett. **124**, 172301 (2020) [9], i.e. measurements of the Λ_c cross-section in heavy-ion collisions and the yield ratio between the Λ_c baryon and the D^0 meson. The reader should also obtain a basic understanding of the physics of open charm in high-energy heavy-ion collisions.

This doctoral thesis is organized in the following manner: In Chapter 1, we introduce the Standard Model of particle physics and the basic properties of a novel state of matter – the quark-gluon plasma (QGP) – and the properties of high-energy heavy-ion collisions in general. Chapter 2 describes the basics of the behavior of the charm quark in heavy-ion collisions and summarizes experimental heavy-flavor measurements at RHIC. The properties of the Λ_c baryon, together with the latest experimental measurements of its behavior, are described in this chapter as well. In Chapter 3, we describe the RHIC accelerator and the STAR detector with its many sub-detectors. We also summarize the results of the author's two service tasks — evaluation of the HFT-clustering algorithm and maintenance and upgrade of the STAR Zero-Degree Calorimeter (ZDC). The next Chapter 4 is dedicated to the methods used in

the reconstruction of the Λ_c baryon in detail. The results of the Λ_c cross-section and Λ_c/D^0 yield ratio measurements are described in Chapter 5 "Results". The thesis is summarized in the last Chapter 6 with an added outlook of future Λ_c measurements in heavy-ion collisions.

Chapter 1

The Physics of Quark-Gluon Plasma

In this chapter, we explain basic concepts of physics of ultra-relativistic heavy-ion collisions, such as the ones that take place at RHIC. First, we briefly talk about the Standard Model of particle physics and the theory of strong interactions — quantum chromodynamics — then we introduce the physics of ultra-relativistic heavy-ion collisions with experimental signatures of the new state of matter – the quark-gluon plasma.

1.1 The Standard Model

The Standard Model of particle physics (SM) is a theoretical framework for elementary particles and their interactions. This model includes several elementary particles in its framework: 12 fermions together with antifermions, all with spin 1/2, and 5 species of bosons with whole-number spins (see Figure 1.1).

The rapid development of detection techniques of cosmic rays and accelerator experiments after the Second World War resulted in a fast discovery of numerous new particles. A new particle ZOO was being filled at an incredible pace and it was the task of particle physicists to find patterns among them. Two physicists — Gell-Man and Zweig — found the quark theory independently and thus mostly completed this task. Most of the particles – hadrons

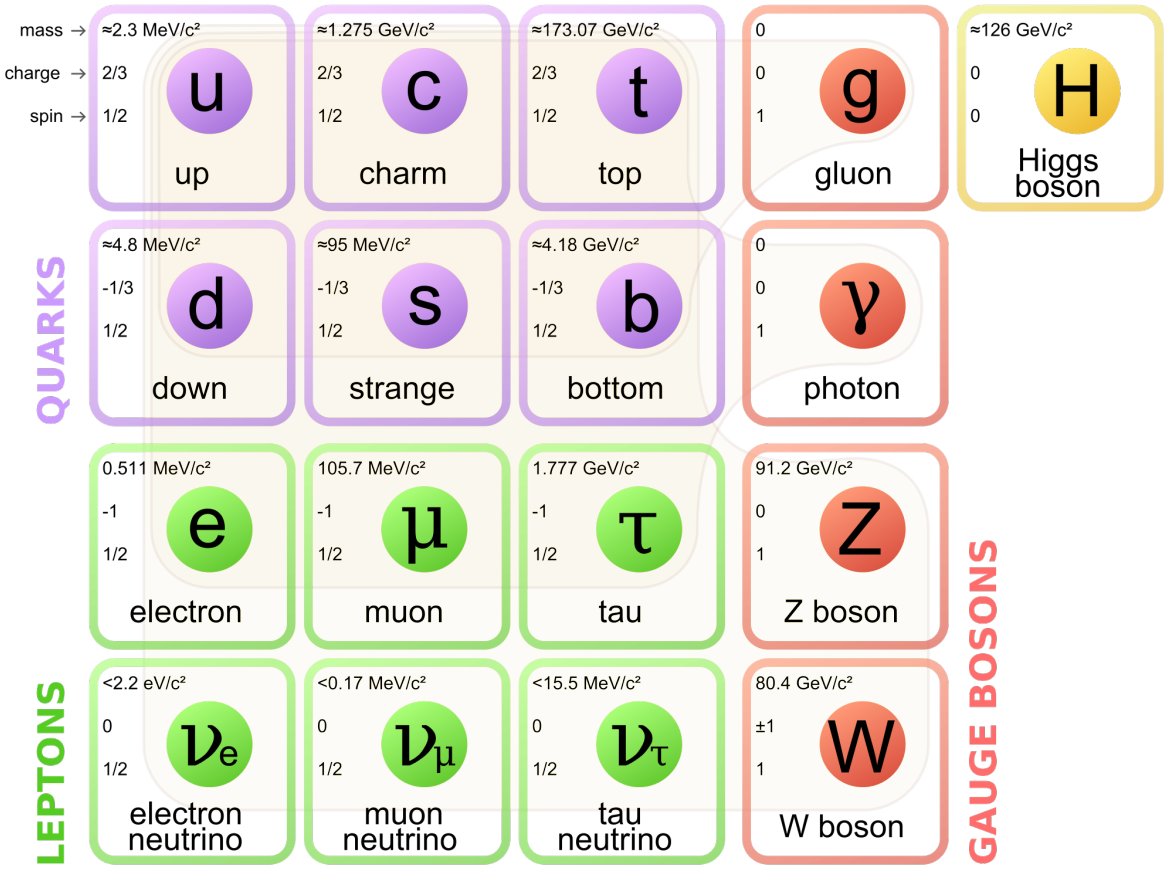

Figure 1.1: Elementary particles in the standard model. Adopted from [12].

– were found to consist of, so called, quarks with a quantum number, so called flavor. At the time, 3 quarks were known: u (up), d (down), and s (strange) with their corresponding antiparticles. Today, these are referred to as light-flavor quarks. In nature, quarks are never found as separate particles. Rather, they are bound in hadrons. This phenomenon, related to strong interaction, is called confinement (more in Section 1.2.2).

In 1974, the discovery of an unexpected particle at two experiments almost simultaneously changed the landscape of particle physics for good. A resonance at the invariant mass of $3.1\,\mathrm{GeV}/c^2$, initially called 'J', was found at the precise e^++e^- pair spectrometer on the Alternating-Gradient Synchrotron (AGS) at Brookhaven National Laboratory (BNL). This find was published in [13]. A day later, the same journal received a paper from the experiment SPEAR at Stanford Linear Accelerator Laboratory (SLAC) [14] that discovered a sharp

resonance at the same invariant mass, wishing to call it ψ. In the end, this particle was called J/ψ and was found to be the long predicted new quarkonium — a meson consisting of a quark and its antiquark — in this case of a newly discovered charm quark (c). In 1976, both directors of their respective experiments: Samuel Chao Chung Ting and Burton Richter received a shared Nobel prize for physics [15].

The next family of heavy quarks followed soon as the third generation of quarks was theoretically predicted by Makoto Kobayashi and Toshihide Maskawa to explain the violation of the CP–symmetry in the weak-force theory [16]. There were other explanations for this phenomenon, but finally, the discussion was settled with the discovery of the bottomonium Υ at the E288 experiment on the Bevalac accelerator at Fermilab [17]. The Υ meson consists of the bottom quark b and its antiparticle $\overline{\mathrm{b}}$. The last quark, so called top (t) was discovered by the D0 experiment at the Tevatron accelerator at Fermilab by measuring the invariant mass of jets [18].

Nowadays, 6 quark flavors are known, divided into 3 generations (or families). The first generation is composed of of u and d quarks, the second consists of s and c, and the third one contains b and t. Strong theoretical and experimental evidence is mounting against the existence of a fourth or further generations [19, 20] so the number 6 may be final.

To the 3 generations of quarks, there are 3 families of leptons. These are fermions that, unlike the quarks, do not interact strongly and thus do not form hadrons. The electron was discovered by J.J. Thompson in the end of the 19th century [21] in an experiment with a cathode in an electric field. This later led him to formulate the plum pudding model of atom. The electron's antiparticle — the positron (e^+) — was discovered much later (in 1930) from the study of cosmic rays in magnetic field by Carl D. Anderson [22]. The same person with his colleague Seth Neddermeyer later discovered the muon (μ^-) in cosmic rays [23]. At the time, the muon was theorized to be the Yukawa particle, i.e. the mediating particle of the strong nuclear force in the nucleus. This was later found out to be false as the muon does not interact strongly and another particle was found in its place — the pi-meson (or pion, π) [24] a meson (consisting of the u and d quarks) that has similar mass [25], but interacts strongly. The third and final generation of charged leptons was discovered at SLAC by finding the

tau-lepton (tauon, τ) [26] at an e^++e^- accelerator. This concluded the search for the SM charged leptons. Today we know 3 families of leptons, that contains the electron, muon, and tauon, together with their antiparticles.

In addition to the charged leptons, there are also neutral ones, called neutrinos (ν). Neutrinos proved somewhat elusive to detect as they do not interact electromagnetically or strongly so even though they are relatively common in nature, they mostly traverse through matter unimpeded. The only interaction, they participate in, is the weak one. Therefore, large volumes and masses of detection material are needed which was realized by C.L. Cowan and F. Reines in 1954 when they constructed a large detector next to a nuclear reactor and detected neutrinos for the first time [27].

Like their charged-lepton brethren, neutrinos come in three generations electron- , muon-, and tauon-neutrinos (ν_e, ν_μ, and ν_τ, respectively) and their antiparticles ($\overline{\nu}_e$, $\overline{\nu}_\mu$, and $\overline{\nu}_\tau$, respectively). The number of neutrino families has been experimentally limited to three by the particle experiments at the Large Electron-Positron (LEP) collider at CERN.

The right-hand side of Figure 1.1 is occupied by bosons. These are whole-number spin particles that mediate interactions between particles. The gluons (g) are responsible for the strong interaction (more on that in Section 1.2) and therefore interact only with quarks and with themselves. Photons (γ) generate the electromagnetic force and interact with charged particles. The weak force is mediated by the heavy W and Z bosons: The W have an elementary charge (+ or $-1\,e$); The Z bosons are electrically neutral and slightly heavier. The weak force interacts with all the SM fermions and is in many ways peculiar. Out of the known forces, it is the only one that does not conserve flavor. It is also the only force (other than the Higgs field or — perhaps — gravity) that interacts with the neutrinos. All of the SM bosons are also called gauge bosons, because their interaction follow the, so called, gauge symmetry.

While the photon was arguably discovered with the theoretical explanation of the photo-electric effect by Einstein and was at the forefront of development of the quantum theory, the other bosons took longer to be experimentally detected. The gluon was detected in 1979 in three-jet events generated from e^+–e^- collisions at the accelerator PETRA at DESY [28].

Both the weak W [29, 30] and Z [31] bosons were discovered also in Europe at the Super Proton-antiproton Synchrotron (SPS) at CERN.

When attempting to unify the electromagnetic and weak theories into a unified electroweak theory, a problem was discovered that the rest masses of the W and Z bosons were not compatible with the gauge symmetry that was needed. Moreover, divergences were found when calculating W–W boson scattering. These issues were elegantly solved by the existence of a new boson with spin 0 which was proposed by Peter Higgs. This boson, therefore, bears his name and was finally discovered in 2012 at the Large Hadron Collider (LHC) by the experiments ATLAS [32] and CMS [33].

The discovery of the Higgs boson concluded the search for the SM elementary particles. Now, the physics of the Higgs boson is in an era of precision measurements of its decays and interactions. In fact, its mass has been measured at $125.38 \pm 0.14\,\mathrm{GeV}/c^2$ [34], the most precisely measured of all the massive bosons. The SMl still, however, does not explain large fields of physics that were observed through cosmological experiments like the, so called, dark matter and dark energy. The SM itself provides room for questions such as the, hierarchy problem of why the masses of particles are set to their measured values. Also, the question of the dominance of matter over anti-matter and the quantum gravity remain to be solved. Therefore, the search for new particles at the LHC or at other experiments is not over. The hope is that at the 10- or 100-TeV scale, there are more particles to be found which would fundamentally change our understanding of physics.

1.2 Quantum Chromodynamics and strong interaction

The strong interaction derives its name from its relative strength, compared to other forces within the standard model. The strong coupling constant is relatively very high at approxiamtely ≈ 1, compared to the electromagnetic coupling constant ($\approx 10^{-2}$) and the weak coupling constant ($\approx 10^{-6}$). It binds quarks into hadrons and has enough strength to bind protons + neutrons together into nuclei, despite their electromagnetic repulsion.

The theory of the strong interaction is called Quantum ChromoDynamics (QCD) which

is a non-Abelian gauge field theory that describes the strong interaction between quarks and gluons. The quarks posses a quantum number called color charge which can have values of 1, 2, or 3 or red, green, and blue. The requirement for 3 colors is found e.g. due to the spin $J = 3/2$ of the baryon Δ^{++} ($u^{\uparrow}u^{\uparrow}u^{\uparrow}$) which otherwise could not exist due to the Pauli exclusion principle. These 3 colors can be represented by the SU(3), therefore QCD is non-Abelian.

The QCD Lagrangean $\mathcal{L}$ can be written as

$$\mathcal{L} = \sum_q \overline{\psi}_{q,a}(i\gamma^\mu \partial_\mu \delta_{ab} - g_s \gamma^\mu t^C_{ab} A^C_\mu - m_q \delta_{ab})\psi_{q,b} - \frac{1}{4} F^A_{\mu\nu} F^{\mu\nu}_A \tag{1.1}$$

where q is the quark flavor, ψ_{qa} is the quark-field spinor with a as a color index which runs between 1 and $N_q = 3$. The γ^μ stands for the Dirac γ matrices and δ_{ab} is the Kronecker Delta. The g_s is the strong coupling constant, the t^C_{ab} are 3×3 matrices that correspond to the 8 generators of the SU(3) group. The A^C_μ is the color field where C stands for the gluon colors, running from 1 to $N_q = 8$. The field tensor $F^A_{\mu\nu}$ is defined as

$$F^A_{\mu\nu} = \partial_\mu A^A_\nu - \partial_\nu A^A_\mu - g_s f_{ABC} A^B_\mu A^C_\nu \tag{1.2}$$

where f_{ABC} is the structure constant of the SU(3) group.

1.2.1 Running coupling constant

Similarly to QED, the QCD is a renormalized theory [35, 36]. As such, the QCD coupling constant is floating in order to avoid ultraviolet divergencies.

In QED, the coupling constant α is not a constant number either. Rather, it is a function of the energy scale Q^2 of the process. The reason for this phenomenon are virtual pairs of electrons and positrons that get created with larger energy and screen the electric charge.

The scale dependency of the coupling constant can be formulated in terms of the β function

$$\begin{aligned} Q\frac{\mathrm{d}\alpha}{\mathrm{d}Q} &\equiv \alpha\beta(\alpha) \\ \beta(\alpha) = \beta_0\frac{\alpha}{\pi} + \beta_1\left(\frac{\alpha}{\pi}\right)^2 &+ \dots\,, \end{aligned} \tag{1.3}$$

where the terms β_0, β_1, ... correspond to 1 loop, 2 loops, etc. The first term is equal to

$$\beta_0 = 2/3\,. \tag{1.4}$$

This restricts the case of one loop diagrams ($\beta(\alpha) \simeq \beta_0\frac{\alpha}{\pi}$). Then $\alpha(Q^2)$ becomes

$$\alpha(Q^2) = \frac{\alpha(Q_0^2)}{1 - \frac{\beta_0\alpha(Q_0^2)}{2\pi}\ln(\frac{Q^2}{Q_0^2})}\,, \tag{1.5}$$

where Q_0 is an arbitrary scale at which the $\alpha(Q^2)$ is known from empirical measurements.

The situation changes, however, in the QCD case. New terms arise from the gluon self-interaction and the first term becomes

$$\beta_0^{\mathrm{QCD}} = \frac{2N_f - 11N_C}{6}\,, \tag{1.6}$$

where $N_C = 3$ is the number of colors and N_f is the number of flavors. From this, the new form of scale dependency can be derived as

$$\alpha_s(Q^2) = \frac{12\pi}{(33 - 2N_f)\ln(\frac{Q^2}{\Lambda_{\mathrm{QCD}}^2})}\,, \tag{1.7}$$

where the arbitrary scale, typical for QCD, is in this case $Q_0 \equiv \Lambda_{\mathrm{QCD}} \approx 220\,\mathrm{MeV}$.

Since most of the QCD problems are impossible to solve analytically, the perturbation theory is often used. For it to be valid, the energy scale must be $\alpha_s \ll 1$ and $Q \gg \Lambda_{\mathrm{QCD}}$. The Λ_{QCD} scale is, therefore, used as an infrared cutoff for the perturbative QCD.

Similarly to QED, the quark color charge is also effectively weakened by the QCD renormalization by the creation of virtual quark-antiquark pairs. Unlike in QED, however, virtual

gluons around the quarks can strengthen their color charge. This effect is called anti-screening and is directly caused by the negative term in Eq. (1.7).

1.2.2 Confinement

Quarks are never observed as free particles, rather they are always bound into objects that are overall colorless, so called hadrons. This is caused by the behavior of the strong force with increasing distance r. The strength of the coupling rises beyond all limits, however at these scales, the perturbation theory is no longer valid.

The efforts to derive the correct form of the quark–(anti)quark potential from first principles are currently still ongoing. However, within the framework of the string model [37], the quark–quark potential is described by the empirical formula

$$V_{\text{strong}}(r) = -\frac{4}{3} \cdot \frac{\alpha_s}{r} + kr \,. \tag{1.8}$$

The first term in Eq. (1.8) is a Coulomb-like potential that dominates at small distances. However, as the distance grows ($r \gtrsim \alpha_s$) the potential becomes governed by the second term. At this point a string is created between the two quarks and, as the distance increases, it will reach a critical distance r_c, at which the energy density is enough to create a quark–antiquark pair. These new quarks start immediately interacting with the original particles which reduces the overall potential and creates colorless objects once again.

1.2.3 Asymptotic freedom

The behavior of the strong coupling constant leads to peculiar behavior of the strong interaction. As can be seen in the formula (1.8), at high energy scales and very small distances, the α_{s} becomes arbitrarily small

$$Q^2 \to \infty \Rightarrow \alpha_{\text{s}} \to 0 \,. \tag{1.9}$$

This phenomenon is called asymptotic freedom as, at very large energy scales, quarks and gluons can effectively move freely, i.e. they behave in an opposite manner to the electromagnetic interaction where the coupling constant gets larger with higher energy.

1.3 Ultra-relativistic heavy-ion collisions

One of the scientific frontiers of the current physical research is the study of properties of matter under extreme conditions. The highest man-made temperatures and pressures yet can be achieved in heavy ion-ion and proton-proton collisions in particle accelerators. In such facilities, a new state of matter — the strongly-coupled quark-gluon plasma (sQGP) [11] is created. One of such accelerators is the Relativistic Heavy Ion Collider (RHIC – described in Section 3.1) located in Brookhaven National Laboratory in the USA. It is capable of reaching the collision energy per nucleon of $\sqrt{s_{\mathrm{NN}}} = 200\,\mathrm{GeV}$. The collisions are called ultra-relativistic because the energy of the nucleons is much higher than their rest masses ($E \gg m$). Note that in this chapter, we use natural units where the speed of light in vacuum is equal to $c = 1$, the Boltzmann constant $k = 1$, and the reduced Planck constant $\hbar = 1$.

1.4 Phase diagram of the quark-gluon plasma (QGP)

Experimental evidence and theoretical predictions suggest that with high enough temperature (around 170 MeV) the usual nuclear matter can enter a new state, the so called strongly-coupled quark gluon plasma (sQGP) [11]. Figure 1.2 shows an illustration of the QCD phase diagram. The y-axis shows the temperature T and the x-axis shows the baryon-chemical potential η_{B} which represents the potential of the difference in numbers between baryons and anti-baryons. In the bottom-left corner, we can see the hadronic matter, where the quarks are always trapped – confined inside hadrons (e.g. the protons at rest have a baryon chemical potential equal to $\eta_{\mathrm{B}} = 938\,\mathrm{MeV}$ and the temperature of $T \approx 0$). As we go higher in temperature in heavy-ion collisions, the baryon density gets lower (the number of anti-baryons, compared to baryons, is increasing). At one point, a transition into a new state of matter occurs — the quark-gluon plasma is created. The temperature is so high that the

quarks and gluons are no longer trapped inside hadrons — they become deconfined.

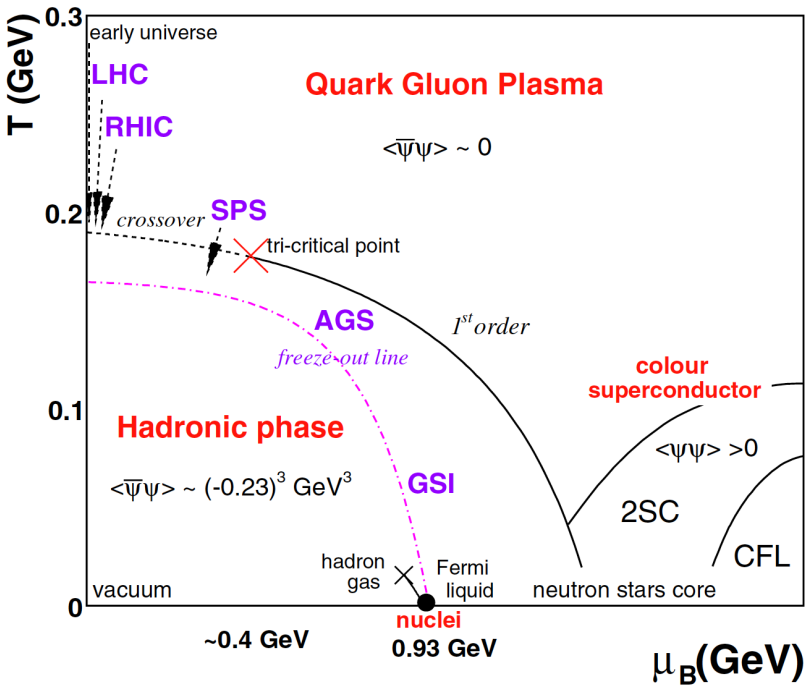

Figure 1.2: The QCD phase diagram. Taken from [38].

At the top RHIC energies ($\sqrt{s_{\rm NN}} = 200\,\text{GeV}$) and at the LHC energies for the Pb+Pb collisions (e.g. $\sqrt{s_{\rm NN}} > 2.76\,\text{TeV}$ in the collider mode), the experimental evidence and lattice–QCD (lQCD) calculations point to a crossover (second-order) transition between the hadron matter and the sQGP [38]. lQCD calculations suggest, however, that at lower temperatures and higher baryon chemical potential, the transition changes to a first-order one. Therefore, in between, there has to be a critical point. RHIC beam energy scan program, in which $\sqrt{s_{\rm NN}}$ is scanned by lowering the energy of the accelerated nuclei, is an ongoing endeavor to find this critical point [39]. Figure 1.2 also shows examples of past and future ion accelerators that will help map the area around the QCD critical point, namely SPS at CERN and AGS at BNL which have both facilitated rich heavy-ion programmes and currently serve as booster accelerators for the LHC and RHIC, respectively. A bit lower is th eaccelerator Facility for Antiproton and Ion Research (FAIR) [40] at the GSI Helmholtz Centre for Heavy Ion Research laboratory that is currently being constructed. FAIR experiments will be able to

measure heavy-ion collisions at lower energy, compared to RHIC or the LHC, but at very high luminosity. On the right-hand side of the QCD phase diagram, lay other exotic states of matter that are theorized to be inside neutron-star cores, e.g. the color superconductor state.

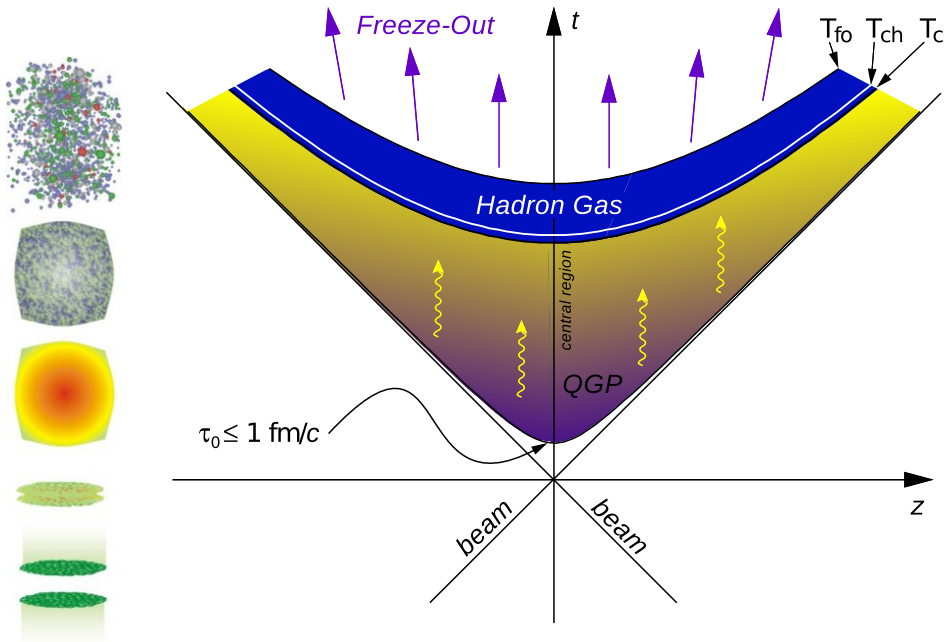

Figure 1.3: The space-time evolution of a heavy-ion collision. Taken from [41].

The space-time evolution of a heavy-ion collision is shown in Figure 1.3. When we look at the proper time around $\tau \simeq 1\,\mathrm{fm}/c$, the local thermodynamic equilibrium is established and from this point on, the system can be described hydrodynamically. This is when the system is going throgh the QGP phase, in which the quarks are deconfined, until it cools down to the temperature of the chemical freeze-out $T_{\mathrm{ch}} \simeq 165\,\mathrm{MeV}$ [42, 43]. From now on, the single quarks become confined again in hadrons – baryons and mesons. The hadrons can, however still interact with each other because the density is high enough; this state of the system is called the hadron gas. After some time, the distances between the hadrons become long enough that the mean free path of the hadrons becomes higher than the volume of the medium. This is called the kinetic freeze-out with the corresponding temperature measured as $T_{\mathrm{fo}} \simeq 100\,\mathrm{MeV}$. At this point, the average bulk velocity is still about $\sim 1/2c$ when the hadrons become free-streaming and can be picked by the detectors.

1.5 Experimental signatures of the QGP

Even though the QGP was theoretically predicted by the lattice QCD and from thermodynamic principles, it took decades, before its formation was experimentally proven at ion–ion colliders such as the SPS at CERN and RHIC at BNL. This was not done by one single measurement, but rather several analyses of the collision products that finally drew the overall picture of the QGP phase. These measurements include spectra of the outgoing particles in A+A collisions with comparison to the p+p counterpart, the azimuthal distribution of particles, or the properties of jets. Today, the formation of the QGP in high-energy heavy-ion collisions is seldom disputed, but these measurements still serve as probes into the properties of this novel strongly-interacting state of matter and — with ever increasing precision — describe the properties of the QGP and provide the needed restrictions to theoretical calculations of the QGP's behavior.

1.5.1 The nuclear modification factor R_{AA}

One of the ways of looking into the properties of the QGP is to compare the spectra of particles produced in p+p collisions $\mathrm{d}N_{\mathrm{AA}}/\mathrm{d}p_{\mathrm{T}}$ and in heavy-ion collisions $\mathrm{d}N_{\mathrm{AA}}/\mathrm{d}p_{\mathrm{T}}$, divided by the average number of binary nucleon-nucleon collisions $\langle N_{\mathrm{coll}} \rangle$. The ratio of these two is called the nuclear modification factor R_{AA}

$$R_{\mathrm{AA}} = \frac{\mathrm{d}N_{\mathrm{AA}}/\mathrm{d}p_{\mathrm{T}}}{\langle N_{\mathrm{coll}} \rangle \, \mathrm{d}N_{\mathrm{pp}}/\mathrm{d}p_{\mathrm{T}}} \tag{1.10}$$

and describes how much the spectrum is modified in nucleus–nucleus collisions.

A beautiful illustration of the modification of particle spectra in central heavy-ion collisions is shown in Figure 1.4. It summarizes R_{AA} measurements of identified particles, performed by the Phenix experiment at RHIC in central Au+Au collisions at $\sqrt{s_{\mathrm{NN}}} = 200\,\mathrm{GeV}$. Its data-points clearly demonstrate that different particles interact differently with the QCD medium, e.g.:

- π^0: pions are greatly suppressed in central Au+Au collisions, compared to p+p. This

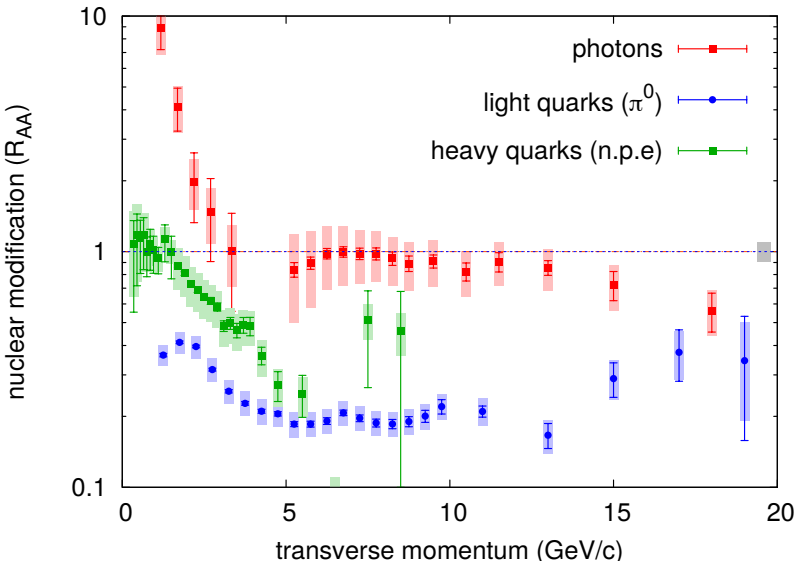

Figure 1.4: R_{AA} vs p_{T} measured by the Phenix experiment in central Au+Au collisions for several light-flavor mesons (π^0), electrons from open-heavy-flavor decays, and direct photons. Taken from [44].

is attributed to momentum loss due to interactions of quarks with the medium and also of formed mesons in the hadron-gas phase.

- heavy-flavor electrons: one of the big surprises at RHIC, even after the observation of jet quenching, was that the suppression for electrons resulting from heavy-flavor electrons was almost as strong as that observed for light mesons, despite the fact that heavy-flavor quarks were not expected to couple strongly to the medium.

- direct photons: the prompt photons, coming from the initial stages of the collision, are not expected to interact with the medium in a significant way. This can be seen at the intermediate and high p_{T}, although there is a hint of suppression at the two data-points with highest p_{T}. At low p_{T}, an enhancement is observed in Au+Au collisions, because of thermal photons generated in later stages of the expansion of the medium.

Similarly to R_{AA}, we can study the nuclear modification by comparing the particle yield in central heavy-ion collisions to peripheral ones, divided by the ratio of the number of binary collisions in these centrality brackets. This ratio is called modiication factor R_{CP} and is

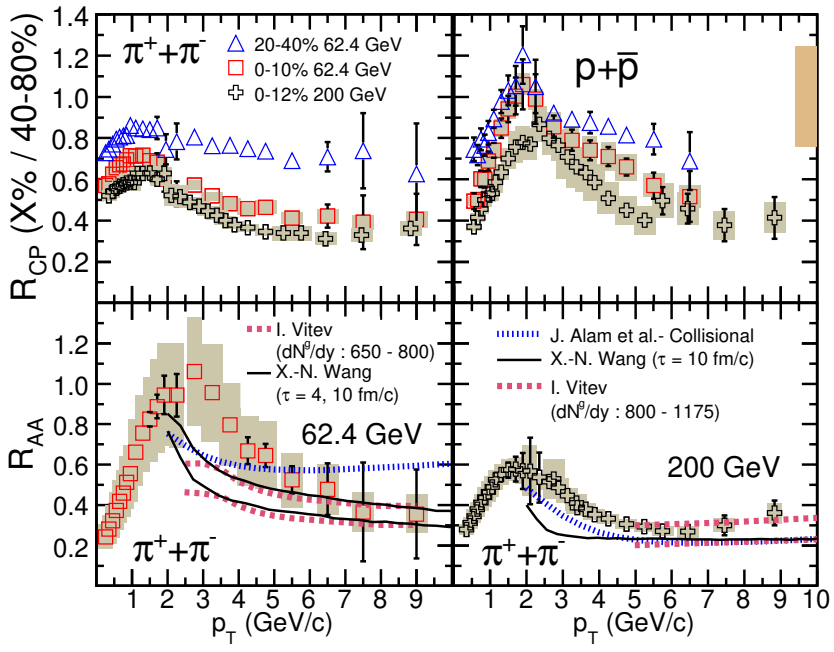

Figure 1.5: Nuclear-modification factors R_{AA} and R_{CP} vs p_{T} for identified π and p, measured by STAR at $\sqrt{s_{\mathrm{NN}}} = 200\,\mathrm{GeV}$ and at $\sqrt{s_{\mathrm{NN}}} = 62.4\,\mathrm{GeV}$. Taken from [45].

defined as

$$R_{\mathrm{CP}} = \frac{\mathrm{d}N_{\mathrm{central}}/\mathrm{d}p_{\mathrm{T}}}{\mathrm{d}N_{\mathrm{peripheral}}/\mathrm{d}p_{\mathrm{T}}} \cdot \frac{\langle N_{\mathrm{coll}}(\mathrm{peripheral})\rangle}{\langle N_{\mathrm{coll}}(\mathrm{central})\rangle}\,. \tag{1.11}$$

Figure 1.5 shows the R_{AA} and R_{CP} of identified π and p in Au+Au collisions at $\sqrt{s_{\mathrm{NN}}} = 200\,\mathrm{GeV}$ and at $\sqrt{s_{\mathrm{NN}}} = 62.4\,\mathrm{GeV}$. R_{AA} of π is compared to several theoretical predictions that include ideal (non-viscous) hydrodynamic calculations and energy loss of quarks with high momenta in the QGP [46–48]. The proton R_{CP} is significantly larger in the intermediate $1.5 < p_{\mathrm{T}} < 3\,\mathrm{GeV}/c$ region. This phenomenon is called baryon enhancement and is attributed to the coalescence hadronization mode in central collisions.

1.5.2 Azimuthal distribution of the collision, the v_n coefficients, and NCQ scaling

Another way of probing the sQGP medium is measuring the distribution of outgoing particles in the azimuthal angle ϕ. To evaluate the properties of this distribution, it is usually

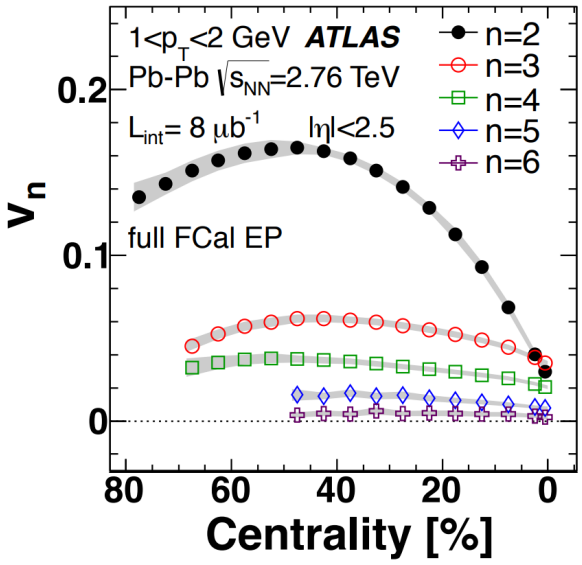

Figure 1.6: v_n coefficients vs centrality in Pb+Pb collisions. Taken from [49].

recalculated in terms of the Fourier expansion

$$E\frac{\mathrm{d}^3N}{\mathrm{d}p^3} = \frac{1}{2\pi}\frac{\mathrm{d}^2N}{p_\mathrm{T}\mathrm{d}p_\mathrm{T}\mathrm{d}y}\left(1 + 2\sum_{n=1}^{\infty} v_n \cos[i(\phi - \psi_n)]\right) \tag{1.12}$$

where ψ_n is the spatial plane of symmetry for the n-th harmonic. The first three v_n coefficients (v_1, v_2, v_3, ...) are called the direct flow, the elliptic flow, and triangular flow coefficients for v_1, v_2, and v_3, respectively. They can be reformulated using the formula

$$v_n = \langle \cos[n(\phi - \psi_n)] \rangle \,, \tag{1.13}$$

where the angular brackets denote the average over all particles in an event.

Figure 1.6 shows the second and further v_n coefficients of charged particles [49], all the way to v_6 in different centrality regions. The shape of the v_n is mainly driven by two competing phenomena: Looking at the elliptic flow v_2, we can notice that, as we move from central (from 0 % on the right-hand side) to more peripheral collisions, the v_2 rises up to $\approx$ 50 % centrality. This can be attributed to increasing eccentricity in the initial collision as in this centrality region, the v_2 value is mostly driven by the pressure gradient. When the impact parameter of the two spherical nuclei increases, the shape of the overlapping region becomes

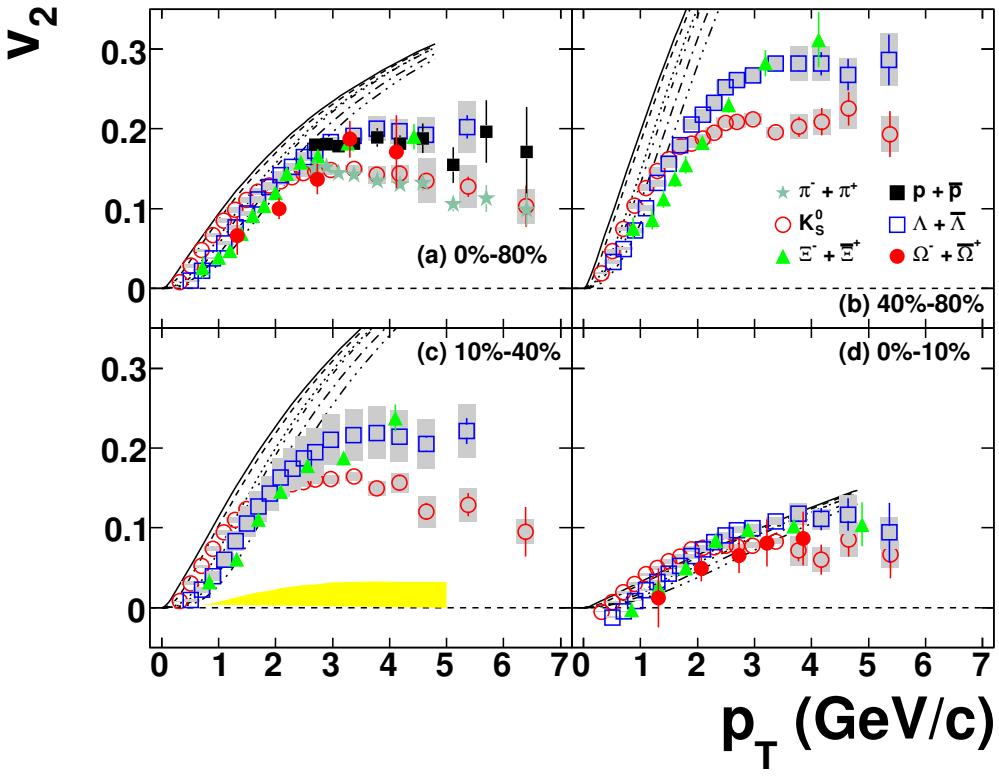

Figure 1.7: v_2 as a function of p_{T} of several hadron species in four centrality regions of Au+Au collisions at $\sqrt{s_{\mathrm{NN}}} = 200\,\mathrm{GeV}$ measured by STAR. Taken from [50].

more oblong, therefore the pressure gradient increases in the direction of the shorter axis. In more peripheral collisions (left-hand side of Figure 1.6), however, this trend is stopped. As the size of the system decreases, v_2 falls in peripheral collisions as the outgoing particles do not have a chance to interact as much.

When looking at the triangular flow v_3, we can observe that the overall trend is similar to v_2, although it is overall smaller. The initial rise in central collisions is caused by the increase in fluctuations in the initial shape of the fireball as the system gets smaller. The downward trend in peripheral collisions is attributed to less interactions in smaller systems like in the case of v_2. Further flow coefficients $v_4 - v_6$ show that the v_n decrease with rising n in intermediate centralities as well.

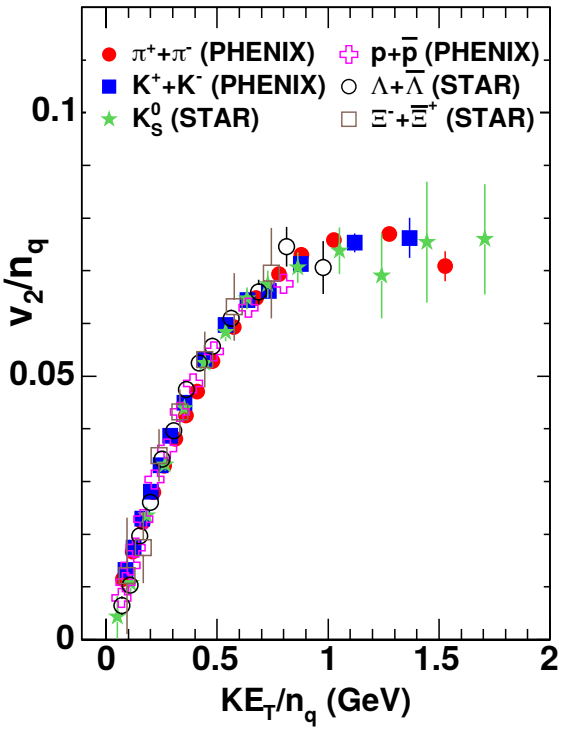

Figure 1.8: v_2/n_q plotted vs $KE_\mathrm{T}/n_\mathrm{q}$ for several hadron species in Au+Au collisions at $\sqrt{s_\mathrm{NN}} = 200\,\mathrm{GeV}$. Taken from [51].

Another way to differentiate the azimuthal anizotropy of ion-ion collisions is to look at the v_n coefficients of different particle species. Figure 1.7 shows the v_2 for several identified hadrons in Au+Au collisions measured by the STAR experiment. The solid yellow band in the plot 1.7(c) represents a non-flow estimate, where particles would fly from the initial collision without interacting with one another. The solid and dashed lines correspond to ideal (non-viscous) hydrodynamic calculations [52] for (from top to bottom) π, K, p, Λ, Ξ, and Ω. These calculations overpredict the data at $p_\mathrm{T} > 2\,\mathrm{GeV}/c$, however at low p_T, they predict the v_2 relatively well. From this, we can conclude that the viscosity in the QGP is very low, and thus the QGP is close to an ideal liquid.

Another observation, that we can draw from Figure 1.7, is that the v_2 is higher for particles with lower mass. This approximate phenomenon is called mass ordering. If we plot the v_2, however, divided by the number of valence quarks n_q as a function of the transverse mass (or

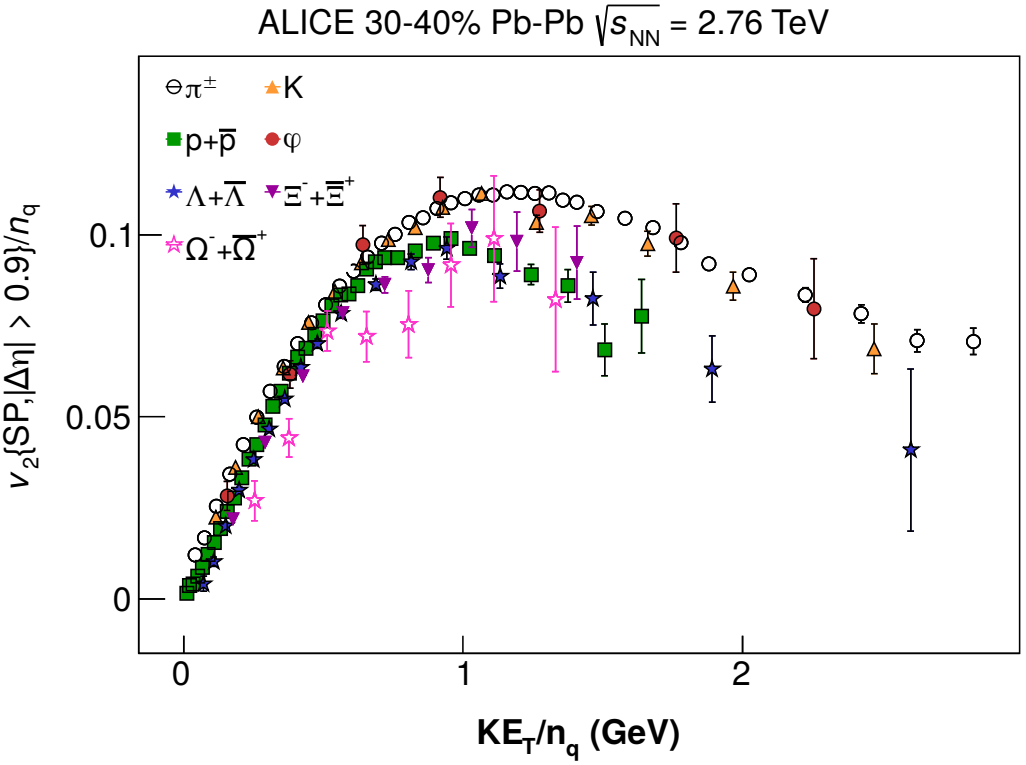

Figure 1.9: v_2/n_q plotted vs KE_T/n_q for several hadron species in Pb+Pb collisions measured by ALICE. Taken from [53].

transverse energy)

$$KE_T = \sqrt{m^2 + {p_T}^2}\,, \tag{1.14}$$

divided by n_q as well, just like in Figure 1.8, we observe that this function aligns remarkably for all the measured hadron species. This phenomenon is called the number-of-constituent-quarks (NCQ) scaling and suggests that the v_2 is driven predominantly by the motion in the quark stage. When performing a higher-precision measurement of the v_2 at higher collision energies, however, such as in Figure 1.9 performed by ALICE at the LHC, the scaling is observed to work only approximately. This can be attributed to the collective behavior in the hadron stage where hadrons interact as single particles.

1.5.3 Jet quenching and parton energy loss

One of the most important signatures that confirmed the creation of the QGP in heavy-ion collisions is the, so called, jet quenching. High-p_{T} partons must be created in the initial stages of the collision as later, the energy density of the medium is not sufficient to boil off or scatter such high-energy partons. These partons loose energy in the medium and later form jets that can further interact with the medium and loose energy even further. They are effectively quenched.

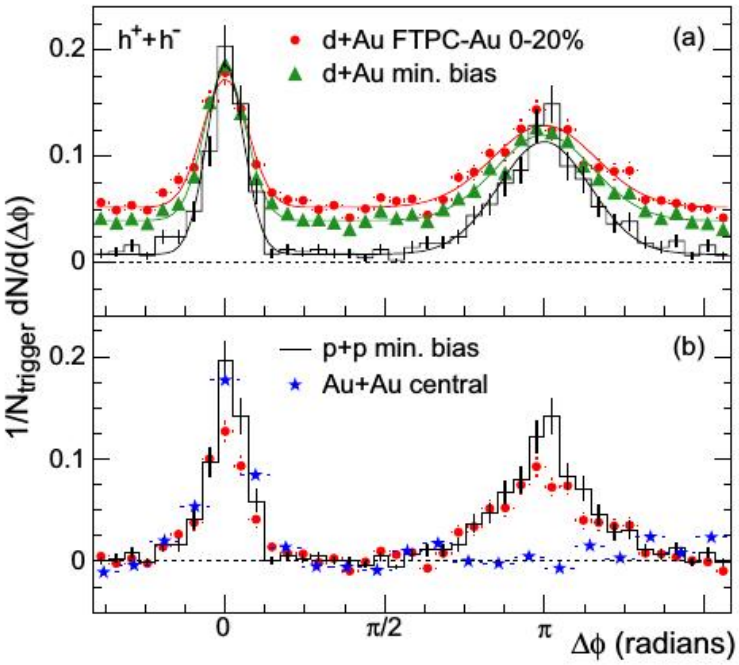

Figure 1.10: Correlations of high-p_{T} charged particles measured in Au+Au, d+Au, and p+p collisions. The trigger particle is measured in the p_{T} range of $4\,\mathrm{GeV}/c < p_{\mathrm{T}} < 6\,\mathrm{GeV}/c$. Taken from [54].

One of the observable signatures of jet-quenching is the correlation of high-energy hadrons in azimuth ϕ in central heavy ion-ion collisions. Most high-energy partons are created in binary processes where two partons have opposite direction of movement ($\Delta\phi = \pi$) due to momentum conservation. This is clearly shown in Figure 1.10 where the trigger particles have a transverse momentum of $4\,\mathrm{GeV}/c < p_{\mathrm{T}} < 6\,\mathrm{GeV}/c$, but the measured particles are required

to have only $p_{\mathrm{T}} > 2\,\mathrm{GeV}/c$. In p+p and d+Au collisions, we observe a peak of correlated particles on the near-side ($\Delta\phi = 0$) and on the away-side ($\Delta\phi = \pi$) of the trigger particle, whereas in Au+Au collisions, this peak is clearly missing. This is due to the energy loss of the away-side going particles in the medium.

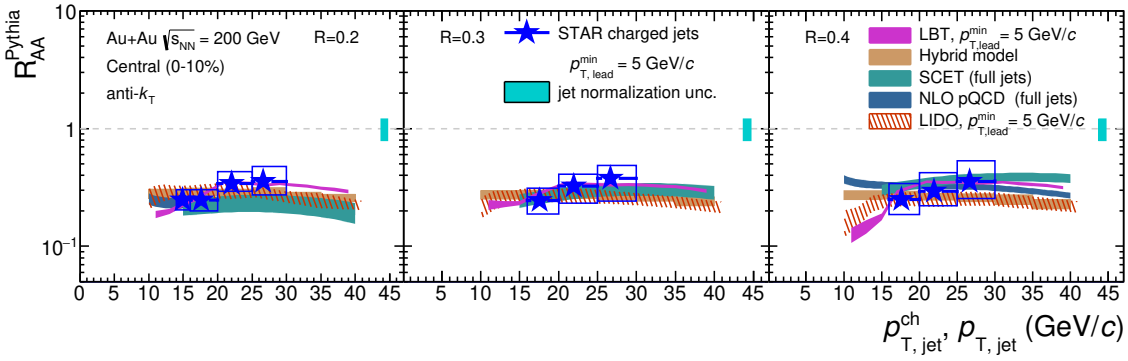

Figure 1.11: Jet nuclear modification factor $R_{\mathrm{AA}}^{\mathrm{Pythia}}$ measured in Au+Au collisions at $\sqrt{s_{\mathrm{NN}}} = 200\,\mathrm{GeV}$, compared to theoretical calculations [55–60]. Taken from [61].

Another way of measuring the properties of jets in heavy-ion collisions is to measure the nuclear modification factor R_{AA}. The p_{T} spectrum of jets that loose energy will be shifted towards lower p_{T} which will result in lower R_{AA}. A recently published paper from STAR [61] shows the jet R_{AA}, measured in Au+Au collisions with PYTHIA [62] used as a p+p reference. This result is shown in Figure 1.11 and correspond to relatively high modification of jets in the heavy-ion collisions. It is, however, consistent with models that include interaction of jets with QGP [55–60].

Chapter 2

Open Heavy Flavor

Open-heavy-flavor hadrons are ones that have a non-zero charm content, meaning that the number of valence-anti-charm quarks is different from the number of valence-charm quarks. In this chapter, we deal with the production of open charm in heavy-ion collisions at RHIC and, in the end, we summarize the current knowledge about the production of the charmed Λ_c baryon in e+e, e+p, p+p, p+A, and A+A collisions.

2.1 Heavy-flavor production in heavy-ion collisions

The heavy quarks such as c or b have much higher masses ($m_c \simeq 1.25\,\mathrm{GeV}/c^2$ and $m_b \simeq 4.5\,\mathrm{GeV}/c^2$ [25]) as compared to the light quarks (u, d, and s) which, together with gluons, make most of the QGP bulk. During most of the expansion (after $\sim 0.1\,\mathrm{fm}/c$ for the c-quarks at top-RHIC energies) the thermal energy of the system is too low to create the heavy quarks [63, 64]. As a result, they can be only produced in hard processes during the very early stages of the collision. Due to their relatively long life times, as compared to the thermally interacting medium, they can experience the whole evolution of the system and can act as excellent probes into the processes of energy loss in the sQGP. Moreover, since their masses are much higher than T_{ch}, the heavy quarks retain their identity and can serve as ideal probes into the hadronization process of the medium, e.g. determine whether lighter quarks are picked up by the heavy quarks or they fragment independently.

The typical momentum exchange of the heavy particles (both quarks and hadrons) is relatively small, compared to the thermal momentum $p^2_{\mathrm{Q,th}} \simeq 2m_{\mathrm{Q}}T$ [64] where m_{Q} is the mass of the particle and T is the temperature of the system. The thermal relaxation time of heavy particles $\tau_{\mathrm{Q}} \simeq \tau_{\mathrm{th}} m_{\mathrm{Q}}/T$ is also much longer than in the bulk medium τ_{th}. The heavy particles, therefore, move akin to Brownian particles in the expanding medium with many small kicks from the bulk particles.

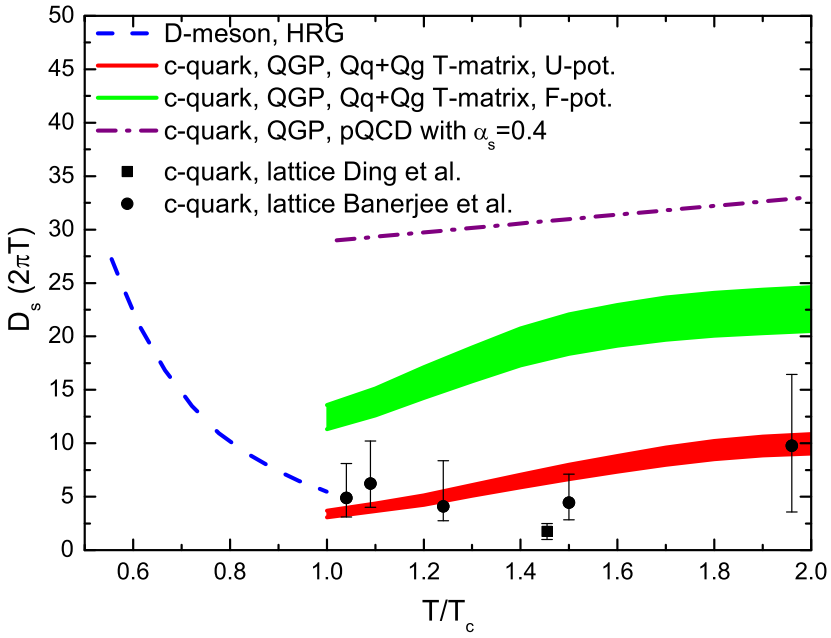

Figure 2.1: Charm-quark spatial diffusion coefficient D_s multiplied by $2\pi T$ at the c-quark momentum limit of $p = 0$, calculated in lQCD (black circles and squares [65, 66]) and compared to models with different elastic interactions of the charm quark. The green and red bands denote a T-matrix approach with heavy-quark+gluon and heavy-quark+light-quark interactions. The bands denote limit cases with the free-quark potential (F-potential) and internal-quark potential (U-potential), calculated in lQCD [67]. The dashed-dotted line denotes a perturbative-QCD (pQCD) approach with strong-interaction constant set as $\alpha_{\mathrm{s}} = 0.4$. The dashed line denotes the diffusion of D-mesons in a hadron-resonance gas [68]. Figure taken from [63].

Phenomenology can greatly benefit from the measurements of the heavy-flavor particles also because several variables that describe the behavior of the heavy quarks in QGP can

be calculated in lQCD. One of these variables is the spatial diffusion coefficient D_s [65, 66], defined by the average displacement squared

$$\langle r^2 \rangle = (2d) D_s t \tag{2.1}$$

where t denotes time and the factor d is the number of spatial dimensions. A small value of the D_s characterizes strong coupling (therefore frequent rescattering of the particle) with the medium. The thermal relaxation τ_{Q} is directly related to the D_s [64]

$$\tau_{\mathrm{Q}} = \frac{m_{\mathrm{Q}}}{T} D_s \,. \tag{2.2}$$

The delay in thermal relaxation of the heavy quarks is, therefore, proportional to m_{Q}/T. This relation suggests that D_s is a general medium property and when scaled by the thermal wavelength of the medium $\lambda_{\mathrm{th}} = 1/(2\pi T)$, one receives a dimensionless property of the medium that has been suggested [69, 70] to be related to the ratio of sheer viscosity to the entropy density η/s

$$D_s(2\pi T) \propto \frac{\eta}{s}(4\pi) \,. \tag{2.3}$$

Figure 2.1 shows theoretical calculations of $D_s(2\pi T)$ from the first principles (i.e. lQCD [65, 66]) and estimates, employing pQCD and the T-matrix in the quantum field theory [67]. The temperature scale is prolonged bellow the critical temperature T_{c} and the diffusion of the D-mesons in the hadron-resonance gas is considered from the calculation [68], because the c-quarks are likely hadronized in a medium with such temperature.

D_s cannot be measured experimentally directly. However with the increasing precision of the data, phenomenological models can make relatively accurate estimates, when comparing the calculations to the experimental data, e.g. the nuclear-modification factor R_{AA} or the elliptic flow coefficient v_2 of the D-mesons with one c-quark.

2.2 Baryon enhancement, baryon to anti-baryon ratio, and coalescence of the Λ_c baryon

An enhancement of strange baryons compared to mesons has been observed in the intermediate-p_T range in central heavy-ion collisions at RHIC [73] and the LHC [74]. This phenomenon is known as strange baryon enhancement and is believed to be one of the key pieces of evidence of the existence of the sQGP. This behavior can be explained via hadronization models that include quark coalescence [75, 76], which is a process in which the quarks are combined to form hadrons. This is a very different process to the quark fragmentation, in which new quarks are created from the vacuum which is the process that governs the hadronization in p+p and e+e collisions.

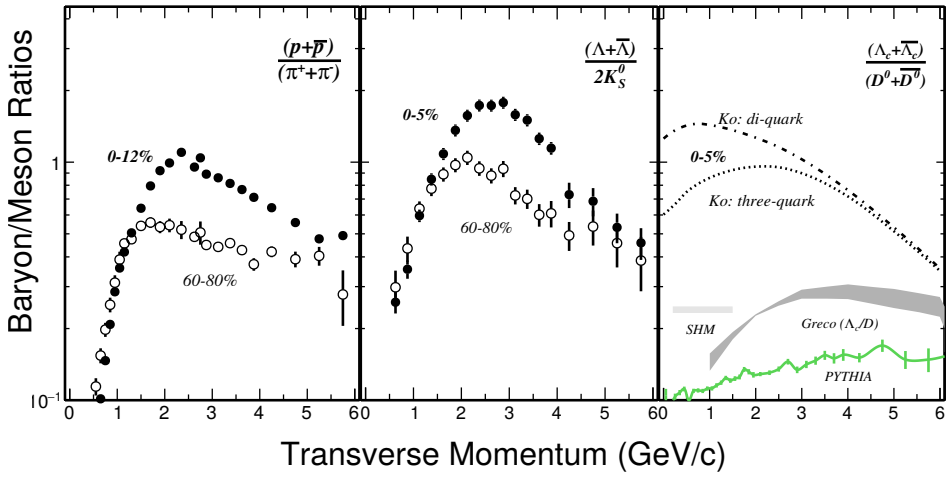

Figure 2.2: Baryon to meson ratio in RHIC Au+Au collisions with the center of mass energy per nucleon $\sqrt{s_{NN}} = 200\,\text{GeV}$ vs transverse momentum (p_T) [77]. Left: Ratio of the invariant yields of p and $\overline{\text{p}}$ over π^+ and π^- at STAR for the centralities 0–12 % and 60–80 % [73]. Middle: ratio of the yields of Λ over K^0_s at STAR for central (0–5 %) and peripheral (60–80 %) collisions. Right: Models of ratios of Λ_c over D^0 [78–80].

The baryon enhancement observed at RHIC is demonstrated in Figure 2.2, in which the left-hand-side panel shows the ratio of the yield of p and $\overline{\text{p}}$ to π^+ and π^-, and the middle panel is a plot of the ratio of Λ^+ and $\overline{\Lambda}^-$ to 2-times the yield of K^0_s, which both contain a strange quark. An enhancement in the p_T region of ∼2–4 GeV/c is clearly observed in the

case of the Λ baryons.

An interesting question (and one of the main topics of this document) is whether the charm baryons follow the same pattern as the strange ones. As the quark compositions of the Λ_c and D^0 are cud and $c\overline{u}$, respectively, we can draw a direct comparison to the measurement of Λ and K^0 (with light and strange valence quarks suu and $s\overline{d}$).

The panel in the right-hand-side panel of Figure 2.2 shows theoretical estimates of the ratio of the yields of Λ_c to D^0. The scenario with no coalescence is demonstrated by the green line which was produced using the PYTHIA simulator [62]. The dashed lines (Ko) show two coalescence models [78]: One where the quarks coalesce as the charm quark with a light di-quark structure and one where all three quarks coalesce. No rescattering in the hadron gas is considered in these two models. The darker gray band (Greco) indicates a model with three-quark coalescence calculated in the framework described in [81] with the results from [82], then the Λ_c and D meson diffusion is calculated, using an effective T–matrix approach [79]. Note that the denominator for this band is the sum of the yields of all D mesons ($D^{\pm}$, D^0, and $\overline{D^0}$). The light gray rectangle (SHM — Scattering with Hadronic Matter) is a model [80] with coalescence of di-quark and the c-quark. This model uses Λ_c diffusion in the hadronic matter, in which the Λ_c is allowed to change into other hadron species when scattering on other hadrons.

Another key signiture of coalescence process is the ratio between the yields of anti-baryons and baryons. Figure 2.3 shows such ratios for different experiments. At STAR, we can observe that with increasing strangeness content, the ratio gets closer to unity. This is because the u and d quarks are more abundant, compared to $\overline{u}$ and $\overline{d}$, due to the non-zero baryon chemical potential.

2.3 Charm production in p+p collisions

Figure 2.4 shows the inclusive cross-section of c–$\overline{c}$ pairs in p+p collisions at mid-rapidity at RHIC, Tevatron, and the LHC [84, 86–89]. At STAR, the total cross-section has been assessed via measurement of the cross-section of D^0 and D^* while assuming that the frag-

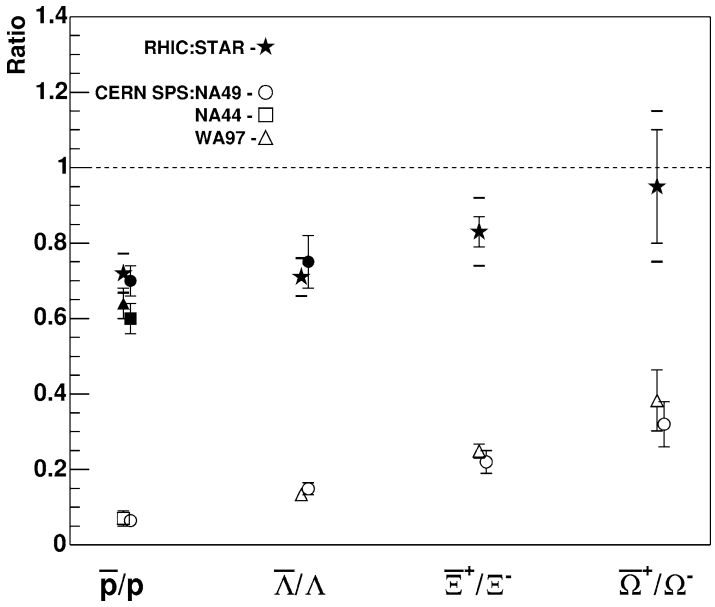

Figure 2.3: Ratio of the yields of baryons compared to anti-baryons measured at SPS and RHIC. The full symbols represent full maximum RHIC energy $\sqrt{s_{\mathrm{NN}}} = 200\,\mathrm{GeV}$ and the empty symbols represent experiments at SPS at CERN with the collision energy per nucleon $\sqrt{s_{\mathrm{NN}}} = 17\,\mathrm{GeV}$. Taken from [83].

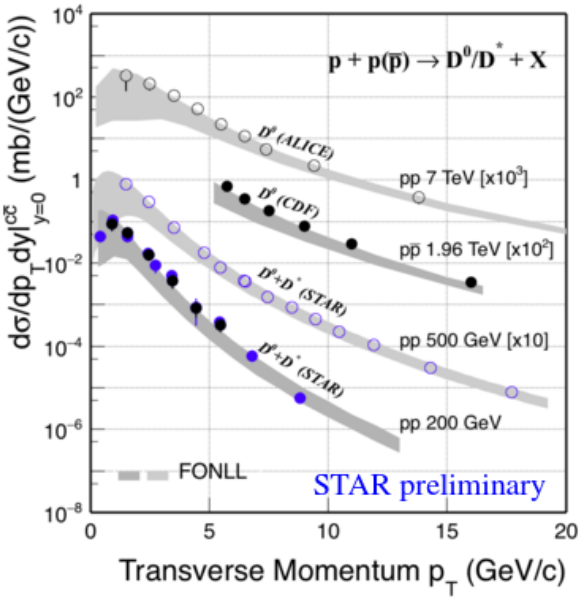

Figure 2.4: Charm quark pair production cross-section [84] at mid-rapidity vs. p_{T} [85–89].

mentation ratios of these mesons is known in p+p collisions at RHIC energies. We can see that throughout the experiments and collision energy $\sqrt{s}$, the data are consistent with the theory calculation using FONLL [85], although they are consistently on the upper limit of FONLL. This may be caused by a non-perturbative contribution to the total cross-section. If the charm quark production is not significantly altered by the nuclear Parton-Distribution Functions (nPDF), we can assume that the number of charm quarks scales with the number of binary collisions (N_{coll}), because charm quarks are created in the early stages in heavy-ion collisions. Therefore, with the charm cross-section known, by measuring the charm hadrons, we obtained calibrated probes into the interaction of quark-gluon plasma.

2.4 D^0 and $\mathrm{D}^{\pm}$ measurements

In p+p collisions, non-strange D-mesons are the most abundant hadrons including charm quarks. This makes them excellent tools for measuring the properties of the charm quarks.

2.4.1 D^0 R_{AA} and R_{CP} nuclear modification factors

Even if the inclusive-charm-quark production scales with N_{coll}, the D^0 spectrum shape can be significantly modified in Au+Au collisions. Fig. 2.5 shows the D^0 nuclear modification factor R_{AA} as a function of p_{T} in several centrality regions of the Au+Au collisions. The new results (black circles) [90] obtained with the HFT (see Section 3.5) are consistent with the published R_{AA} from 1.1 B minimum-bias events taken in the years 2010 and 2011 without the HFT (blue empty diamonds) [91]. For the new results, a much better precision is achieved despite the less statistics used. Compared to p+p collisions, the D^0 production is significantly suppressed at low and high p_{T} in central collisions which indicates strong interactions between charm quarks and the medium.

STAR has recently published [90] a high-precision measurement of the D^0 nuclear-modification factor R_{CP} (40–60 %). R_{CP} greatly benefits from the precision of the HFT, since it can be used in both central and peripheral collisions.

The D^0 R_{CP} measurement is shown in Figure 2.6. In the high-p_{T} region ($p_{\mathrm{T}} \gtrsim 3\,\mathrm{GeV}$), the

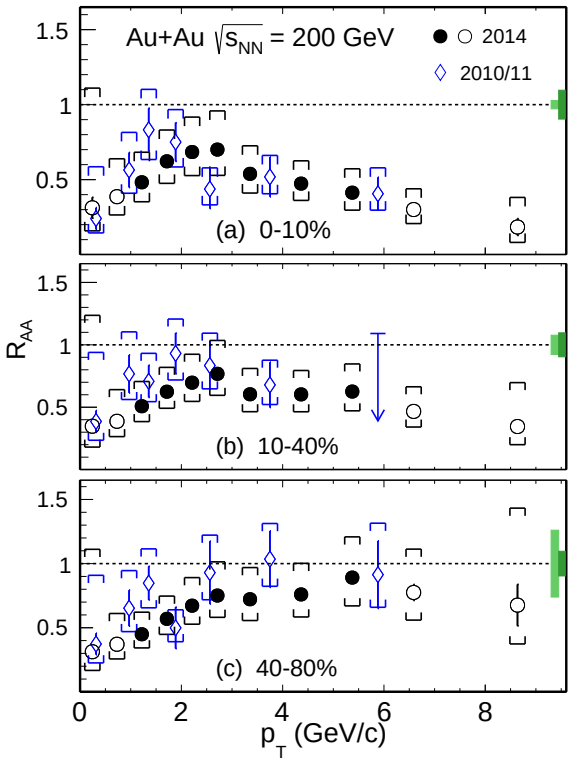

Figure 2.5: D^0 R_{AA} [90] measured in 0–10 % (a), 10–20 % (b), and 20–40 % (c) central Au+Au collisions at $\sqrt{s_{NN}} = 200\,\text{GeV}$ as a function of p_T. The light and dark green vertical bands around unity are uncertainties related to the N_{coll} in Au+Au collisions and the global normalization in the p+p collisions, respectively [91].

D^0 production is increasingly suppressed with centrality. The R_{CP} is compared to two models that include charm-quark diffusion. The Duke model [92,93] uses Langevin calculation of the charm-quark diffusion. Both radiative and collisional energy loss processes are included in this model. The hadronization of the charm quark is calculated in a hybrid approach that combines both fragmentation and coalescence. In the LBT (Linearized Boltzmann Transport) model [94, 95] a jet-transport framework is extended to include heavy quarks. The hadronization is handled in the same hybrid approach as in the Duke model. These models also agree with the D^0 v_2 measurement shown in the next section.

As an important crosscheck, STAR has measured the $D^{\pm}$ meson production as well. Figure 2.7 shows the nuclear modification factor R_{AA} in Au+Au collisions, recorded in 2014

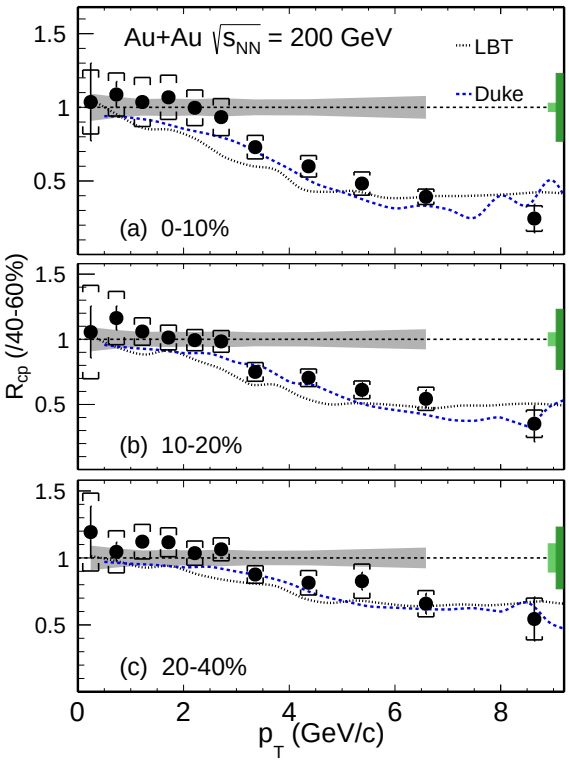

Figure 2.6: D^0 R_{CP} [90], with the 40–60 % centrality spectrum as a reference, measured in 0–10 % (a), 10–20 % (b), and 20–40 % (c) central Au+Au collisions at $\sqrt{s_{NN}} = 200\,\text{GeV}$ as a function of p_T. The light and dark green vertical bands around unity are uncertainties related to the N_{coll} in Au+Au collisions and the global normalization in the p+p collisions, respectively. The gray bands around unity depict the systematic uncertainty due to corrections on the uncertainty of the position of the primary vertex. The measurement is compared to model calculations [92–95].

and 2016 [96]. The $D^{\pm}$ production is consistent with the D^0 [90] in the whole p_T range in both, 0–10 % and 10–40 % centrality brackets.

2.4.2 D^0 azimuthal anisotropy, v_2, v_3, and the charm diffusion coefficient

Another way of probing the interactions of the charm quark with the sQGP medium is measuring the distribution of charmed hadrons in the azimuthal angle by measuring the Fourier terms v_n [50]. For light hadrons. The change in pressure normally drives the v_n

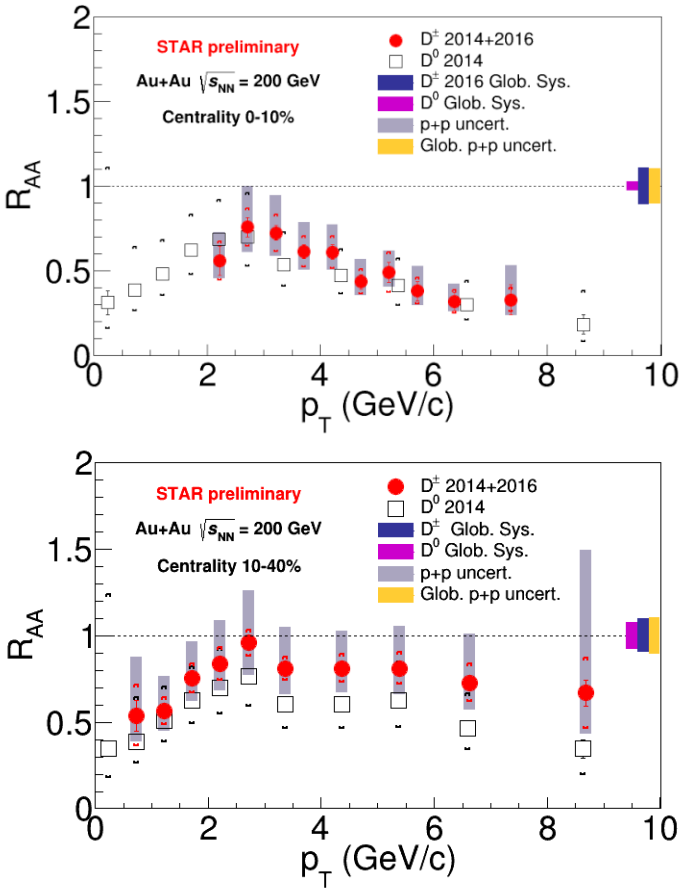

Figure 2.7: $D^{\pm}$ meson R_{AA} in 0–10 % (top) and 10–40 % (bottom) central Au+Au collisions. The gray bands depict the D^0 uncertainty in p+p collisions [90, 96]. The dark blue (yellow) band refers to the global uncertainty in Au+Au (p+p) collisions. Taken from [96].

coefficients as they move from areas with large pressure into areas with lower. Charm quarks are, however, created in hard collisions during the early stages of the evolution of the medium and because their masses are much higher than the QCD scale $m_c \gg \Lambda_{QCD}$ of the medium properties, their masses are not affected by the QCD medium. This makes the c-quarks compelling probes to the behavior of the medium as they are carried away in a similar fashion to Brownian particles in liquids or gases.

The HFT enables the measurement of the D^0 v_2 for the first time at RHIC, as shown in Figure 2.9. The v_2 values were calculated from 0–80 % central Au+Au collisions at $\sqrt{s_{NN}} =$ 200 GeV recorded in 2014 and 2016. The vertical bars (brackets) indicate the statistical

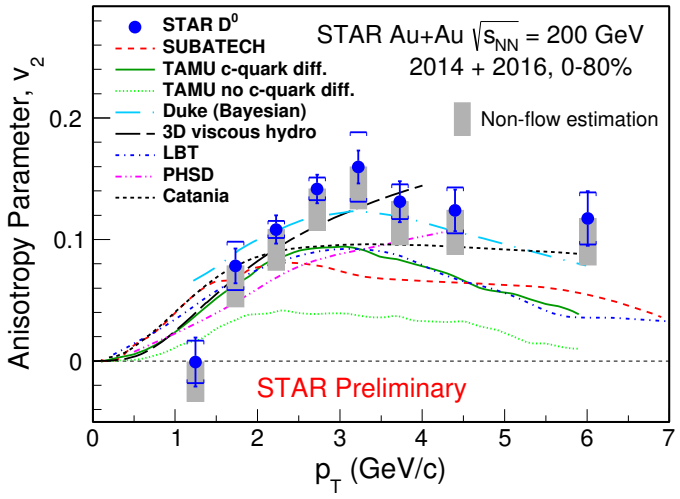

Figure 2.8: D^0 v_2 as a function of p_T for Au+Au collisions at $\sqrt{s_{NN}} = 200\,\text{GeV}$ [97], compared to theoretical calculations [92–95, 98–104].

(systematic) uncertainties while the gray bands represent the estimated non-flow contribution inferred from D meson–hadron correlations in p+p collisions. The data show that the v_2 is significantly larger than 0 above $1.5\,\text{GeV}/c$.

Several models [92–95, 98–104] are compared to the measurements of R_{AA} in Figure 2.5 and v_2 in 0–80 % centrality in Figure 2.8. The 3D viscous hydrodynamic calculation with AMPT initial conditions, tuned to the light-hadrons v_2 [103, 104], describes the D^0 v_2 data well which points to the thermal equilibrium between the c-quarks and the medium.

Another way of parametrizing the v_2 is using the number of valence quarks n_q and the transverse mass $m_T = \sqrt{{p_T}^2 - m_0^2}$, where m_0 is the rest mass of the particle. Figure 2.9 shows v_2/n_q of the D^0 [97] and several lighter hadrons [50] plotted versus $(m_T - m_0)/n_q$ in 10–40 % central Au+Au collisions. The v_2/n_q of the light-flavor hadrons follows the same pattern with relatively high precision. Remarkably, as shown in this Figure, the D^0 follow the NCQ scaling of the light-flavor hadrons at the RHIC top energy. This suggests that the charm quarks from D^0 were close to thermal equilibrium with the sQGP medium.

Models that incorporate diffusion of the charm quark with various values of the diffusion coefficient multiplied by the temperature $2\pi T D_s$ [92–95, 98–102] were compared to the R_{AA},

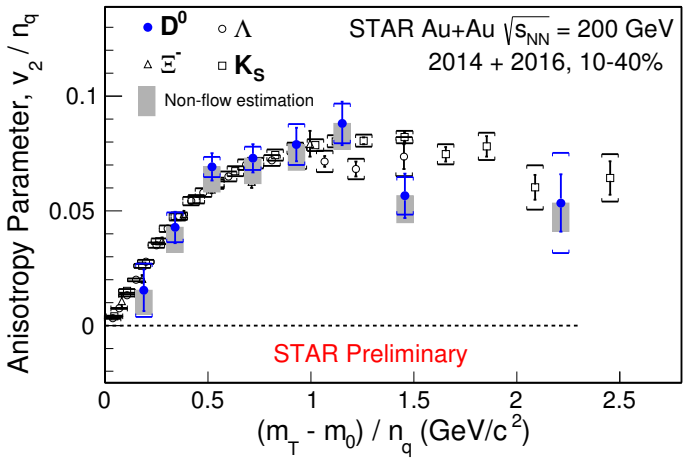

Figure 2.9: D^0 v_2/n_q, where n_q is the number of valence quarks, as a function of $(m_T - m_0)/n_q$ for Au+Au collisions at $\sqrt{s_{NN}} = 200\,GeV$ with centrality of 10–40 % compared to strange hadrons v_2/n_q [50, 97].

v_2, and v_3 data. The PHSD (Parton-Hadron-String Dynamics — pink dash-double-dot line in Figure 2.8) model [98, 100] uses the dynamical quasiparticle model to calculate an effective potential of the charm quark to the medium. It describes the data with $2\pi TD_s$ ~5–12. It is consistent with the data with the predicted transport coefficient of $2\pi TD_s$ ~3–6. The group from TAMU [99] (blue in 2.5 and full green lines in 2.8) employs a non-perturbative T-matrix approach with the assumption that two-body interactions can be described by a potential, which is a function of the transferred 4-momentum. Two scenarios of this model are plotted in Figure 2.8: one with no c-quark diffusion (lighter green) and one where the c-quark diffuses (darker green). The data clearly prefer the latter scenario in which c-quarks flow. This model predicts the charm quark diffusion coefficient multiplied by temperature as $3 \leq 2\pi TD_s \lesssim 11$. The SUBATECH group [101] (green in 2.5 and dashed red in 2.8) uses a pQCD approach with the Hard Thermal Loop (HTL) approximation for soft collisions. In this approach, the diffusion coefficient is within $2 \leq 2\pi TD_s \leq 4$. The model by the Duke university group [92, 93] uses $2\pi TD_s$ as a free parameter. The full red curve shown in Figure 2.5 and the cyan dot-dash curve from 2.8b use the value $2\pi TD_s = 7$ which is fixed to match the D^0 R_{AA} measured at the LHC. The Duke model can describe the shape

of R_{AA} well, however it systematically underestimates the v_2. The other two models are consistent with both R_{AA} and v_2 data. The inferred estimates of the diffusion coefficient of $2 \lesssim 2\pi D_s < 12$ are consistent with the lattice QCD calculations [65, 66] in the sensitive temperature range, corresponding to $\sqrt{s_{\mathrm{NN}}} = 200\,\mathrm{GeV}$ (between ∼1–2 T_{c}, where T_{c} is the temperature of the critical point).

2.5 Measurement of the $\overline{\mathrm{D}^0}/\mathrm{D}^0$ ratio

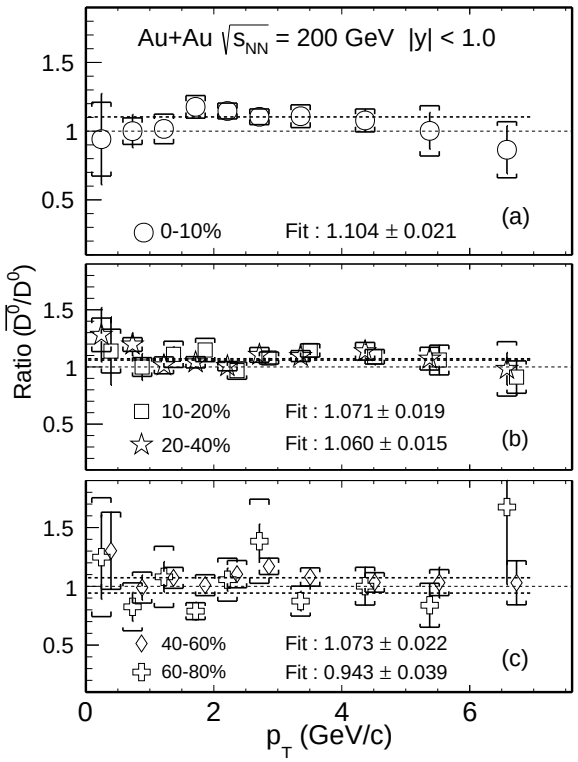

Figure 2.10: $\overline{\mathrm{D}^0}/\mathrm{D}^0$ invariant yield ratio at mid-rapidity ($|y| < 1$). The dashed lines illustrate constant function fits to the $\overline{\mathrm{D}^0}/\mathrm{D}^0$ ratios [90].

So far, we have discussed combined measurements of both D^0 and its antiparticle $\overline{\mathrm{D}^0}$. The charm quarks are produced in pairs, therefore, we would expect the same number of D^0 and $\overline{\mathrm{D}^0}$. The Statistical-Hadronization Model [107], however, suggests that the $\overline{\Lambda_{\mathrm{c}}{}^-}/\Lambda_{\mathrm{c}}{}^+$ is lower than unity and the c-quarks can get, therefore, depleted, compared to $\bar{\mathrm{c}}$-quarks. Figure 2.10

shows the $\overline{D^0}/D^0$ invariant-yields ratio plotted versus p_T, together with constant function fits of the data [90]. Although the ratio is at 1 when divided into p_T bins, the overall ratio is significantly larger than unity in the 0–60 % most central collisions. E.g. in the 0–10 % most central collisions, the fit is $4.9\,\sigma$ higher than unity.

2.6 D_s measurements

Thanks to the HFT, the D_s meson, consisting of a charm quark and a strange quark, is measured for the first time at RHIC [108]. Such measurements can shed more light on the mechanism of the charm quark coalescence.

In Figure 2.11, the yield ratio of D_s/D^0 measured by STAR is shown as a function of p_T [108]. The D^0 spectrum is obtained from the published STAR data [90]. No significant change of the ratio with centrality is observed. Moreover, the measured D_s/D^0 ratio is consistent within uncertainties with a similar measurement from minimum-bias Pb+Pb collisions measured by ALICE [109]. To compare our measurement to the D_s/D^0 in p+p collisions, PYTHIA 6.4 [62] is used, tuned to $\sqrt{s_{NN}} = 200\,\text{GeV}$ (green curve) and $\sqrt{s_{NN}} = 7\,\text{TeV}$ (magenta curve). The PYTHIA simulations are consistent with the ALICE measurement [110] of the D_s/D^0 ratio in p+p collisions (small brown circles). The STAR measurement is significantly enhanced compared to the p+p ratio in all the centrality brackets.

In Figure 2.12, we compare the D_s/D^0 yield ratio, as a function of p_T, to several theoretical predictions that incorporate quark coalescence in their calculations. The Tsinghua model [112] stands out as the only one that includes sequential coalescence in which the D_s hadronize earlier than D^0, denoted as Tsinghua (seq. coal.). This model does not count with any hadronization through fragmentation, only coalescence. The Catania model [113] can compare scenarios with only coalescence hadronization – Catania (coal.) – and with both, fragmentation and coalescence – Catania (coal.+frag.). The He, Rapp [114] calculation incorporates in itself resonance recombination model that conserves the number of heavy quarks, energy, and momentum. This model includes both, fragmentation and coalescence hadronization scenarios. The Cao,Ko model [115] also contains fragmentation and

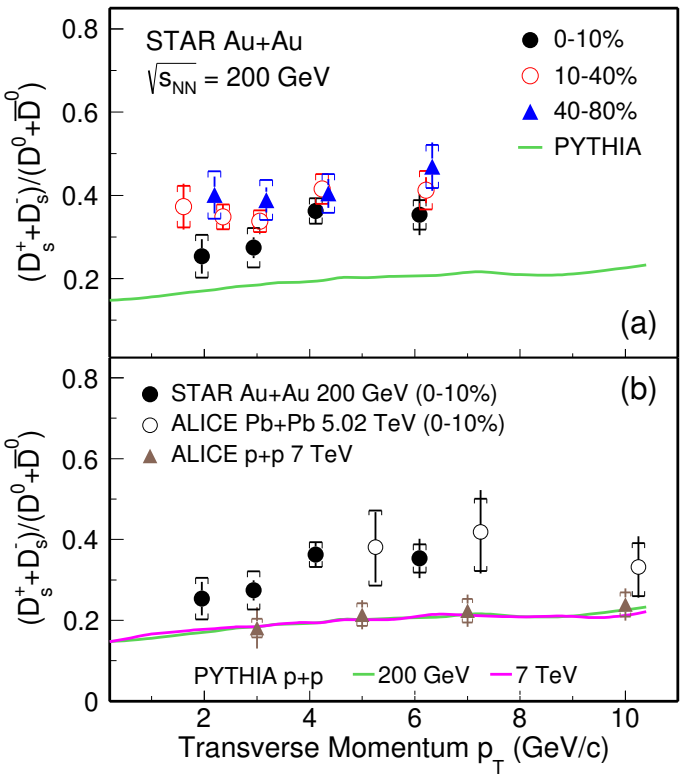

Figure 2.11: (a) D_s/D^0 yield ratio, measured in 0–10 % (full circles), 10–40 % (empty circles), and 40–80 % (triangles) central Au+Au collisions at $\sqrt{s_{NN}} = 200\,\text{GeV}$. (b) D_s/D^0 ratio in 0–10 % most central collisions, measured by STAR, compared to 0–10 % central Pb+Pb collisions (empty circles) [109] and p+p collisions (brown triangles) [110] measured by ALICE. The magenta and green curves denote PYTHIA simulations [62] tuned to p+p collisions at $\sqrt{s} = 7\,\text{TeV}$ and 200 GeV, respectively. Taken from [108].

coalescence, and energy conservation.

In the $p_T > 4\,\text{GeV}/c$ region, the measured D_s/D^0 yield ratio in 0–10 % most central collisions features the same general enhancement, compared to the PYTHIA p+p simulation, as models that include quark coalescence Tsinghua, Catania (coal.), He,Rapp, and Cao,Ko. There is, however, some tension in the lower-p_T region. On the other hand, the Catania (coal.+frag.) model describes the data in the low-p_T region, but fails to predict the high-p_T data points. The Tsinghua calculation for 20–40 % centrality is close to the measured data as shown in Figure 2.12(b). Overall, this comparison shows that charm-quark coalescence in

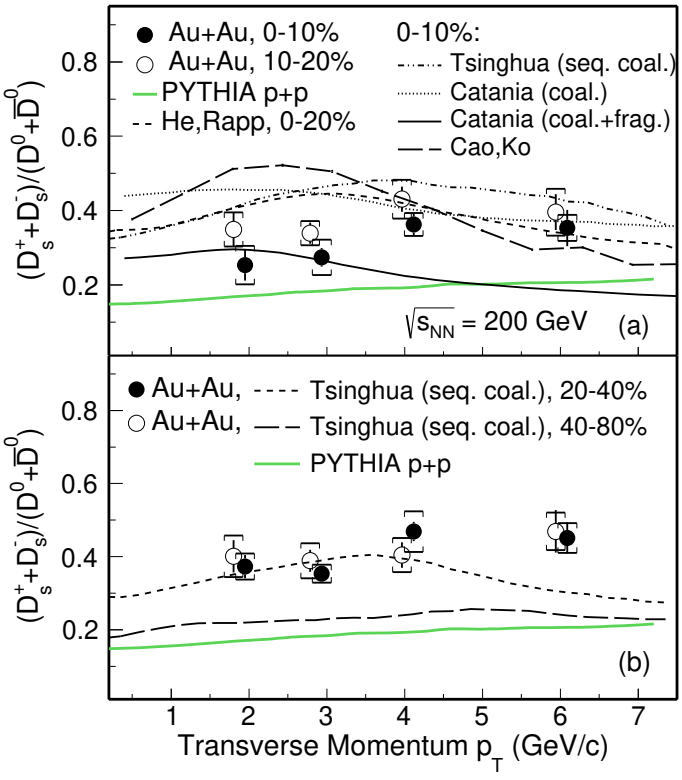

Figure 2.12: Top: The D_s/D^0 yield ratio in 0–10 % (full circles) and 10–20 % (empty circles) central Au+Au collisions at $\sqrt{s_{NN}} = 200\,\text{GeV}$, compared to theoretical predictions, calculated in central collisions (a), more peripheral collisions (b), and PYTHIA simmulation [62] in p+p collisions at $\sqrt{s_{NN}} = 200\,\text{GeV}$ (green curve). Taken from [108].

the surrounding QGP plays a significant role in the hadronization process.

2.7 Λ_c baryon measurements

In this section, we summarize the history of Λ_c measurements that have been published up to this point. We hope to convince the reader that the physics of production of charmed baryons is not yet understood and definitely compelling. Unfortunately, the facts, that the direct reconstruction is typically done from 3-body decays and that the lifetime times the speed of light is only $c\tau = 60\,\mu\text{m}$, makes these analyses relatively challenging.

2.7.1 Λ_c baryon

Table 2.1: Decay channels of Λ_c that can be used in its reconstruction [25]. Note that the $\Lambda_c^+ \rightarrow p^+ + K^- + \pi^+$ channel can have various resonances as an intermediate step in the decay.

Decay channel		Branching ratio
$\Lambda_c^+ \rightarrow$	$p^+ + K^- + \pi^+$ (all)	5.0 %
	$p^+ + K^*$	1.6 %
	$\Delta^{++} + K^-$	0.86 %
	$\Lambda^0(1520) + \pi^+$	1.8 %
	Nonresonant	2.8 %
$\Lambda_c^+ \rightarrow$	$p^+ + \overline{K}^0$	2.3 %
$\Lambda_c^+ \rightarrow$	$\Lambda^0 + \pi^+$	1.07 %

The Λ_c baryon has a quark content of c, u, and d [25]. It is the lightest charmed baryon with the rest mass of $m = 2286.46 \pm 0.14\,\mathrm{MeV}/c^2$. Its decay length is, however, quite short $c\tau = 60.0 \pm 1.8\,\mu\mathrm{m}$ which makes the reconstruction challenging, especially in heavy-ion collisions. The measurement of Λ_c is possible via the leptonic channels ${\Lambda_c}^+ \rightarrow e^+ + \nu_e + X$ or ${\Lambda_c}^+ \rightarrow \mu^+ + \nu_\mu + X$, however, the energy information is lost because of the outgoing neutrino, which cannot be detected, and therefore, the leptons cannot be separated from the ones from D and B mesons decay. Possible channels for the direct reconstruction of the Λ_c with all the decay products detected are listed in Table 2.1. In these channels all the decay particles can be reconstructed and, thus, the mass and momentum can be fixed.

2.7.2 Λ_c/D^0 ratio in e+e and e+p collisions

The Λ_c/D^0 ratio is sensitive to the hadronization properties of the charm quark. In Table 2.2 we summarize the results of the Λ_c/D^0 ratio measurements in e+e and e+p collisions. Other than the measurement performed by ZEUS on data recorded from e+p collision at HERA I,

the data are consistent between various experiments which suggests that Λ_c and D^0 hadronize via the same process in e+e and e+p collisions. This process is believed to be the vacuum fragmentation of the charm quark.

Table 2.2: Summary of the measurements of the Λ_c/D^0 in e+e and e+p collisions at different center-of-mass energies.

	$\Lambda_c/D^0 \pm \text{stat.} \pm \text{syst.}$	System	$\sqrt{s}\,(\text{GeV})$	Notes
CLEO [116]	$0.119 \pm 0.021 \pm 0.019$	e+e	10.55	
ARGUS [117, 118]	0.127 ± 0.031	e+e	10.55	
LEP average [119]	$0.113 \pm 0.013 \pm 0.006$	e+e	91.2	
ZEUS DIS [120]	$0.124 \pm 0.034^{+0.025}_{-0.022}$	e+p	320	$1 < Q^2 < 1000\,\text{GeV}^2$, $0 < p_T < 10\,\text{GeV}/c$, $0.02 < y < 0.7$
ZEUS γp HERA I [121]	$0.220 \pm 0.035^{+0.027}_{-0.037}$	e+p	320	$130 < W < 300\,\text{GeV}$, $Q^2 < 1\,\text{GeV}^2$, $\lvert\eta\rvert < 1.6$, $p_T > 3.8\,\text{GeV}/c$
ZEUS γp HERA II [122]	$0.107 \pm 0.018^{+0.009}_{-0.014}$	e+p	320	$130 < W < 300\,\text{GeV}$, $Q^2 < 1\,\text{GeV}^2$, $\lvert\eta\rvert < 1.6$, $p_T > 3.8\,\text{GeV}/c$

2.7.3 Λ_c in p+p and p+Pb collisions at the LHC

The Large Hadron Collider (LHC) is the largest proton and heavy-ion collider in the world, with a circumference of 27 km. The experiments at the LHC can benefit from the large cross-section Measurements of Λ_c in both, p+p and p+Pb collisions have been reported at the experiments ALICE (A Large-Ion-Collider Experiment) and the LHCb.

ALICE [123] is a multipurpose detector dedicated to heavy-ion physics with excellent

particle-identification (PID) capabilities. The layout of ALICE is similar to that of STAR (see chapter 3 for more detail). The key detectors that enable the Λ_c measurement are the Time-Projection Chamber (TPC) for tracking and particle identification (PID), the Time-Of-Flight (TOF) and Transition-Radiation (TRD) detectors, used for additional PID, and importantly, the Inner Tracking System (ITS) for vertexing. Until now, the ITS consisted of 6 layers of silicon detectors, but currently, it is undergoing a major overhaul upgrade that will greatly benefit the future open-heavy-flavor measurements. The ITS will consist of 7 layers of silicon detectors, all based on the MAPS technology.

The LHCb [124] is dedicated to the physics of beauty and charm and has recently joined the heavy-ion physics program. It is a 20 m long spectrometer arm designed for forward rapidities. The Λ_c measurement especially benefits from the new Vertex Locator (VELO) [125] pixel detector. VELO is followed by the first RICH for PID, the main tracker, the second RICH, and calorimeters for additional PID.

The measurement of the ratio of Λ_c/D^0 from ALICE [126] and the preliminary ratio from the LHCb [127,128] are shown in Figure 2.13. The left-hand-side plot shows the ratio of Λ_c/D^0 versus p_T from ALICE from both p+p and p+Pb collisions at mid-rapidity and the right-hand-side figure plots the Λ_c/D^0 from ALICE and LHCb against rapidity y. The Λ_c were reconstructed at ALICE from several decay channels: $\Lambda_c^{\pm} \to \pi^{\pm} + K^{\mp} + p^{\pm}$, $\Lambda_c^{\pm} \to K_s^0 + p^{\pm}$, and $\Lambda_c^{\pm} \to \Lambda + e^{\pm} + \nu_e$. However, only the results from the first two are shown in this figure to decrease the size of the error bars. The ratio in p+p was compared to Monte Carlo p+p event generators PYTHIA8 with Monash tune and a tune that includes a model of string fragmentation beyond leading color [129], DIPSY tune [130], and Herwig7 which uses a cluster hadronization mechanism [131]. The PYTHIA tune with the string fragmentation beyond leading color tune is closest to the measured ratio, however all of these generators dramatically underestimate the data. Moreover, the generators do not depend on rapidity and fail to reconstruct the trend in the data. This suggest that new tunes have to be developed to take these measurements into account.

The Λ_c/D^0 was also measured in p+Pb collisions at ALICE and is consistent with the one in p+p within error bars. The data were also compared to a calculation [132] obtained

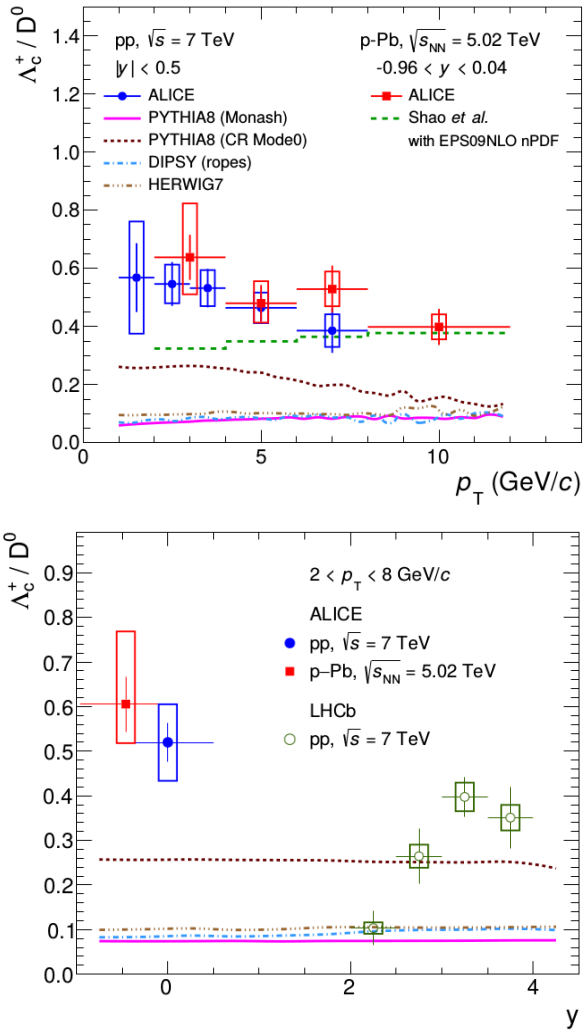

Figure 2.13: The Λ_c/D^0 ratio measured in p+p and p+Pb collisions at ALICE [126] and the LHCb [127, 128]. In the top panel vs p_T and in the bottom panel vs rapidity.

from a parametrization of the p+p data, using the EPS09NLO nuclear modification factors. There is a slight tension between this prediction and the data although not a significant one.

2.7.4 Λ_c in Pb+Pb collisions at the LHC

Λ_c measurement in Pb+Pb collisions [133] from ALICE has also been recently published, using the $\sqrt{s_{NN}} = 5.02\,\text{TeV}$ data. The measurement was obtained, using the $\Lambda_c^{\pm} \to K_s^0 + p^{\pm}$ channel.

The measurement of the ratio of Λ_c/D^0 is shown in Figure 2.14. The left-hand-side plot

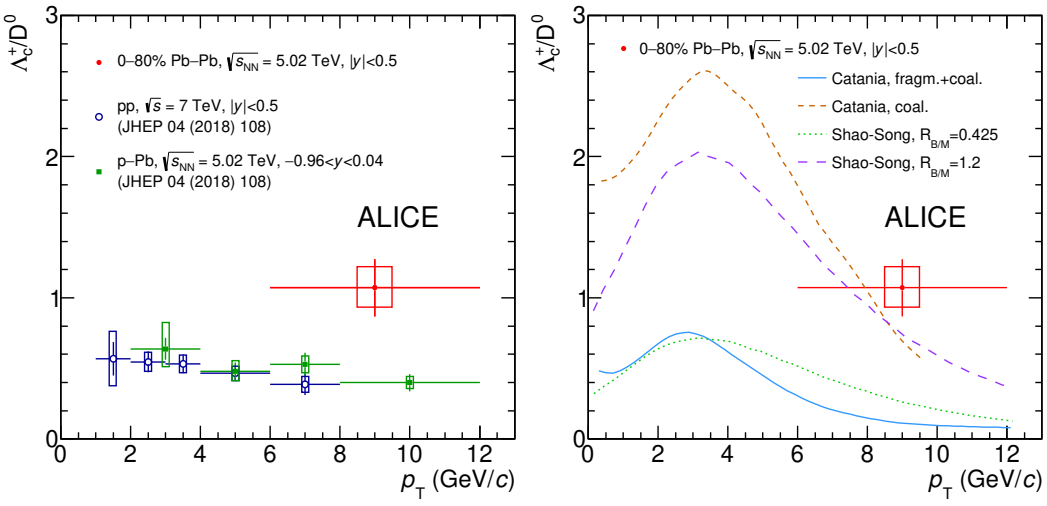

Figure 2.14: The Λ_c/D^0 ratio measured in Pb+Pb collisions by the ALICE experiment [133], compared to the p+Pb and p+p collisions (left) and model calculations [78, 113, 134–136] (right).

shows comparisons with p+p and p+Pb measurements from the previous section. The Λ_c/D^0 ratio is significantly higher in Pb+Pb collisions. This increase is usually explained by the process of quark coalescence. The right-hand-side figure is compared to model calculations. The Catania model uses two different treatments of hadronization: One which uses only quark coalescence and one where fragmentation takes over in high p_T. The scenario with coalescence only is closer to the data. The Shao-Song model [135, 136] implements coalescence in such a way that quark combination takes place with a fraction of momentum of the hadron and does not take into account the spatial and momentum distribution of the quarks in a hadron. The ratio of single charm baryons and mesons $R_{B/m}$ is treated as a free parameter in the model. The curve obtained with $R_{B/m} = 0.425$, needed to obtain the p+p and p+Pb data, does not describe the Pb+Pb data and the one with $R_{B/m} = 1.2$, which fits the Pb+Pb data, has a tension with the p+p and p+Pb data.

Thanks to the measurements of Λ_c in p+Pb, described in previous section, ALICE was able to publish the nuclear modification factor R_{AA} which is shown in Figure 2.15. The baseline was obtained by scaling the Λ_c yield in p+Pb collisions at $\sqrt{s_{NN}} = 5.02\,\text{TeV}$ by $1/A$ ($A = 208$). Even though the Λ_c/D^0 ratio is much higher than in p+Pb collisions, the

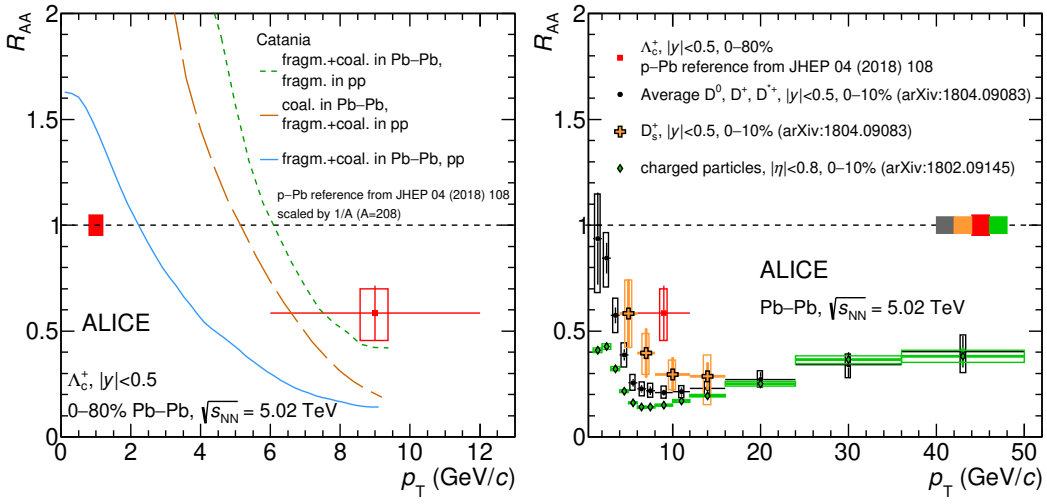

Figure 2.15: Nuclear modification factor R_{AA} of the Λ_c baryon, measured by the ALICE experiment [133]. Left: Compared to model calculations [134]; Right: Compared non-strange D mesons, D_s [137], and charged particles [138].

R_{AA} is bellow unity in the measured p_T range, because the D^0 are also suppressed in Pb+Pb collisions. In the left-hand-side plot, a comparison to Catania model calculations [134], that include three different hadronization mechanisms, is shown. The green short-dashed line illustrates a scenario that includes both vacuum fragmentation and charm-quark coalescence in Pb+Pb, but only fragmentation in p+p. The orange long-dashed line includes only coalescence in Pb+Pb collisions and coalescence plus fragmentation in p+p. Finally, the blue solid line represents fragmentation plus coalescence in both collision systems. This comparison shows that it is crucial to also describe the Λ_c production mechanism in p+p collisions at the LHC energies to draw conclusions about the R_{AA}. The limited precision of this first measurement, however, does not allow to discern between the different hadronization scenarios. The right-hand-side panel of Figure 2.15 compares the R_{AA} of Λ_c in 0–80 % most central Pb+Pb collisions to that of non-strange D mesons, D_s, and charged particles in 0–10 % most central collisions. The R_{AA} of charged particles is lower by more than 2σ, compared to non-strange D mesons, which are compatible within the uncertainties with the D_s. ALICE observes a hint of enhancement of the Λ_c baryon, compared to the D^0 mesons by $\sim 1.7\sigma$ [133]. This observation is qualitatively consistent with the scenario where significant portion of the charm

quarks hadronize via the coalescence mechanism.

2.8 Future measurements of the Λ_c baryon at the LHC

At the time of writing this thesis, the LHC has concluded its second run and is closed for the Long Shutdown II. This period can be used for upgrades of its detectors and analyses of the data recorded during the Run 2. Here, we list several upgrades and analyses that concern the Λ_c baryon.

2.8.1 Λ_c in p+A collisions at the LHCb with SMOG

The LHCb has recently joined the heavy-ion physics program with the unique capability to use different particle species and energy ranges thanks to its new fixed-target mode of operation. The System for Measuring Overlap with Gas (SMOG) [139] is a detection system primarily dedicated to precision luminosity measurement. It injects an inert gas (He, Ne, or Ar) with the pressure of $\sim 10^{-7}$ mbar into the beam pipe to be able to perform beam-gas imaging, but this inert gas can also serve as a fixed target for the beam. The center of mass energy per nucleon can vary inside $69\,\text{GeV} \leq \sqrt{s_{\text{NN}}} \leq 115\,\text{GeV}$ for the beam energy from 2.5 TeV to 7 TeV. So far, the Λ_c have been analyzed in p+Ar collisions at $\sqrt{s_{\text{NN}}} = 110\,\text{GeV}$.

The decay channel $\Lambda_c^{\pm} \to \pi^{\pm} + \text{K}^{\mp} + \text{p}^{\pm}$ was used for this measurement [140]. The invariant mass of the pKπ triplets can be seen in Figure 2.16. Detector effects are still under study for the Λ_c spectra at LHCb.

2.8.2 ALICE Inner-Tracking System (ITS) upgrade

The innermost part of the ALICE detector, the Inner-Tracking System (ITS), is undergoing a major overhaul upgrade with emphasis on open-heavy-flavor measurements [141]. In concept, the ITS sensors are similar to the STAR-HFT-Pixel [2] layers. The ITS is going to consist of 7 layers of MAPS pixel sensors out of which the innermost layer will be inside the beam pipe. This will provide the ITS with unparalleled tracking resolution while also improving the speed of the detector. Figure 2.17 shows the projection of statistical uncertainties Λ_c/D^0

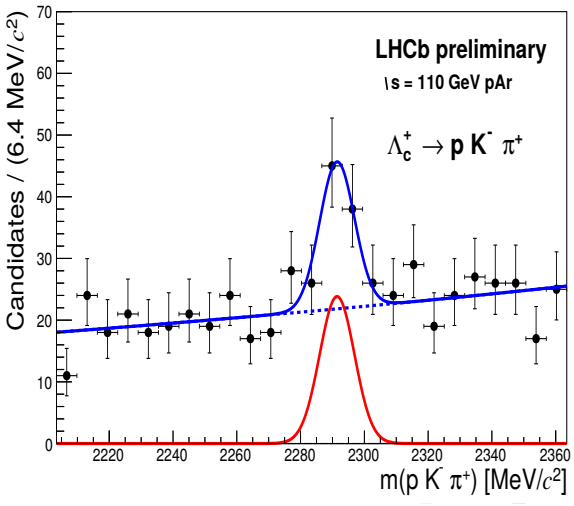

Figure 2.16: Invariant mass spectrum of the p+K+π triplets in p+Ar collisions with fixed target at $\sqrt{s_{\mathrm{NN}}} = 110\,\mathrm{GeV}$ at LHCb with SMOG [140].

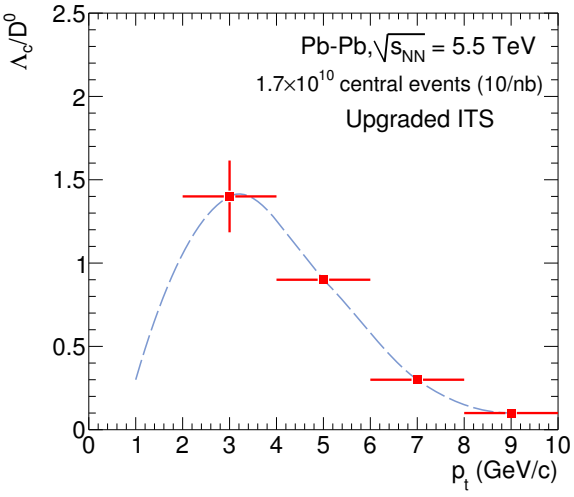

Figure 2.17: Projection of statistical uncertainties of the Λ_c/D^0 measurement with the improved resolution of ALICE ITS using 1.7×10^{10} central collisions (0–10 %), corresponding to an integrated luminosity of $10\,\mathrm{nb}^{-1}$ [141].

ratio measurement in 0–10 % most central Pb+Pb collisions. The new ITS will allow for a differentiated measurement of the Λ_c invariant yield in both p_T and centrality.

Chapter 3

Solenoidal Tracker at Relativistic-Heavy-Ion Collider

The method of choice for the study of Quark-Gluon Plasma, which was discussed at length in the previous chapter, are collisions of relativistic-heavy nuclei. These are achieved in laboratory on particle accelerators. The work in this thesis was performed at Relativistic Heavy-Ion Collider (RHIC). The strngths of this accelerator are the capability to collide several species of nuclei, as well as polarized protons, at various energies.

Four experiments have operated at RHIC so far: Phobos, Brahms[1], PHENIX[2], and finally, recording data at the time of writing this thesis: STAR. Phobos and Brahms were decommissioned after concluding their physics programs in 2005 and 2006, respectively, and PHENIX which stopped its operation in 2017 is currently being replaced by a new experiment: the sPHENIX [142]. This state-of-the-art experiment will be able to measure charged particles with high rate in the entire azimuth. It will feature a time-projection chamber with a continuous readout, as well electromagnetic and hadronic calorimeters which will make it a perfect tool for measuring jets and heavy flavor.

[1]Broad RAnge Hadron Magnetic Spectrometers
[2]Pioneering High Energy Nuclear Interaction eXperiment

3.1 Relativistic-Heavy-Ion Collider (RHIC)

RHIC [144, 145] is a circular accelerator located in the Brookhaven National Laboratory (BNL) in the USA. It is a versatile accelerator capable of colliding several species of nuclei (Au+Au, d+Au, Au+^{3}He, Au+Cu, U+U, ...) at center-of-mass energies per nucleon ranging $\sqrt{s_{\mathrm{NN}}} = (3.9\text{–}200)\,\mathrm{GeV}$ in a collider mode or down to $\sqrt{s_{\mathrm{NN}}} = 3.0\,\mathrm{GeV}$ using a fixed target [146]. This versatility allows for studying various properties of the QGP since, by changing the collision system, we are able to vary the initial geometry and energy density, pressure, and electromagnetic-field profiles. Moreover, RHIC has a unique capability to collide polarized protons with the center-of-mass energy up to $\sqrt{s} = 500\,\mathrm{GeV}$ [147]. The overview of the RHIC runs between 2013 and 2019 is summarized in Table 3.1. The energies per nucleon E_1 and E_2 were taken from [143] and $\sqrt{s_{\mathrm{NN}}}$ was calculated as

$$\sqrt{s_{\mathrm{NN}}} = \sqrt{m_{\mathrm{N1}}^2c^4 + m_{\mathrm{N2}}^2c^4 + 2E_1E_2 - 2\sqrt{E_1^2 - m_{\mathrm{N1}}^2c^4}\sqrt{E_2^2 - m_{\mathrm{N2}}^2c^4}} \tag{3.1}$$

where m_{N1} and m_{N2} are the masses of an average nucleon in the collided ion.

3.1.1 RHIC Accelerator Complex

Ions and protons are accelerated in several stages before colliding in one of the RHIC experiments at the desired energy. Ions are generated in the Electron Beam Ion Source (EBIS [148]) which provides all stable ion beam source ranging from deuterons to uranium. A part of the EBIS is the Linac which can reach energies up to[3] 200 MeV. The EBIS can switch different ion species in the order of seconds which was important for the 2018 isobar running with zirconium and xenon.

The ions then enter the circular Booster Synchrotron which accelerates them enough to enter the Alternating Gradient Synchrotron (AGS [150]). This is an accelerator that fulfilled a rich physics program, including three Nobel-prize discoveries, before the RHIC facility was constructed. From AGS, the ions enter the AGS-to-RHIC (AtR [151]) transfer line. Finally, the ions are injected into RHIC where they are accelerated to their final energies.

[3] 200 MeV can be reached in the case of protons

Table 3.1: Summary of RHIC runs between 2013 and 2020 with integrated luminosity at the STAR experiment [143].

Year	Species	$\sqrt{s_{\mathrm{NN}}}$ (GeV)	Luminosity (nb^{-1})
2013	polarized p+p	499.8	5.00×10^{5}
2014	Au+Au	14.6	2.12×10^{-2}
	Au+Au	200.0	20.7
	^{3}He+Au	203.5	61.4
2015	polarized p+p	200.4	1.85×10^{5}
	polarized p+Au	202.4	640
	polarized p+Al	202.5	1.54×10^{3}
2016	Au+Au	200.0	21.9
	d+Au	200.7	134
	d+Au	62.4	21.1
	d+Au	19.7	3.44
	d+Au	39.0	10.0
2017	polarized p+p	499.8	5.44×10^{5}
	Au+Au	54.4	0.477
2018	^{96}Zr+^{96}Zr	200.0	3.91
	^{96}Ru+^{96}Ru	200.0	4.00
	Au+Au	27.0	0.282
	Au+Au fixed target	3.0	5.4×10^{-2}
	Au+Au fixed target	7.2	3.5×10^{-2}
2019	Au+Au	9.8	0.151
	Au+Au	7.3	0.132
	Au+Au fixed target	7.3	1.1×10^{-2}
	Au+Au	3.85	3.6×10^{-3}
	Au+Au fixed target	3.85	1.1×10^{-3}
	Au+Au	4.59	4.2×10^{-2}
	Au+Au fixed target	4.59	7.0×10^{-3}
	Au+Au fixed target	31.2	1.1×10^{-2}
	Au+Au	100.0	8.0×10^{-2}
2020	Au+Au	5.75	0.143
	Au+Au	4.59	0.176
	Au+Au fixed target	31.2	2.3×10^{-2}
	Au+Au fixed target	19.5	2.3×10^{-2}
	Au+Au fixed target	13.5	2.5×10^{-2}
	Au+Au fixed target	9.8	2.1×10^{-2}
	Au+Au fixed target	7.3	2.4×10^{-2}
	Au+Au fixed target	5.75	2.4×10^{-2}
	Au+Au fixed target	26.5	6.5×10^{-2}

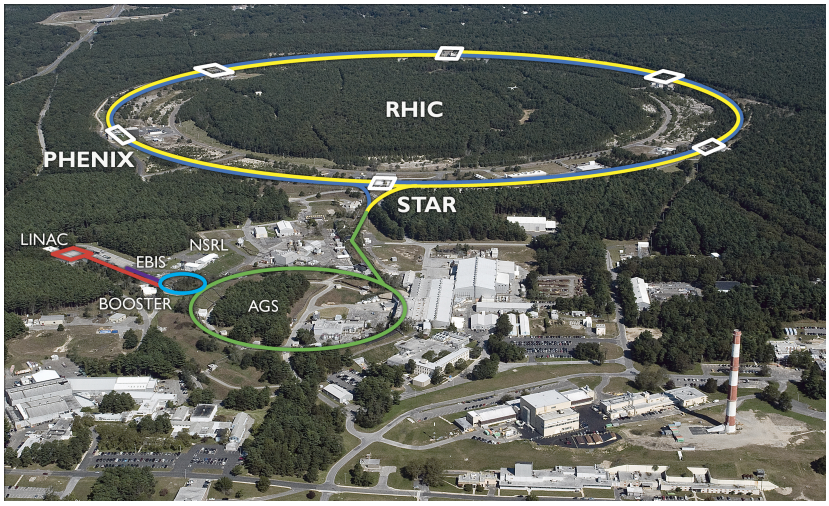

Figure 3.1: Diagram of the RHIC accelerator complex [149].

Protons experience a similar journey to the ions. However, they are produced by ionizing hydrogen gas and then injecting them directly into the Linac. Then they continue to be accelerated in the same way as the ions. One of the unique capabilities of RHIC is the ability to produce polarized protons up to 500 GeV, which is facilitated by the so-called Siberian-Snake magnets in the RHIC accelerator ring. In the end, the protons are collided in one of the six crossing points. Currently, the only experiment, measuring collisions is STAR, as PHENIX is undergoing an upgrade into the new experiment called sPHENIX.

3.2 Solenoidal Tracker At RHIC (STAR)

The Solenoidal Tracker At RHIC (STAR) [152] is a multipurpose detector with full azimuth conerage dedicated to studying ultrarelativistic heavy-ion collisions and polarized proton–proton collisions.. It excells in charged-particle tracking in events with high track multiplicities and particle identification, while also featuring a full azimuth electromagnetic calorimeter and a muon detector. Currently in 2021, STAR is the only detector system running at RHIC.

The main barrel of STAR is enclosed in a water-cooled magnet with a magnetic field of 0.5 T. The magnet contains the following detectors: Time -Projection Chambre (TPC — Section 3.3), the GEM Chambers to Monitor the TPC Tracking Calibrations (GMT),

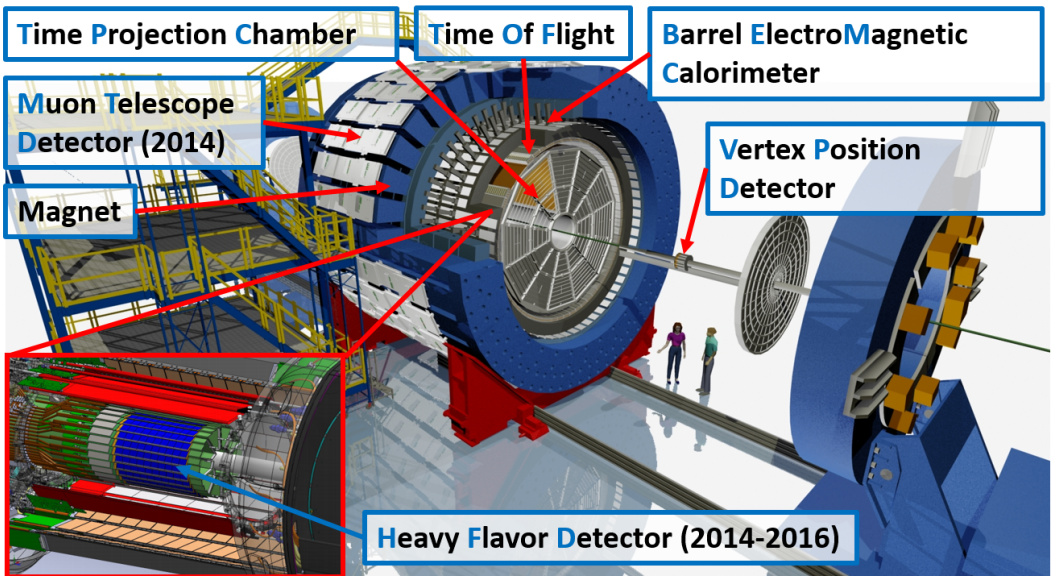

Figure 3.2: Overview of the STAR detector.

which is a set of 8 GEM detectors, used for the calibration of the TPC callibration, and Time-Of-Flight (TOF) Detector (Section 3.4). In 2014, STAR received two major upgrades concerning the heavy flavor measurements: The Heavy Flavor Tracker (HFT — section 3.5), and the Muon Telescope Detector (MTD) which consists of fast Multi-wire Resistive Plate Chambers (MRPC) palced outside the magnet. The main purpose of the MTD is to detect muons, which can easily traverse the volume of the magnet. The important detectors for the open-charm hadrons reconstruction are HFT, TPC, TOF, ZDC, and VTX.

3.3 Time-Projection Chamber (TPC)

It is not an exaggeration to say that the Time-Projection Chamber [153] is the beating heart of STAR. It combines the role of the main tracking detector with the ionizing-energy-loss ($\mathrm{d}E/\mathrm{d}x$) information for particle identification (PID). The TPC is able to provide excellent tracking of particles down to low p_{T} with the large multiplicities at top RHIC energies.

When a charged particle traverses through the TPC, it ionizes the gas in the TPC volume. Then, the created negative charge (electrons) drifts towards the anodes where it encounters

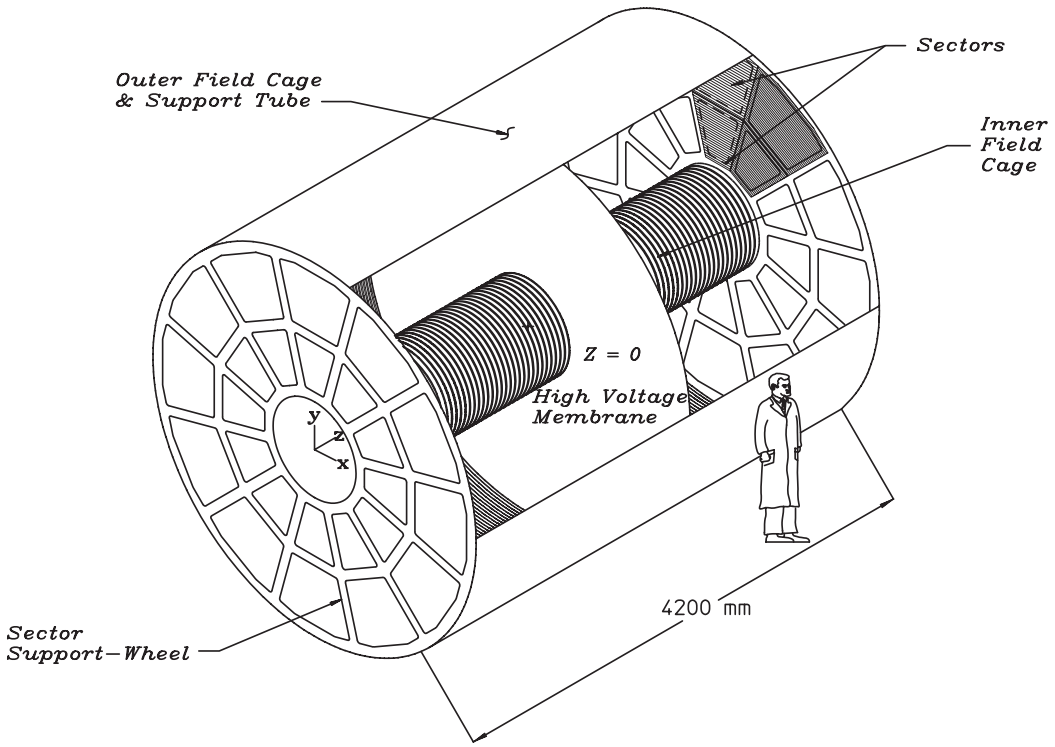

Figure 3.3: Overview of the STAR Time-Projection Chamber [153].

20 µm wide wires which amplify the signal that is, consequently, measured. The position in the transverse plane to the beam line (the xy-direction) is measured thanks to the granularity of the TPC anodes, and the position along the beam line (in the z-direction) is fixed by the time, taken by the electrons to drift to the anodes. Hence, the spatial position of the track is fixed. The drift velocity of the electrons in the P10 gas is calibrated every several hours via a laser calibration system [154].

The layout of the TPC is shown in Figure 3.3. It is barrel-shaped with an outer radius of 2 m, inner radius of 0.5 m and length of 4.2 m with the beam pipe going through the center. This barrel is filled with the P10 gas: a mixture of 90 % argon and 10 % methane. It covers the full azimuth ($0 < \phi < 2\pi$) and the outer edge covers the pseudorapidity range of $|\eta| < 1$. In the center ($z = 0$), it is divided into two halves by the, so called, Central Membrane which is connected to an electric potential of -28 kV. The sides of the cylinder consist of the, so called, field cage that ensures that the electric field in the TPC stays uniform.

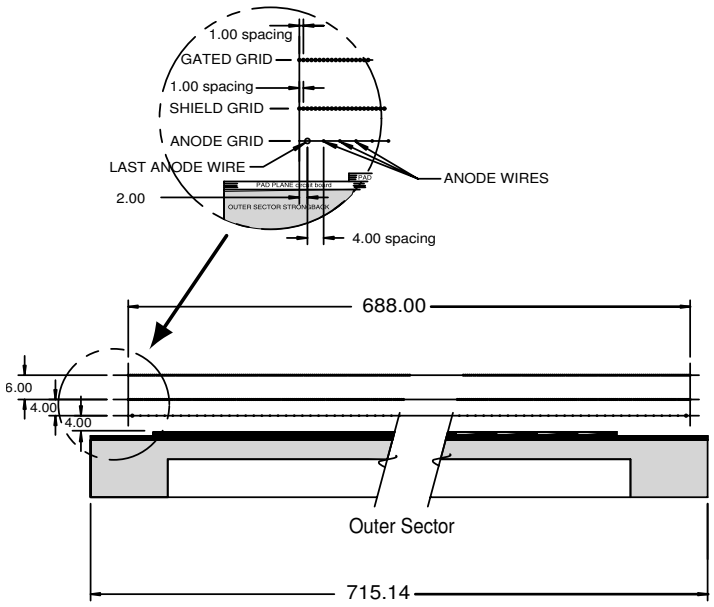

Figure 3.4: Side view of the TPC-outer-sector pad plane. The bubble shows additional information on the wire planes of the anodes [153].

The bases of the TPC cylinder are grounded and equipped with multi-wire proportional chambers (MWPC) as sensitive detectors. Each side consists of 12 sectors, numbered like on a clock and split into the inner and outer parts. Side (the xy-plane) view of the sectors is shown in Figure 3.4. Each MWPC consists of three planes of wires mounted over one plane of sensitive pads. Going from inside of the TPC volume out, the innermost plane of wires makes the, so called, gating grid. This part acts like a camera shutter that does not allow any electrons to enter the MWPC and it stops the ions from escaping the MWPC into the drift area where they would distort the electric field. It also lowers the amount of noise in the MWPC as ions are discharged by the wires. The second row of wires is called the Shield Grid and it terminates the amplification region created by the outermost plane of wires: the Anode Grid. Here, the drifting electrons are multiplied in avalanches around the wires where the voltage differentials are high. These wires are set on potential of $\sim$1350 V which sets the signal multiplication to $\sim$20$\times$: A value selected as a sweet spot between spatial resolution and the signal amplification. The signal is subsequently read out from the rectangular pads behind the anode wires. The pads are placed so that they always have an anode wire in the

middle and their pitch is 6.7 mm along the wires and 20 mm across (same as the distance between the wires).

Until the run 2018, the inner part utilized 13 rows and outer part with 32 rows of pads, the inner sectors, however, underwent a substantial upgrade in the year 2019 [155], called iTPC. This upgrade increased the number of sensitive pad rows in the inner sector to the same number as in the outer sectors. This greatly increased the efficiency, resolution, and pseudorapidity coverage of the TPC which, in turn, enabled the fixed-event measurements at STAR with the endcap-Time-Of-Flight (eTOF) detector in 2019 and, in the future, it will be able to facilitate the measurement of electron+ion and electron+polarized-proton collisions after the upgrade to eRHIC.

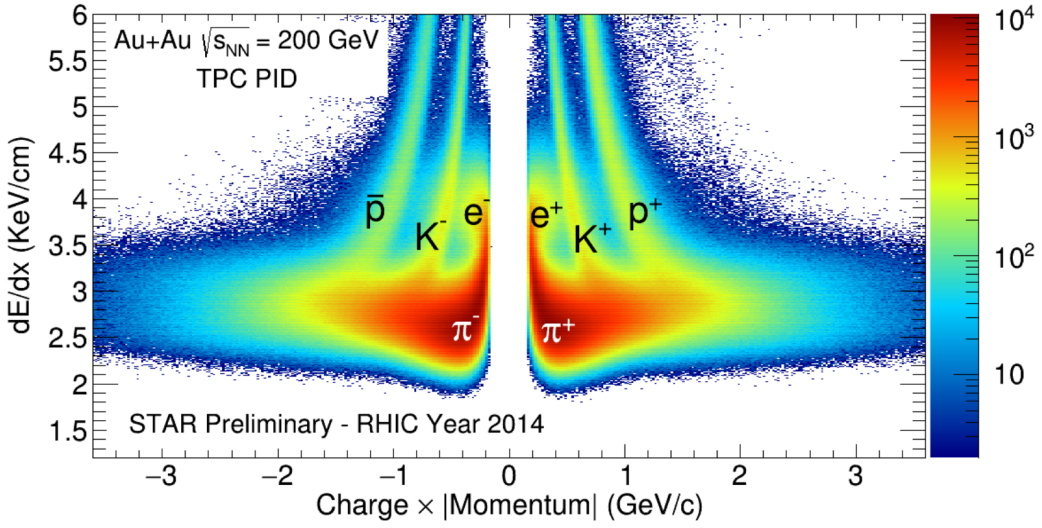

Figure 3.5: PID capabilities of the TPC via $\mathrm{d}E/\mathrm{d}x$ separation in the 2014 Au+Au run at $\sqrt{s_{\mathrm{NN}}} = 200\,\mathrm{GeV}$.

The TPC provides excellent momentum-measuring and PID capabilities in a high particle-multiplicity environment of the heavy-ion collisions. A graph, that shows particle-species separation capabilities of the TPC, is shown in Figure 3.5.

3.4 Time-Of-Flight Detector (TOF)

The main purpose of the Time-Of-Flight (TOF) detector [156] is to extend the PID capabilities of STAR into higher momenta via the measurements of the time of flight of charged particles from its point of origin (or vertex) to the TOF detector, thus measuring its velocity. TOF was partially installed at STAR in 2009 and the remainder was added in 2010 to make it fully operational.

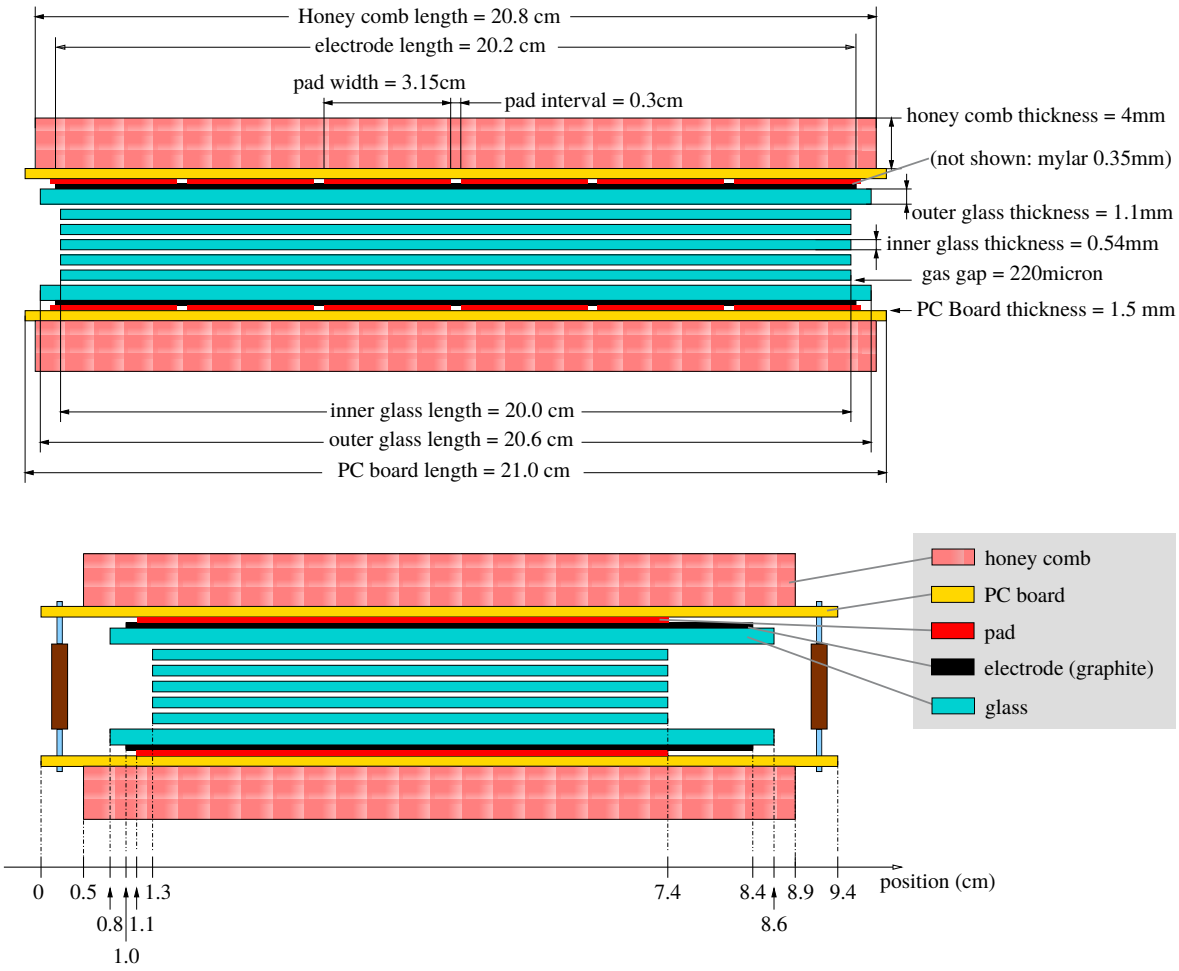

Figure 3.6: Layout of the TOF MRPC [156]. The upper and lower images show views of the longer and shorted edge, respectively. The two views do not show the same scale.

TOF detector consists of 120 trays of Multi-gap Resistive Plate Chambers (MRPC) [157] that cover $|\eta| \lesssim 0.96$ and $0 < \phi < 2\pi$. The time of the original collision is measured by the

Vertex Position Detector (VPD — see section 3.7). The leading edge of the signal is sampled with 25 ps binning. Corrections can be made for the decay products of particles that decayed outside of the primary vertex, e.g. K^0 or Λ.

Figure 3.6 shows two side views of the TOF tray. A MRPC basically consists of a stack of resistive plates with uniform gas gaps in between. A high voltage is applied to the graphite electrodes that have electrically floating glass plates in between. Typical resistivity of the glass plates is in the order of $10^{13}\,\Omega$/cm. A charged particle going through the tray generates electrical avalanches in the gas gaps. The signal is read out via copper pads on the outside of the graphite electrodes, separated by 0.35 mm of mylar. Because of the high resistivity of the glass plates, they are transparent to the charge induction in the gaps. The signal is the sum of all avalanches in the gas gaps in between the opposing copper pads. The gas consists of 95 % Freon R134a and 5 % iso-butane. This gas mixture was chosen for its dielectric strength and electronegativity. The trays are mechanically supported poly-carbonate (PC) boards on each side, glued to honeycomb structures that are rigid while having a low material budget.

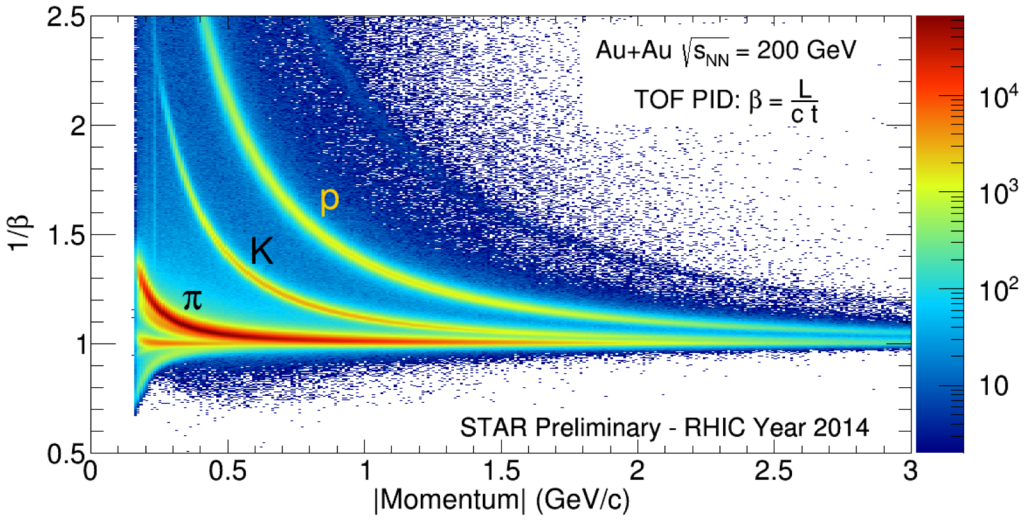

Figure 3.7: PID capabilities of the TOF via measurement of the inverse velocity $1/\beta$ versus p_{T}in the 2014 Au+Au run at $\sqrt{s_{\mathrm{NN}}} = 200\,\mathrm{GeV}$.

The PID capabilities of TOF are demonstrated in Figure 3.7. The fraction of the speed

of light in vacuum β is calculated as

$$\beta = \frac{L}{ct} \tag{3.2}$$

where L is the path-length from the primary vertex (PV) and t is the flight time, measured by TOF. A clear separation of the particle species is visible. Moreover, it reaches further in p_{T}, compared to $\mathrm{d}E/\mathrm{d}x$ PID of the TPC shown in Figure 3.5.

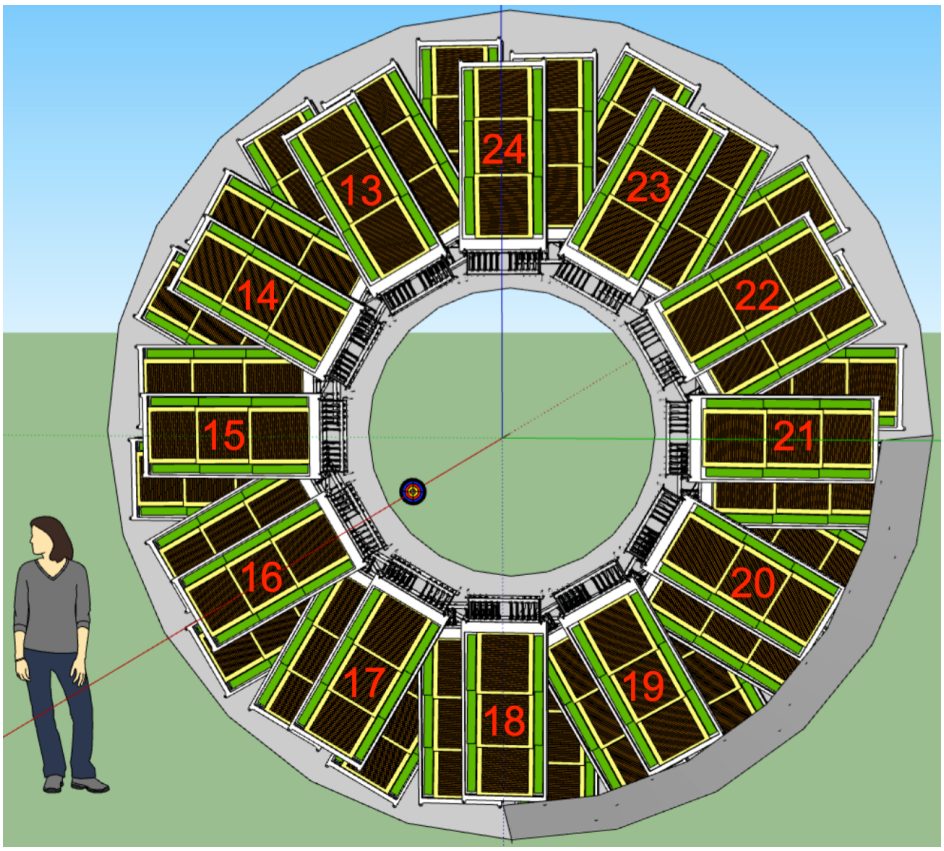

Figure 3.8: Illustration of the endcap-Time-Of-Flight detector layout [158].

In 2019, the time-of-flight coverage of STAR was greatly expanded by a new upgrade to the STAR detector: the endcap-Time-Of-Flight detector (eTOF [158]). This detector was developed in collaboration with the Compressed Baryonic Matter (CBM [159]) experiment as eTOF doubles as a test of the CBM Time-Of-Flight detector. eTOF consists of trays of similar design to the TOF mounted to the endcap of the TPC. The layout is shown in Figure 3.8. eTOF enhances the pseudorapidity reach of PID via time-of-flight measurements

down to at least $\eta > 1.5$ [160].

3.5 Heavy Flavor Tracker (HFT)

The Heavy Flavor Tracker (HFT) was installed at STAR for the years 2014–2016 data taking [1–3]. It resides between the beam pipe and the TPC which makes it the innermost subdetector of STAR. The HFT subdetectors are summarized in Table 3.2. The HFT consists of 4 layers of silicon detectors — from the outermost layer in: A double-sided strip detector, called Silicon Strip Tracker/Detector (SST/SSD) which waa previously installed at STAR and has been refurbished and upgraded with new electronics; Next, the second outermost layer is formed by conventional silicon pad detectors of the Intermediate Silicon Tracker (IST) with rectangular pads; Last, but not least, the two innermost layers consist of the Pixel (PXL) Detector that employs the novel MAPS technology that was used for the first time in a collider experiment. Figure 3.9 shows the layout of the HFT.

Table 3.2: HFT subdetectors, their average radii from the center of the beam pipe, and pitches of the sensitive pads. For the SSD, the hit resolutions $\sigma_{r\phi}$ and σ_z are listed, instead of the pitch, because it is a double sided strip detector where the strips are not perpendicular [3].

System	Type	Radius [cm]	Pitch–$r\phi$ [µm]	Pitch–z [µm]
SSD	Double-sided strip detector	22	$\sigma = 20$	$\sigma = 740$
IST	Silicon pad detector	14	600	6000
PXL	Silicon pixel detector	2.7, 8	20.7	20.7

The purpose of the IST and the SSD is to guide the track from the TPC to the innermost layers of HFT–PXL in the high-track-multiplicity environment of STAR. Figure 3.10 illustrates the improvement of the tracking resolution with each layer of the HFT. The PXL especially provides an unparalleled pointing precision thanks to its high granularity as well as the proximity to the primary vertex. For the runs with the HFT, the beam pipe had to be replaced with a narrower one, in order to accommodate for the low radius of the inner-

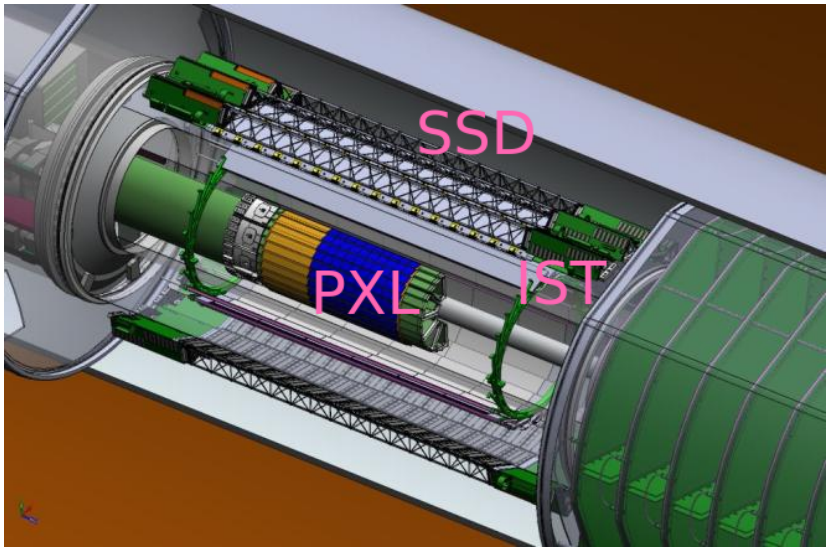

Figure 3.9: Render of the HFT installed inside STAR [3].

most layer of PXL. The resolution of the distance of closest approach (DCA resolution) of identified particles can be seen in Figure 3.11. For high-momentum tracks, the resolution is as low as 20 µm.

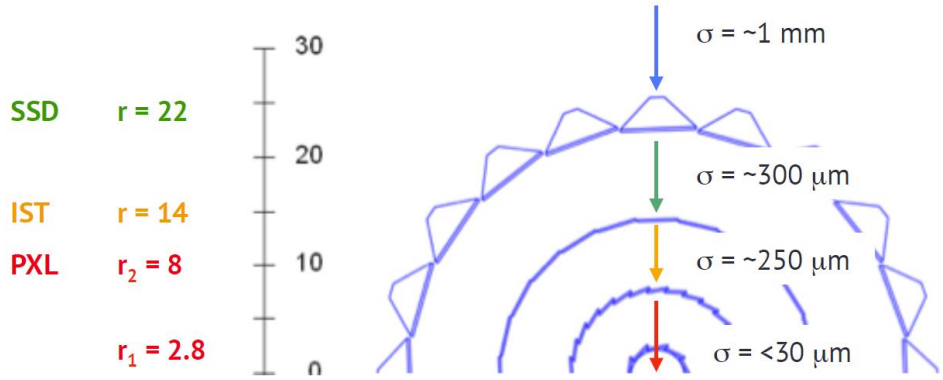

Figure 3.10: Average resolution improvement with each layer of the HFT, going from the TPC down to the innermost layer of the PXL detector. Taken from [5].

Great care was used when engineering the mechanical support so that it is lightweight while providing enough support that allows for cooling of the system. The entire HFT is mounted on a novel structure on rails so that it can be removed and replaced within 24

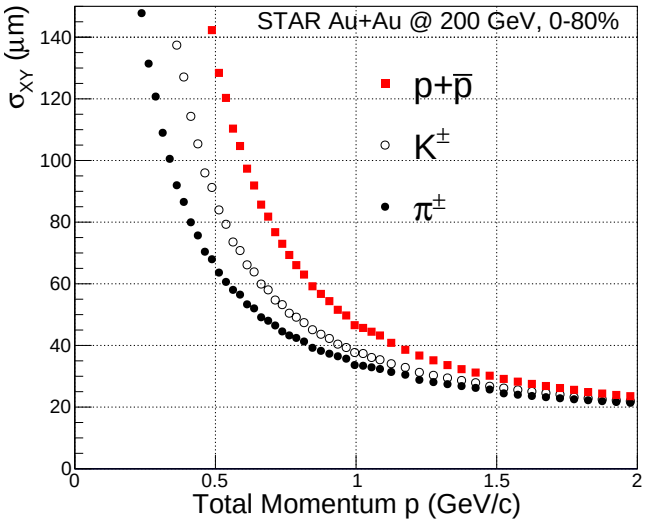

Figure 3.11: Distance of Closest Approach (DCA) from the PV in the xy-plane for identified particles. Taken from [97].

hours. This structure also provides air flow for cooling. For PLX and SSD air cooling is sufficient, but the IST is also liquid cooled.

3.5.1 Silicon-Strip Detector (SSD)

The Silicon-Strip Detector (SSD) is a refurbished detector with upgraded electronics that can facilitate the high collision rates in runs 2014 and 2016. The SSD consists of 20 ladders 67 cm in length with double-sided silicon strip wafers, mounted 22 cm from the center of the beam pipe. The strips are 95 µm wide and 4.2 cm long and are crossed at an angle of 35 mrad, oriented to prioritize the resolution in the $r\phi$ direction. The material of the SSD amounts to ∼1 % of the radiation length.

3.5.2 Intermediate Silicon Tracker (IST)

The Intermediate Silicon Tracker (IST) is a single-sided silicon-pad detector with rectangular pads of 600 µm × 6 mm. It is located between the PXL detector and the SSD at a radius of 14 cm. The IST consists of 24 ladders with 6 sensors each, supported on kapton mechanical

structure with cooling tubes. The IST is cooled by the Novec 7200 liquid which is a dielectric, it evaporates quickly in the event of a spill, and it is not harmful to the environment. The material budget of the IST is calculated as ∼1.5 % of the radiation length.

3.5.3 Pixel (PXL) detector

The two innermost layers of the HFT consist of the Pixel (PXL) detector which employs a unique design as it is the first detector using the Monolithic Active-Pixel Sensor (MAPS) technology. This enables the pixel sensors to have a miniscule pixel pitch of 20.7 µm while maintaining a small material budget.

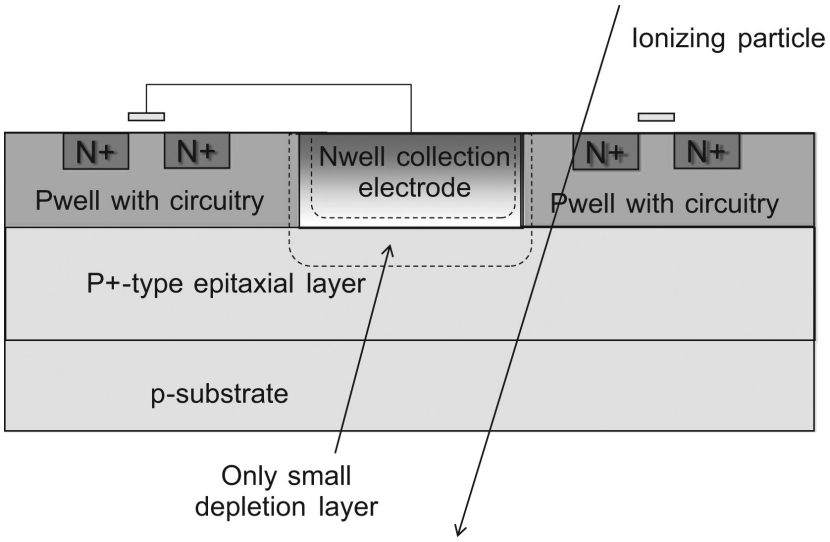

Figure 3.12: Illustration of the MAPS technology principle [161].

Compared to conventional bump-bonded pixel sensors, the advantage of the MAPS technology is that it incorporates the front-end electronics (FEE), such as amplifiers and discriminators, inside the pixels themselves. The MAPS uses one layer of silicon instead of two layers in traditional pixels which reduces the material budget and cost of the detector. Moreover, the pixels can be made smaller as they benefit from the advancement of the CMOS-printing technology in the industry. An illustration of a cut through a MAPS wafer is shown in Figure 3.12. The FEEs can be incorporated on the same silicon wafer, because they are shielded inside a deep P-well while the signal electrons are read out via an N-well. When a charged

particle traverses the PXL detector, a cloud of electron-hole pairs is created predominantly in the P+-type epitaxial layer. Then some of the electrons drift into the depleted zone around the N-well collection electrode via diffusion, and are subsequently picked up as signal. A single-particle hit is typically read out by multiple N-wells and it creates a cluster of several wounded pixels. This improves the resolution of the pixel sensor as the position of multiple pixels can be averaged as a probable position of the particle impact.

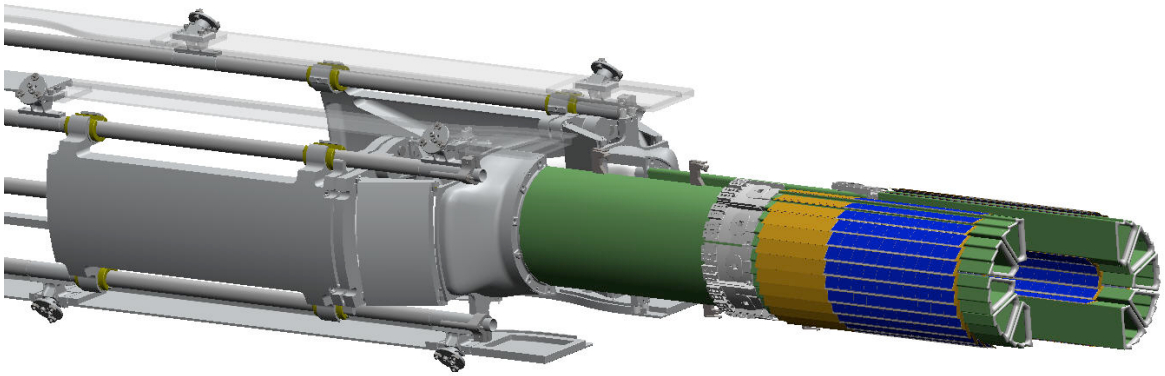

Figure 3.13: Layout of the PXL detector mounted on the supporting structure [3].

The layout of the PXL detector, mounted on the HFT-support structure, is illustrated in Figure 3.13. The sensors themselves are on the right-hand side of the image, marked by a blue color. The PXL consists of two concentric barrels, each 20 cm long, first one at a radius of 2.7 cm and the second one at 8 cm. The sensors are organized into ladders, 10 in the inner barrel and 30 in the outer one. The support structure for the PXL consists of 10 roughly trapeziodal kapton sections, each supporting three ladders from the outer layer and one ladder from the inner one. The innermost layer is placed right on the beam pipe which had to be made anew to accommodate for the small radius of the PXL. The sensors are milled so that the material budget of each layer was lowered to only 0.5 % of the radiation length.

The combination of the small pixel pitch, the small radius of the first layer, and the low material budget of the PXL make for a before-unforseen pointing resolution of the HFT.

This is crucial for the precise measurements of open-heavy-flavor hadrons that decay relatively close to the PV such as the Λ_c with $c\tau \approx 60\,\mu m$.

HFT Slow Simulator Evaluation and comparison to measured data

The process of charge deposition in MAPS is illustrated in Figure 3.14. When an ionizing particle passes through a MAPS wafer, it generates a cloud of electrons and holes that can drift to several pixels where they are collected inside the CMOS N-wells and, subsequently, measured as signal.

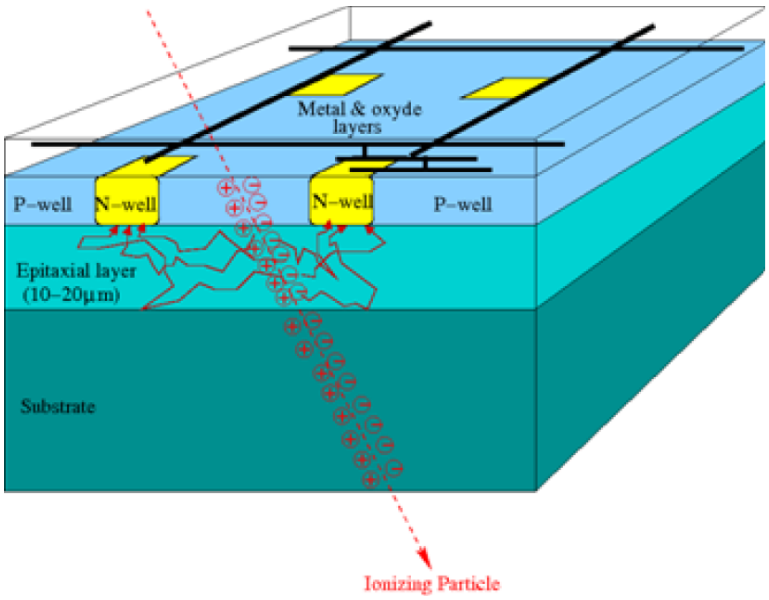

Figure 3.14: An illustration of particle energy deposition and charge transport in a MAPS chip [162].

Every analysis of measured data depends on reliable Monte-Carlo simulation for corrections of the efficiency of the detectors. At STAR, GEANT3 [4] is typically used for simulating the detector response to an ionizing particle. However, GEANT does not take into account processes in thin silicon wafers, so the detector response has to be simulated outside of the GEANT environment and then embedded into the GEANT simulation.

Two types of detector simulators are employed for PXL, the so called, fast simulator and slow simulator. The fast simulator takes a position where a track crossed the detector, smears

it according to the detector resolution, and calculates the efficiency of the detector, according to the particle species and its p_{T}. The slow simulator, on the other hand, simulates deposited energy of the particle inside the detector and generates detector response to the pixel layer. The slow simulator can create a more realistic picture of the detector response, including noise in the detector. This is crucial when using the clustering and tracking algorithms on the simulated detectors. Slow simulator is mainly used in embedding of the simulated tracks in measured data as it requires information on the level single pixels. The fast simulation is adequate when simulated data are not mixed with the measured ones, because, typically, only the position of the hits is required.

A tool for simulation of the MAPS-detector response — MAPS digitizer or "DIGMAPS" — has been developed at Strasbourg University [162]. This model simulates the relatively complicated process from a passing particle to the output of the MAPS sensor in the following steps: energy deposition, charge transport of the electron–hole pairs, digitization of the ADC with added noise.

1. The **energy deposition** is calculated via a Landau distribution with the PDF [163]

$$P(x, \mathrm{MPV}, \mathrm{width}) = \frac{1}{\pi} \int_0^\infty \mathrm{e}^{-s \cdot y - s \ln s} \cos(\pi s)\, \mathrm{d}s\,, \qquad y = \frac{x - \mathrm{MPV}}{\mathrm{width}} \tag{3.3}$$

   where MPV $= 80\,\mathrm{e}^-/\mu\mathrm{m}$ and width $= 18\,\mathrm{e}^-/\mu\mathrm{m}$. The effective thickness of the sensor is calculated as $L_{\mathrm{epi}}/\cos\theta$ where L_{epi} is the width of the epitaxial layer and θ is the angle between the passing-particle trajectory and the normal to the sensor plane.

2. The **charge transport** is simulated as a sum of a gaussian and a Lorentzian with the center in the middle of the track's intersection with the MAPS wafer. This ditribution has described the test beam data the best. The charge is then deposited on 25 N-wells around the center of the distribution.

3. In the **digitization** step, noise is introduced into each pixel with a Gaussian distribution, and then the pixels with the number of electrons higher than a set ADC threshold are counted as wounded.

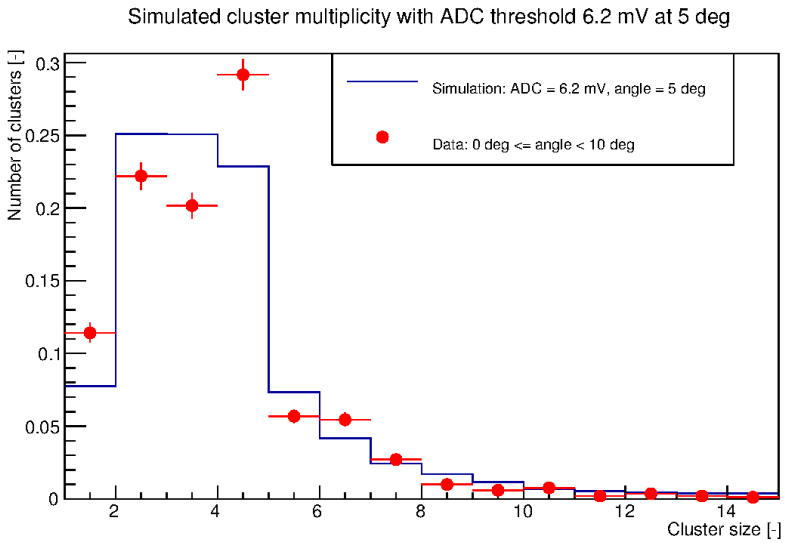

Figure 3.15: Pixel slow-simulator-cluster size compared to cosmic data at the angle of 0–10°.

The DIGMAPS package can be run in the simulation mode that returns a map of wounded pixels or it can be run in a stand-alone mode, without any GEANT, in which it clusterizes the pixels into hits.

DIGMAPS has several free parameters that have to be tuned through data. In this test, we use parameters tuned on minimum-ionizing particles (MIP) from beam tests with the exception of the ADC threshold which can be set for each pixel row individually, and is tuned several times during the run. The value 6.2 mV has proven to reproduce the data the best.

The DIGMAPS model had to be verified with measured data from run 2014 to ensure that the PXL-slow simulator is accurate. Cluster sizes were compared between the measured data and the Digmaps simulation. At first, cosmic data with zero-magnetic field were used, because data from collisions were not available yet. This data also proved useful when comparing them to the beam tests, because MIP are used in both cases.

The cosmic tracks are selected as follows: Only tracks, that traverse through the center barrel of the HFT and have 4 hits in the PXL and 2 hits in the IST, are selected. At least one of the hits has to have a cluster size of two or more. These precautions are applied to

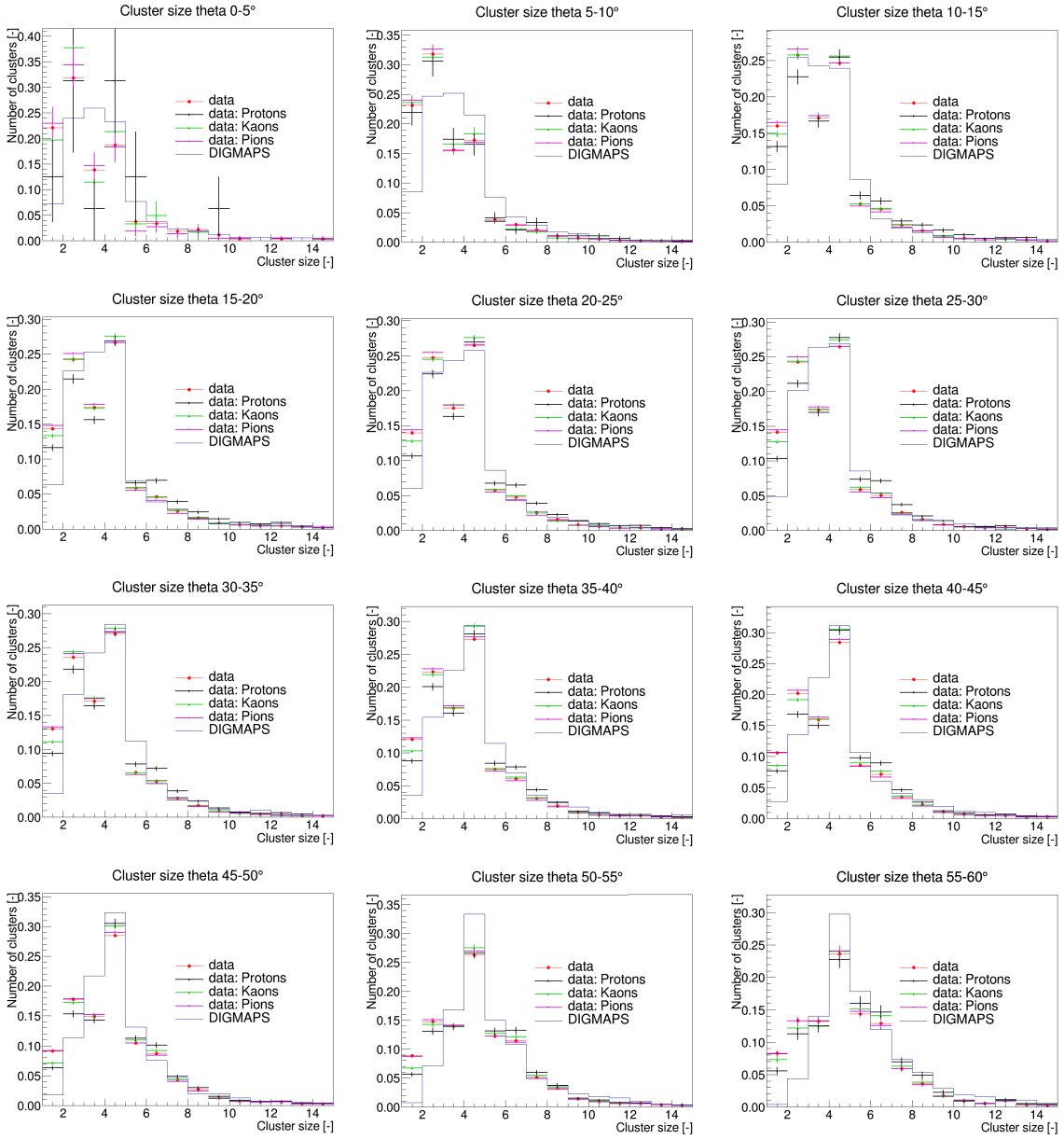

Figure 3.16: Comparison of cluster size of the Slow simulator and global identified tracks (left) and primary (tracks that originate in the primary vertex) track only (right) [5].

eliminate fake tracks that merely connect noise hits. The hits are chosen within a square window 6 mm × 6 mm around the center of the track. Only 1 hit may be present inside the square.

Measured-cluster data were compared to the DIGMAPS simulations for angles up to

$\theta < 60°$. Figure 3.15 shows a comparison of PXL cluster sizes between the cosmic data at impact angles $0° < \theta < 10°$ and DIGMAPS generated at 5°. Both, the distributions from simulation and data, are normalized to unity for easier comparison. ADC threshold of 6.2 mV was used for the DIGMAPS simulation. The number of hits rises with more pixels until the cluster size of 4, then it drops steeply. The width and the overall shape of the cluster-size distribution is reproduced well in DIGMAPS, however the dip at 3-pixel clusters does not show in the simulation which is, however, not considered a significant problem as it likely has little effect on the pointing resolution.

A similar evaluation was later performed with Au+Au collisions at the center-of-mass energy per nucleon $\sqrt{s_{\mathrm{NN}}} = 200\,\mathrm{GeV}$ from run 2014 [5]. This time, the cluster sizes generated by DIGMAPS are compared to the clusters in tracks from identified particles and all charged tracks (see Figure 3.16). In general, Protons have slightly higher cluster sizes, compared to pions and kaons, however the overall shape stays the same and is reproduced by DIGMAPS.

Overall, DIGMAPS have proven to be a useful tool that is incorporated in the PXL slow simulator. The cluster-size distributions copy the data well enough so that the resolution of the HFT and the efficiency are reproduced with sufficient accuracy.

3.6 Zero Degree Calorimeter (ZDC)

The Zero Degree Calorimeter (ZDC) [6] is placed on both sides of the RHIC tunnel behind the first dipole magnet. This placement gives the ZDC the unique capability of measuring the energy of non-charged particles, such as spectator neutrons, without any contribution of the charged particles, because the neutral particles continue in a straight line and the charged ones are deflected by the RHIC magnetic field. The ZDC serves as an important trigger detector, it is used to determine the frequency of collisions, and thanks to the Shower-Maximum Detector (SMD) [7], can be utilized for the measurement of the collision event plane, and the polarization of the protons.

The ZDC consists of two identical sides, both placed in the RHIC tunnel, behind the first deflecting magnets. Each side consists of 3 towers made of a tungsten absorber, sensitive

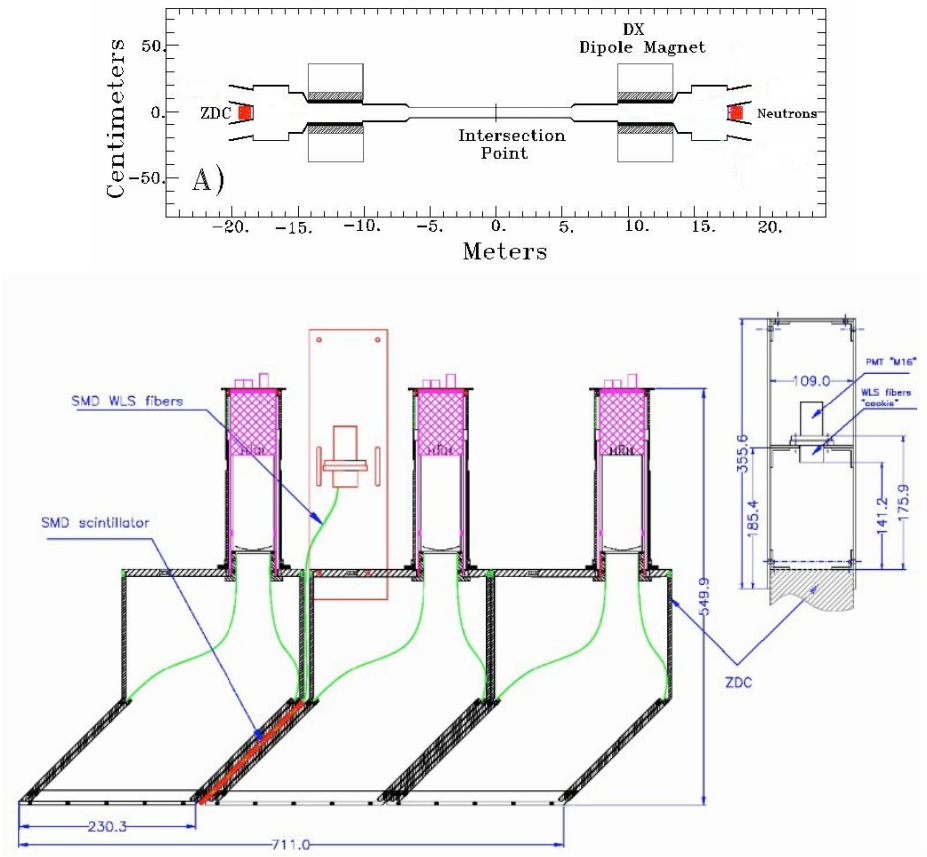

Figure 3.17: ZDC positions in the RHIC tunnel (top image) and the ZDC layout (bottom image) [7].

volume, consisting of plastic optical fibers, and a photomultiplier tube (PMT). A layout of the ZDC detector and the positions of the two ZDC sides are shown in Figure 3.17. A photo of the ZDC assembly is shown in Figure 3.18. As a neutral particle traverses the absorber, it creates a shower which emits Cherenkov radiation in the plastic fibers which are bundled together at a 45° angle to increase their sensitivity. The ZDC towers do not use scintillators, because the deposited energy (tens to thousands of GeV) is high enough that the Cherenkov radiation in the fibers is sufficient. The light is then carried into the PMT which is placed freely on the optical fibers bundle without any optical grease or glue.

Behind the first tower, there is the SMD, consisting of two overlaid layers of scintillator strips placed perpendicularly to the z direction. The SMD adds spatial information to the

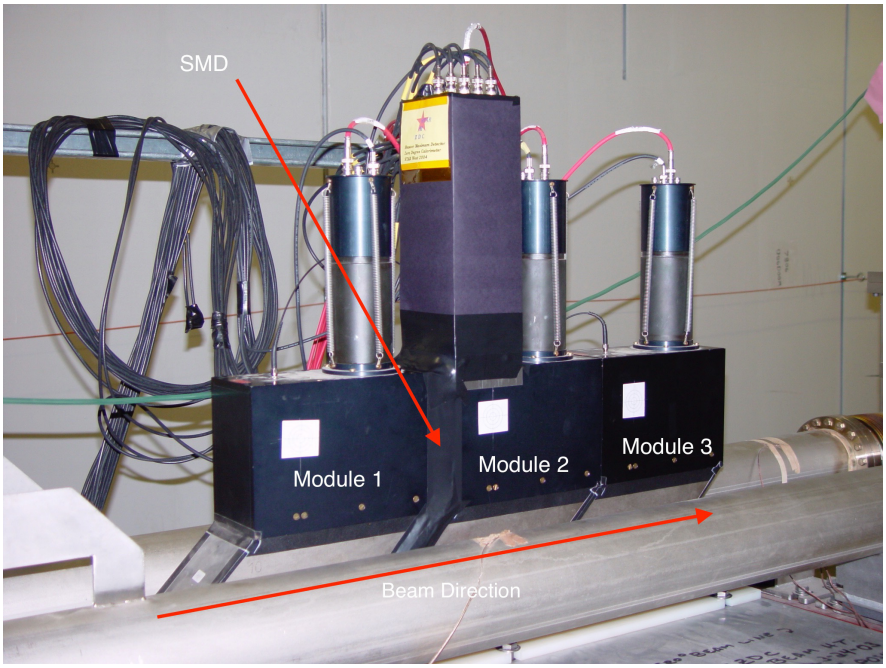

Figure 3.18: Photo of the ZDC assembly installed between RHIC accelerator tubes [7].

ZDC which is crucial to the event-plane determination, using spectator particles, and for the determination of the proton polarization. The scintillator strips are glued to optical fibers which lead the emitted light into a 16-channel PMT (enclosed in the black box on top of the assembly in Figure 3.18).

The entire detector is placed on rails between the RHIC accelerator tubes and can be manipulated using a chain crank.

3.6.1 Calibration of the ZDC towers

At the start of each ion run, the ZDC towers are calibrated, because the the PMT loose gain during the inter-run periods. The ion energy per nucleon has to be $E_{\mathrm{N}} \gtrsim 40\,\mathrm{GeV}$ for this calibration to be successful as below this energy, the ZDC is not sensitive enough. This calibration is typically performed during the first week of RHIC collisions when all the detectors are being commissioned for data taking. In this section, we describe the whole calibration procedure.

When an ultra-peripheral collision occurs, with a high probability, the nucleus is excited

and loses energy by emiting neutrons (typically one or two). These neutrons have low momenta (units to tens of MeV/c) in the frame of the emitting nucleus. Therefore, in the laboratory frame, the neutron momenta do not differ significantly from the per-nucleon momentum of the emitting nucleus (i.e. $\sim$100 GeV/c from a Au ion at top RHIC energy). These neutrons manifest themselves in the ZDC in the form of Single- and Double-Neutron Peaks (SNP and DNP, respectively), where the SNP has the energy per nucleon of the beam and the DNP has double the energy of the SNP, i.e. if the ion beam has $\sqrt{s_{\mathrm{NN}}} = 200$ GeV, the SNP will sit at 100 GeV and the DNP at 200 GeV.

The ADC readout value is proportional to the energy loss in the sensitive volume and the high voltage applied to the PMT. Therefore, we can calibrate the output of the ZDC towers by changing the high voltage (HV) applied to the PMTs.

When a single neutron, emitted from a nucleus at 100 GeV, hits the three towers of the ZDC, simulations show that the ratio of energy loss in the three towers should be approximately 6:3:1 [164]. We analyze the SNP created in heavy-ion collisions and adjust the high voltage so that the ADC value distribution of each tower matches the ideal ratio of 6:3:1 as closely as possible. Equally, we expect the ZDC single-neutron peak (SNP) to be at the same ADC value in both, the East and the West side. In reality, these two conditions are not achieved precisely, but the voltages are adjusted in an iterative process to be close to the ideal case.

For the calibration, in each step, we take a dedicated ZDC run with $\sim$10 M events (at full luminosity, this takes less than 5 min). Then, we look at the resulting SNP. For an illustration of the SNP see Figure 3.19. During the calibration, we change the voltages until at least 1 standard deviation of the SNP is in the ZDC measured range. Also, the ratio between the gain of the ZDC towers is corrected to match the ideal ratio 6:3:1. If the position of the SNP is too low and/or the ratio between the towers' gain is wrong, the voltage in the PMT has to be adjusted and then the whole procedure has to be repeated until the ratio of the gains approximates the desired one well enough.

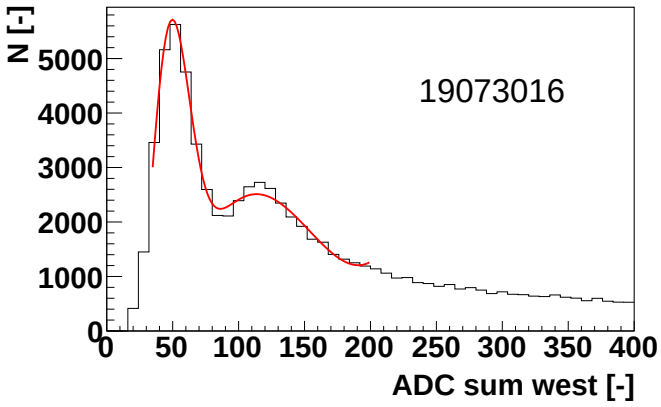

Figure 3.19: Single-neutron and double-neutron peaks for the West towers for in a 2018 test run.

The gain on the PMTs follows a power law

$$G = aU^b \tag{3.4}$$

where G is a gain and U stands for voltage. The coefficients a and b differ for each PMT, but approximately they are close to the values of [165]

$$b = 4.2\,, \qquad a = 4.0\,. \tag{3.5}$$

These values were used before the run 2018, however, in 2018, the PMTs were taken out for refurbishment and the values a and b were measured for all the PMTs. This measurement is described in Section 3.6.2.

The desired position of the SNP is usually set as 60 ADC values. The gain at the SNP is obtained via a fit of the gain, using two gaussians for the SNP and DNP on an exponential background (which empirically fits the background the best)$. The mean of the DNP gaussian is set as 2× the mean of the SNP. To calculate the desired voltages we use the formula

$$U_{\text{result}} = U_{\text{current}} \left(\frac{G_{\text{desired}}}{G} \frac{R_{\text{desired}}}{R} \right)^{1/b} \tag{3.6}$$

where G is the current position of the neutron peak, G_{desired} is the desired position of the neutron peak (currently 60), R_{desired} is the desired ratio between the gain of the ADC SUM tower and the current tower, and R is the current ratio.

3.6.2 ZDC Tower PMT replacement and calibration

The calibrations, described in the previous section, have shown that the yield from SNP in the ZDC towers is lowering in between the RHIC runs each year. The possible causes include gas leaks into the PMTs, slow decremental loss of the PMT dinodes properties, or darkening of the ZDC optical fibers.

In 2018, before the isobar (^{96}Zr and ^{96}Ru) running at $\sqrt{s_{\text{NN}}} = 200\,\text{GeV}$, the ZDC towers were thoroughly tested and several PMTs were replaced. The original goal was to replace all of the ZDC PMTs with spares from the Broad RAnge Hadron Magnetic Spectrometers (Brahms) experiment, however a check had to be made, whether the spares performance exceeded one of the original PMTs.

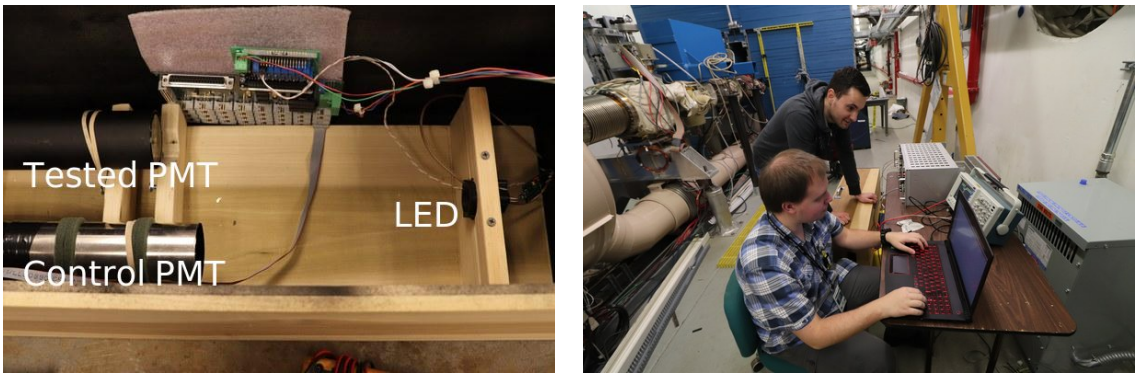

Figure 3.20: Photos of the ZDC-PMT and spare-PMT-candidate test setup. Left: Inside of the black box. Right: The entire setup deployed inside the RHIC tunel.

A photo of the experimental setup is shown in Figure 3.20. It consists of a flashing weak LED light, a control PMT, and the tested PMT, all enclosed in a wooden black box. The LED is controlled by a Beagle Board, powered via a USB charger which supplies the control PMT as well. The tested PMT uses an external high-voltage (HV) power supply. Both, the tested PMT and the control are read out in an oscilloscope that uses the control PMT as a

trigger. The main purpose of the control PMT is, however, to measure the light output of the LED and ensure that it is stable throughout the measurement.

The first measurement consisted of measuring the gain performance of the Brahms-spare PMTs. All data from the test are available in [166]. Gain at a set HV of 2500 V was measured as well as the a test whether a second pulse — a, so called, afterpulse — appears behind main pulse caused by the LED flash. The afterpulses are caused by ionized gas inside of the PMT and may indicate that the sealing on the tubes had been compromised. The gain was measured as height of the pulse in the oscilloscope. The requirements for the PMTs were high gain, stability throughout our measurement, low afterpulsing, and similar time performance to the PMTs, already used in the ZDC towers.

90 PMTs were cleaned and tested, however — except for 2 PMTs — the Brahms spares did not exceed the performance of the PMTs they were supposed to replace. The 2 well-performing PMTs were selected as replacements for the PMTs in the towers with the lowest gains. Moreover, all of the spares had relatively large afterpulses, compared to the old ZDC towers which, however, afterpulse as well.

Next, all the PMT from the ZDC towers and the chosen spares were tested for linearity of gain vs the light input. The voltage on the LED light was risen and the increase in gain was compared to the control PMT which had been previously proven to be linear. The results were fitted by a linear function. All of the ZDC towers and the tested spares followed a linear response to the change of light input.

An important measurement for the calibration of the ZDC, described in the previous section, is the response of the gain to the increase of HV on the PMT. The gain follows a power law (3.4) in which the exponent b has to be measured to make the calibration more precise and less time consuming in the beginning of the run. The results of the tests are plotted in Figure 3.21. The HV varied between 1500 V and 3500 V where the highest HV value of 3500 V is outside of the operating range of the ZDC power supply, but serves as a stability check of the PMTs. All the PMTs follow the power law (3.4), however two of the original ZDC towers – ZDC East2 and ZDC West3 had low gains overall and were replaced in the end.

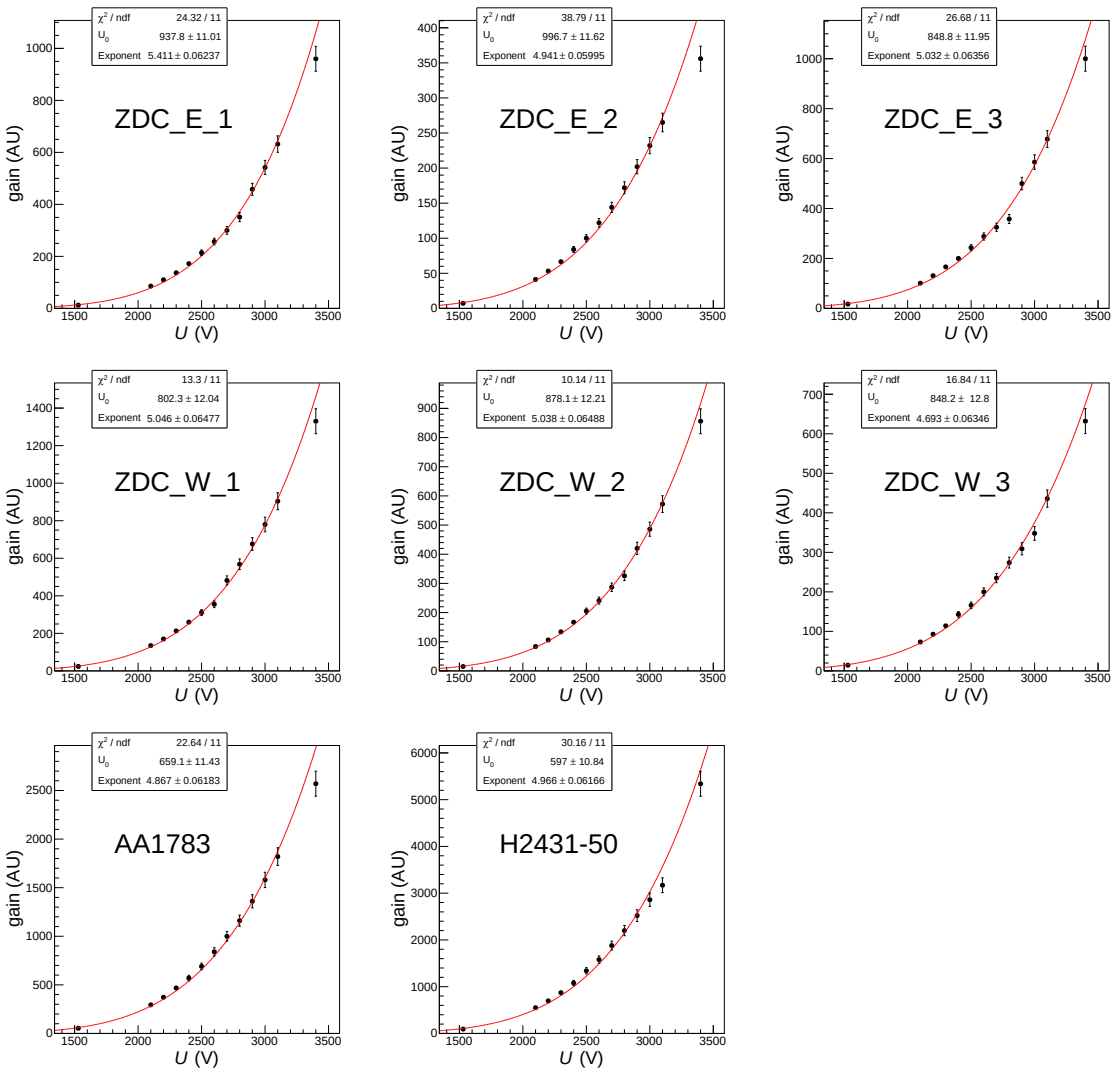

Figure 3.21: Measurement of the dependence of the PMT gain on the applied high voltage. All the ZDC towers were measured as well as two spares that were used instead of ZDC East3 and ZDC West3. AA1783 and H2431-50 are serial numbers of the PMTs. The data are fitted by the power law (3.4) where $a = 1/U_0$ and b is the Exponent.

According to this measurement and the calibration, several swaps of the PMTs were decided and 2 PMTs were replaced by the Brahms spares. The swaps and operating voltages, that are used since the calibration in Run 2018, are summarized in Table 3.3. The new PMTs were installed at the furthermost places from the IP, because of the lower light output of the last ZDC towers, as afterpulses fall linearly with the initial pulses.

Table 3.3: Swaps and final ZDC voltages after the calibration performed for the 2018 isobar run.

	Tower	Swapped with	Operating voltage [V]
East	1	same	2444
	2	swapped from East3	2633
	3	new AA1783	2329
West	1	same	2431
	2	same	3000
	3	new H2431-50	2101

3.7 Vertex-Position Detector (VPD)

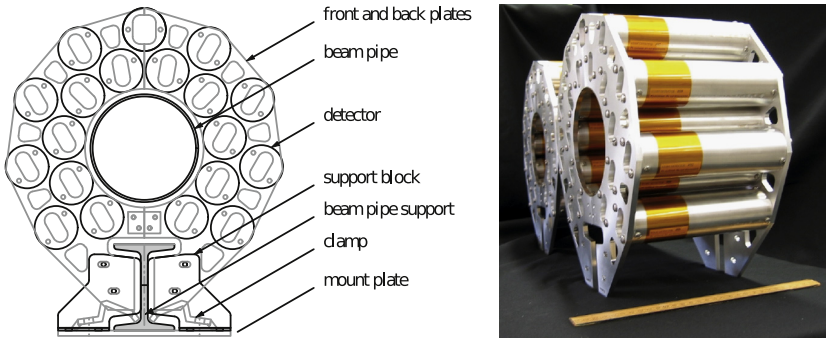

Figure 3.22: VPD assembly [167].

The VPD [167] consists of two identical assemblies, positioned 5.7 m from the center of STAR. A schematic picture of an assembly can be seen in Figure 3.22. Each of them is made of 19 detectors, consisting of a lead converter, followed by a fast plastic scintillator read by a photo-multiplier tube. The main purpose of the VPD is to measure photons from π^0 decays in forward direction and thus accurately measure the time of the collision, as well as the position of the primary vertex with the resolution of ~ 1 cm and ~ 2.5 cm for Au+Au and p+p collisions, respectively.

3.8 STAR forward upgrade: Forward Calorimeter System and Forward Tracking System

Currently, STAR is preparing new upgrades in the forward pseudorapidity region $2.5 < \eta < 4$ [168]. This upgrade has a rich physics program, consisting of diverse topics from cold QCD to heavy-ion physics. STAR will be able to explore QCD properties in the low regions of Bjorken x. This region of QCD is not currently well understood and the new STAR measurements will have a transformative effect. The measurement of the Drell-Yan process will be enabled for the first time at RHIC. Moreover, this forward upgrade will also enable the study of longitudinal structure of initial state of the evolution of heavy-ion collisions and study of the transport properties of the QGP. In order to achieve this, the forward detector system will have supreme detection capability of neutral pions, photons, electron pairs, jets and leading hadrons.

The layout of this upgrade is shown in Figure 3.23. Two detector systems are being developed: the Forward Calorimeter System (FCS) with an electromagnetic and hadronic calorimeters, and the Forward Tracking System (FTS). To achieve the upgrade's goals, the design requirements for the FTS are the track-charge separation ability, 30 % momentum resolution for tracks with $0.2 < p_{\mathrm{T}} < 2\,\mathrm{GeV}/c$, and more than 80 % efficiency at 100 track multiplicity per event. The FCS-electromagnetic calorimeter should achieve accuracy of $10\,\%/\sqrt{E}$ in p+p and p+ion collisions and $20\,\%/\sqrt{E}$ in ion+ion collisions and the FCS-hadron calorimeter $10\,\% + 50\,\%/\sqrt{E}$.

The FTS consists of three radially oriented discs of silicon detectors, called the Forward Silicon Tracker (FST), and three larger discs outside of the TPC, called Forward sTGC Tracker (FTT). The FST is made out of silicon micro-strip sensors similar to the IST (see Section 3.5.2). As the name suggests, the FTT is made of three discs small-strip Thin Gap Chambers (sTGC) [169], similar to the ones already installed at the ATLAS detector [170].

The FCS-electromagnetic calorimeter uses a refurbished lead-scintilator-sandwich detector, originally used by PHENIX [171]. The FCS-hadronic calorimeter consists or scintilator-iron-sandwich towers. Both of these detectors are read out by similar silicon photomultipliers

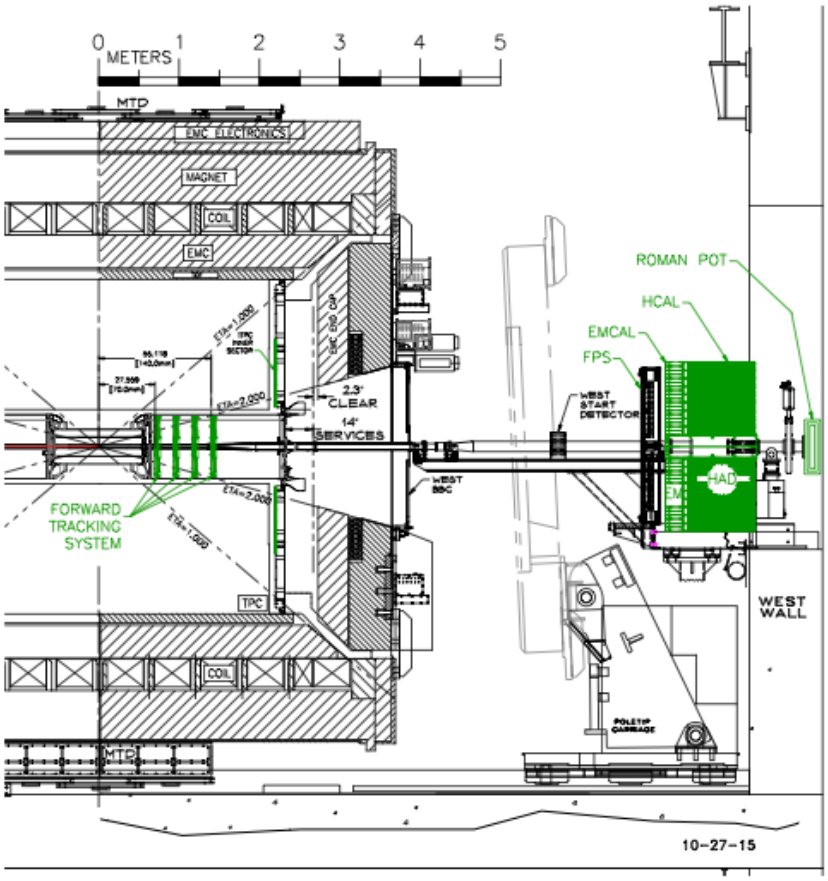

Figure 3.23: Layout of the STAR forward upgrade plan. Taken from [168].

and FEEs. This is the first hadronic calorimeter installed at STAR.

Both FCS electromagnetic and hadronic calorimeters are already installed at STAR and being tested while taking Au+Au data. Several modules of the FTS are being tested inside of STAR and the entire system is ready to be installed this year (in 2021) and take data from the polarized p+p collisions at $\sqrt{s} = 510\,\text{GeV}$ that are planned to take place at RHIC in 2022.

Chapter 4

Reconstruction of the Λ_c Baryon in Au+Au Collisions

$\Lambda_c^{\pm}$ is the lightest baryon containing a charm quark. As such, it is an excellent probe into the behavior of the QGP alongside precise measurements of D mesons. However, the combination of facts that it has an extremely short lifetime times the speed of light $c\tau \sim 60\,\mu m$ and the the useful decay for a direct reconstruction is a three-body decay into $\pi^{\pm}$, $K^{\mp}$, and $p^{\pm}$, makes this measurement challenging. $\pi^{\pm}$, $K^{\mp}$, and $p^{\pm}$ are the most abundant particles coming out of heavy-ion collisions which implies that any measurement of $\Lambda_c^{\pm}$ has to deal with a large background.

The $\Lambda_c^{\pm}$ were measured for the first time in heavy-ion–ion collisions [77] at the STAR experiment at RHIC. In particular, the Λ_c measurement was enabled by the Heavy Flavor Tracker (HFT) [1] upgrade that took data in the years 2014–2016. The HFT is described in more detail in section 3.5. In this chapter, the measurement of the Λ_c from signal extraction to the ratios of Λ_c/D^0 are described. These results were published in J. Adam et al., *"First Measurement of Λ_c Baryon Production in Au+Au Collisions at $\sqrt{s_{NN}} = 200\,GeV$"*, Phys. Rev. Lett. **124**, 172301 (2020) [9]. As one of the primary authors, I will describe the entire analysis, published in this paper, in more detail than is possible within the scope of an an article in a scientific journal.

4.1 Event and track selection

In this analysis, we use data recorded by STAR from Au+Au collisions at $\sqrt{s_{\mathrm{NN}}} = 200\,\mathrm{GeV}$ taken in 2014 and 2016. The Au+Au collisions are selected so that the PV is valid and is reconstructed fully inside the volume of the HFT. The distance of the PV from the center of the TPC along the z-axis is required to be $|v_z| < 6\,\mathrm{cm}$ and the difference between the v_z determined from the tracks and the one determined by the VPD has to be less than 3 cm. In addition, the distance from the center along the x, y plane $v_r = \sqrt{v_x^2 + v_y^2}$ is required to be less than 2 cm.

For the Λ_c analysis, we use triplets of pions, Kaons, and pions. The HFT tracking is required which means: In the 2014 data, the tracks are required to have at least one hit in each pixel layer and a hit in the IST (the SSD is not used in the tracking in 2014); in 2016 data, we require at least one hit in each pixel layer and at least one hit in either IST or SSD. In the TPC, tracks were selected to ensure that they are not fakes consisting of hits that do not come from one particle, but e.g. a combination of noise or hits from several tracks combined into one. We require the number of hits $N_{\mathrm{hits}} \geq 20$ and the ratio to maximum number of hits in the track trajectory $N_{\mathrm{hits}}/N_{\mathrm{hits\ max}} > 0.52$. The minimum track p_T was chosen as $0.5\,\mathrm{GeV}/c$ to save computation time and because bellow, the Λ_c cannot be extracted as they are drowned in the combinatorial background.

The PID-selection criteria are summarized in Table 4.1. Looser cuts were applied to the $\pi^\pm$, because of their higher relative abundance, compared to $\mathrm{K}^\mp$ and $\mathrm{p}^\pm$. In the TPC, we compare the $\mathrm{d}E/\mathrm{d}x$ value of the track to the width of the distribution $\sigma_{\mathrm{d}E/\mathrm{d}x}$ of each particle species at the track momentum

$$N_\sigma = \frac{\mathrm{d}E/\mathrm{d}x}{\sigma_{\mathrm{d}E/\mathrm{d}x}}\,. \tag{4.1}$$

We set the cut at $|N_\sigma| < 3$ for $\pi^\pm$ and $|N_\sigma| < 2$ for $\mathrm{K}^\mp$ and $\mathrm{p}^\pm$.

For the PID in TOF, we use the, so called, hybrid approach: The time of flight information is used if the track is matched to a TOF hit. The cut on the fraction β of the speed of light, compared to the supposed speed of the particle divided by c at its momentum p and supposed

rest mass m of the respective particle species is set as

$$\left|\Delta\frac{1}{\beta}\right| = \left|\frac{1}{\beta} - \frac{1}{\beta_{\text{sup}}}\right| = \left|\frac{1}{\beta} - \frac{p}{\sqrt{m^2c^2 + p^2}}\right| < 0.03 \tag{4.2}$$

for all particles. For protons and kaons, we use the hybrid approach for high-p_{T} tracks and we require the TOF hit for tracks with $p_{\text{T}} < 3\,\text{GeV}/c$ and $p_{\text{T}} < 2\,\text{GeV}/c$, respectively. For pions, we use the hybrid approach throughout the whole p_{T} spectrum. All tracks are then saved and combined into triplets so that additional cuts can be applied.

Table 4.1: PID selection criteria for Λ_c-daughter candidates.

Particle species	$\mathrm{d}E/\mathrm{d}x$ cut	Hybrid-TOF region	$\Delta(1/\beta)$ cut
$\pi^{\pm}$	$3\,\sigma_{\mathrm{d}E/\mathrm{d}x}$	All tracks	0.03
$\mathrm{K}^{\mp}$	$2\,\sigma_{\mathrm{d}E/\mathrm{d}x}$	$p_{\text{T}} \geq 2\,\text{GeV}/c$	0.03
$\mathrm{p}^{\pm}$	$2\,\sigma_{\mathrm{d}E/\mathrm{d}x}$	$p_{\text{T}} \geq 3\,\text{GeV}/c$	0.03

4.2 Centrality determination

The centrality of the collision is determined by the number of tracks N_{tracks} with at least 10 TPC hits in the rapidity range $|\eta| < 0.5$ and DCA $< 3\,\text{cm}$. This number is then corrected with regards to the geometrical efficiency according to v_z and to the TPC efficiency, according to instant luminosity. Figure 4.2 shows the centrality definitions extracted from Monte-Carlo simulations [172,173], using the Glauber Model. This model was used to extract the number of binary nucleon–nucleon collisions N_{coll} and the number of participants N_{part} as well.

4.3 Topological reconstruction and cuts optimization

In the three-body $\Lambda_c{}^{\pm}$ decay, all the three daughter particles come practically from the same secondary vertex (SV), even in the case of the decays through resonances, because they decay

Table 4.2: Centrality definitions in 2014 and 2016 Au+Au collisions at $\sqrt{s_{\mathrm{NN}}} = 200\,\mathrm{GeV}$, extracted from Glauber-Model simmulations.

Centrality (%)	N_{tracks} 2014	N_{tracks} 2016	$\langle N_{\mathrm{coll}} \rangle$	$\langle N_{\mathrm{part}} \rangle$
75–80	10–15	8–13	10.48	11.82
70–75	15–21	13–20	16.11	16.68
65–70	21–30	20–29	24.59	23.25
60–65	30–41	29–40	36.13	31.15
55–60	41–56	40–55	52.77	41.27
50–55	56–73	55–72	75.36	53.46
45–50	73–94	72–94	105.25	67.93
40–45	94–119	94–119	143.54	84.71
35–40	119–148	119–150	191.83	103.99
30–35	148–182	150–185	253.13	126.52
25–30	182–221	185–226	328.99	152.31
20–25	221–266	226–273	422.49	181.93
15–20	266–317	273–327	537.52	215.98
10–15	317–376	327–389	677.99	254.90
5–10	376–443	389–461	852.75	299.95
0–5	> 443	> 461	1066.5	348.74

very fast. In reality, however, it is rather challenging to recognize a ${\Lambda_c}^{\pm}$ decay from random combinations of $\pi^{\pm}$, $K^{\mp}$, and $p^{\pm}$, because of the detector resolution and because the ${\Lambda_c}^{\pm}$ decay close to the PV. Moreover, $\pi^{\pm}$, $K^{\mp}$, and $p^{\pm}$ are the most abundant charged particles in a typical Au+Au collision, creating a large number of random combinations.

Thanks to the excellent resolution of the HFT, it is possible to reduce the combinatorial background enough that the signal coming from Λ_c decays can be separated. This is done using cuts on the topology of the reconstructed tracks. $\pi^{\pm}$-, $K^{\mp}$-, and $p^{\pm}$-track candidates are collected and ordered into triplets and then their SV is reconstructed as follows:

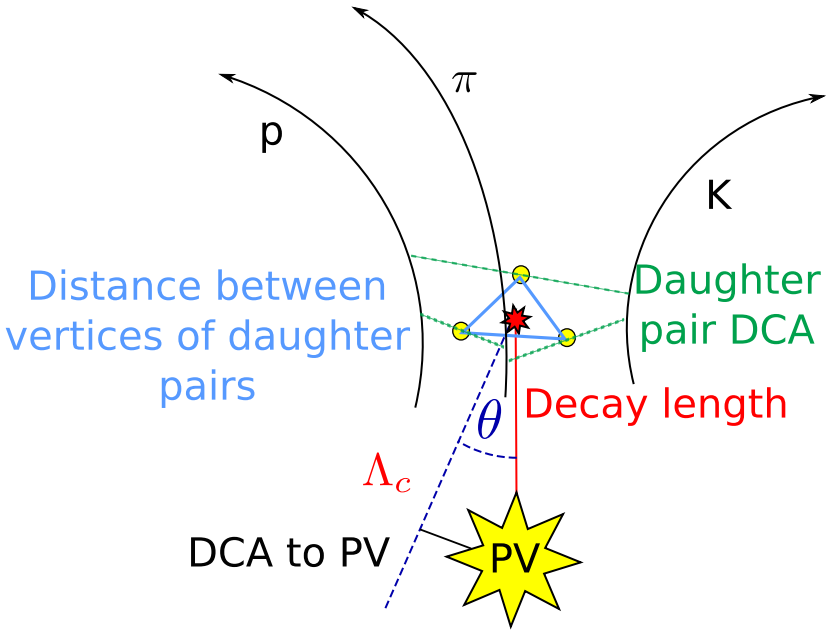

Figure 4.1: Illustration of variables used for topological cuts for the Λ_c analysis.

First, the distance of closest approach (DCA) of the PV (yellow star in Figure 4.1) to each track helix is calculated and an initial cut is applied. Next, we proceed with the reconstruction of the SV itself: Since the SV is very close to the PV (in the order of tens of μm), the track helices can be approximated via straight lines. This approximation has been shown to have negligible effect on all the topological variables and saves the computational time by ∼2 orders of magnitude since the points of closest approach (PCA) of two lines can be calculated analytically. The PCA is calculated for each combination of two tracks, i.e. we end up with 6 PCA. The vector average of each two PCA is stored as the, so called, vertex of daughter pairs (VDP – yellow circles in Figure 4.1)

$$\overrightarrow{\mathrm{VDP}}_{i,j} = \frac{1}{2}\left(\overrightarrow{\mathrm{PCA}}_i + \overrightarrow{\mathrm{PCA}}_j\right) . \tag{4.3}$$

Finally, the SV position (red star in Figure 4.1) is calculated as an average of all the PCA

$$\overrightarrow{\mathrm{SV}} = \frac{1}{6}\sum_{i=1}^{6} \overrightarrow{\mathrm{PCA}}_i . \tag{4.4}$$

At this point, the time of flight information of the daughter particles is corrected since their point of origin is known. The TOF PID selection is then reapplied.

Since the Λ_c daughter tracks come from the same SV, the signal differs from the background in several key topological variables. The chosen ones are shown in Figure 4.1 and they are listed here:

- The distance between the reconstructed PV and SV: the "Decay length" (full red line),
- the distances of closest approach (DCA) of each daughter track to the PV,
- the maximum distance between each pair of daughter tracks (green dashed lines),
- the maximum distance of pair vertices (full light blue lines),
- the cosine of the angle θ between reconstructed momentum of the triplet (vector extended by the dashed dark blue line) and the line between SV and PV (full red line).

The difference between the data and background is illustrated in Figure 4.2 from Run 2014. While there is not a clear-cut separation between the signal and the background, using multivariate analysis, we can optimize the selection criteria for Λ_c candidates.

To save computation time and disc space, the Λ_c-candidate triplets were pre-selected in both, the signal and the background. Table 4.3 shows the pre-selection criteria for the 2014 and 2016 data samples. The 2016-data set utilizes slightly more stringent cuts, because the training on the 2014-data set has shown that the open cuts are not needed.

To optimize the selection criteria (or cuts) on the topological variables, we maximize the significance s of the Λ_c signal

$$s = \frac{S}{\sigma_{S+B}} \tag{4.5}$$

where S is the number of Λ_c signal counts, σ_{S+B} is the uncertainty of obtaining the signal. If we apply this to the most common background estimations, we get

$$s_{\text{wrong-sign}} \simeq \frac{S}{\sqrt{S + \frac{4}{3}B_{\text{wrong-sign}}}}\,, \qquad s_{\text{mixed}} \simeq \frac{S}{\sqrt{S + B_{\text{mixed}}}} \tag{4.6}$$

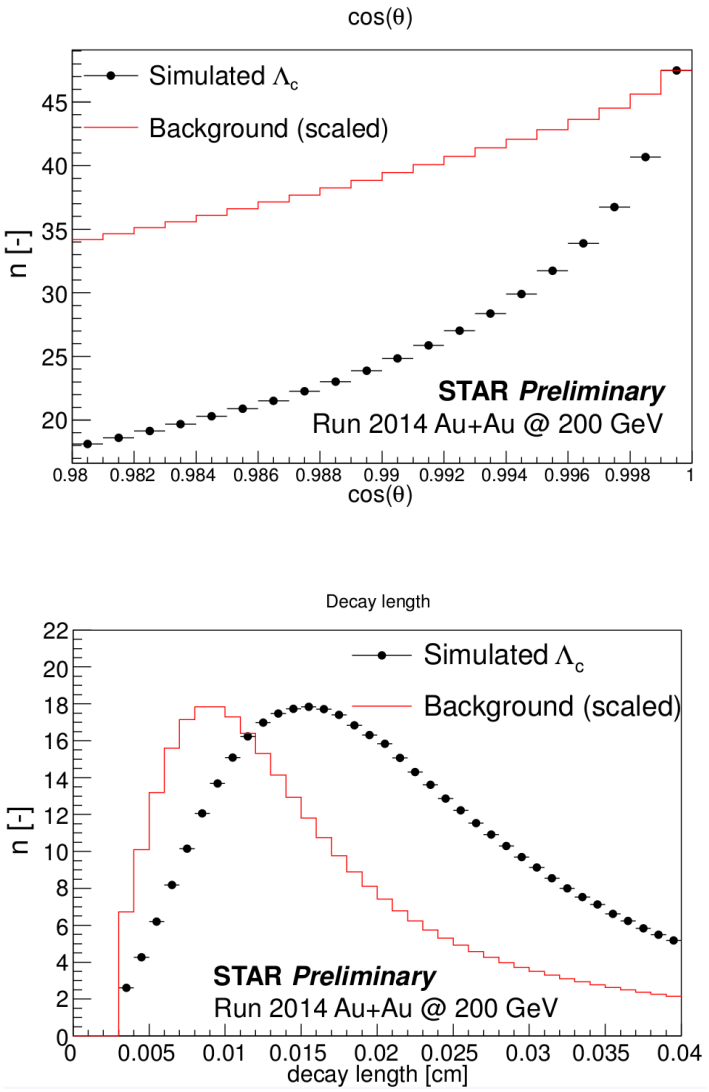

Figure 4.2: Examples of topological variables used for selection criteria: Top panel: Decay length; Bottom panel: cos(θ). The red line is the background from data with a wrong charge sign combination and the signal is extracted from the data-driven Monte Carlo simulation.

where $B_{\text{wrong-sign}}$ is a background estimate, using the wrong-sign method, and B_{mixed} uses the mixed-event method. The factor 4/3 comes from combinatorics of the wrong sign background estimate. In a very large pool of $\pi^{\pm}$, $K^{\mp}$, and $p^{\pm}$, there are 3× more combinations of wrong-sign triplets than there are correct ones. Therefore, the error of the signal is $\sqrt{S+B}$ and the error of the background estimate is $\sqrt{\frac{1}{3}B_{\text{wrong-sign}}}$. Because the uncertainties are not correlated, we can calculate the final error as $\sqrt{S+\frac{4}{3}B_{\text{wrong-sign}}}$. In the case of the mixed-

Table 4.3: Pre-selection cuts used on the 2014- and 2016-training samples.

Variable	2014	2016
$\cos(\theta)$	> 0.95	> 0.99
Decay length	$> 50\,\mu m$	$> 100\,\mu m$
Daughter pair DCA	$< 100\,\mu m$	$< 100\,\mu m$
DCA to PV	$< 100\,\mu m$	$< 100\,\mu m$
DCA of π, K, and p to PV	$> 50\,\mu m$	$> 50\,\mu m$

event background extraction, we expect the number of events to be large, thus we can neglect the contribution from the background estimate. Since $B_{\text{wrong-sign}}$ and B_{mixed} are about equal — albeit with different uncertainties — the approximation (4.6) clearly shows that the mixed event background estimate gives higher significance s_{mixed} than $s_{\text{wrong-sign}}$, however, in the case of the Λ_c, only slightly.

4.3.1 Number of generated signal and background triplets for training

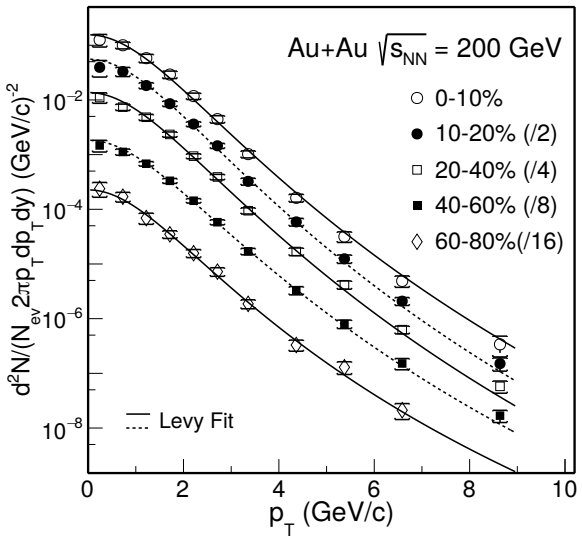

Figure 4.3: D^0 p_T spectra measured by STAR [90] in different centralities, used in the estimate of the number of signal triplets S.

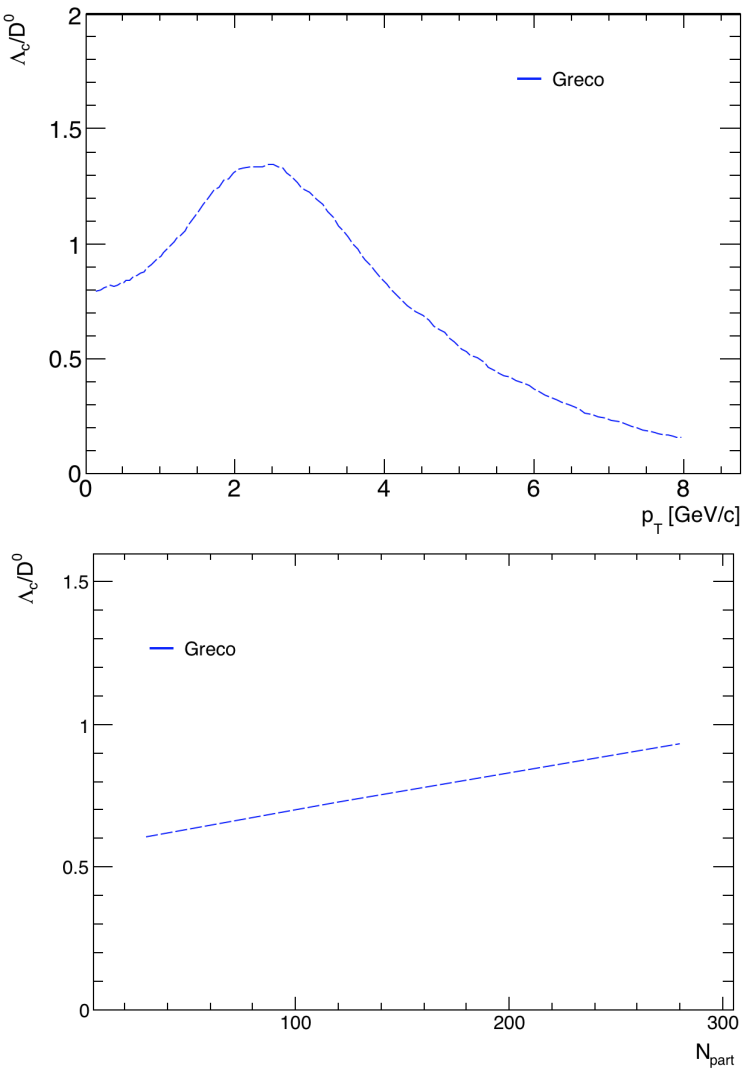

Figure 4.4: Model calculation [113] of the ratio of Λ_c/D^0 used in the calculation of the number of signal candidates S. The top plot shows the dependence on p_T and the bottom plot the dependence on the centrality.

The number of background triplets B is taken directly from data and is not modified for the training. The signal triplets, on the other hand, are generated with a flat distribution in p_T and y, and their number S is later scaled to resemble the physical spectrum of Λ_c in heavy-ion collisions, measured by STAR. We used the measured spectrum of D^0 $S_{D^0}(p_T, \text{cent})$ shown in figure 4.3 [90] and then we scaled it with the ratio $R(p_T, \text{cent})$ of D^0/Λ_c, according

to the formula

$$S = R(p_{\mathrm{T}}, \mathrm{cent})\, 2\pi p_{\mathrm{T}}\, \mathrm{d}p_{\mathrm{T}}\, \mathrm{d}y\, 2S_{\mathrm{D}^0}(p_{\mathrm{T}}, \mathrm{cent})\, N_{\mathrm{Event}}(\mathrm{cent})\, F_{\mathrm{Br}}\, \epsilon_{\text{pre-tune}} \tag{4.7}$$

where N_{Event} is the number of events with the centrality, F_{Br} is the branching ratio of the p, K, π three-body-decay channel, and $\epsilon_{\text{pre-tune}}$ is the efficiency of detecting the triplet with the STAR detector evaluated with the data-drive fast simulator (see Section 4.4), using the pre-tune cuts from Table 4.3. For the ratio R, the Greco-model calculation [113] was used. The dependence of R on p_{T} and centrality is shown in Figure 4.4.

4.3.2 Boosted Decision Trees

Because of the relatively very short lifetime of the Λ_{c} ($c\tau \approx 60\,\mu\mathrm{m}$ [25]), the measurement of the Λ_{c} is quite difficult even with the HFT. Therefore, machine learning methods had to be used to improve the signal extraction from data via selecting proper secondary vertices. In our analysis, the selection criteria were optimized via the Toolkit for Multivariate Analysis (TMVA) Package [174], using the Boosted Decision Trees (BDT) method — a well-established method for supervised machine learning.

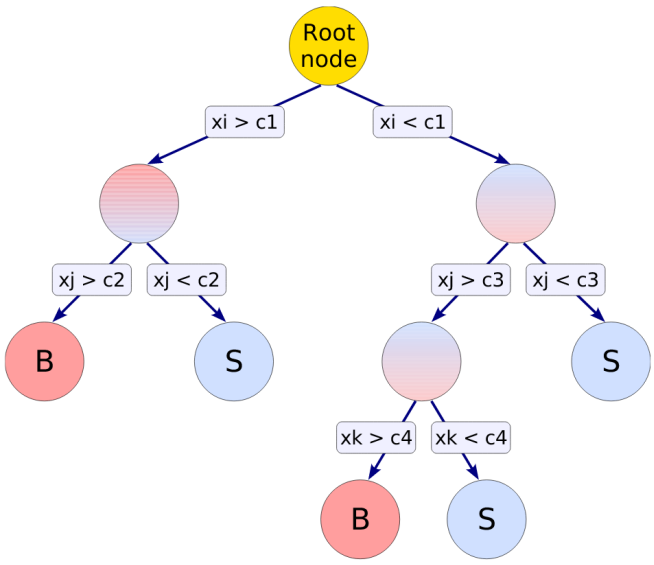

Figure 4.5: An illustration of principle of decision-tree-based algorithms [174].

The advantages, compared to set (so-called rectangular) cuts in each variable, is that the BDT selects a hyperplane in the N-dimensional space of N selected variables. Thus, we avoid the, so called, dimensionality problem — the fact that straight cuts tend to fail in many-dimensional spaces, i.e. the significance limit in infinite dimension space goes to zero. Even in as few as two dimensions, however, the BDT tend to produce a higher significance of the signal. In this analysis, the significance of the Λ_c improved approximately by a factor of two using the BDT, compared to rectangular cuts.

An illustration of a decision tree is shown in Figure 4.5. Decision-tree-based algorithms recursively separate the data into binary subsets. At each node a decision is made whether the input is more signal-like or background-like, according to one of the training variables. The training is performed in each node to maximize the "information" gained by the decision. This is done until a stop criterion — typically a maximum depth of the tree, no more information is gained, etc. — is met. Large tree depths can, however, lead to overtraining. The BDT algorithm solves this issue by using a large number of trees with low depths (usually 3–5). In the boosted approach (hence the name), the trees are constructed sequentially where the misclassified trees have a larger weight. The final response is a weighted sum of the individual decision trees. In this analysis, BDT with 800 trees of maximum depth of 5 was used.

Approximately half of the simulated events are used for training and half for the validation of the BDT method, especially for the overtraining check. The BDT training was performed separately for different centrality (0–20 %, 20–50 %, 50–80 %, 10–60 %, and 10–80 %) and p_T (2.5–3.5 GeV/c, 3.5–5.0 GeV/c, 5.0–8.0 GeV/c, and 3.0–6.0 GeV/c) ranges. The results of signal (blue – full) and background (red – hatched) are shown in Figure 4.6. The points show the training sample and the boxes show the validation sample. There is a clear separation between the signal and the background with BDT response. A clear indication of overtraining would be if the distributions significantly differed from each other which did not occur.

The signal and background efficiencies ϵ (top panels) vs the BDT response and significances (bottom panels) vs the BDT response are shown in Figures 4.7–4.10, where $\epsilon = N_{\text{pre-tune}}/N_{\text{passed}}$ in which the numbers of triplets are $N_{\text{pre-tune}}$, that passed the pre-tune cuts, and N_{passed} that passed the more stringent cuts, performed by the BDT. For significance,

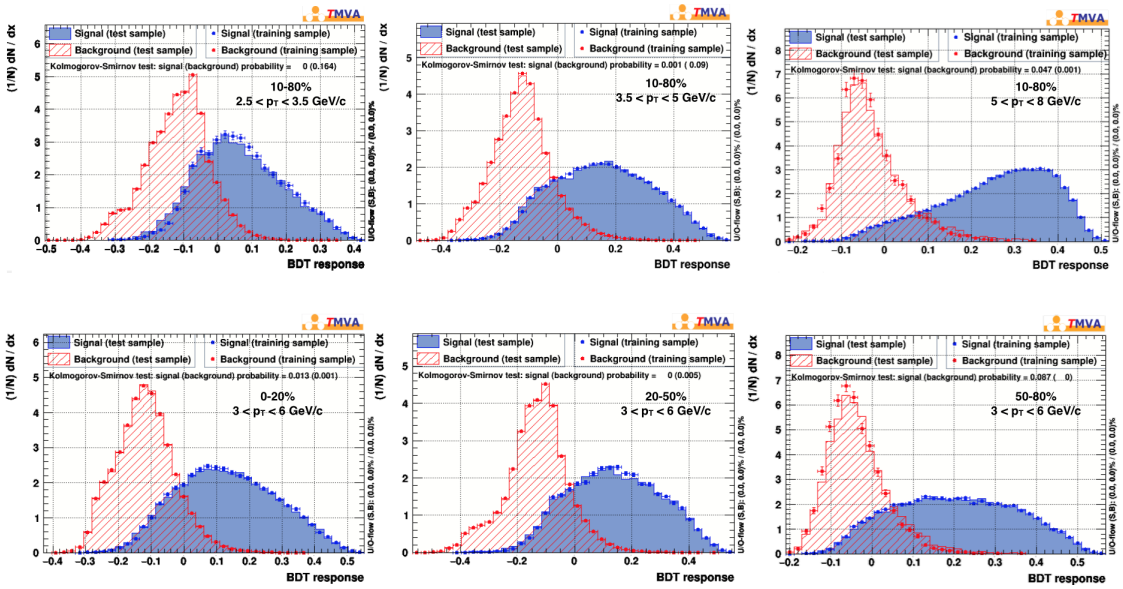

Figure 4.6: BDT response in centrality and p_{T} bins for signal and background.

we used the $s_{\text{wrong-sign}}$ in Formula (4.6). Figures 4.7 and 4.8 are from the 2014 data-taking and 4.9 and 4.10 are from 2016, where the first figure is always split into p_{T} intervals in 10–80 % central collisions and the bottom panel is always split into centrality intervals with $3\,\mathrm{GeV}/c < p_{\mathrm{T}} < 6\,\mathrm{GeV}/c$. The highest significance was chosen as the optimal BDT tune.

Figure 4.11 shows the comparison between the raw signal, exctracted from the 2014 data, using rectangular cuts (with a set value) and BDT, in the left- and right-hand plots, respectively. The signal-to-background ratio was improved by the BDT and the background was suppressed by ∼3–4 orders of magnitude. The significance of the signal was improved by ∼50 % which is a crucial improvement for the separation of the signal into p_{T} and centrality intervals, and for testing of the validity of theoretical models.

4.4 Data-driven fast simulation

The data-driven fast simulation is a novel approach of making a realistic monte-carlo model of all the detector variables. Its vast advantage over GEANT-based [4] simulations is the computational speed without sacrificing accuracy. Compared to HIJING [175] simulation of

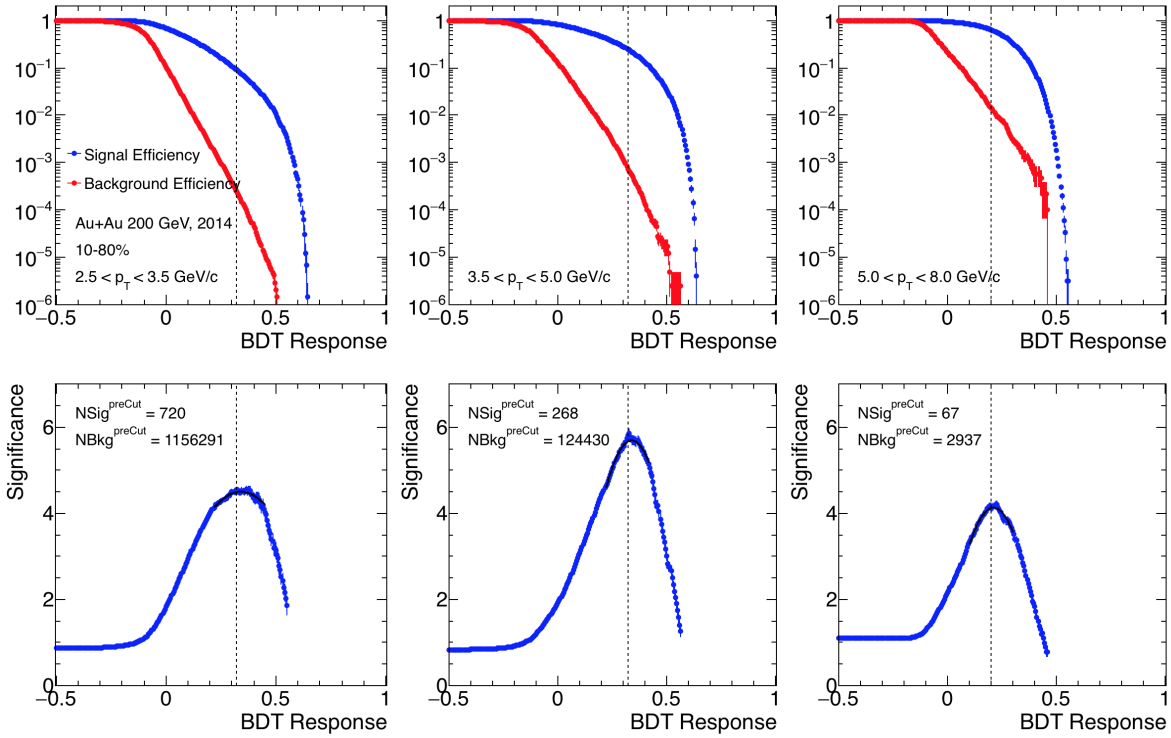

Figure 4.7: Signal and background efficiency (top) and significance (bottom) versus BDT response in the 10–80 % central Au+Au collisions recorded in 2014.

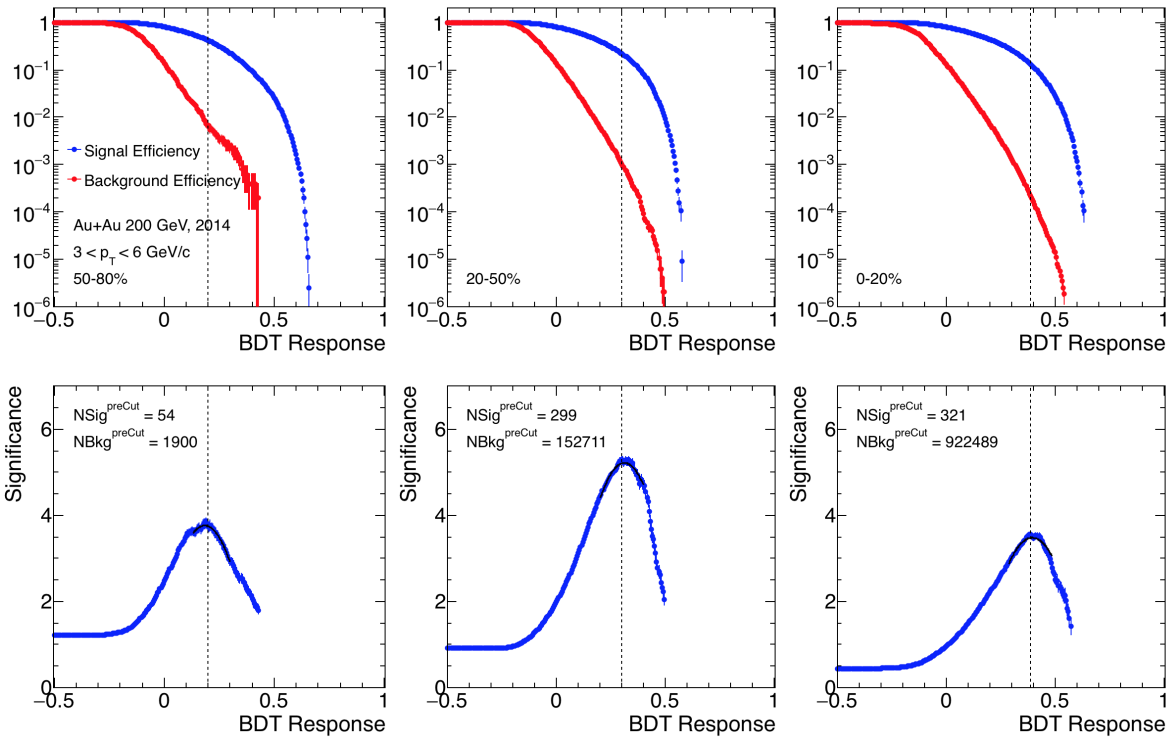

Figure 4.8: Signal and background efficiency (top) and significance (bottom) versus BDT response for $3\,\mathrm{GeV}/c < p_\mathrm{T} < 6\,\mathrm{GeV}/c$ in different centrality intervals, in 2014 data.

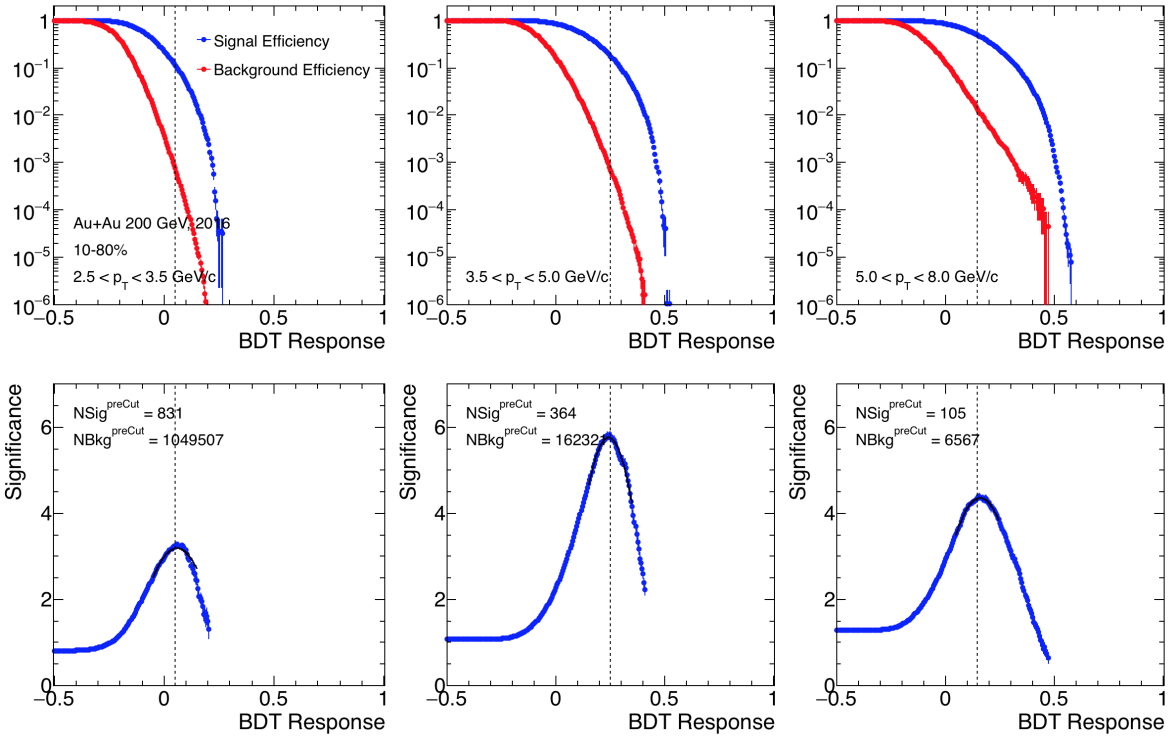

Figure 4.9: Signal and background efficiency (top) and significance (bottom) versus BDT response in the 10–80 % central Au+Au collisions recorded in 2016.

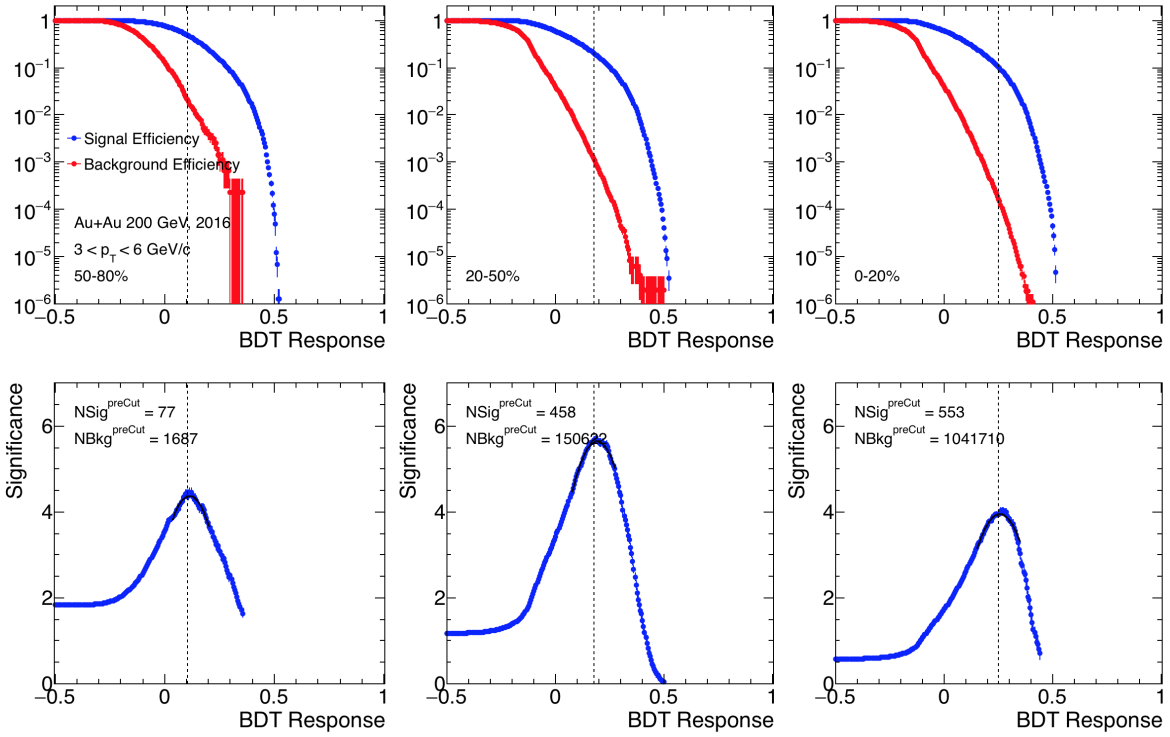

Figure 4.10: Signal and background efficiency (top) and significance (bottom) versus BDT response for $3\,\mathrm{GeV}/c < p_\mathrm{T} < 6\,\mathrm{GeV}/c$ in different centrality intervals, in 2016 data.

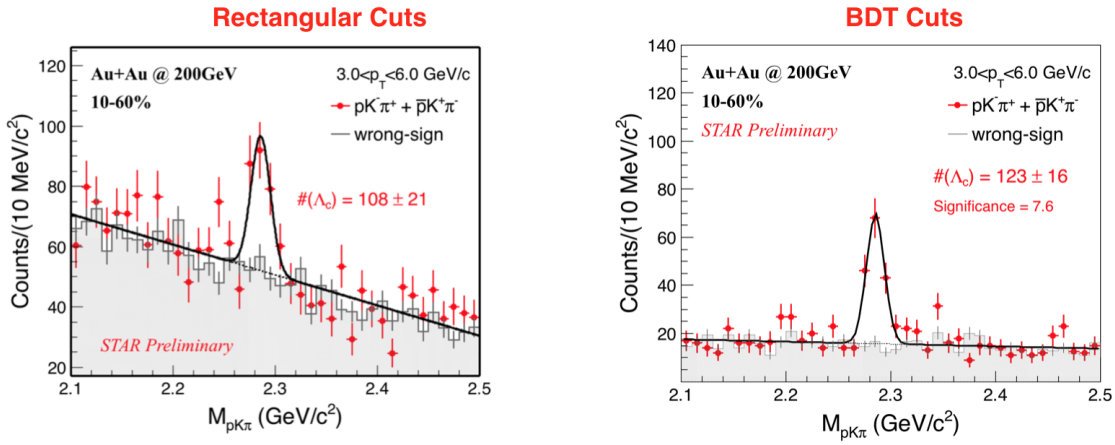

Figure 4.11: Invariant mass spectrum of the p+K+π triplets in Au+Au collisions with $\sqrt{s_{\mathrm{NN}}} = 200\,\mathrm{GeV}$ at centrality 10–60 %, recorded in 2014, with a transverse momentum cut of $3\,\mathrm{GeV}/c < p_{\mathrm{T}} < 6\,\mathrm{GeV}/c$. In the left-hand-side plot, the cuts were optimized, using the rectangular cuts and in the right-hand-side, using the BDT. The solid circles are the correct-charge combinations and the grey histogram represents scaled wrong-charge triplets.

central Au+Au collisions decayed into a GEANT3 model of the STAR detector, the data-driven fast simulation is ∼7 orders of magnitude faster.

The detector response is simulated in the following steps:

- First, $\Lambda_c{}^{\pm}$ are produced in EvtGen [176] decayer uniformly in p_{T} and rapidity y, within $0.5\,\mathrm{GeV}/c < p_{\mathrm{T}} < 10\,\mathrm{GeV}/c$ and $|y| < 1$. EventGen is a PYTHIA8-based simulator of particle-decay topology and dynamics, including the three-body weak-sector Dalitz decays, such as the Λ_c-three-body decay.

- Next, the Λ_c are decayed via the three-body decay, and via K*+$p^{\pm}$ and $\Lambda(1520\,\mathrm{GeV}/c^2)$+$\pi^{\pm}$ resonance decays with the measured branching ratios, according to [25], into $p^{\pm}$, $K^{\mp}$, and $\pi^{\pm}$.

- The momenta of daughter particles are smeared, according to resolution, obtained from the embedding of GEANT simulated $p^{\pm}$, $K^{\mp}$, and $\pi^{\pm}$ tracks into measured Au+Au events in the TPC. The efficiency of the TPC is obtained in the same way.

- The HFT properties are obtained from measured data in this simulation, hence the

name of this simulator:

- TPC and HFT tracking are independent, therefore, the HFT efficiency is obtained from the ratio of HFT tracks divided by all the TPC tracks.
- The daughter tracks positions are smeared according to resolution of the DCA of the primary tracks to the PV. In the case of $\pi^{\pm}$ and $K^{\mp}$ the DCA distributions of inclusive tracks are used, because the contributions of secondary tracks were proven to be negligible in an independent simulation. The $p^{\pm}$ have to be corrected for the Λ-baryon decays.
- The PV has a finite resolution as well and its position has to be smeared. In the central Au+Au collisions this can be neglected as the DCA resolution is much worse than the PV, however in the peripheral collisions the PV position has to be smeared, according to HIJING simulation of these events in a GEANT model of STAR.

This simulation has been verified, using simulated $\Lambda_c^{\pm}$ decays in full HIJING simulations of Au+Au events in a GEANT model of STAR, as well as the embedding of GEANT-simulated $\Lambda_c^{\pm}$ decays in measured Au+Au collisions.

4.5 Mixed-event background subtraction

In the mixed-event method for subtraction of the combinatorial background, tracks from different events are mixed together, therefore they cannot be correlated. The advantage of this method, compared to e.g. the wrong-sign method, is that the number of such mixed events is only limited by the computing power. Therefore, the background can be measured very precisely by mixing with a large number of events – see e.g. the formula (4.6).

There are several caveats to implementing the mixed-event method in three-body-decay analyses with topological selection. The events are always mixed within the same centrality and v_z bin. Figure 4.12 illustrates, how the mixed-event method is performed. In this example, we show a buffer of 5 events of the same centrality and v_z: First, protons are

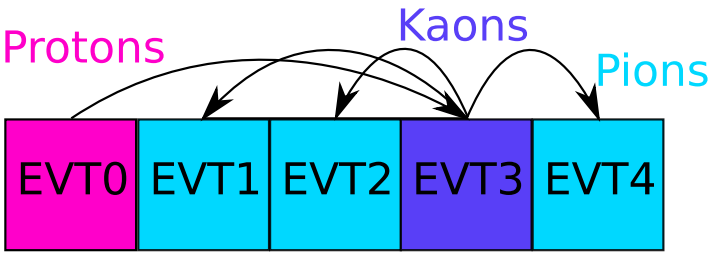

Figure 4.12: Illustration of the three-body event-mixing method. Protons from one event are mixed with kaons from another event and saved as pairs. Pions are then added from different events.

combined with kaons from another event and saved as pairs. Then we can add pions from all the remaining events. We can make 12 (3×4) combinations in a buffer of 5 events.

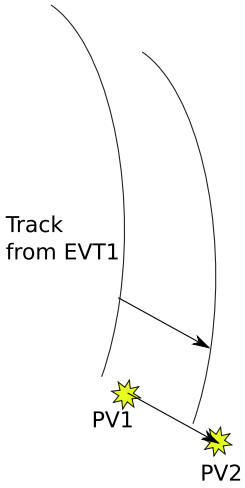

Figure 4.13: Illustration of track shifting in the mixed-event background-subtraction method.

Because of the topological cuts, the tracks have to be shifted when they are mixed into another event. Figure 4.13 shows the mixing of a track into another event. When a track is being added into another event, it has to be shifted by the relative position of the events' primary vertices, i.e.: When a track from an event with a PV coordinates $\overrightarrow{\mathrm{PV1}}$ is mixed into an event with a PV location $\overrightarrow{\mathrm{PV2}}$, all of the track's coordinates have to be shifted by $\overrightarrow{\mathrm{PV2}} - \overrightarrow{\mathrm{PV1}}$.

Figure 4.14 shows the comparison of the mixed-event and wrong-sign combinatorial-background-subtraction methods. This invariant-mass spectrum from 2014 data does not

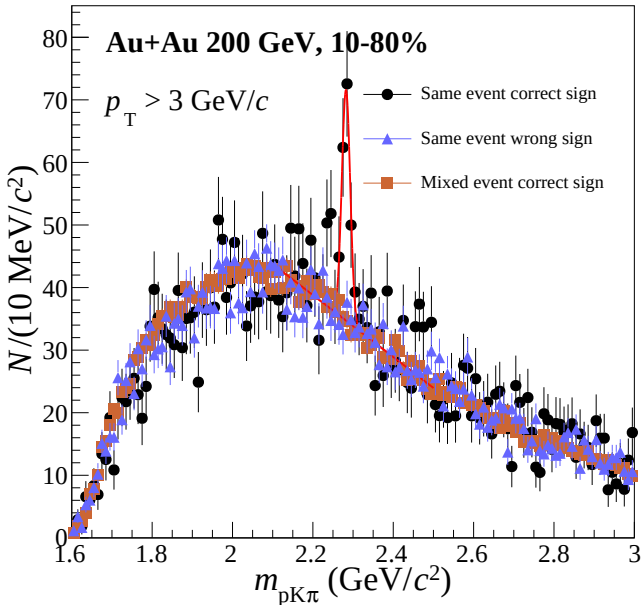

Figure 4.14: Invariant-mass spectrum of the p+K+π triplets in Au+Au collisions with $\sqrt{s_{\mathrm{NN}}} = 200\,\mathrm{GeV}$ taken in 2014 at centrality 10–80 % with a transverse momentum cut of $p_{\mathrm{T}} > 3\,\mathrm{GeV}/c$. Mixed-event and wrong-sign combinatorial-background-subtraction methods are compared.

use the final topological cuts optimized by BDT, but rather only rectangular cuts. We can easily observe that the overall shape of the mixed-event background copies the wrong-sign triplets. The significance for this topological-cut set improved from $s_{\text{wrong-sign}} = 5.6$ to $s_{\text{mixed}} = 5.9$ — see the approximate formula (4.6). This improvement is rather modest, therefore the wrong-sign method was used in further analysis to conserve computational time. The mixed-event method is, however, used when checking the difference between Λ_{c}^{+} and Λ_{c}^{-} (see Section 4.9.4). In this case the wrong-sign background-subtraction method cannot be used as the shape of the background can be different for different charge combinations. Figure 4.15 shows the invariant-mass spectra for Λ_{c}^{+} and Λ_{c}^{-} from 2014, using the same topological cuts as in Figure 4.14. For both p^{+}+K^{-}+π^{+} and p^{-}+K^{+}+π^{-} triplet combinations, the shape of the mixed-event background copies the the shape of the same-event invariant mass spectrum outside of the Λ_{c}^{+} and Λ_{c}^{-} peaks.

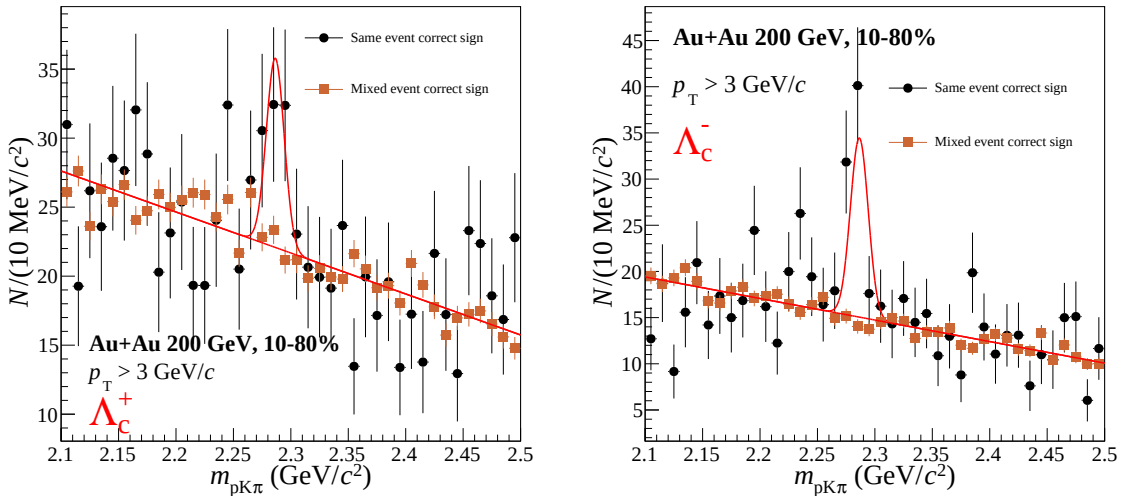

Figure 4.15: Invariant-mass spectrum of the p^++K^-+π^+ (left) and p^-+K^++π^- (right) triplets in Au+Au collisions taken in 2014 with $\sqrt{s_{NN}} = 200\,\text{GeV}$ at centrality 10–80 % with a transverse momentum cut of $p_T > 3\,\text{GeV}/c$.

4.6 Raw-signal extraction

The raw signal of $\Lambda_c^\pm$ is extracted using the invariant mass spectra via, so-called, bin-counting and a combination of the wrong-sign and side-band background-subtraction methods. The spectra of the wrong-sign triplets are fit by a second order polynomial to constrain the shape of the correct-sign combinations. Subsequently, we fit the peak in the correct-sign spectrum by a Gaussian + a second order polynomial for background. The mean of the Gaussian is set as the PDG [25] Λ_c mass value $2.28646\,\text{GeV}/c^2$, but the other parameters are allowed to vary. The background polynomial is constrained by the wrong-sign shape, where only the constant term can vary to allow for a potential correlated background, however the slope and the curvature are fixed. The final $\Lambda_c^\pm$ raw yield is evaluated as counts, under 3 standard deviations of the center of the Gaussian, minus the background, evaluated from the polynomial fit.

The BDT-cuts optimization provided enough significance of the Λ_c that the signal could be devided into 3 p_T and centrality intervals in both, 2014 and 2016 data sets. Figures 4.16–4.19 show the invariant-mass spectra of p, K, π combinations with the wrong-sign polynomial

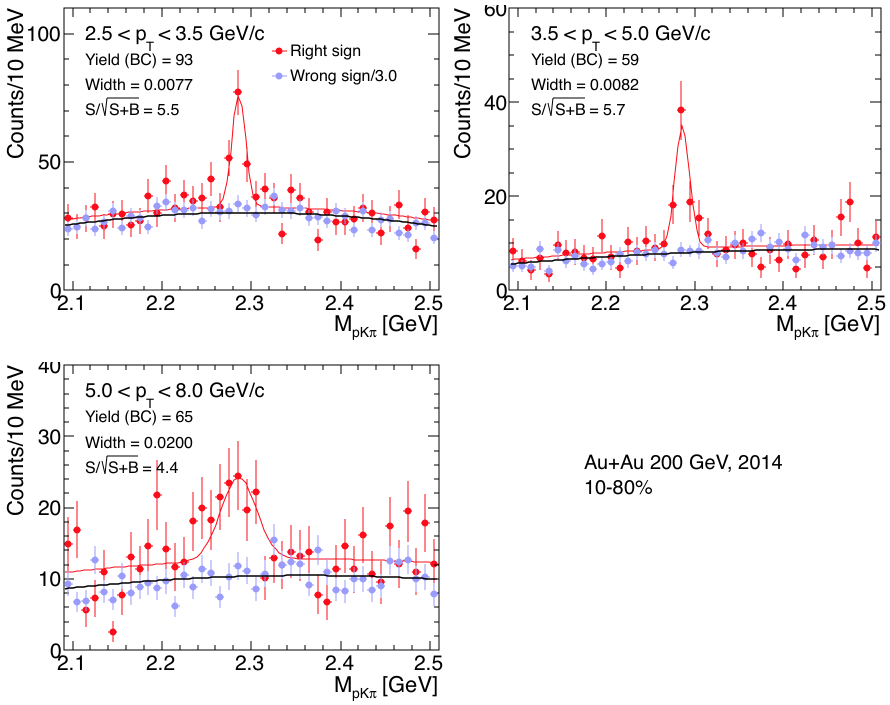

Figure 4.16: Invariant mass distribution of p, K, π triplets, showing the Λ_c peak, obtained using BDT cuts in different p_T intervals in 10–80 % central Au+Au collisions from 2014.

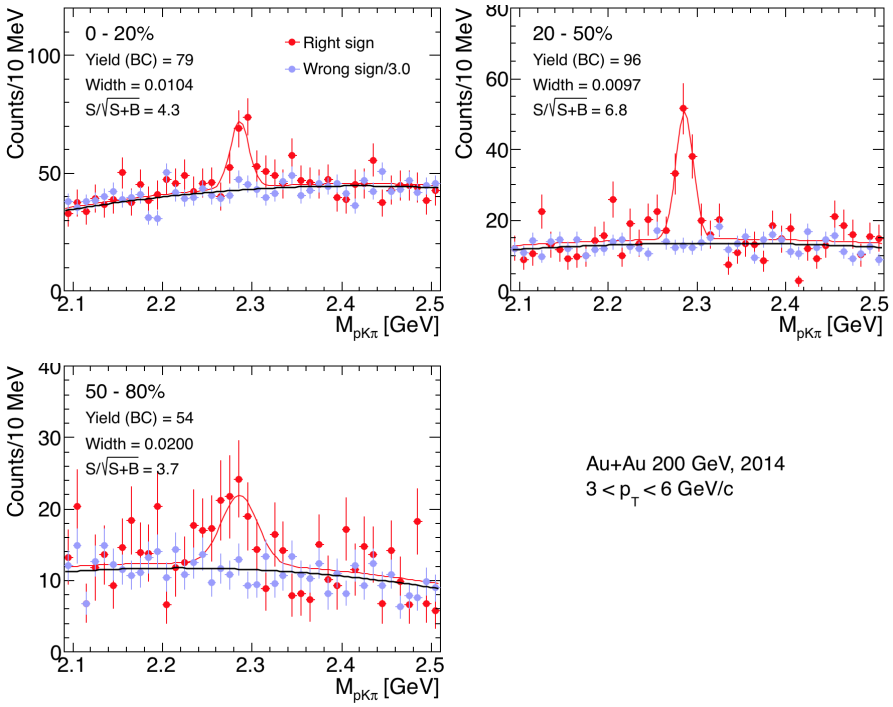

Figure 4.17: Invariant mass distribution of p, K, π triplets with $3 < p_T < 6\,\mathrm{GeV}/c$, showing the Λ_c peak, obtained using BDT cuts in different centrality intervals in Au+Au collisions from 2014.

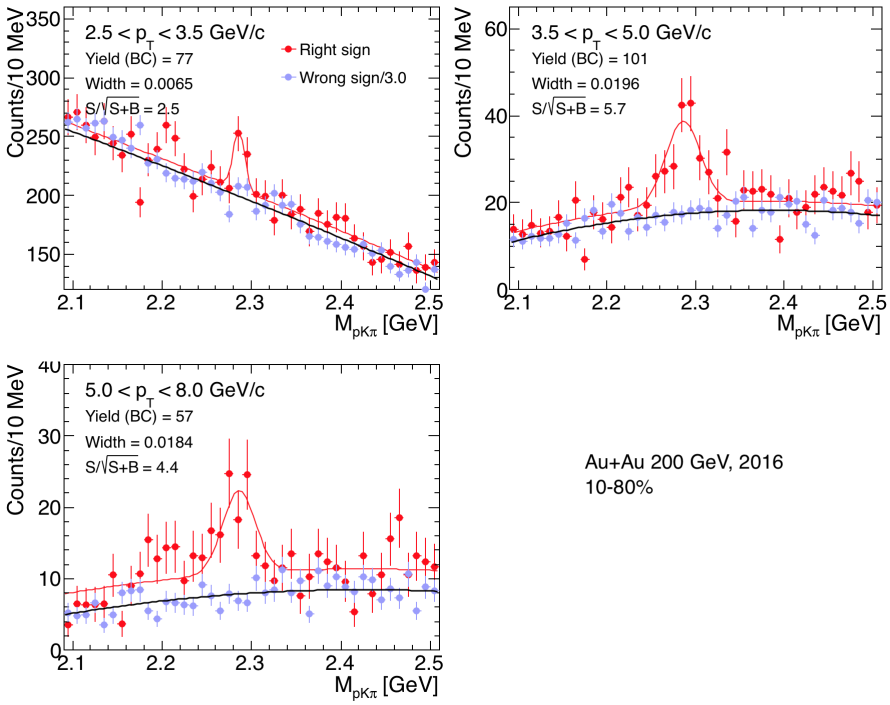

Figure 4.18: Invariant mass distribution of p, K, π triplets, showing the Λ_c peak, obtained using BDT cuts in different p_T intervals in 10–80 % central Au+Au collisions from 2016.

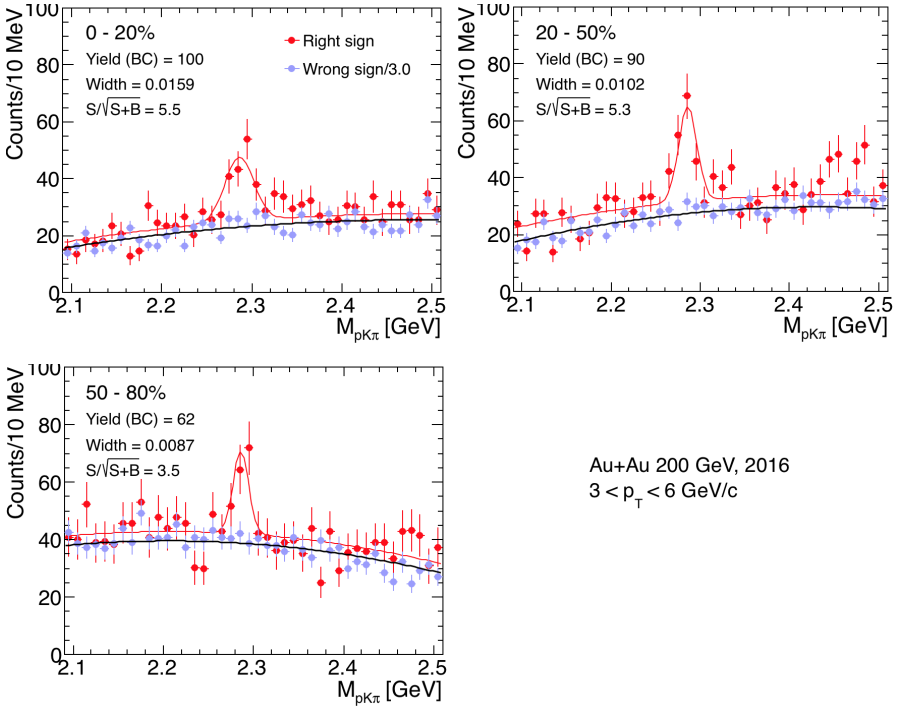

Figure 4.19: Invariant mass distribution of p, K, π triplets with $3 < p_T < 6\,\mathrm{GeV}/c$, showing the Λ_c peak, obtained using BDT cuts in different centrality intervals in Au+Au collisions from 2016.

fit (blue) and the signal fit (red) for different p_{T} (Figures 4.16 and 4.18) and centrality (4.17 and 4.19) intervals in Au+Au collisions recorded in 2014 (4.16 and 4.17) and 2016 (4.18 and 4.19). There are approximately 3× more wrong-sign triplets in the combinatorial background, compared to the right sign, therefore we scaled the wrong-sign-triplets count by 1/3. For significance, we use the formula $\sigma = S/\sqrt{S+B}$, in this instance, which is a good approximation for this method as many points are used for the fit. Figures 4.16–4.19 show that, thanks to BDT, the $\Lambda_{\mathrm{c}}^{\pm}$ yield is large enough to be divided into three p_{T} and centrality intervals in both, 2014 and 2016 data samples which is crucial the comparison of our measurement to theoretical calculations.

4.7 Efficiency correction

To calculate the real yield of the Λ_{c} baryons in Au+Au collisions, the raw yields have to be corrected for efficiency of the detectors and of the used analysis method. We assume that the efficiencies of the various subdetectors and applied cuts are independent, therefore we can factorize this correction into several parts. The final efficiency $\epsilon_{\Lambda_{\mathrm{c}}}$ is a product of the detection efficiency in the TPC ϵ_{TPC} and the HFT ϵ_{HFT}, as well as the probability that the Λ_{c} triplets passed the BDT cuts ϵ_{BDT} and the particle-identification cuts ϵ_{PID}. The full correction can be written as

$$\epsilon_{\Lambda_{\mathrm{c}}} = \epsilon_{\mathrm{TPC}} \times \epsilon_{\mathrm{PID}} \times \epsilon_{\mathrm{HFT}} \times \epsilon_{\mathrm{BDT}} \times \Delta\epsilon_{\mathrm{sec}} \times \Delta\epsilon_{\mathrm{vtx}}\,, \tag{4.8}$$

where $\Delta\epsilon_{\mathrm{sec}}$ denotes the correction for the secondary contribution to the Λ_{c} yield and $\Delta\epsilon_{\mathrm{vtx}}$ is the correction for the resolution of the primary vertex position.

4.7.1 TPC tracking efficiency

The acceptance and efficiency of tracking are evaluated, by embedding of Monte-Carlo (MC) generated p, K, and π tracks into measured Au+Au collision events in order to take into account the real accupancy and pileup in the data. The Au+Au collisions are randomly selected over the measured time period. The MC tracks are generated with a flat p_{T}, y,

and ϕ distributions so that their number does not exceed 5 % of the track multiplicity in the Au+Au event. The generated MC tracks are subsequently passed through the full GEANT [4] simulation of the STAR-detector geometry. The combined signal is then processed in the same way as in real data. The TPC tracking efficiency $\epsilon_{\mathrm{TPC}}(\mathrm{daughter})$ is a ratio of the tracks that satisfy the track selection criteria N_{rec} divided by all simulated tracks N_{emb}

$$\epsilon_{\mathrm{TPC}}(\mathrm{daughter}) = \frac{N_{\mathrm{rec}}(|\eta| < 1 \cap N_{\mathrm{hits}} \geq 20 \cap N_{\mathrm{hits}}/N_{\mathrm{hits\ max}} > 0.52 \cap \mathrm{DCA} < 1.5\,\mathrm{cm})}{N_{\mathrm{emb}}(|\eta| < 1)}\,. \tag{4.9}$$

Because the efficiencies of detection of different tracks are independent, the final efficiency ϵ_{TPC} is calculated as a product of the daughter efficiencies

$$\epsilon_{\mathrm{TPC}} = \prod_{\mathrm{daughter=p,\ K,\ \pi}} \epsilon_{\mathrm{TPC}}(\mathrm{daughter})\,. \tag{4.10}$$

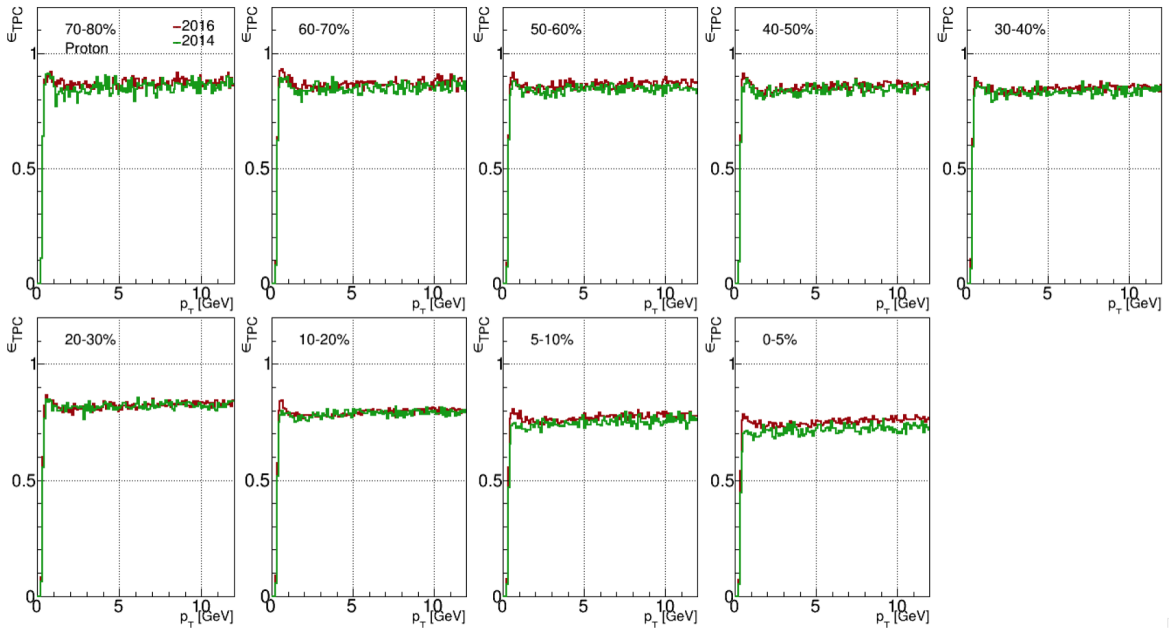

Figure 4.20: TPC tracking efficiency of protons $\epsilon_{\mathrm{TPC}}(\mathrm{p})$ plotted vs p_{T} in various centrality intervals. The red and green histograms are evaluated from 2016 and 2014 data taking, respectively.

Figures 4.20, 4.21, and 4.22 show the TPC tracking efficiency of p, K, and π, respectively.

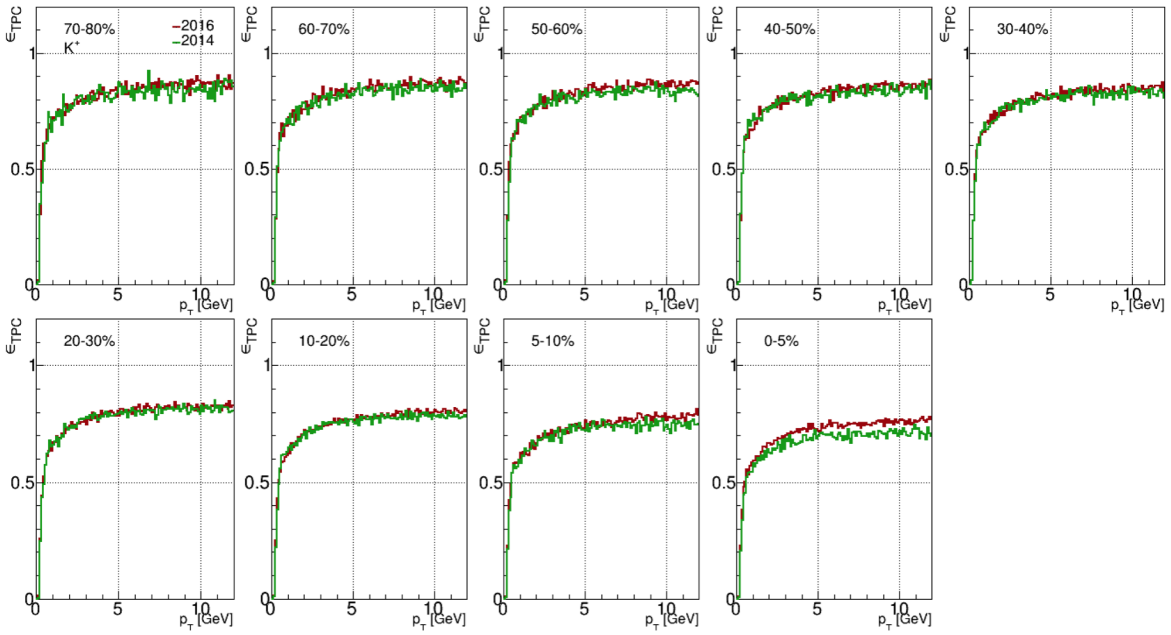

Figure 4.21: TPC tracking efficiency of kaons $\epsilon_{\mathrm{TPC}}(\mathrm{K})$ plotted vs p_{T} in various centrality intervals. The red and green histograms are evaluated from 2016 and 2014 data taking, respectively.

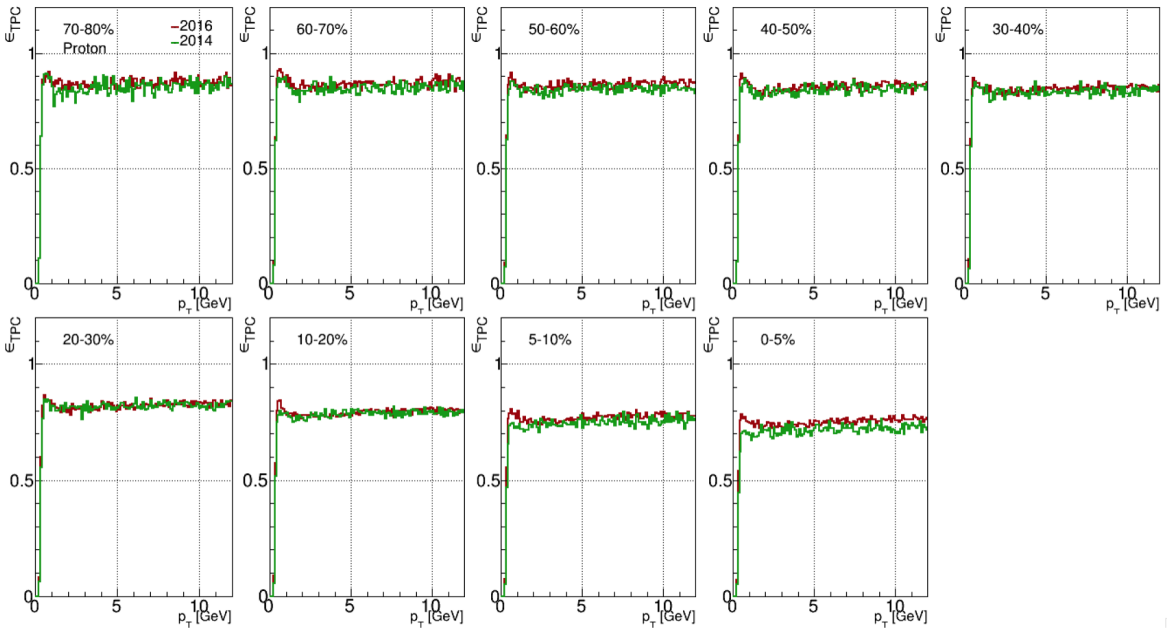

Figure 4.22: TPC tracking efficiency of pions $\epsilon_{\mathrm{TPC}}(\pi)$ plotted vs p_{T} in various centrality intervals. The red and green histograms are evaluated from 2016 and 2014 data taking, respectively.

The efficiencies are comparable between 2014 and 2016 with a similar p_T dependence. In 2016, the efficiency rose slightly, however, due to a different tracking algorithm — the so called StiCA — based on cellular automaton. The efficiency of kaons has a rising tendency in p_T, because high-p_T K are more likely to traverse the TPC volume before they decay.

4.7.2 TOF matching efficiency

The matching efficiency of tracks in TOF ϵ_{TOF} is evaluated from data as a fraction of good TPC tracks (i.e. those that pass the tracking requirements as described in Section 4.1) that have a good hit in TOF with the measured velocity divided by the speed of light $\beta > 0$. The matching efficiencies for p, K, and π are shown in Figure 4.23 for two centrality intervals. ϵ_{TOF} stays constant for $p_T > 2\,\mathrm{GeV}/c$ at $\sim 60\,\%$. The PID is done using the $\mathrm{d}E/\mathrm{d}x$ information in the TPC. The $p^{\pm}$ and $K^{\mp}$ show non-monotonic behavior below $2\,\mathrm{GeV}/c$. Studies show that this is caused by purity changes in this p_T region [90].

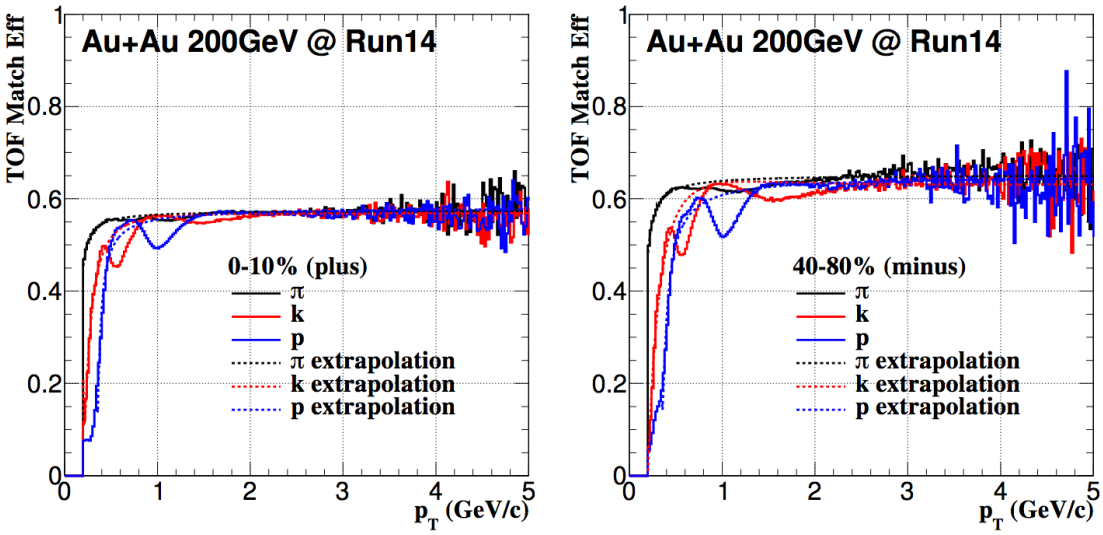

Figure 4.23: TOF matching efficiencies for p, K, and π versus p_T in run 2014 for two different centrality ranges.

The TOF matching efficiencies for π^+, K^+, and p^+, compared to their antiparticles, are shown in Figure 4.24. The efficiencies are comparable to 2014 which shows stable performance in both runs.

The centrality dependence of ϵ_{TOF} is shown in Figure 4.25. The efficiency increases

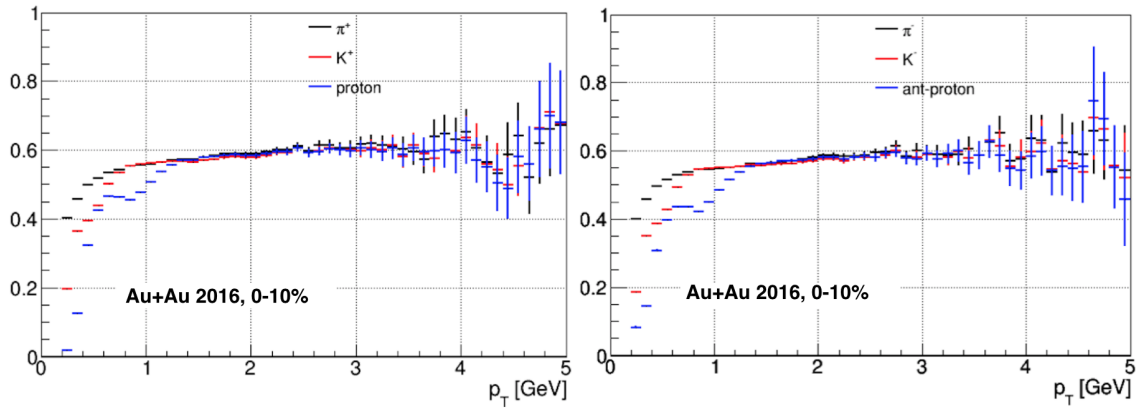

Figure 4.24: TOF matching efficiencies for π^+, K^+, and p^+ and their antiparticles versus p_T in run 2016 in 0–10 % most central Au+Au collisions.

towards more peripheral collisions, most likely because of lower occupancy.

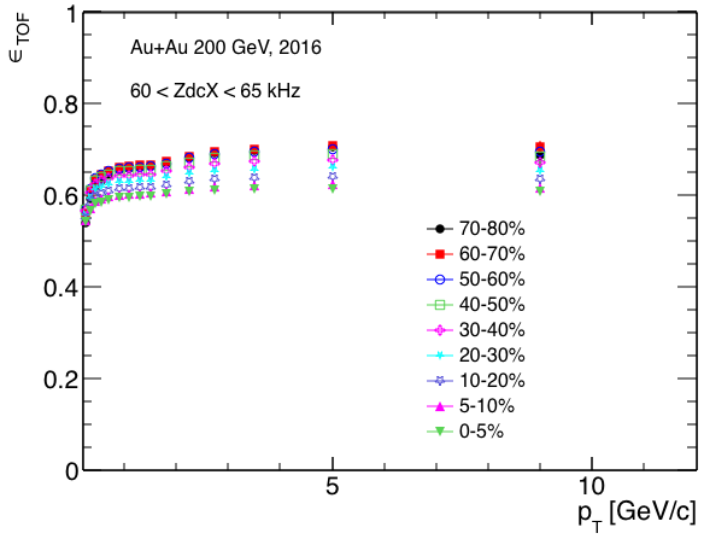

Figure 4.25: TOF matching efficiency of TPC tracks as a function of p_T in different centrality intervals measured in 2016.

Another factor, that needs to be taken into consideration, is the contribution of out-of-time pileup, i.e. stacking of multiple collisions in one measuring window of the TPC. This will decrease the TOF matching efficiency during high-luminosity-beam conditions as TOF has more precise timing and is not affected as much by the pileup. Figure 4.26 shows ϵ_{TOF} for different ZDC-crossing-rate (ZdcX) intervals as these can be used as good proxies for the

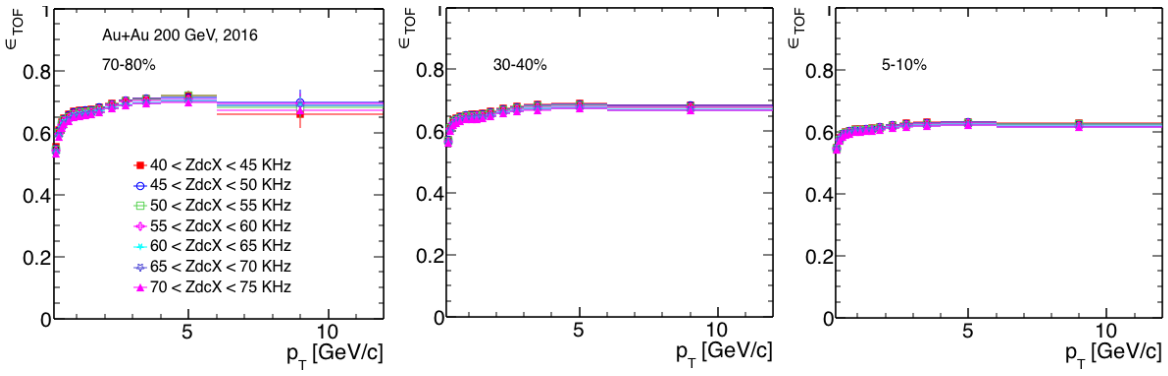

Figure 4.26: TOF matching efficiency of TPC tracks as a function of p_{T} in different ZDC-crossing-rate intervals in 2016 for three different centrality ranges.

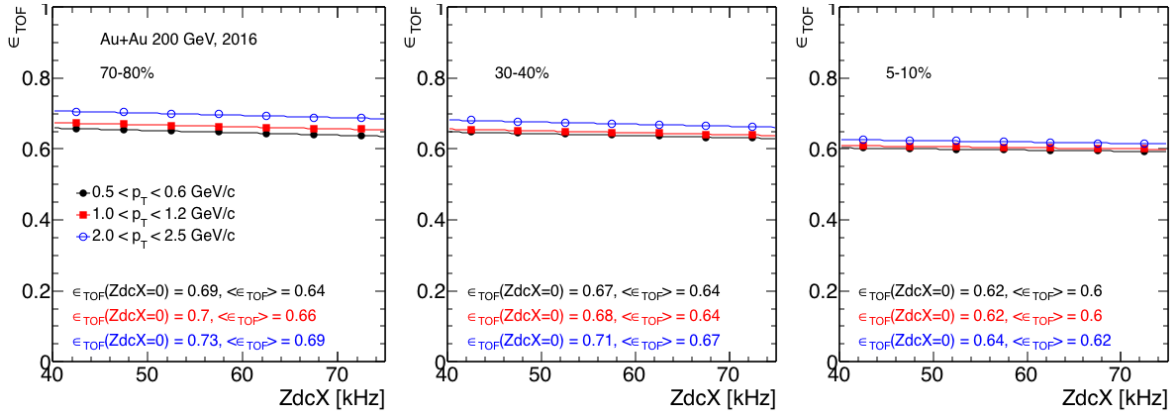

Figure 4.27: TOF matching efficiency of TPC tracks as a function of the ZDC-crossing rate in 2016 for three different p_{T} and centrality ranges.

instantaneous luminosity. We observe only a small change in the efficiency which indicates only a small dependence on the luminosity. The dependence on the ZDC-crossing rate is shown in Figure 4.27. As we observe a linear dependence, we fit the TOF efficiency by a first-order polynomial and extrapolate the dependence to zero which indicates the highest bias of our pileup. This extrapolation shows a maximum 3 % dependence of the efficiency on pileup which is taken into account in the systematic uncertainties.

4.7.3 PID efficiency

To evaluate the efficiency of the PID cuts, we have to generate almost pure samples of p, K, and π. This is done using the decays of Λ, ϕ, and K_s, respectively.

The efficiencies of the $n\sigma_{dE/dx}$ cut $\epsilon_{n\sigma}$ for π, K, and p are shown in Figure 4.28. The plots are fit by smooth functions which we use in the analysis and we use them for extrapolation in high p_T where we expect the efficiencies to be constant.

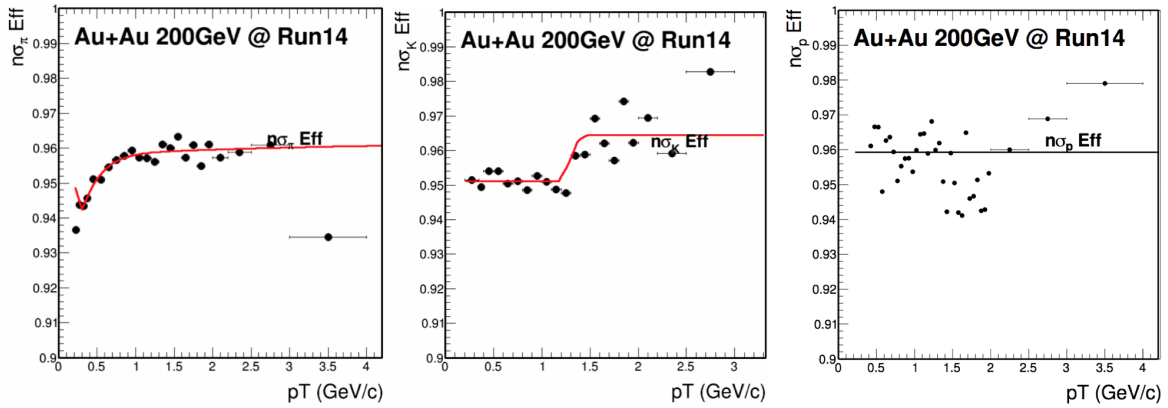

Figure 4.28: Efficiency of the $n\sigma_{dE/dx}$ cut in the TPC as a function of p_T for π, K, and p, from left to right.

The $1/\beta$ efficiencies $\epsilon_{1/\beta}$ are shown in Figure 4.29. The points labeled "counting" are extracted from the yields by applying the $1/\beta$ cut directly, whereas the ones labeled "fitting" we extracted via Gaussian fits of the distribution with the center in the theoretical $1/\beta_{\text{particle}}$ value. The lower efficiency in the counting method is caused by a contamination by other hadrons and is quoted in the systematic-error calculation.

The final PID efficiency ϵ_{PID} is calculated for each particle separately in the p_T intervals with the clean-PID cuts (see Table 4.1)

$$\epsilon_{\text{PID}}(\text{clean}) = \epsilon_{n\sigma} \times \epsilon_{1/\beta} \times \epsilon_{\text{TOF}}\,, \tag{4.11}$$

whereas with the hybrid-PID cuts

$$\epsilon_{\text{PID}}(\text{hybrid}) = \epsilon_{n\sigma} \times \epsilon_{1/\beta} \times \epsilon_{\text{TOF}} + \epsilon_{n\sigma} \times (1 - \epsilon_{\text{TOF}})\,. \tag{4.12}$$

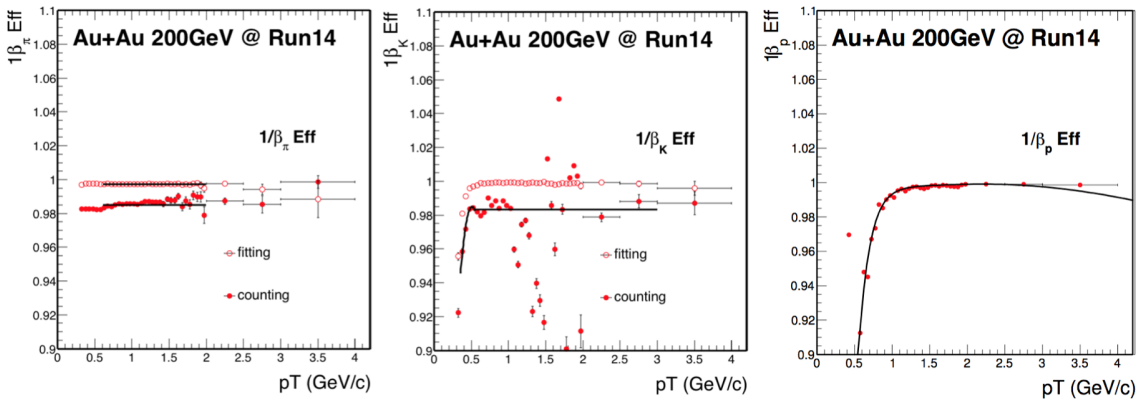

Figure 4.29: Efficiency of the $1/\beta$ cut in the TOF as a function of p_T for π, K, and p, from left to right.

4.7.4 TPC, HFT, and BDT-cuts efficiencies

The efficiencies of the TPC (ϵ_{TPC}), the HFT (ϵ_{TPC}), and the BDT are convoluted and are highly dependent on centrality of the collisions and p_T, η, and ϕ of the tracks. A novel approach was, therefore used to simulate all these detector effects and evaluate all these efficiencies at once: We use the, so called, data-driven fast simulator (see Section 4.4). The Λ_c are generated with flat p_T and y distributions and are, in turn, decayed into daughter particles, which are simulated as traversing through the STAR detector with all the effects of the detector.

The TPC efficiency depends on p_T and centrality of the tracks. The HFT efficiency is evaluated depending on p_T, η, and ϕ of each daughter particle. The TOF and PID cuts are evaluated as well like in the previous chapter. The kinematic cuts, the looser cuts before the BDT (TopoPre) and the BDT cuts are applied in the same manner as in the analysis on the smeared simulated tracks of the Λ_c daughters.

Figures 4.30–4.33 show the efficiency as a function of p_T (4.30, 4.32) and centrality (4.31, 4.33) in 2014 (4.30, 4.31) and 2016 (4.32, 4.33). The black points show the efficiency of the TPC and acceptance of the detector, the red points add the HFT-matching efficiency, the blue points add the PID efficiency ϵ_{PID}, the magenta points add the loose TopoPre cuts, and, finally, the green points show the final efficiency with the BDT cuts applied on top. The

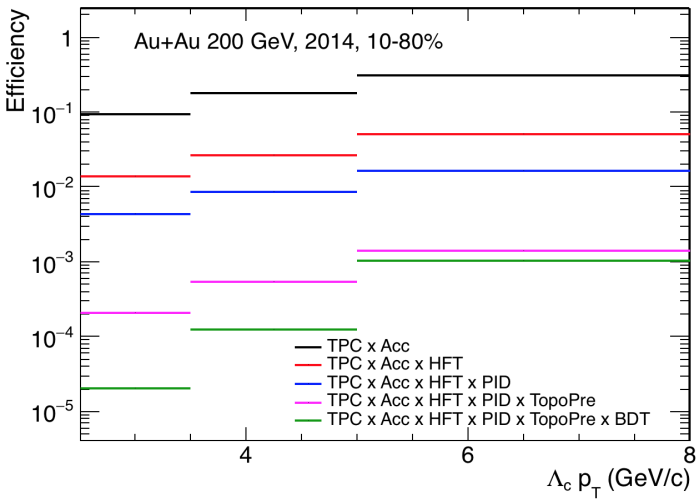

Figure 4.30: Efficiency of the reconstruction of Λ_c as a function of p_T in the 2014 data in the 10–80 % centrality interval.

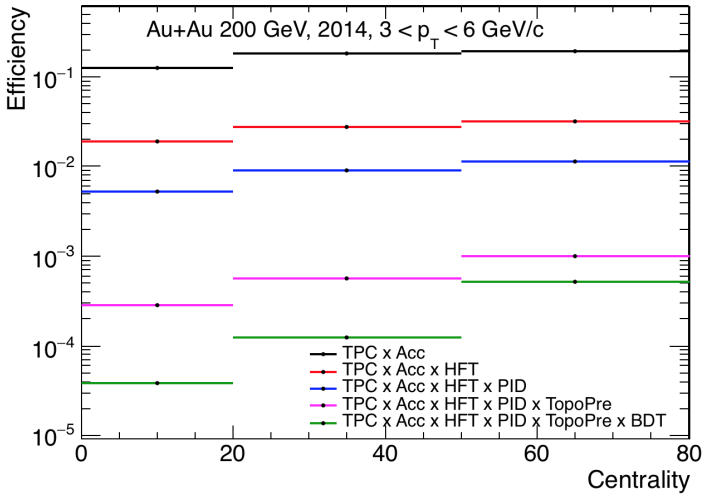

Figure 4.31: Efficiency of the reconstruction of Λ_c as a function of centrality for $3\,\mathrm{GeV}/c < p_T < 6\,\mathrm{GeV}/c$ in the 2014 data.

efficiency can be as low as $\sim 2 \times 10^{-5}$ and rises with higher p_T and with more peripheral collisions.

4.8 Corrected spectra

The raw spectra are corrected, using the efficiencies from the previous section. The fully corrected spectra are shown in Figure 4.34 as a function of p_T in the 10–80 % centrality interval. The corrected spectra as a function of centrality are shown in Figure 4.35. The results from the two runs are consistent within statistical uncertainty intervals.

4.9 Systematic uncertainties

So far in this chapter, all of the results were described with only statistical uncertainties. Here, we describe other sources of uncertainties that may arise from the used method of analysis, the detector, etc. We will discuss the uncertainties one by one:

4.9.1 Tracking and PID uncertainties

The uncertainty of the TPC tracking was evaluated from embedding studies [90]. It was estimated as 3 % for a single track. The TOF-matching uncertainty comes from a variation of the matching efficiency with pileup, as discussed in Section 4.7.2. This uncertainty is evaluated as 3 % at the single-track level. The evaluation of the PID efficiency uncertainty is described in Section 4.7.3 and comes from from the difference between bin counting and fit of the Gaussian $\mathrm{d}E/\mathrm{d}x$ and TOF distributions. It is evaluated as 2 % per track.

4.9.2 Uncertainty of the yield extraction

By default, we use a Gaussian fit of the signal on top of a second order polynomial fit of the background scaled by 1/3. The yield is then extracted by bin counting within a 3 standard deviations σ from the mean of the Gaussian fit minus the integral of the background polynomial within the same range. The shape of this polynomial is fixed, but the constant term is allowed to vary when fitting the right-sign distribution.

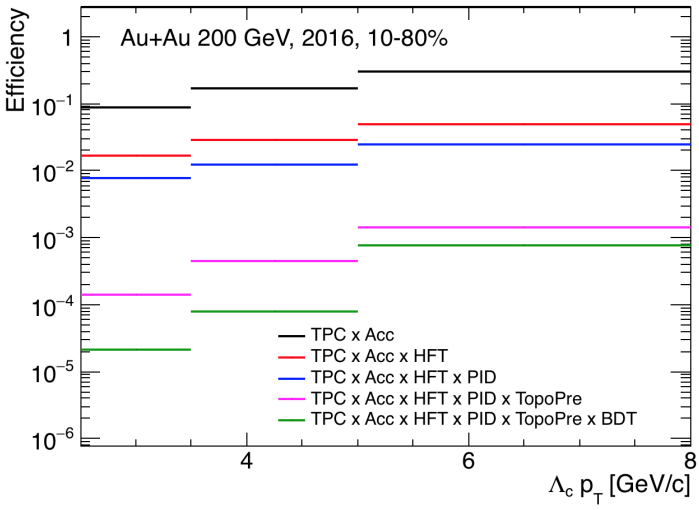

Figure 4.32: Efficiency of the reconstruction of Λ_c as a function of p_T in the 2016 data in the 10–80 % centrality interval.

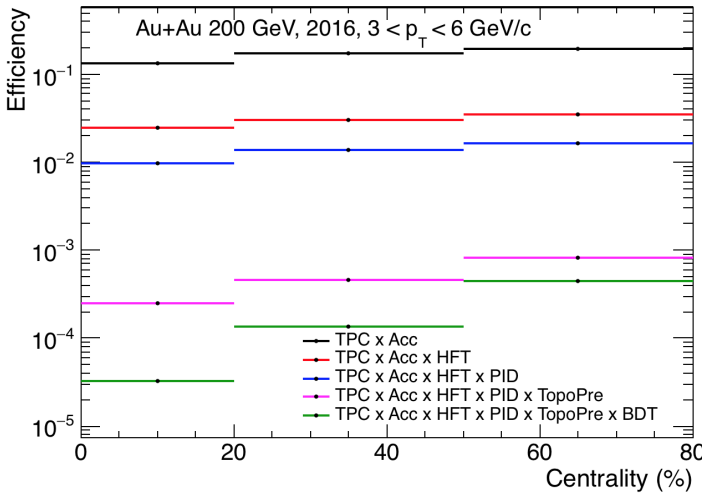

Figure 4.33: Efficiency of the reconstruction of Λ_c as a function of centrality for $3\,\mathrm{GeV}/c < p_T < 6\,\mathrm{GeV}/c$ in the 2016 data.

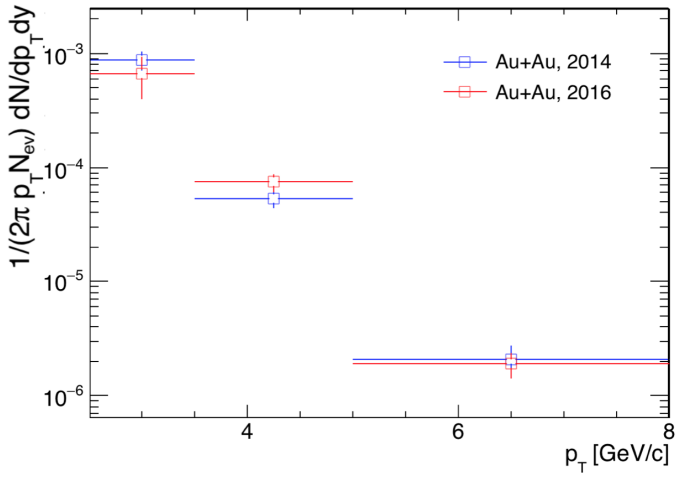

Figure 4.34: Fully corrected Λ_c spectra as a function of p_T in the 10–80 % centrality interval, plotted for 2014 and 2016. Only statistical uncertainties are shown.

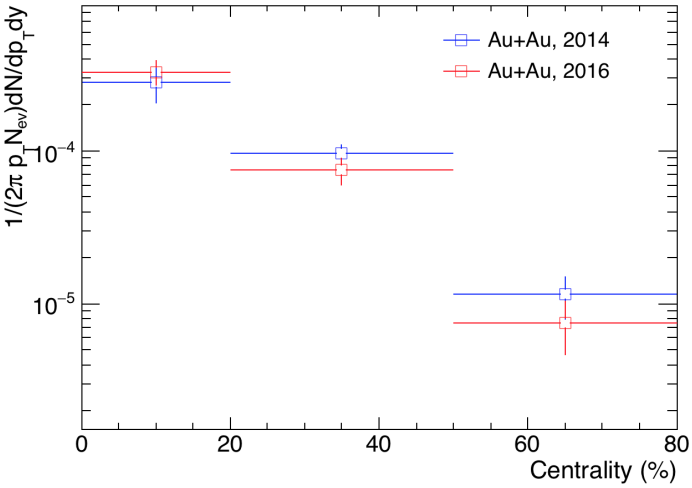

Figure 4.35: Fully corrected Λ_c spectra as a function of centrality with $3\,\mathrm{GeV}/c < p_T < 6\,\mathrm{GeV}/c$, plotted for 2014 and 2016. Only statistical uncertainties are shown.

To establish the contribution of the fit procedure to the systematic uncertainty, the following procedure is undertaken: The default range of the fit in invariant mass is 2–2.6 GeV/c^2, but to estimate the systematic uncertainty of this boundary, we vary it to 2.05–2.55 GeV/c^2 and also 2.1–2.5 GeV/c^2. When varying the range, the shape of the background polynomial is always fit anew. To vary the background subtraction procedure, the linear term is allowed to vary when fitting the right-sign triplets, also a fourth order polynomial is used as a background

estimation. Furthermore, as a crosscheck, we used the scaled right-sign distribution to subtract the background directly. The right-sign triplets describe the background well except the high-p_{T} bin. These procedures are shown in FIgure 4.36 for the $2.5\,\mathrm{GeV}/c < p_{\mathrm{T}} < 3.5\,\mathrm{GeV}/c$ interval from Au+Au collisions taken in 2014.

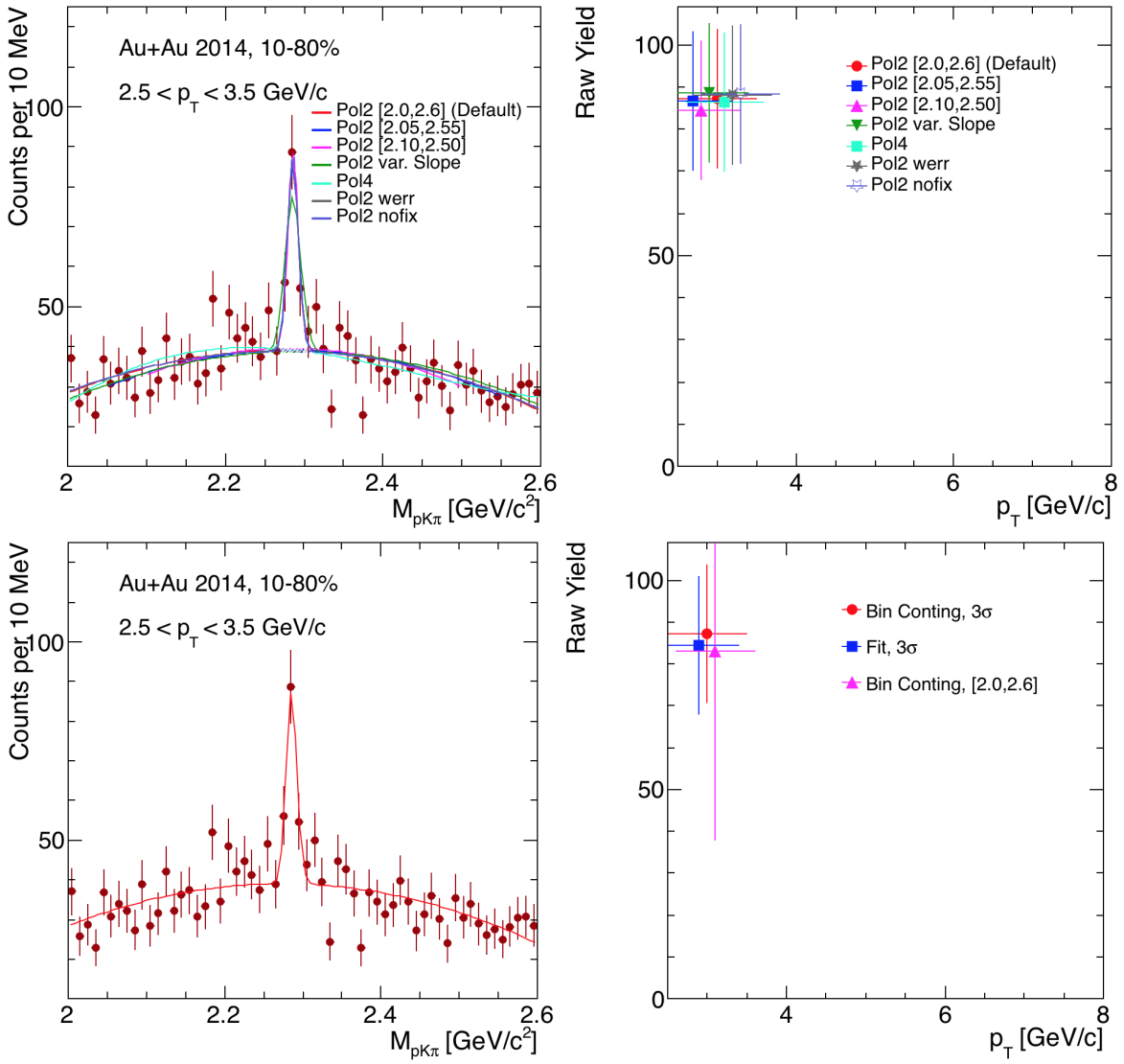

Figure 4.36: Variation of the yield extraction procedure for the evaluation of the systematic error. Several fitting procedures of the invariant mass of the p, K, π triplets, recorded in 2014 at $2.5\,\mathrm{GeV}/c < p_{\mathrm{T}} < 3.5\,\mathrm{GeV}/c$, are shown on the left-hand side. The resulting Λ_{c} yields are plotted on the right-hand side. The top plots show the variation of background estimation procedures and the bottom plots show the yield calculation procedures.

The yield is extracted by bin counting within a 3σ interval around the Gaussian-fit mean. To vary this approach, two additional evaluations are performed: In the first one, the signal is calculated by integrating the Gaussian directly. In the second one, the yield is extracted from bin counting from the extended range of 2–2.6 GeV/c^2. The default approach of bin counting within 3σ and within the extended range are consistent with each other.

4.9.3 BDT-cuts variation

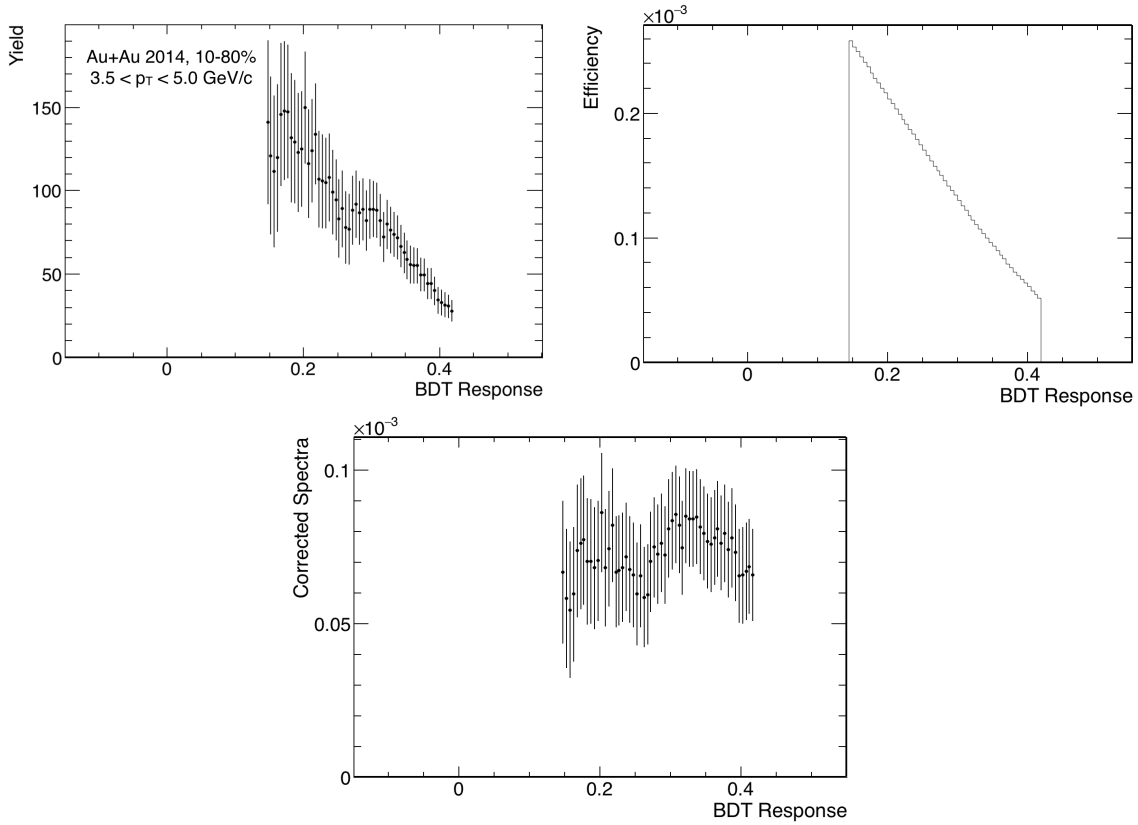

Figure 4.37: The raw yields (top left), reconstruction efficiencies (top right), and the efficiency-corrected invariant yields (bottom) obtained by varying the BDT response cut in the 3.5 GeV/c < p_T < 5 GeV/c and 10–80 % centrality interval in the 2014 data.

To ensure the stability of our choice of the BDT cuts, we varied them to see that the final result remains stable even with different choices. The cuts are varied so that the significance stays above 3. This usually means that the signal-reconstruction efficiency is varied within at

least ±50 %. Figure 4.37 shows an example of the BDT response variation in the $3.5\,\mathrm{GeV}/c < p_\mathrm{T} < 5\,\mathrm{GeV}/c$ and 10–80 % centrality bin in the 2014 data. Raw yields, efficiencies, and also the resulting corrected invariant yields are plotted with statistical uncertainties as a function of the BDT response. Even though the raw yields and the efficiencies vary by more than 7 %, the corrected invariant yields are consistent within 10–15 %.

To calculate the systematic uncertainty of the corrected spectra, we have to evaluate the uncertainty of the difference in the corrected yield. When varying the BDT cuts, we obtain a sample of the Λ_c that is a subset or a superset of the sample with the default cuts. The statistical uncertainties of subsets are calculated in the following manner: Let us denote a sample T with its subset S statistical uncertainties σ_S and σ_T which can be calculated in a Poissonian distribution as $\sigma_S = \sqrt{n_S}$ and $\sigma_T = \sqrt{n_T}$, where n_S is the number of Λ_c in the sample S and n_T in T. The corresponding mean values are μ_S and μ_T with the difference $\Delta = \mu_T - \mu_S$ and its statistical uncertainty

$$\sigma_\Delta = \sqrt{|\sigma_T^2 - \sigma_S^2|} \sim \sqrt{n_T - n_S}\,. \tag{4.13}$$

The mean values μ_T and μ_S are the corrected spectra in our case. As a systematic uncertainty, we quote the maximum of $|\Delta| - \sigma_\Delta$.

Figure 4.38 shows an example of the inference of the BDT-systematic-uncertainty contribution. First, the invariant yield is calculated for each set of the varied cuts and then the difference Δ is calculated with its uncertainty σ_Δ. This plot corresponds to the the $3.5\,\mathrm{GeV}/c < p_\mathrm{T} < 5\,\mathrm{GeV}/c$ and 10–80 % centrality interval in the 2014 data.

4.9.4 Charge dependence of efficiency

In the analysis of the $\Lambda_\mathrm{c}/\mathrm{D}^0$ ratio, we combine the Λ_c^+ and $\overline{\Lambda_\mathrm{c}^-}$, and D^0 and $\overline{\mathrm{D}^0}$, and in the simulations, we produce the same number of particles and antiparticles. The efficiency of reconstruction of the daughter tracks depends slightly on the charge of the daughter particles and there is some evidence [90] that the $\Lambda_\mathrm{c}^-/\Lambda_\mathrm{c}^+$ratio is not exactly unity. Figure 4.39 shows the dependence of the HFT ratio (i.e. ratio between the HFT and TPC tracks) of identified

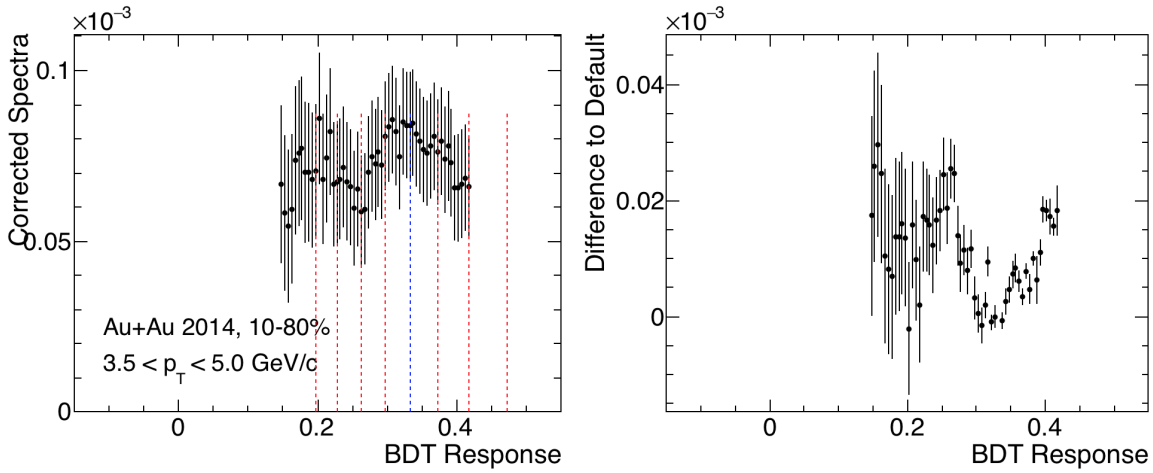

Figure 4.38: The invariant yields of Λ_c (left) and the difference from the default yield as a function of the BDT response in the $3.5\,\mathrm{GeV}/c < p_\mathrm{T} < 5\,\mathrm{GeV}/c$ and 10–80 % centrality interval in the 2014 data. The dashed lines show the default cuts (blue) and cuts at ±25 %, ±50 %, ±75 %, and ±100 % from the default.

particles. The difference in detection efficiency is always slightly higher in positively charged particles.

Figure 4.40 shows the efficiency of Λ_c^+ compared to Λ_c^- and their ratio is plotted in Figure 4.41. Because the charge dependence of the daughter particles partially cancels out, the of the efficiency does not depend on the charge very much and the difference can be cited as a systematic uncertainty. The HFT ratio depends on the charge in the order of 2 %.

4.9.5 Dependence of efficiency on the shape of the p_T spectrum

The reconstruction efficiency of the Λ_c is calculated in relatively broad p_T bins and can, therefore, be influenced by the shape of the p_T spectrum within each bin. Figure 4.42 shows three different spectra shapes. In this analysis, the default shapes (red) were chosen as the D^0 spectra in each centrality bin. Two modifications were chosen for comparison: One is from the Λ_c/D^0 ratio from PYTHIA [177] and the other uses a quark-coalescence model by the Greco group [178].

The comparison of the three spectra shapes is shown in Figure 4.43. The efficiency is

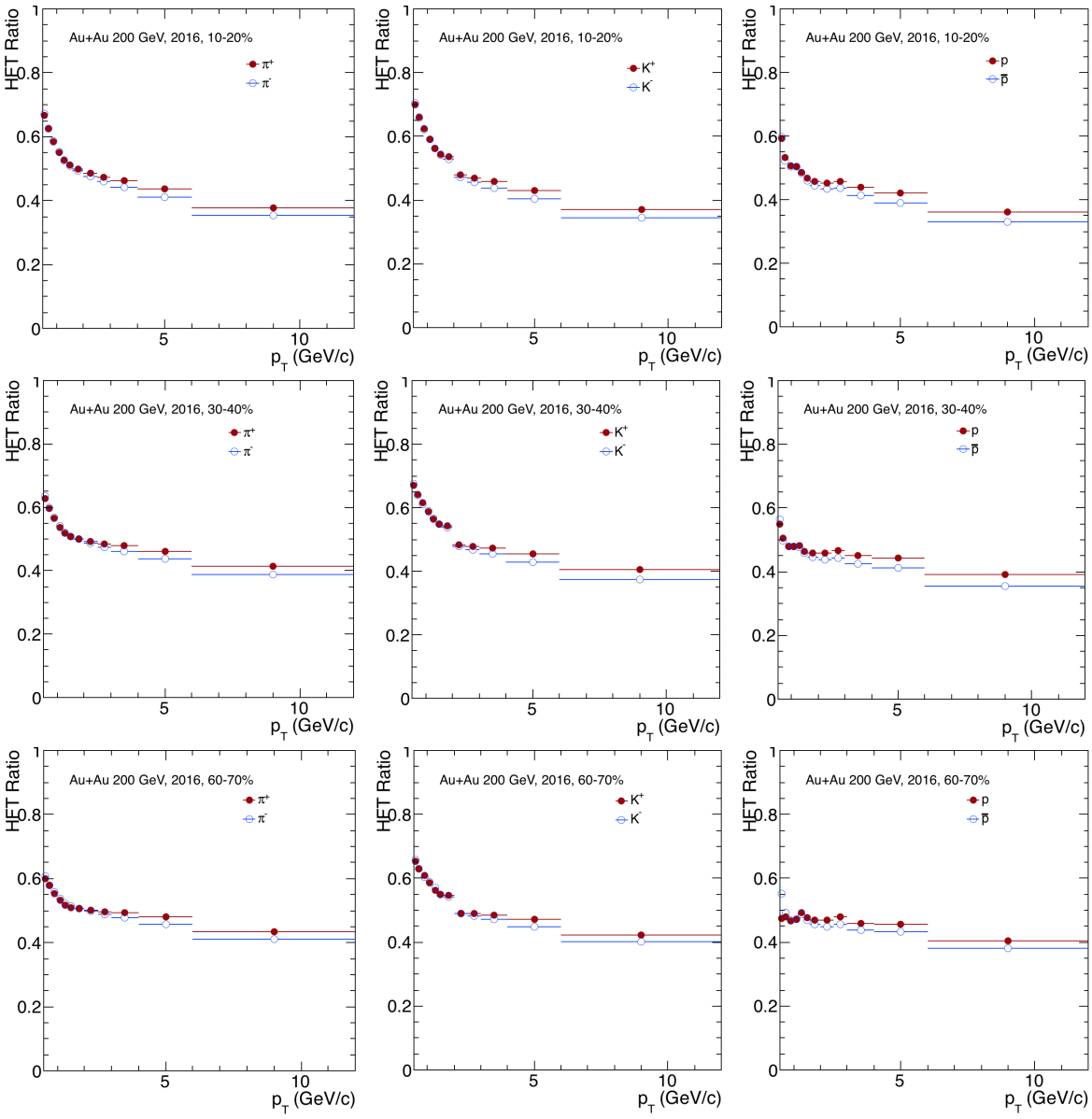

Figure 4.39: Charge dependence of the ratio between the number HFT and TPC tracks for p, K, and π as a function of p_{T} in several different centrality intervals in the 2016 data.

not modified much by the usage of the Λ_c/D^0 ratio from PYTHIA. When using the Greco model, the efficiency is modified by $\sim 5\,\%$ in low p_{T} and it rises to $\sim 10\,\%$ in high p_{T}. The ratio between the efficiencies, that use the PYTHIA and Greco modifications, is shown in Figure 4.44. The differences between the spectra are propagated into the systematic uncertainties.

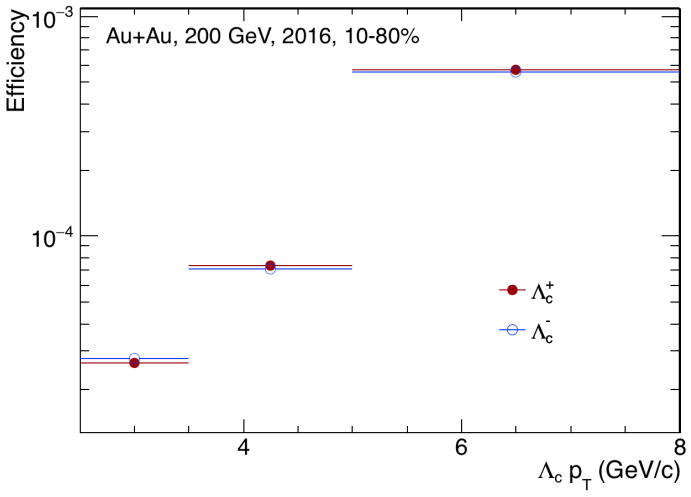

Figure 4.40: The difference in reconstruction efficiency between Λ_c^+ and Λ_c^- as a function of p_T in the 10–80 % centrality range.

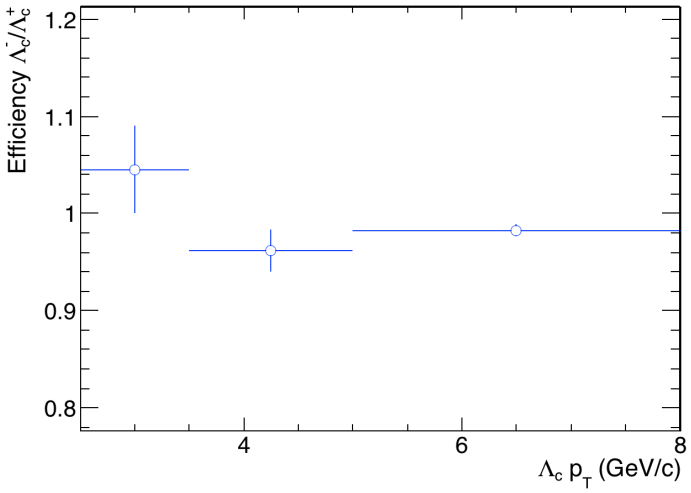

Figure 4.41: Ratio between Λ_c^+ and Λ_c^- reconstruction efficiencies as a function of p_T in the 10–80 % centrality range.

4.9.6 Primary-vertex resolution

The data-driven FastSim is a capable simulator for the reconstruction efficiency and the tracking resolution of the HFT, however, as it does not simulate full events, there may be an additional uncertainty coming from the resolution of the position of the primary vertex (PV). This effect is expected to play a larger role in peripheral collisions, because there are

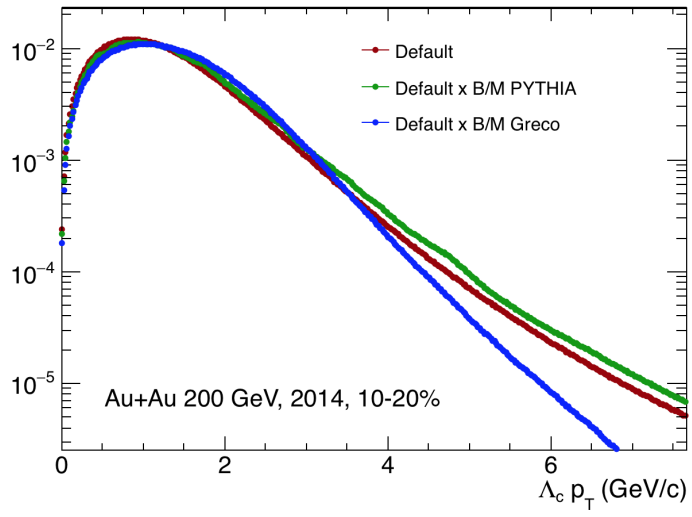

Figure 4.42: The shape of the Λ_c spectra as depicted by three different models. The default (red) is the D^0 spectrum. The green line depicts the default modified by the Λ_c/D^0 ratio from PYTHIA [177] and the blue line is modified by a coalescence model (Greco [178]) calculation.

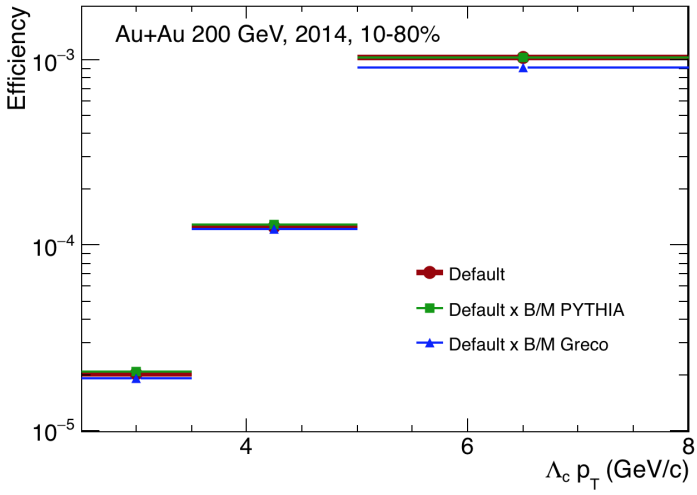

Figure 4.43: Λ_c reconstruction efficiencies, using different shapes of the spectra.

fewer tracks pointing to the PV. For the evaluation, events were simulated in HIJING [175], ran through a full GEANT 3 [4], and then embedded into the measured minimum-bias (MB) data. The effect of the PV resolution is evaluated by comparing the efficiency from FastSim to the one from the HIJING+MB simulations.

Figure 4.45 shows the efficiencies from the HIJING embedded into MB data, compared to

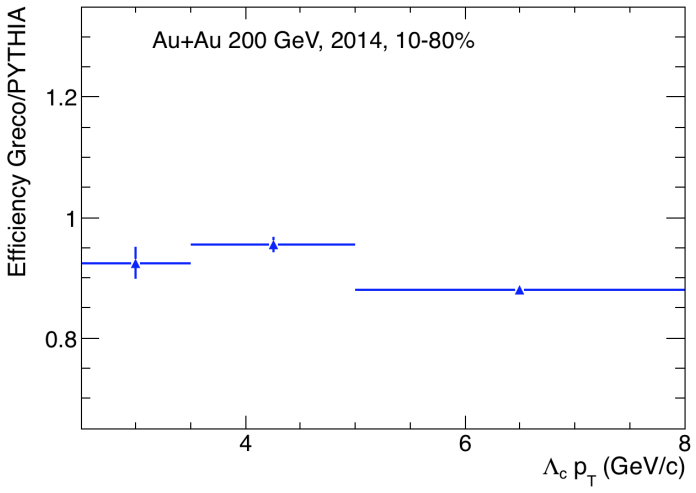

Figure 4.44: Ratio of efficiencies calculated using the spectrum modified by the ratio of Λ_c/D^0 from PYTHIA [177] and by a quark-coalescence model by the Greco group [178].

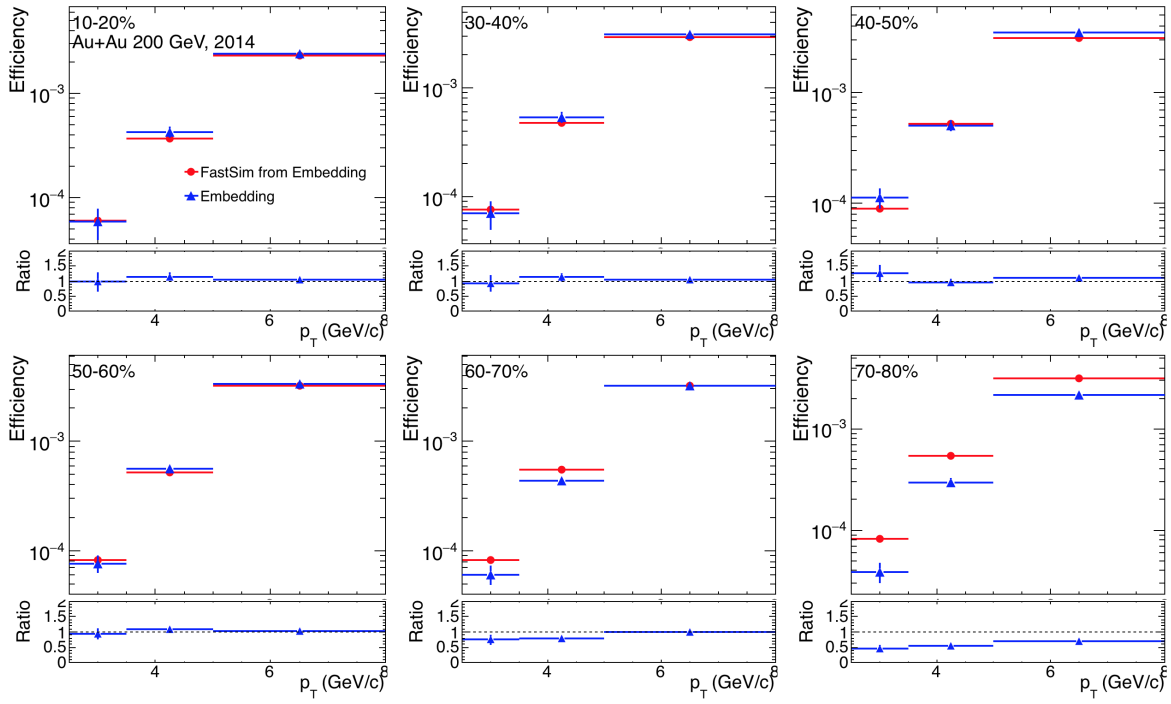

Figure 4.45: Λ_c reconstruction efficiencies as functions of p_T for different centralities from FastSim and HIJING simulations embedded in MB data for 2014. The smaller panels represent the ratio of the two.

the FastSim. As expected, they differ more in the peripheral collisions with up to $\sim 40\,\%$ difference in the 70–80 % centrality interval and approximately $\sim 10\,\%$ in the 60–70 % bin. For centralities bellow 60 %, the efficiencies are consistent within statistical uncertainties. The most peripheral point is 50–80 % in centrality which is shown in Figure 4.46. The efficiencies are consistent within 10 % in this centrality interval which is quoted as the systematic uncertainty.

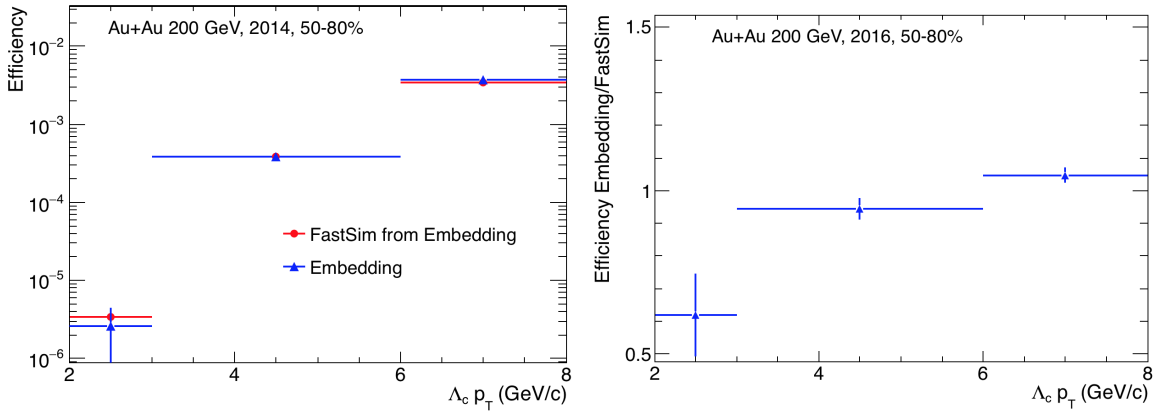

Figure 4.46: Left: Λ_c reconstruction efficiencies as functions of p_T in the 50–80 % centrality bin from FastSim and HIJING simulations embedded in MB data for 2014. Right: Ratio of the two efficiencies vs p_T.

The same study was performed in the 2016 data which is shown in Figures 4.47 and 4.48. The efficiencies show a similar behavior as in 2014 with the largest difference in the most peripheral collisions. In the 50–80 % centrality bin, the agreement is down to 5 % and is consistent within 10 % including the statistical uncertainty. The 10 % systematic uncertainty is quoted in this bin such as in the 2014 data.

4.9.7 Particle misidentification and double counting

In our analysis method, there is a finite probability that one or more daughter particles are misidentified as other hadrons. When this happens to two daughters and they are swapped, the signal is artificially enhanced as the Λ_c candidate is counted twice. In our case, we only need to consider the swap between $p^{\pm}$ and $\pi^{\pm}$, because the kaons have opposite charge. The contribution of this double counting is rather small as the Λ_c mass peak will be shifted and

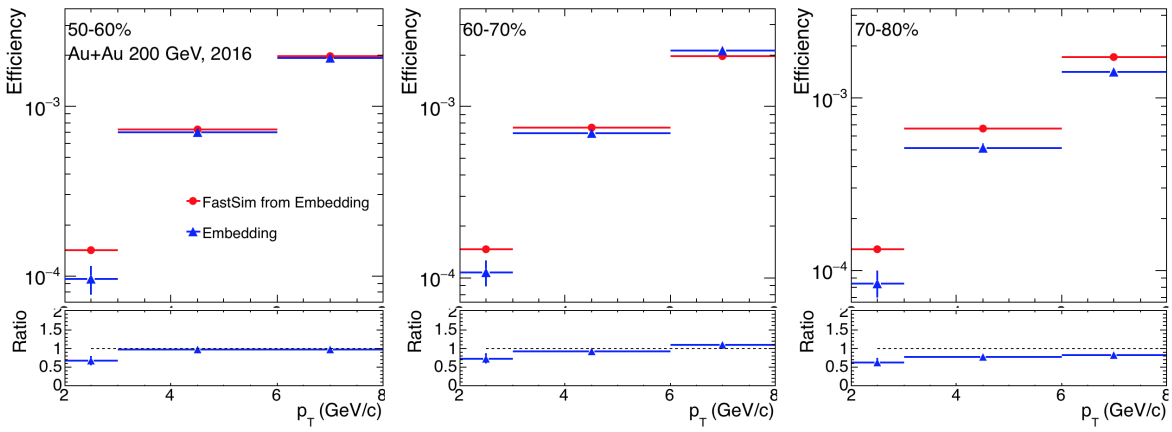

Figure 4.47: Λ_c reconstruction efficiencies as functions of p_T for different centralities from FastSim and HIJING simulations embedded in MB data for 2016. The smaller panels represent the ratio of the two.

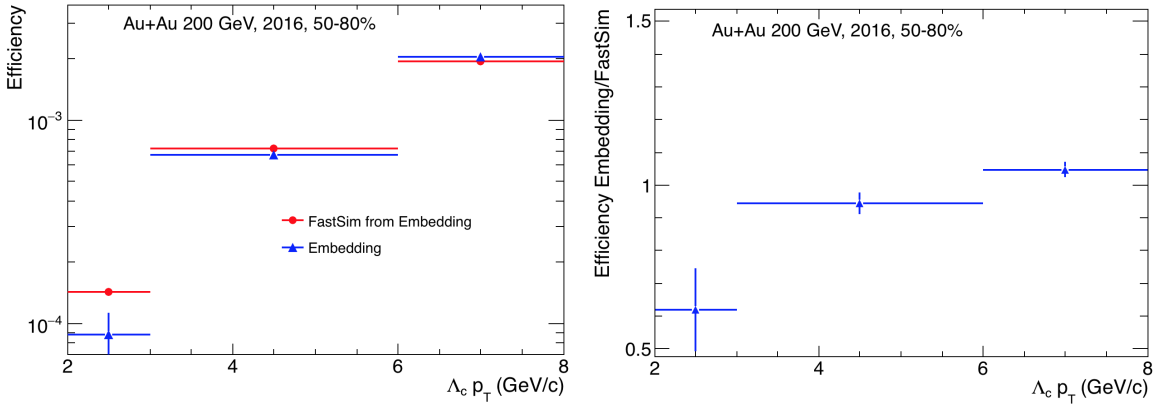

Figure 4.48: Left: Λ_c reconstruction efficiencies as functions of p_T in the 50–80 % centrality bin from FastSim and HIJING simulations embedded in MB data for 2016. Right: Ratio of the two efficiencies vs p_T.

the protons have especially high purity, because of the TOF requirement in their PID. The upper limit of this contribution is, therefore, quoted in the systematic uncertainty and is evaluated as follows:

The dE/dx distribution of a particle species generally follows a Gaussian distribution for a fixed p_T. Pure samples of pions and protons from the decays of K^0_s and Λ, respectively, were used. Figures 4.49 and 4.50 show the invariant mass of the reconstructed K^0_s and Λ

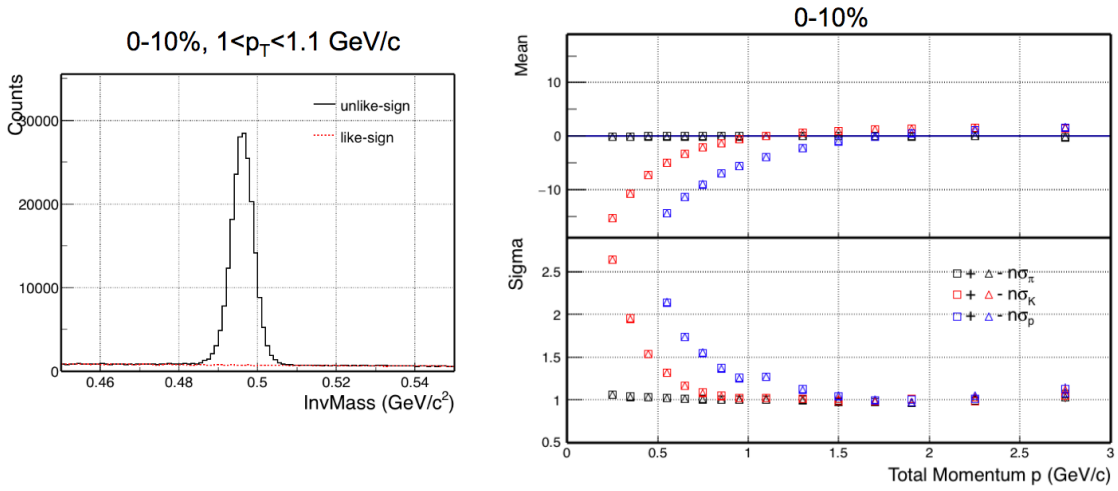

Figure 4.49: Left: Invariant mass distribution of the K^0_s sample. Right: Mean and width of the pion dE/dx distribution, compared to the theoretical values for pions (black), kaons (red), and protons (blue), evaluated in terms of $\sigma_{dE/dx}$ of the respective hadron.

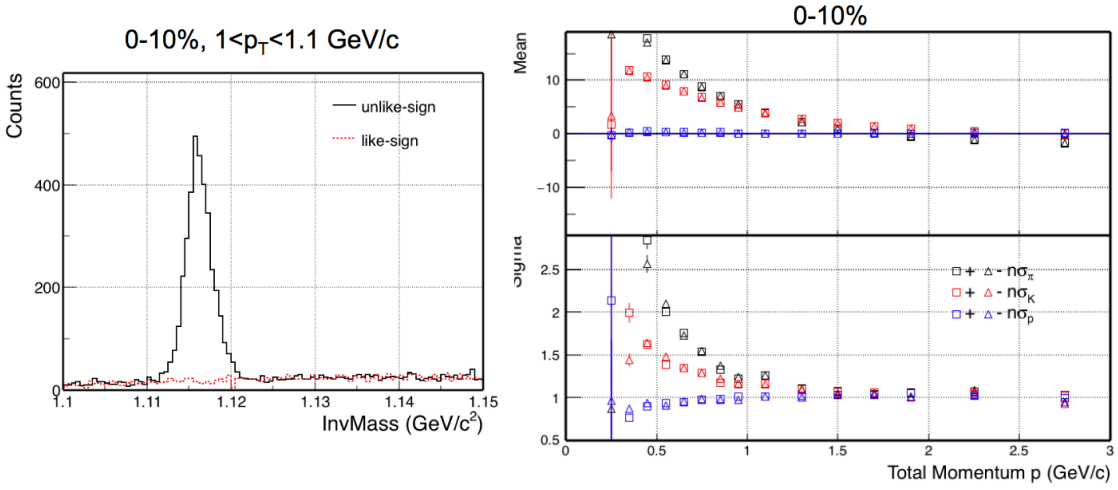

Figure 4.50: Left: Invariant mass distribution of the Λ sample. Right: Mean and width of the proton dE/dx distribution, compared to the theoretical values for pions (black), kaons (red), and protons (blue), evaluated in terms of $\sigma_{dE/dx}$ of the respective hadron.

samples, as well as the mean and the width of the dE/dx distributions of the pure pions and protons in terms of the width $\sigma_{dE/dx}$ of other particle species. Figure 4.51 depicts the shape of the dE/dx distributions of daughter species in terms of $\sigma_{dE/dx}$ of other particle species in

several p_T intervals. All these figures show good separation in low p_T.

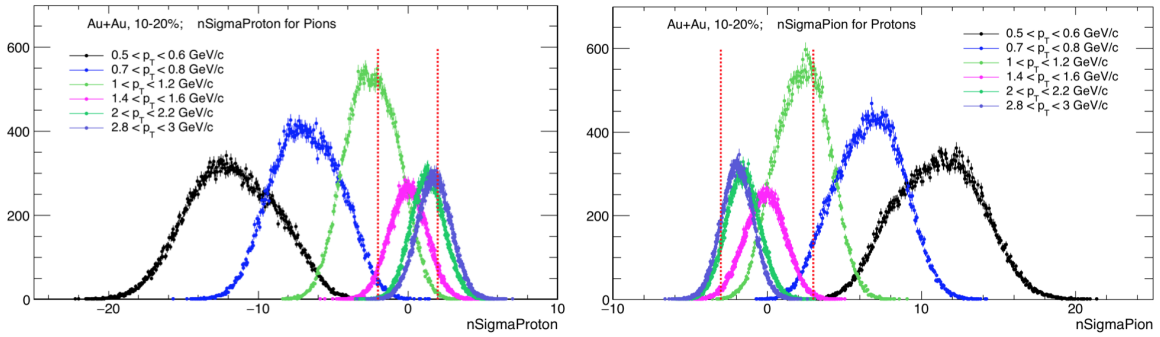

Figure 4.51: $\mathrm{d}E/\mathrm{d}x$ distributions for various p_T intervals measured for pions (left) and for protons (right).

The same procedure can be performed to evaluate the separation in PID in TOF. Figure 4.52 shows $1/\beta$ distributions of protons and pions in several p_T regions. These distributions are used to evaluate the overlap between pions and protons. The vertical lines indicate the $1/\beta$ cuts of the other particle (protons with pions $1/\beta$ distribution and vice versa). Both the $\mathrm{d}E/\mathrm{d}x$ and $1/\beta$ distributions are shown in the 10–20 % centrality interval, however the centrality dependence is negligible in this case.

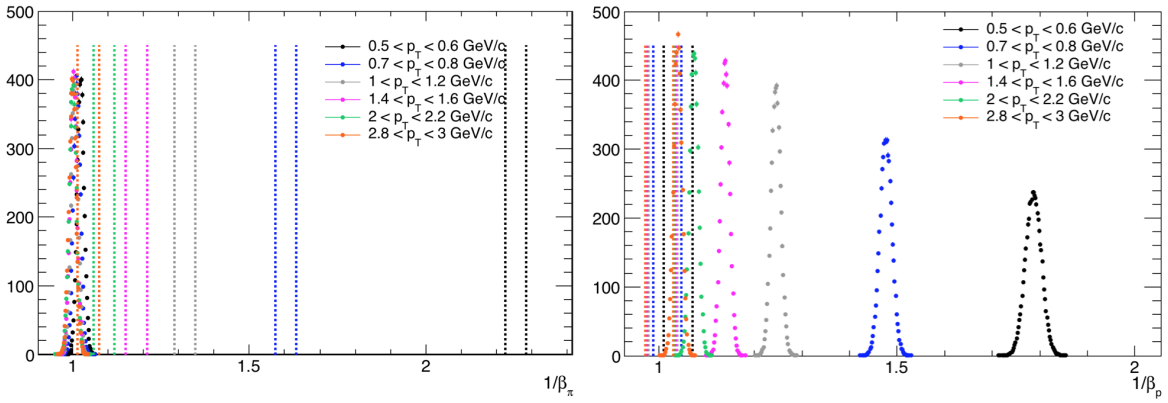

Figure 4.52: $1/\beta$ distributions for various p_T intervals measured for pions (left) and for protons (right). The vertical lines denote the TOF $1/\beta$ cuts for protons (left) and pions (right).

Figure 4.53 shows the overall probabilities of misidentification of pions as protons and

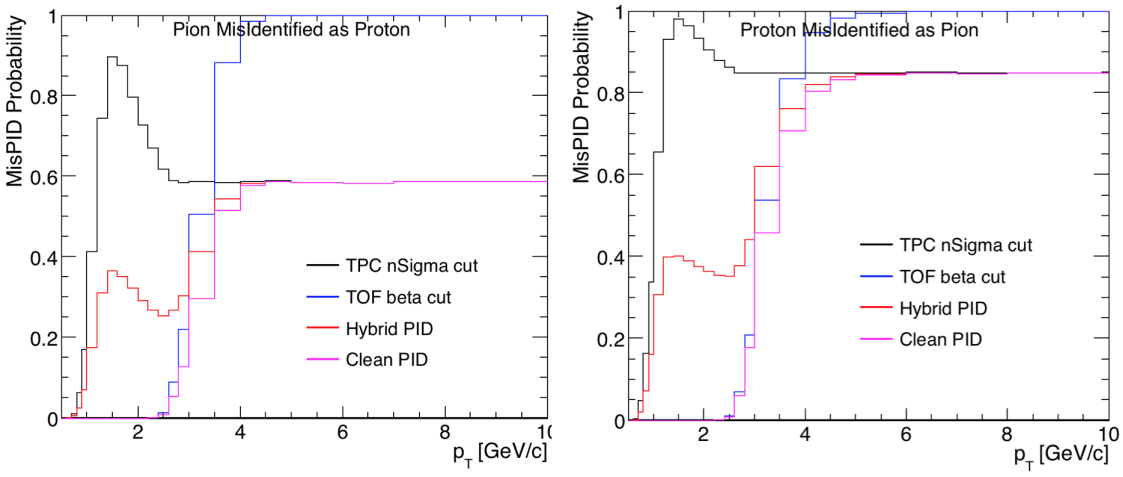

Figure 4.53: Probabilities for pions to be misidentified as protons (left) and protons to be misidentified as pions (right) for several different selection criteria.

vice versa for several selection criteria. The probability for pions with $p_{\mathrm{T}} < 3\,\mathrm{GeV}/c$ to be misidentified as protons is close to zero, because we require both, TOF and TPC-dE/dx information in this region.

The probability of double counting of the Λ_{c} triplets is shown in Figure 4.54 for both 2014 and 2016 data taking. The overall probability would be lower than 3 % in the p_{T} region of our analysis, however we have to also consider the shift in invariant mass of the misidentified p, K, π triplets. To estimate this contribution, ${\Lambda_{\mathrm{c}}}^{\pm}$ decays were simulated in the Fastsim package with swapped $\pi^{\pm}$ and $\mathrm{p}^{\pm}$. The invariant-mass distribution of the doubly misidentified triplets is plotted in Figure 4.55. Only the $5\,\mathrm{GeV}/c < p_{\mathrm{T}} < 8\,\mathrm{GeV}/c$ range is considered as the lower-p_{T} Λ_{c} triplets have a very low chance to be misidentified. The mass peaks are shifted by approximately $400\,\mathrm{MeV}/c^2$ with $\sim 3.2\,\%$ of overlap. The overall contribution of the misidentified triplets is, therefore, much smaller than 1 % which is the quoted contribution to the systematic uncertainties.

4.9.8 Summary of systematic uncertainties

All the sources of systematic uncertainties are summarized in Tables 4.4 and 4.5 in different p_{T} and centrality intervals, respectively. The uncertainties are cited for both, the p_{T} and

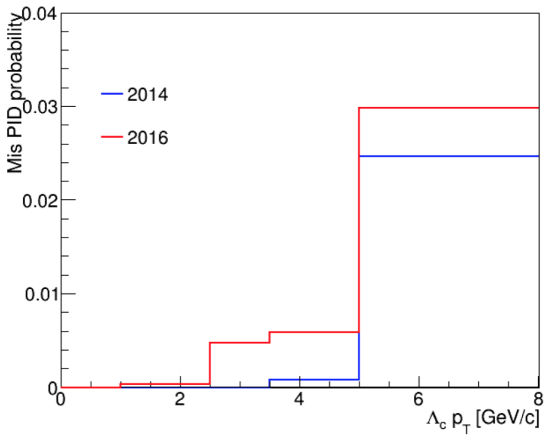

Figure 4.54: Double-counting probability due to PID as a function of p_{T} in the 2014 and 2016 data taking.

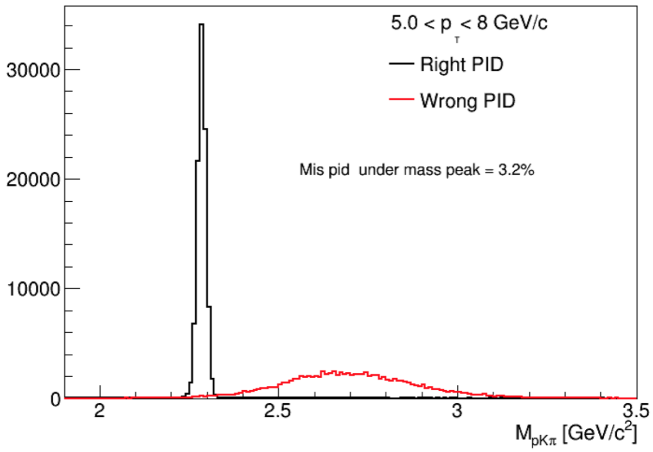

Figure 4.55: Simulated invariant mass of daughters of simulated Λ_c decays with swapped $\pi^{\pm}$ and $p^{\pm}$ (red), and correctly identified triplets (black).

centrality spectra (S) and the Λ_c/D^0 ratio (R). The TOF-matching and PID uncertainties are taken to be fully correlated between the 2014 and 2016 data-taking periods. The branching ratio is cited from the latest PDG value [25] of 5.3 %. The Monte-Carlo closure and are correlated as well, whereas the BDT-cut variation and the yield-extraction contributions are considered uncorrelated. The combined uncertainties are calculated using the standard error propagation. The source of uncertainties in the 'other' column consist of the uncertainties from the secondary correction ($\sim$ 4 %) and on the D^0 spectra ($\sim$ 5–12 % [90]). The D^0

Table 4.4: Summary of systematic and statistical uncertainties of the Λ_c spectrum (S) and the Λ_c/D^0 ratio (R) in the 10–80 % centrality interval in different p_T bins.

p_T (GeV/c)	TPC+TOF+PID+BR	Yield	BDT cut	Closure	Other	Total	Stat.
2.5 – 3.5	15.1 %(S) 7.2 %(R)	5.9 %	14.3 %	15 %	11.9 %	27 %(S) 25 %(R)	17.8 %
3.5 – 5.0	15.1 %(S) 7.2 %(R)	5.7 %	13.6 %	8 %	11.9 %	24 %(S) 21 %(R)	12.7 %
5.0 – 8.0	15.1 %(S) 7.2 %(R)	14.8 %	13.7 %	5 %	16.1 %	27 %(S) 26 %(R)	16.5 %

Table 4.5: Summary of systematic and statistical uncertainties of the Λ_c spectrum (S) and the Λ_c/D^0 ratio (R) within the $3\,\mathrm{GeV}/c < p_T < 6\,\mathrm{GeV}/c$ interval in different centrality bins.

Centrality	TPC+TOF+PID+BR	Yield	BDT cut	Closure	Other	Total	Stat.
0 – 20 %	15.1 %(S) 7.2 %(R)	11.5 %	14.4 %	10 %	14.8 %	26 %(S) 22 %(R)	15.3 %
20 – 50 %	15.1 %(S) 7.2 %(R)	13.2 %	10.0 %	10 %	14.8 %	25 %(S) 21 %(R)	12.0 %
50 – 80 %	15.1 %(S) 7.2 %(R)	6.2 %	14.3 %	10 %	14.8 %	35 %(S) 32 %(R)	25.5 %

uncertainties are included for the Λ_c/D^0 ratio (R), but not for the spectra (S).

In general, the systematic uncertainties vary between 21 % and 32 % for the Λ_c/D^0 ratio (R) and 24 % and 35 % for the spectra (S), where the highest is quoted in the 50–80 % centrality bin which reflects the highest statistical uncertainty of 25.5 %. The lowest uncertainties are quoted in the $3.5\,\mathrm{GeV}/c < p_T < 5.0\,\mathrm{GeV}/c$ and the 20–50 % bin in centrality where the statistical uncertainty is the lowest as well (12.7 % and 12.0 %, respectively).

4.10 Feed-down from bottom hadrons

The measured Λ_c do not necessarily originate directly in the collision, but can be a product of bottom-hadron decays. This contribution is called the feed-down. The total bottom cross-section of at $\sqrt{s} = 200\,\mathrm{GeV}$ is only 1 % that of the charm, according to FONLL calculations [85]. However, the feed-down contribution may vary with p_T.Moreover, the reconstruction efficiency of non-prompt Λ_c may be higher than that of the prompt Λ_c because they decay further from the PV. The highest contribution to the $\Lambda_c^{\pm}$ spectrum comes from the

decay of Λ_b^0 baryons with the inclusive branching ratio (BR) of the $\Lambda_c^\pm$ decay of $\sim 10\,\%$. The $B^\pm$ meson has an inclusive BR into the $\Lambda_c^\pm$ of $\sim 2\,\%$ and the B^0 of $\sim 5\,\%$ [25].

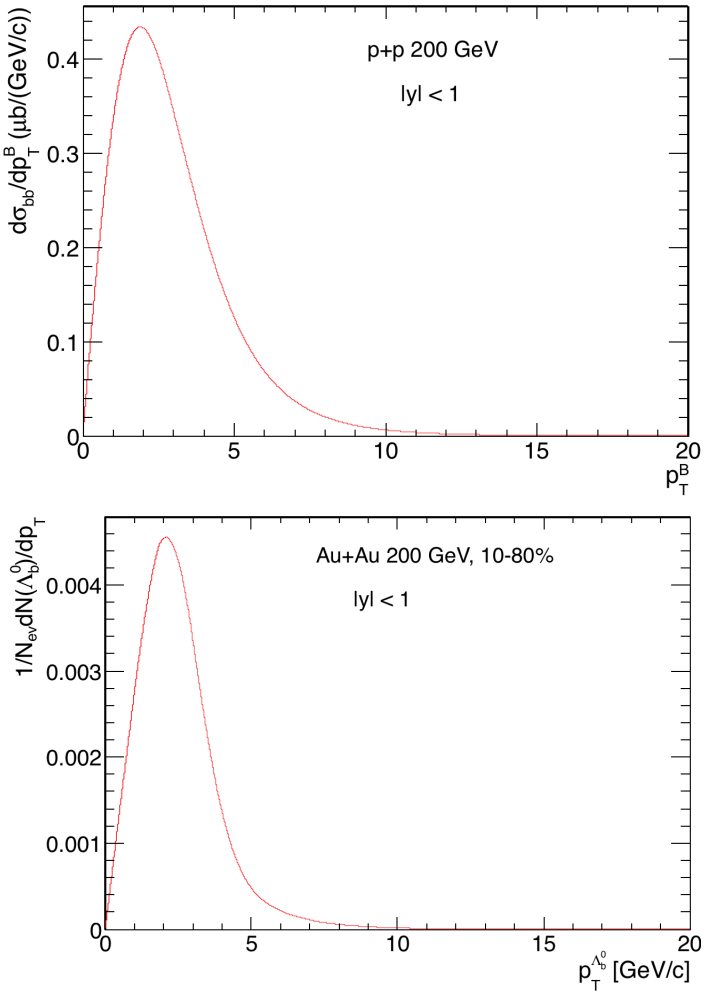

Figure 4.56: The bottom cross-section from FONLL [85] (upper limit) in p+p collisions at $\sqrt{s} = 200\,\text{GeV}$ (top panel) and the Λ_b^0 in 10–80 % central Au+Au collisions at $\sqrt{s_{\text{NN}}} = 200\,\text{GeV}$ (bottom panel).

The total cross-section of the bottom hadrons in p+p collisions at $\sqrt{s} = 200\,\text{GeV}$ from FONLL [85] as a function of p_T is shown in the top panel of Figure 4.56. We used the upper limit of the uncertainty band to be conservative. The bottom panel shows the Λ_b^0 yield in 10–80 % central Au+Au collisions at $\sqrt{s_{\text{NN}}} = 200\,\text{GeV}$, obtained by scaling the p+p cross-section by the average N_{bin} of ≈ 198 for the 10–80 % centrality bin and normalizing it by the non-single difractive cross-section of 30 mb in p+p [179]. The resulting yield has been

also scaled by the same baryon-to-meson enhancement as measured in the charm sector [112]. This is larger than that observed in p+p collisions. The R_{AA} of the Λ_{b}^{0} is considered to be 1 in this conservative estimate.

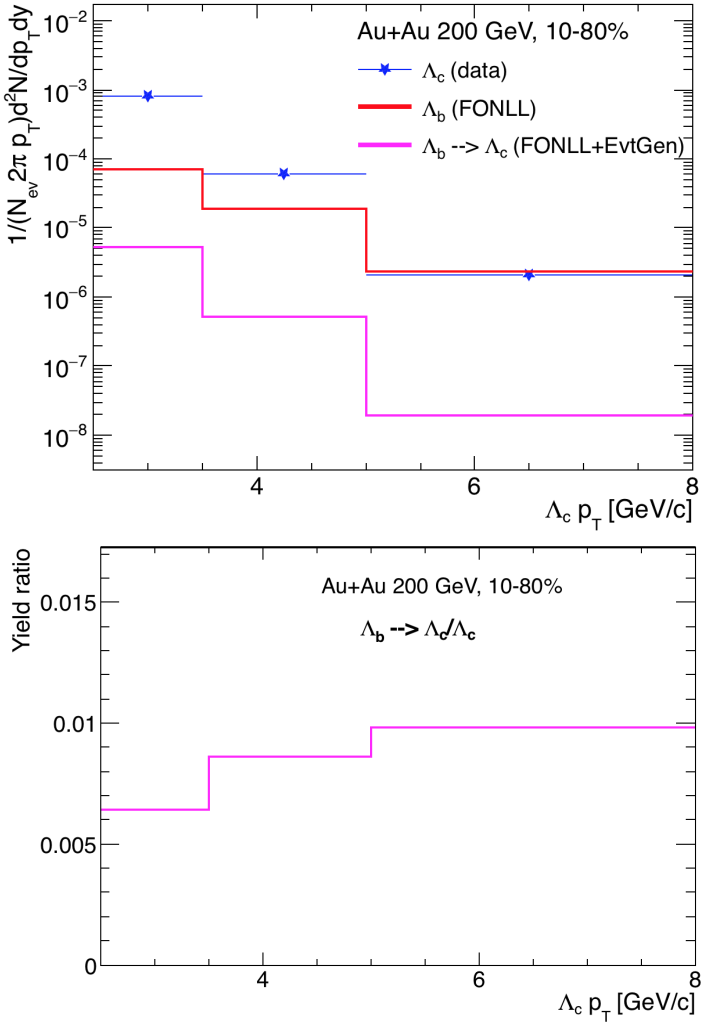

Figure 4.57: (Top panel) Measured $\Lambda_{\mathrm{c}}^{\pm}$ p_{T} spectrum, compared to the feed-down contribution from the Λ_{b}^{0} baryon. (Bottom panel) The ratio between the feed-down contribution from Λ_{b}^{0} and the inclusive $\Lambda_{\mathrm{c}}^{\pm}$ spectrum a function of p_{T}.

The Λ_{b}^{0} decay was simulated in the `EvtGen` package with a branching ratio of $\Lambda_{\mathrm{b}}^{0} \rightarrow \Lambda_{\mathrm{c}} + l + \overline{\nu_l}$ as 5 % [25] and of $\Lambda_{\mathrm{b}}^{0} \rightarrow \Lambda_{\mathrm{c}} + \pi^{+} + \pi^{-} + l + \overline{\nu_l}$ of 5.6 %, where l is a lepton and $\overline{\nu_l}$ is an antineutrino of the same family. Figure 4.57 shows the Λ_{b}^{0} spectrum obtained from FONLL and the Λ_{c} feed down, compared to the measured Λ_{c} spectrum. The bottom

panel shows the ratio of the measured Λ_c from the Λ_b^0 decays divided by the measured p_T spectrum. As can be seen, the contribution from the Λ_b^0 is small ($< 1\,\%$ in all measured p_T intervals). The contributions from the B^0 and $B^{\pm}$ were not evaluated, but are clearly to be expected $\sim 1\,\%$, based on the Λ_b^0.

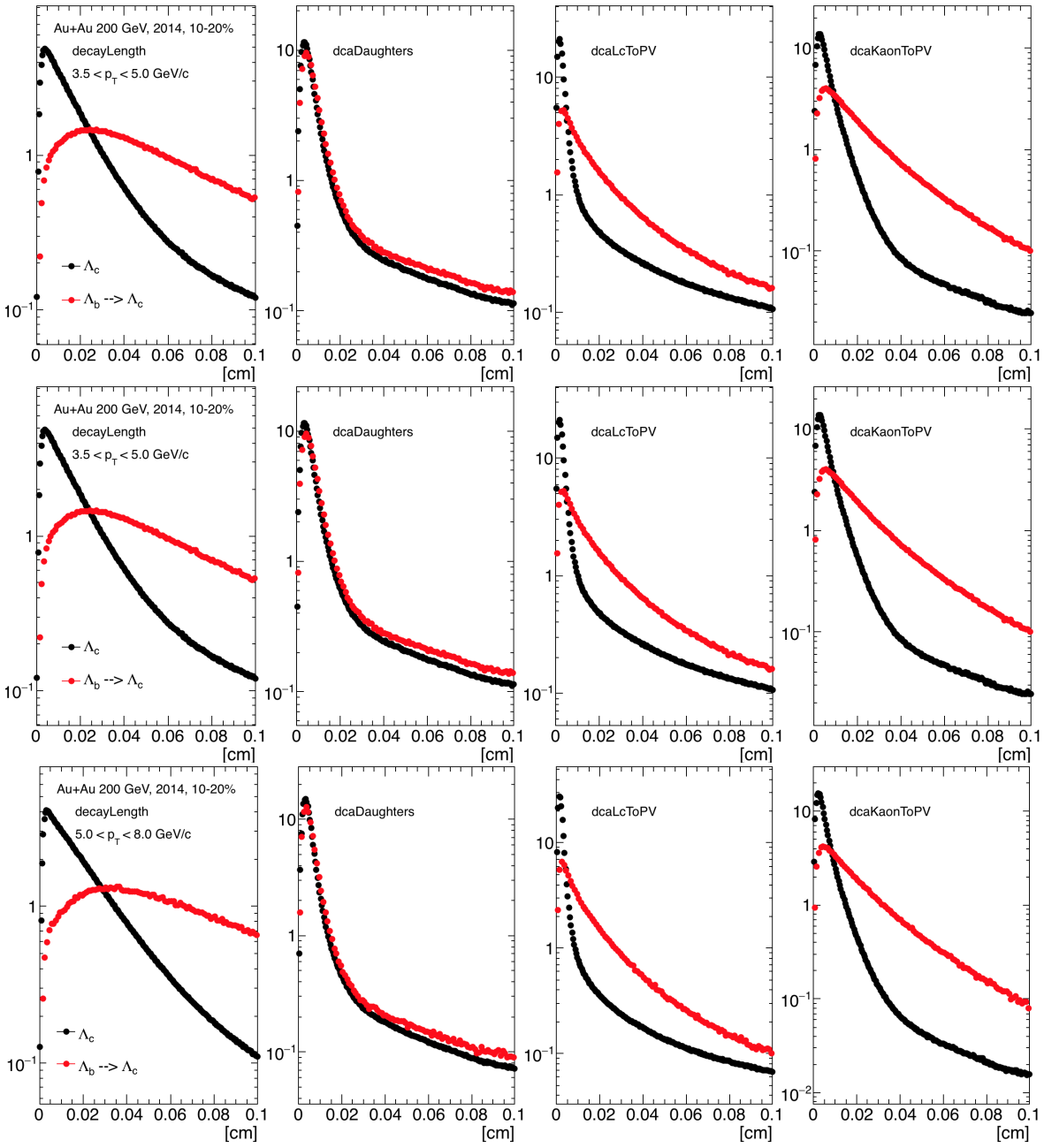

Figure 4.58: Topological variables of the simulated prompt Λ_c decays and the Λ_c from the Λ_b^0 feed down.

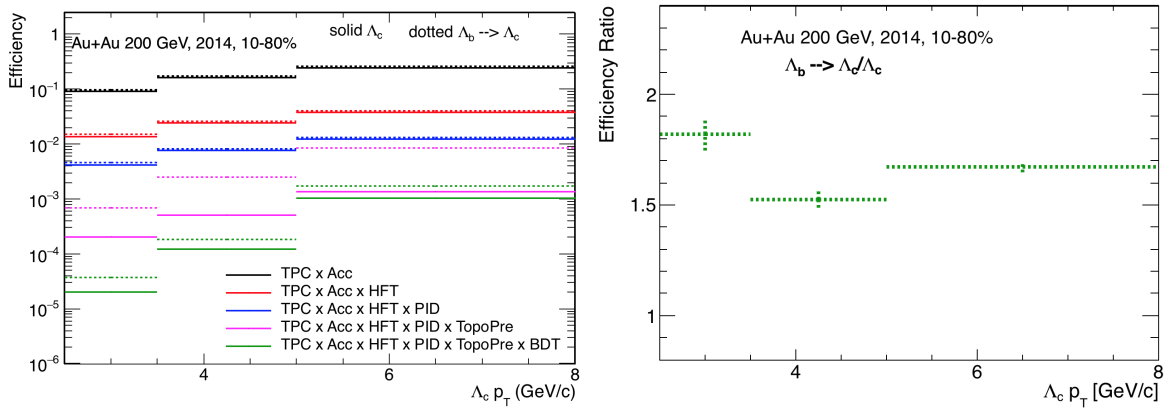

Figure 4.59: (Left) reconstruction efficiency of various topological cuts of prompt Λ_c and Λ_c from the Λ_b^0 feed down in the 2014 data in the 10–80 % centrality interval. (Right) Ratio of the non-prompt and prompt reconstruction efficiencies.

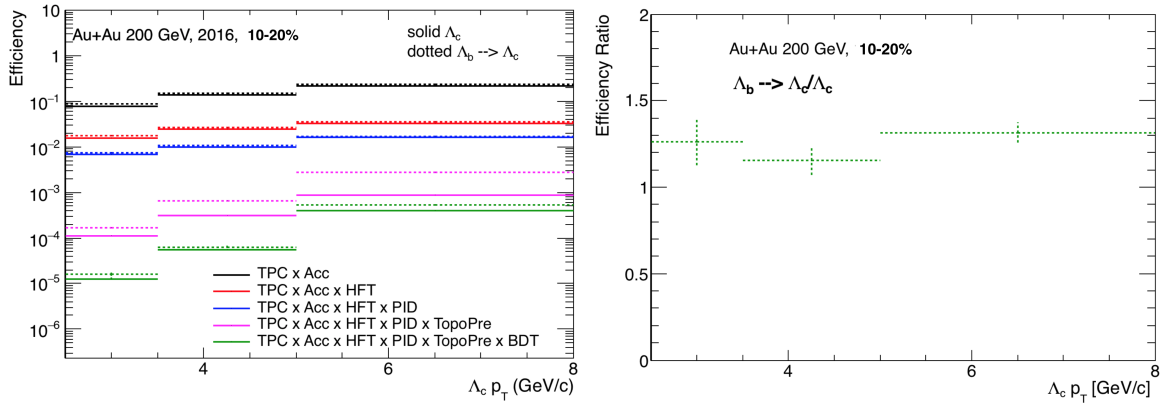

Figure 4.60: (Left) reconstruction efficiency of various topological cuts of prompt Λ_c and Λ_c from the Λ_b^0 feed down in the 2016 data in the 10–20 % centrality interval. (Right) Ratio of the non-prompt and prompt reconstruction efficiencies.

The reconstruction efficiencies of the Λ_c, coming from the Λ_b^0 feed down, are evaluated in the `FastSim` package. Figure 4.58 shows the distributions of various topological variables of the simulated prompt Λ_c, as compared to the Λ_c from the Λ_b^0 feed down in several different p_T intervals. The decay length, the DCA of single daughters to the PV, and the DCA of Λ_c to the PV is higher in the Λ_b^0 feed-down, making the efficiency of the cuts in these variables smaller for the prompt the Λ_c. DCA between the daughters was slightly smaller in the prompt Λ_c, thus the reconstruction efficiency is higher for the prompt case in this variable.

The total reconstruction efficiencies in of the Λ_c from the Λ_b^0 decay is compared to the prompt Λ_c in the left panel of Figure 4.59 for the 2014 data and of Figure 4.60 in the 2016 data. The right panels of these figures show the ratios between the non-prompt ($\Lambda_b^0 \to \Lambda_c$) reconstruction efficiency and the prompt one. The efficiencies are larger in the non-prompt case by $\sim$ 40–80 % in both, 2014 and 2016 at all p_T intervals. With the reconstruction efficiency taken into account, the non-prompt contribution to the measured Λ_c remains lower than 4 % at all p_T. The bottom feed-down is, therefore, small and is not propagated into the final uncertainties.

Chapter 5

Results

In this chapter, we summarize the main results of this thesis, i.e. the invariant-mass spectra of the p, K, π triplets and the invariant yield of the Λ_c baryon. We also compare the results to several existing model predictions.

5.1 Invariant-mass spectrum

The procedurre to obtain the invariant-mass spectrum of the p, K, π triplets is described in Section 4.6. In Figure 5.1, we show the combined invariant-mass spectrum from the 2014 and 2016 running at $\sqrt{s_{\mathrm{NN}}} = 200\,\mathrm{GeV}$. The precision of the HFT as well as the supervised machine learning method enable the measurement to be divided into several p_{T} and centrality intervals out of which 0–20 % most central collisions are shown in the top panel and 10–80 % in the bottom panel. The background was estimated with the wrong-sign combinations, i.e. ones that cannot make a ${\Lambda_c}^+$ or a ${\Lambda_c}^-$. From combinatorics, on average, in a Au+Au collision, there are 3× more wrong-sign random combinations than the correct ones, therefore the background is scaled by a factor of 1/3. The solid line depicts a fit of Gaussian plus second-order polynomial to the right-sign combinations where the shape of the polynomial is fixed, using the spectrum of the wrong-sign combinations. The significance of the Λ_c signal are ∼6.9 and ∼11 in the 10–80 % and 0–20 % centrality intervals, respectively.

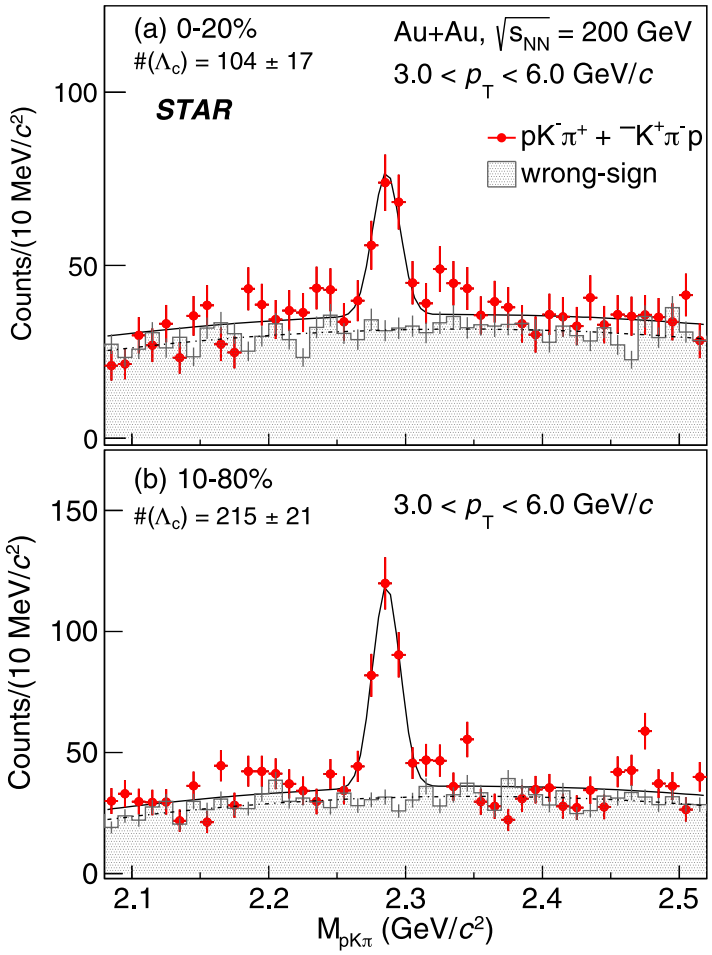

Figure 5.1: Invariant-mass spectrum of $\mathrm{p}^+ + \mathrm{K}^- + \pi^+$ and $\overline{\mathrm{p}}^- + \mathrm{K}^+ + \pi^-$ triplets in (a) the 0–20 % most central Au+Au collisions and (b) 10–80 % centrality interval. The chequered histogram denotes the spectrum of the wrong-sign combinations, scaled by a factor of 1/3.

5.2 Total cross-section

The Λ_c invariant yields in the 10–80 % centrality class are summarized in Table 5.1, together with statistical and systematic uncertainties. The 10–80 % centrality interval was chosen for the measurement differentiated in p_T, because it had the highest significance.

Table 5.1: $\Lambda_c^{\pm}$ invariant yields with statistical and systematic uncertainties in the 10–80 % centrality interval.

p_T (GeV/c)	$1/(2\pi\, p_T N_{evt})\, d^2N/dp_T\, dy$ (GeV/c)
2.5 – 3.5	$8.2 \times 10^{-4} \pm 1.4 \times 10^{-4}$ (stat.) $\pm 2.4 \times 10^{-4}$ (sys.)
3.5 – 5.0	$6.0 \times 10^{-5} \pm 7.7 \times 10^{-6}$ (stat.) $\pm 1.5 \times 10^{-5}$ (sys.)
5.0 – 8.0	$2.1 \times 10^{-6} \pm 3.8 \times 10^{-7}$ (stat.) $\pm 5.5 \times 10^{-7}$ (sys.)

5.3 Λ_c/D^0 ratio

The baryon-to-meson ratio has been measured in the charm sector for the first time at RHIC. The ratio of Λ_c/D^0 yields is shown in Figure 5.2 in three p_T bins for the 10–80 % centrality class. The top panel 5.2(a) compares the baryon-to-meson ratio in the charm sector to the strange- and light-flavor hadrons [73, 181]. The Λ_c/D^0 ratio is comparable in magnitude to the Λ/K^0_s and p/π ratios and exhibits the same p_T dependence in the measured p_T region.

The bottom panel 5.2(b) shows a comparison of the measured Λ_c/D^0 ratio to several theoretical calculations. The measured values are significantly enhanced, compared to the latest PYTHIA 8.24 release calculation (Monash tune [182]) without the color reconnection (CR). The implementation with the CR (mode 2 in [130]) describes the Λ_c/D^0 ratio in p+p and p+Pb [126–128] at the LHC (see Section 2.7.3). It is however inconsistent with the Au+Au data points. Without CR, the model is ruled out with a p value of 1×10^{-4} ($\chi^2/\mathrm{NDF} = 20.7/3$) and the model with CR gives a p value of 0.04 ($\chi^2/\mathrm{NDF} = 8.2/3$), using a reduced χ^2 test.

The panel 5.2(b) also shows comparison to several model calculations that employ charm-quark coalescence (Ko *et al.* three quarks/di-quarks [78], Ko *et al.* with flow [183], Catania [184], Tshingua [112], Rapp *et al.* [114]). These models differ in the spectra of light and heavy quarks in the QGP, that they considered, as well as their modelling of the space-time correlations between the quarks during coalescence, and the treatment of the excited states and heavy hadrons that decay into Λ_c and D^0. Most of the models give predictions that

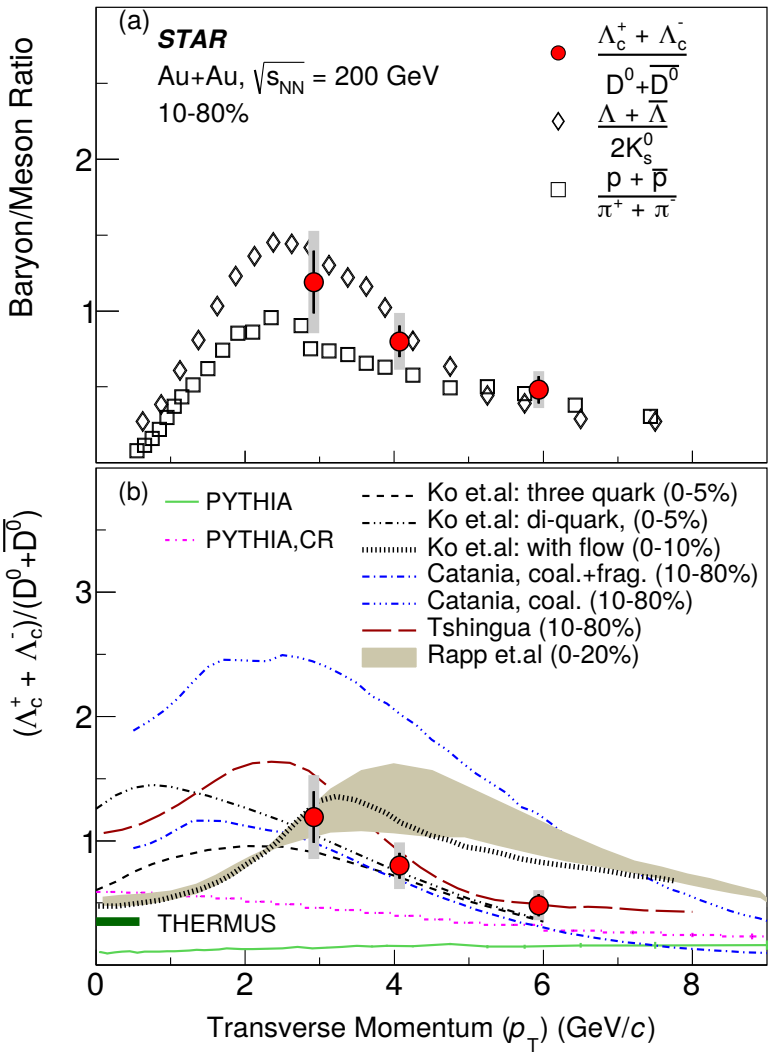

Figure 5.2: Measured Λ_c/D^0 ratio as a function of p_T at midrapidity ($|y| < 1$) in Au+Au collisions at $\sqrt{s_{NN}} = 200\,\text{GeV}$ in 10–80 % centrality, (a) compared to the baryon-to-meson ratios in the light and strange sectors and (b) various model calculations. The vertical lines and shaded boxes are the statistical and systematic uncertainties, respectively. The green line on the vertical axis of the bottom (b) plot is the p_T-integrated Λ_c/D^0 ratio from the THERMUS [180] model calculation with a freeze-out temperature of $T_{ch} = 160\,\text{MeV}$.

compare well to the measured p_T dependence of the ratio.

A reduced χ^2 test of the models has been carried out, taking into account the finite width of each p_T bin in the data. The Catania group's calculation, including only the quark coalescence, overpredict the measurement at all p_T with a reduced χ^2 of 26.1. The calculation

from Ko *et al.* with flow gives a χ^2 of 4.8, mainly because it overpredicts the measurement in the two highest p_{T} bins. Note that the centrality range in the calculation is different from the measurement. Otherwise, the coalescence-model predictions are consistent with the measured data.

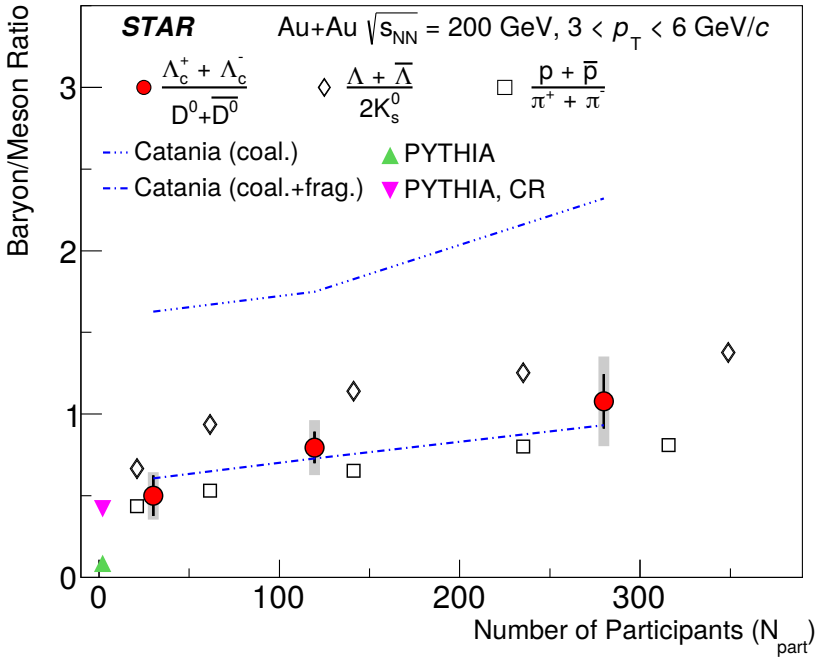

Figure 5.3: Measured Λ_c/D^0 ratio in the $3\,\mathrm{GeV}/c < p_{\mathrm{T}} < 6\,\mathrm{GeV}/c$ interval (solid red circles). The open diamonds and squares denote the $(\Lambda + \overline{\Lambda})/2K_s^0$ and $(p + \overline{p})/(\pi^+ + \pi^-)$, i.e. the baryon-to-meson ratios in the strange and light sectors, respectively. The dashed lines show the Catania model [184], using quark coalescence with and without fragmentation of heavy hadrons. The up and down triangles indicate the ratios from PYTHIA 8.24 model p+p collisions in the same p_{T} region without [182] and with [130] color reconnection, respectively.

The centrality dependence of the Λ_c/D^0 ratio is denoted in Figure 5.3 as plotted as a function of the number of participants N_{part}, in the $3\,\mathrm{GeV}/c < p_{\mathrm{T}} < 6\,\mathrm{GeV}/c$ range. The measured points correspond to centrality intervals (from left to right) 50 % – 80 %, 20 % – 50 %, and 0 % – 20 %. The Λ_c/D^0 ratio shows an increasing trend towards more central collisions. This trend is quantitatively similar to ones in the baryon-to-meson in the light and strange sectors. The data are also consistent with the coalescence-model calculation by

the Catania group [184]. Moreover, the $\Lambda_{\mathrm{c}}/\mathrm{D}^0$ ratio in the 0 % – 20 % centrality interval is measured as $1.08 \pm 0.16(\mathrm{stat.}) \pm 0.26(\mathrm{sys.})$ which is higher than the PYTHIA 8.24 calculation for p+p in the same p_{T}range without CR (by 3.1 standard deviations σ) and with CR (by 2.1σ).

5.4 p_{T}-integrated $\Lambda_{\mathrm{c}}/\mathrm{D}^0$ ratio

The coalescence-model curves in Figure 5.2(b) were used to extrapolate the p_{T} spectrum to $p_{\mathrm{T}} = 0\,\mathrm{GeV}/c$ and to calculate the p_{T}-integrated $\Lambda_{\mathrm{c}}/\mathrm{D}^0$ ratio. The shapes of the model curves were used and scaled to the measured ratio. The mean of the extrapolated curves was used as the central value and their maximum difference is quoted as an extra source of systematic uncertainty.

The p_{T}-integrated $\Lambda_{\mathrm{c}}/\mathrm{D}^0$ ratio is calculated as $0.80 \pm 0.12(\mathrm{stat.}) \pm 0.22(\mathrm{sys., data}) \pm 0.41(\mathrm{sys., models\ extrapolation})$. This value is consistent within uncertainties with the value 0.35, calculated from the THERMUS [180] model with the freeze-out temperature of $T_{\mathrm{ch}} = 160\,\mathrm{MeV}$, shown in Figure 5.2(b). The Λ_{c} make, therefore, a sizeable contribution to the total charm yield in heavy-ion collisions.

Chapter 6

Conclusion and outlook

In this thesis, the first direct reconstruction of Λ_c in Au+Au collisions at $\sqrt{s_{NN}} = 200\,\text{GeV}$ is reported. Baryon-to-meson ratio in the charm sector has been measured in the form of Λ_c/D^0 yield ratio.

The measurement of the Λ_c in heavy-ion collisions represents a challenging task, due to the short life time ($c\tau \approx 60\,\mu\text{m}$) and the large combinatorial background, because the direct reconstruction requires three body decays that involve pions, protons, and kaons which are abundant products of Au+Au collisions. This measurement was enabled thanks to the utilization of the new silicon detector HFT whose two innermost layers were placed very close to the interaction point and utilize the MAPS technology for the first time in heavy-ion experiments. Because of this, the innermost layers of the HFT have excellent track-pointing resolution to secondary vertices of particle decays. Machine-learning techniques were utilized to separate the signal from the combinatorial background, which come mostly from the primary vertex. The relatively large number of the Λ_c, that was obtained thanks to these detection techniques as well as the large statistical sample, recorded by STAR in the years 2014 and 2016, allowed for the Λ_c/D^0 measurement to be differentiated in the transverse momentum and centrality for the first time in heavy-ion collisions.

The Λ_c/D^0 yield ratio in Au+Au collisions at midrapidity ($|y| < 1$) is significantly larger than that in p+p collisions simulated by PYTHIA and is comparable with the baryon-to-meson ratios in the light- and strange-flavor sectors in the same kinematic region. The

measured ratio is also compatible with models that include charm-quark coalescence in the hadronization process. The Λ_c/D^0 ratio increases with more central collisions which is also consistent with models that include charm-quark coalescence.

The p_T-integrated Λ_c/D^0 ratio was obtained by extrapolating the measurement to low p_T and is calculated as $0.80 \pm 0.12(\text{stat.}) \pm 0.22(\text{sys., data}) \pm 0.41(\text{sys., models extrapolation})$. This shows that the Λ_c make a sizable contribution to the total charm yield in heavy-ion collisions at RHIC. The p_T-integrated ratio is also consistent with the THERMUS model, in our comparison calculated with the thermal freeze-out temperature of $T_{ch} = 160\,\text{MeV}$.

Two service tasks were performed as a part of this thesis: Work on the slow simulator for the HFT-Pixel detector and, secondly, maintenance, calibration, and documentation of the STAR Zero Degree Calorimeter (ZDC).

The HFT recorded data at STAR the years 2014–2016 and was a critical upgrade for the precise measurements of open-charm hadrons, including enabling the measurement of the Λ_c. The HFT-Pixel slow-simulator implementation and evaluation helped with the clustering component of the embedding procedure, in which simulated tracks are embedded into measured collisions at STAR.

The ZDC plays a vital role for triggering and the assessment of instant luminosity at STAR, and the determination of centrality in ion–ion collisions. The task was to ensure smooth operation of this critical component during the data taking at STAR. The ZDC was calibrated, using the single-neutron peak, at the start of each run. The performance of the ZDC photo-multiplier tubes has been evaluated and several have been upgraded to ones with higher gain. Moreover, the entire setup of the ZDC, together with the control, trigger, and readout electronics have been documented [8].

Thanks to the HFT and the large data samples of Au+Au collisions, recorded in 2014 and 2016, STAR has performed measurements that can draw an overall picture of the behavior of the charm quark in heavy-ion collisions. From the understanding of energy loss and collective movement of the charm quark in the QCD medium, provided by the D^0 and $D^\pm$ R_{AA}, v_2, and v_3 measurements, to the understanding of the hadronization process, given by the Λ_c and D_s measurements.

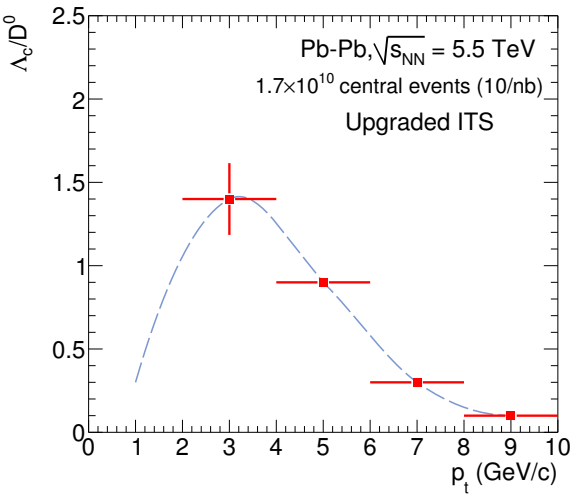

Figure 6.1: Projection of statistical uncertainties of the Λ_c/D^0 measurement with the improved resolution of ALICE ITS using 1.7×10^{10} central collisions (0–10 %), corresponding to an integrated luminosity of $10\,\mathrm{nb}^{-1}$ [141].

ALICE detector at the LHC at CERN is currently undergoing an overhaul upgrade of its Inner Tracking System which will consist of 7 layers of MAPS pixel sensors. When finished, this will greatly improve ALICE's tracking accuracy, and as a result, the separation of secondary vertices of open-heavy-flavor hadrons from the primary vertex. At the LHC energies of $\sqrt{s_{\mathrm{NN}}} = 5.5\,\mathrm{TeV}$, the cross-section of charm-quark production is larger than at RHIC, and ALICE plans to collect a large sample of Pb+Pb collisions. All of this is planed, in part, to create a next-level-of-precision measurement of the Λ_c, which will provide, together with other precise measurements of other open-heavy-flavor hadrons, an accurate quantitative understanding of the behavior of the charm quarks in the QGP, as well as heavy-quark hadronization in heavy-ion collisions. A projection of the error bars of the Λ_c/D^0 yield ratio measurement from LHC Run-3 Pb+Pb sample, that will be recorded by ALICE with the ITS upgrade, is shown in Figure 6.1.

Another promising development is currently being built at RHIC. A new detector sPHENIX [142] is currently being developed in place of the now phased-out PHENIX detector. The sPHENIX will have a TPC with PID capabilities and a vertex detector – Monolithic-Active-Pixel-Sensor-based Vertex Detector (MVTX) [186] with excellent granularity. Moreover, it

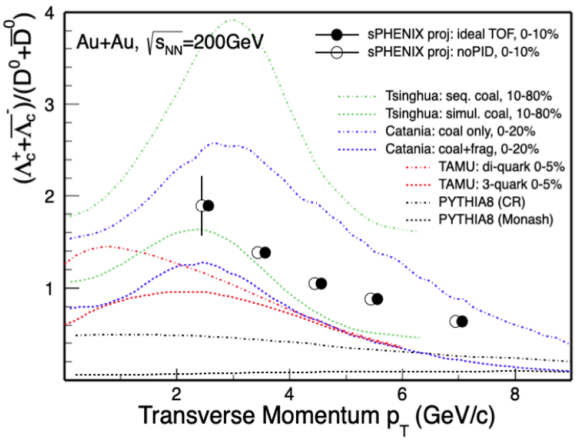

Figure 6.2: Projection of statistical uncertainties of the Λ_c/D^0 measurement with the sPHENIX detector, compared to theoretical calculations [112, 114, 130, 182, 184]. Taken from [185].

will be able to collect data at high rate and thus collect a large sample of Au+Au collisions at $\sqrt{s_{\mathrm{NN}}} = 200\,\mathrm{GeV}$. Figure 6.2 shows the projection of statistical uncertainties of the Λ_c/D^0 yield ratio for the sPHENIX variant with PID equivalent to STAR TOF detector and for the variant with no PID at all. The projections are compared to theoretical calculations described in Chapter 5 which shows that the sPHENIX will have excellent rejection capability to select more realistic theoretical models.

Bibliography

[1] L. Greiner *et al.*, "*A MAPS based vertex detector for the STAR experiment at RHIC*", Nucl. Inst. Meth. A **650**, 68 (2011).

[2] E. Anderssen *et al.*, "*HFT proposal*", `http://rnc.lbl.gov/~wieman/hft_final_submission_version.pdf`.

[3] D. Beavis *et al.*, "*The HFT Technical Design report*", (2011), `https://drupal.star.bnl.gov/STAR/starnotes/public/sn0600`.

[4] R. Brun, F. Bruyant, M. Maire, A. C. McPherson, and P. Zanarini, *GEANT 3: user's guide Geant 3.10, Geant 3.11; rev. version* (CERN, Geneva, 1987).

[5] J. Kvapil, "*Study of the properties of charm mesons with HFT detector*", Research Project, Czech Technical University in Prague (2016).

[6] C. Adler *et al.*, "*The RHIC zero-degree calorimeters*", Nucl. Inst. Meth. A **499**, 433 (2003).

[7] H. Crawford *et al.*, "*Proposed Addition of a Shower Max Detector to the STAR Zero Degree Calorimeters*", (2003), `https://drupal.star.bnl.gov/STAR/system/files/ZDC-SMD.pdf` (cited on February 16, 2021).

[8] L. Kramarik and M. Simko, "*Zero Degree Calorimeter Operator's Manual*", (2017), `http://www.star.bnl.gov/~msimko/ZDCopsManual.pdf`.

[9] STAR Collaboration, J. Adam *et al.*, "*First Measurement of* Λ_c *Baryon Production in* $\mathrm{Au}+\mathrm{Au}$ *Collisions at* $\sqrt{s_{NN}} = 200\,\mathrm{GeV}$", Phys. Rev. Lett. **124**, 172301 (2020).

[10] M. Simko, "*Heavy-flavor-triplets mixed-event background estimation code*", `https://github.com/mirsimko/mixedEventTripletMaker` (cited on February 14, 2021).

[11] M. Gyulassy, "*The QGP Discovered at RHIC*", arXiv:0403032[nucl-th] (2004).

[12] "*Figure: Standard model of elementary particles*", `https://upload.wikimedia.org/wikipedia/commons/0/00/Standard_Model_of_Elementary_Particles.svg` (cited on September 22, 2020).

[13] J. J. Aubert *et al.*, "*Experimental Observation of a Heavy Particle J*", Phys. Rev. Lett. **33**, 1404 (1974).

[14] J. E. Augustin *et al.*, "*Discovery of a Narrow Resonance in e^+e^- Annihilation*", Phys. Rev. Lett. **33**, 1406 (1974).

[15] Nobel Media AB 2021, "*Nobel prize 1976 press release*", NobelPrize.org , `https://www.nobelprize.org/prizes/physics/1976/press-release/` (cited on February 14, 2021).

[16] M. Kobayashi and T. Maskawa, "*CP-Violation in the Renormalizable Theory of Weak Interaction*", Prog. Theor. Phys. **49**, 652 (1973).

[17] S. W. Herb *et al.*, "*Observation of a Dimuon Resonance at 9.5 GeV in 400-GeV Proton-Nucleus Collisions*", Phys. Rev. Lett. **39**, 252 (1977).

[18] D0 Collaboration, S. Abachi *et al.*, "*Search for High Mass Top Quark Production in $p\overline{p}$ Collisions at $\sqrt{s} = 1.8$ TeV*", Phys. Rev. Lett. **74**, 2422 (1995).

[19] J. Bulava, K. Jansen, and A. Nagy, "*Constraining a fourth generation of quarks: Non-perturbative Higgs boson mass bounds*", Phys. Lett. B **723**, 95 (2013).

[20] O. Eberhardt *et al.*, "*Impact of a Higgs Boson at a Mass of 126 GeV on the Standard Model with Three and Four Fermion Generations*", Phys. Rev. Lett. **109**, 241802 (2012).

[21] J. Thomson, Cathode rays, the electrician, vol. 39, no. 104, also published in, in *Proceedings of the Royal Institution* Vol. 30, pp. 1–14, 1897.

[22] C. D. Anderson, "*The apparent existence of easily deflectable positives*", Science **76**, 238 (1932).

[23] C. D. Anderson and S. H. Neddermeyer, "*Cloud Chamber Observations of Cosmic Rays at 4300 Meters Elevation and Near Sea-Level*", Phys. Rev. **50**, 263 (1936).

[24] C. Lattes, H. Muirhead, G. Occhialini, and C. Powell, "*Processes involving charged mesons*", Nature **159**, 694 (1947).

[25] Particle Data Group, C. Patrignani *et al.*, "*Review of Particle Physics*", Chin. Phys. **C40**, 100001 (2016).

[26] W. Bacino *et al.*, "*Measurement of the Threshold Behavior of $\tau^+\tau^-$ Production in e^+e^- Annihilation*", Phys. Rev. Lett. **41**, 13 (1978).

[27] F. REINES and C. L. Cowan jun., "*The Neutrino*", Nature **178**, 446 (1956).

[28] J. Ellis, M. K. Gaillard, and G. G. Ross, "*Search for gluons in e+e− annihilation*", Nucl. Phys. B **111**, 253 (1976).

[29] G. Arnison *et al.*, "*Experimental observation of isolated large transverse energy electrons with associated missing energy at $\sqrt{s}$ = 540 GeV*", Phys. Lett. B **122**, 103 (1983).

[30] M. Banner *et al.*, "*Observation of single isolated electrons of high transverse momentum in events with missing transverse energy at the CERN pp collider*", Phys. Lett. B **122**, 476 (1983).

[31] M. Holder *et al.*, "*Measurement of the neutral to charged current cross section ratio in neutrino and antineutrino interactions*", Phys. Lett. B **71**, 222 (1977).

[32] G. Aad *et al.*, "*Observation of a new particle in the search for the Standard Model Higgs boson with the ATLAS detector at the LHC*", Phys. Lett. B **716**, 1 (2012).

[33] S. Chatrchyan *et al.*, "*Observation of a new boson at a mass of 125 GeV with the CMS experiment at the LHC*", Phys. Lett. B **716**, 30 (2012).

[34] CMS Collaboration, A. Sirunyan *et al.*, "*A measurement of the Higgs boson mass in the diphoton decay channel*", Phys. Lett. B **805**, 135425 (2020).

[35] G. 't Hooft and M. Veltman, "*Regularization and renormalization of gauge fields*", Nucl. Phys. B **44**, 189 (1972).

[36] C. Bollini and G. Giambiagi, "*Dimensional Renormalization: The Number of Dimensions as a Regularizing Parameter*", Il Nuovo Cimento **12B**, 20 (1972).

[37] B. Andersson, G. Gustafson, G. Ingelman, and T. Sjöstrand, "*Parton fragmentation and string dynamics*", Phys. Rep. **97**, 31 (1983).

[38] R. Pasechnik and M. Šumbera, "*Phenomenological Review on Quark–Gluon Plasma: Concepts vs. Observations*", Universe **3**, 7 (2017).

[39] STAR Collaboration, J. Adam *et al.*, "*RHIC Beam Use Request For Runs 18 and 19*", (2017), `https://drupal.star.bnl.gov/STAR/system/files/star-beam-request-2017_0.pdf`.

[40] "*FAIR home page*", `https://fair-center.eu` (cited on February 16, 2021).

[41] H. Caines, "*What's interesting about strangeness production? An overview of recent results*", J. Phys. G **31**, S101 (2005).

[42] ALICE Collaboration, B. Abelev *et al.*, "*Pion, Kaon, and Proton Production in Central Pb-Pb Collisions at* $\sqrt{s_{\mathrm{NN}}} = 2.76$ *TeV*", Phys. Rev. Lett. **109**, 252301 (2012).

[43] STAR Collaboration, B. I. Abelev *et al.*, "*Systematic measurements of identified particle spectra in pp,* $d + \mathrm{Au}$*, and* $\mathrm{Au} + \mathrm{Au}$ *collisions at the STAR detector*", Phys. Rev. C **79**, 034909 (2009).

[44] PHENIX Collaboration, "*The PHENIX Experiment at RHIC Decadal Plan 2011–2020*", `https://www.bnl.gov/npp/docs/pac0611/akiba_Phenix_Decadal_Plan_YA_final.pdf` (cited on December 8, 2020).

[45] B. Abelev *et al.*, "*Energy dependence of $\pi^{\pm}$, p and p^{-} transverse momentum spectra for Au+Au collisions at $\sqrt{s_{\mathrm{NN}}} = 62.4$ and 200 GeV*", Phys. Lett. B **655**, 104 (2007).

[46] A. K. Dutt-Mazumder, J.-e. Alam, P. Roy, and B. Sinha, "*Stopping power of hot QCD plasma*", Phys. Rev. D **71**, 094016 (2005).

[47] X.-N. Wang, "*Energy dependence of jet quenching and lifetime of dense matter in high-energy heavy-ion collisions*", Phys. Rev. C **70**, 031901 (2004).

[48] I. Vitev and M. Gyulassy, "*High-p_T Tomography of d+Au and Au+Au at SPS, RHIC, and LHC*", Phys. Rev. Lett. **89**, 252301 (2002).

[49] ATLAS Collaboration, G. Aad *et al.*, "*Measurement of the azimuthal anisotropy for charged particle production in $\sqrt{s_{NN}} = 2.76$ TeV lead-lead collisions with the ATLAS detector*", Phys. Rev. C **86**, 014907 (2012).

[50] STAR Collaboration, B. I. Abelev *et al.*, "*Centrality dependence of charged hadron and strange hadron elliptic flow from $\sqrt{s_{NN}} = 200$ GeV Au+Au collisions*", Phys. Rev. C **77**, 054901 (2008).

[51] PHENIX Collaboration, A. Adare *et al.*, "*Scaling Properties of Azimuthal Anisotropy in Au+Au and Cu+Cu Collisions at $\sqrt{s_{\mathrm{NN}}} = 200$ GeV*", Phys. Rev. Lett. **98**, 162301 (2007).

[52] P. Huovinen and P. Ruuskanen, "*Hydrodynamic Models for Heavy Ion Collisions*", Annual Review of Nuclear and Particle Science **56**, 163 (2006).

[53] B. Abelev *et al.*, "*Elliptic flow of identified hadrons in Pb–Pb collisions at $\sqrt{s_{\mathrm{NN}}} = 2.76$ TeV*", J. High Energy Phys. **2015**, 190 (2015).

[54] STAR Collaboration, J. Adams *et al.*, "*Evidence from* $d+\mathrm{Au}$ *Measurements for Final-State Suppression of High-*p_T *Hadrons in* $\mathrm{Au}+\mathrm{Au}$ *Collisions at RHIC*", Phys. Rev. Lett. **91**, 072304 (2003).

[55] I. Vitev and B.-W. Zhang, "*Jet Tomography of High-Energy Nucleus-Nucleus Collisions at Next-to-Leading Order*", Phys. Rev. Lett. **104**, 132001 (2010).

[56] Y.-T. Chien and I. Vitev, "*Towards the understanding of jet shapes and cross sections in heavy ion collisions using soft-collinear effective theory*", J. High Energy Phys. **2016**, 23 (2016).

[57] Y.-T. Chien, A. Emerman, Z.-B. Kang, G. Ovanesyan, and I. Vitev, "*Jet quenching from QCD evolution*", Phys. Rev. D **93**, 074030 (2016).

[58] J. Casalderrey-Solana, D. C. Gulhan, J. G. Milhano, D. Pablos, and K. Rajagopal, "*Angular structure of jet quenching within a hybrid strong/weak coupling model*", J. High Energy Phys. **2017**, 135 (2017).

[59] Y. He, T. Luo, X.-N. Wang, and Y. Zhu, "*Linear Boltzmann transport for jet propagation in the quark-gluon plasma: Elastic processes and medium recoil*", Phys. Rev. C **91**, 054908 (2015).

[60] Y. He *et al.*, "*Interplaying mechanisms behind single inclusive jet suppression in heavy-ion collisions*", Phys. Rev. C **99**, 054911 (2019).

[61] STAR Collaboration, J. Adam *et al.*, "*Measurement of inclusive charged-particle jet production in Au + Au collisions at* $\sqrt{s_{NN}} = 200$ *GeV*", Phys. Rev. C **102**, 054913 (2020).

[62] T. Sjöstrand, S. Mrenna, and P. Skands, "*PYTHIA 6.4 physics and manual*", J. High Energy Phys. **2006**, 026 (2006).

[63] A. Andronic *et al.*, "*Heavy-flavour and quarkonium production in the LHC era: from proton–proton to heavy-ion collisions*", Eur. Phys. J. C **76**, 107 (2016).

[64] F. Prino and R. Rapp, "*Open heavy flavor in QCD matter and in nuclear collisions*", J. Phys. G: Nucl. Part. Phys. **43**, 093002 (2016).

[65] D. Banerjee, S. Datta, R. Gavai, and P. Majumdar, "*Heavy quark momentum diffusion coefficient from lattice QCD*", Phys. Rev. D **85**, 014510 (2012).

[66] H.-T. Ding *et al.*, "*Charmonium properties in hot quenched lattice QCD*", Phys. Rev. D **86**, 014509 (2012).

[67] F. Riek and R. Rapp, "*Quarkonia and heavy-quark relaxation times in the quark-gluon plasma*", Phys. Rev. C **82**, 035201 (2010).

[68] M. He, R. J. Fries, and R. Rapp, "*Thermal relaxation of charm in hadronic matter*", Phys. Lett. B **701**, 445 (2011).

[69] G. D. Moore and D. Teaney, "*How much do heavy quarks thermalize in a heavy ion collision?*", Phys. Rev. C **71**, 064904 (2005).

[70] R. C. Hwa and X.-N. Wang, *Quark-Gluon Plasma 4* (WORLD SCIENTIFIC, 2010).

[71] P. Langevin, "*Sur la theorie du mouvement brownien*", C. R. Acad. Sci. **146**, 530 (1908).

[72] D. S. Lemons and A. Gythiel, "*Paul Langevin's 1908 paper "On the Theory of Brownian Motion" ["Sur la théorie du mouvement brownien," C. R. Acad. Sci. (Paris) 146, 530–533 (1908)]*", Am. J. Phys. **65**, 1079 (1997).

[73] STAR Collaboration, G. Agakishiev *et al.*, "*Strangeness Enhancement in Cu-Cu and Au-Au Collisions at* $\sqrt{s_{NN}} = 200\,\mathrm{GeV}$", Phys. Rev. Lett. **108**, 072301 (2012).

[74] ALICE Collaboration, B. Abelev *et al.*, "K^0_S *and* Λ *Production in Pb-Pb Collisions at* $\sqrt{s_{NN}} = 2.76\,\mathrm{TeV}$", Phys. Rev. Lett. **111**, 222301 (2013).

[75] A. Bialas, "*Quark model and strange baryon production in heavy ion collisions*", Phys. Lett. B **442**, 449 (1998).

[76] J. Zimányi, T. Biró, T. Csörgő, and P. Lévai, "*Quark liberation and coalescence at CERN SPS*", Phys. Lett. B **472**, 243 (2000).

[77] G. Xie for the STAR collaboration, "Λ_c *Production in Au+Au Collisions at* $\sqrt{s_{NN}} =$ *200 GeV measured by the STAR experiment*", arXiv:1704.04353 [nucl-ex] (2017).

[78] Y. Oh, C. M. Ko, S. H. Lee, and S. Yasui, "*Ratios of heavy baryons to heavy mesons in relativistic nucleus-nucleus collisions*", Phys. Rev. C **79**, 044905 (2009).

[79] S. Ghosh, S. K. Das, V. Greco, S. Sarkar, and J.-e. Alam, "*Diffusion of* Λ_c *in hot hadronic medium and its impact on* Λ_c/D *ratio*", Phys. Rev. D **90**, 054018 (2014).

[80] S. H. Lee, K. Ohnishi, S. Yasui, I.-K. Yoo, and C. M. Ko, "Λ_c", Phys. Rev. Lett. **100**, 222301 (2008).

[81] V. Greco, C. Ko, and R. Rapp, "*Quark coalescence for charmed mesons in ultrarelativistic heavy-ion collisions*", Phys. Lett. B **595**, 202 (2004).

[82] H. van Hees, M. Mannarelli, V. Greco, and R. Rapp, "*Nonperturbative Heavy-Quark Diffusion in the Quark-Gluon Plasma*", Phys. Rev. Lett. **100**, 192301 (2008).

[83] STAR Collaboration, J. Adams *et al.*, "*Strange antiparticle-to-particle ratios at mid-rapidity in* $\sqrt{s_{\rm NN}} = 130$ *GeV Au+Au collisions*", Phys. Lett. B **567**, 167 (2003).

[84] D. Tlustý and the Star collaboration, "*Open charm measurements in p+p collisions at STAR*", J. Phys. Conf. **509**, 012078 (2014).

[85] M. Cacciari, P. Nason, and R. Vogt, "*QCD Predictions for Charm and Bottom Quark Production at RHIC*", Phys. Rev. Lett. **95**, 122001 (2005).

[86] G. Xie for the STAR collaboration, "*Nuclear Modification Factor of* D^0 *Meson in Au+Au Collisions at* $\sqrt{s_{\rm NN}} = 200$ *GeV*", Nucl. Phys. A **956**, 473 (2016).

[87] STAR Collaboration, B. Abelev *et al.*, "*Measurement of charm production at central rapidity in proton-proton collisions at* $\sqrt{s} = 7$ *TeV*", J. High Energy Phys. **2012**, 128 (2012).

[88] CDF Collaboration, D. Acosta *et al.*, "*Measurement of prompt charm meson production cross sections in $p\bar{p}$ collisions at $\sqrt{s} = 1.96$ TeV*", Phys. Rev. Lett. **91**, 241804 (2003).

[89] STAR Collaboration, L. Adamczyk *et al.*, "*Measurements of D^0 and D^* production in p+p collisions at $\sqrt{s}$*=200 GeV", Phys. Rev. D **86**, 072013 (2012).

[90] STAR Collaboration, J. Adam *et al.*, "*Centrality and transverse momentum dependence of D^0-meson production at mid-rapidity in Au + Au collisions at $\sqrt{s_{NN}} = 200$ GeV*", Phys. Rev. C **99**, 034908 (2019).

[91] STAR Collaboration, L. Adamczyk *et al.*, "*Observation of D^0 Meson Nuclear Modifications in* Au + Au *Collisions at* $\sqrt{s_{\rm NN}} = 200$ GeV", Phys. Rev. Lett. **113**, 142301 (2014).

[92] S. Cao, G.-Y. Qin, and S. A. Bass, "*Heavy-quark dynamics and hadronization in ultrarelativistic heavy-ion collisions: Collisional versus radiative energy loss*", Phys. Rev. C **88**, 044907 (2013).

[93] S. Cao, G.-Y. Qin, and S. A. Bass, "*Energy loss, hadronization, and hadronic interactions of heavy flavors in relativistic heavy-ion collisions*", Phys. Rev. C **92**, 024907 (2015), and private communication.

[94] S. Cao, T. Luo, G.-Y. Qin, and X.-N. Wang, "*Linearized Boltzmann transport model for jet propagation in the quark-gluon plasma: Heavy quark evolution*", Phys. Rev. C **94**, 014909 (2016).

[95] S. Cao, T. Luo, G.-Y. Qin, and X.-N. Wang, Private communication .

[96] J. Vanek for the STAR Collaboration, "*Production of $D^{\pm}$ mesons in Au+Au collisions at $\sqrt{s_{NN}}$ = 200 GeV measured by the STAR experiment*", Poster at ICHEP2020 (2020).

[97] STAR Collaboration, L. Adamczyk *et al.*, "*Measurement of D^0 Azimuthal Anisotropy at Midrapidity in* Au + Au *Collisions at* $\sqrt{s_{NN}} = 200$ GeV", Phys. Rev. Lett. **118**, 212301 (2017).

[98] H. Berrehrah *et al.*, "*Transport coefficients of heavy quarks around T_c at finite quark chemical potential*", Phys. Rev. C **90**, 051901 (2014).

[99] M. He, R. J. Fries, and R. Rapp, "*Heavy-quark diffusion and hadronization in quark-gluon plasma*", Phys. Rev. C **86**, 014903 (2012).

[100] T. Song *et al.*, "*Tomography of the quark-gluon plasma by charm quarks*", Phys. Rev. C **92**, 014910 (2015).

[101] M. Nahrgang, J. Aichelin, S. Bass, P. B. Gossiaux, and K. Werner, "*Elliptic and triangular flow of heavy flavor in heavy-ion collisions*", Phys. Rev. C **91**, 014904 (2015).

[102] H. Berrehrah, E. Bratkovskaya, W. Cassing, P. B. Gossiaux, and J. Aichelin, "*Heavy quark scattering and quenching in a QCD medium at finite temperature and chemical potential*", Phys. Rev. C **91**, 054902 (2015).

[103] L. Pang, Q. Wang, and X.-N. Wang, "*Effects of initial flow velocity fluctuation in event-by-event (3+1)D hydrodynamics*", Phys. Rev. C **86**, 024911 (2012).

[104] L.-G. Pang, Y. Hatta, X.-N. Wang, and B.-W. Xiao, "*Analytical and numerical Gubser solutions of the second-order hydrodynamics*", Phys. Rev. D **91**, 074027 (2015), and private communication.

[105] O. Kaczmarek, "*Continuum estimate of the heavy quark momentum diffusion coefficient κ*", Nucl. Phys. A **931**, 633 (2014).

[106] B. Svetitsky, "*Diffusion of charmed quarks in the quark-gluon plasma*", Phys. Rev. D **37**, 2484 (1988).

[107] A. Andronic, P. Braun-Munzinger, K. Redlich, and J. Stachel, "*Statistical hadronization of charm in heavy-ion collisions at SPS, RHIC and LHC*", Phys. Lett. B **571**, 36 (2003).

[108] STAR Collaboration, J. Adam *et al.*, "*Observation of $D_s^{\pm}/D^0$ enhancement in Au+Au collisions at $\sqrt{s_{\rm NN}}$ = 200 GeV*", (2021), arXiv:2101.11793[hep-ex].

[109] ALICE Collaboration, S. Acharya *et al.*, "*Measurement of D^0, D^+, D^{*+} and D_s^+ production in Pb-Pb collisions at $\sqrt{s_{NN}} = 5.02$ TeV*", J. High Energy Phys. **10**, 174 (2018).

[110] ALICE Collaboration, S. Acharya *et al.*, "*Measurement of D-meson production at mid-rapidity in pp collisions at $\sqrt{s} = 7$ TeV*", Eur. Phys. J. C **77**, 550 (2017).

[111] D. Tlusty, "*A Study of Open Charm Production in p+p Collisions at STAR*", Ph.D. Thesis, Czech Technical University in Prague (2014).

[112] J. Zhao, S. Shi, N. Xu, and P. Zhuang, "*Sequential Coalescence with Charm Conservation in High Energy Nuclear Collisions*", arXiv:1805.10858 [hep-ph] .

[113] S. Plumari, V. Minissale, S. K. Das, G. Coci, and V. Greco, "*Charmed hadrons from coalescence plus fragmentation in relativistic nucleus-nucleus collisions at RHIC and LHC*", Eur. Phys. J. C **78**, 348 (2018).

[114] M. He and R. Rapp, "*Hadronization and Charm-Hadron Ratios in Heavy-Ion Collisions*", Phys. Rev. Lett. **124**, 042301 (2020).

[115] S. Cao *et al.*, "*Charmed hadron chemistry in relativistic heavy-ion collisions*", Phys. Lett. B **807**, 135561 (2020).

[116] CLEO Collaboration, P. Avery *et al.*, "*Inclusive production of the charmed baryon $\Lambda_c{}^+$ from e^+e^- annihilations at $\sqrt{s} = 10.55$ GeV*", Phys. Rev. D **43**, 3599 (1991).

[117] H. Albrecht *et al.*, "*Observation of the charmed baryon Λ_c in e^+e^- annihilation at 10 GeV*", Phys. Lett. B **207**, 109 (1988).

[118] ARGUS Collaboration, H. Albrecht *et al.*, "*Inclusive production of D^0,D^+ and $D^{*+}(2010)$ mesons in B decays and nonresonant $e^+ + e^-$ annihilation at 10.6 GeV*", Zeitschrift für Physik C **52**, 353 (1991).

[119] L. Gladilin, "*Fragmentation fractions of c and b quarks into charmed hadrons at LEP*", Eur. Phys. J. C **75**, 19 (2015).

[120] The ZEUS Collaboration, H. Abramowicz *et al.*, "*Measurement of D^+ and Λ_c^+ production in deep inelastic scattering at HERA*", J. High Energy Phys. **2010**, 9 (2010).

[121] The ZEUS Collaboration, "*Measurement of charm fragmentation ratios and fractionsin photoproduction at HERA*", Eur. Phys. J. C **44**, 351 (2005).

[122] The ZEUS Collaboration, H. Abramowicz *et al.*, "*Measurement of charm fragmentation fractions in photoproduction at HERA*", J. High Energy Phys. **2013**, 58 (2013).

[123] K. Aamodt *et al.*, "*The ALICE experiment at the CERN LHC*", J. Inst. **3**, S08002 (2008).

[124] A. A. Alves *et al.*, "*The LHCb Detector at the LHC*", J. Inst. **3**, S08005 (2008).

[125] LHCb Collaboration, Report No. CERN-LHCC-2013-021. LHCB-TDR-013, 2013 (unpublished).

[126] ALICE Collaboration, S. Acharya *et al.*, "Λ_c^+ *production in pp collisions at* $\sqrt{s} = 7$ *TeV and in p–Pb collisions at* $\sqrt{s_{\rm NN}} = 5.02$ *TeV*", J. High Energy Phys. **04**, 108 (2018).

[127] R. Aaij *et al.*, "*Prompt charm production in pp collisions at* $\sqrt{s} = 7$ *TeV*", Nucl. Phys. B **871**, 1 (2013).

[128] LHCb Collaboration, P. Spratlin *et al.*, "*Private Communication*".

[129] J. R. Christiansen and P. Z. Skands, "*String formation beyond leading colour*", J. High Energy Phys. **2015**, 3 (2015).

[130] C. Bierlich and J. R. Christiansen, "*Effects of color reconnection on hadron flavor observables*", Phys. Rev. D **92**, 094010 (2015).

[131] M. Bähr *et al.*, "*Herwig++ physics and manual*", Eur. Phys. J. C **58**, 639 (2008).

[132] J.-P. Lansberg and H.-S. Shao, "*Towards an automated tool to evaluate the impact of the nuclear modification of the gluon density on quarkonium, D and B meson production in proton–nucleus collisions*", Eur. Phys. J. C **77**, 1 (2016).

[133] ALICE Collaboration, S. Acharya *et al.*, "Λ_c^+ *production in Pb–Pb collisions at* $\sqrt{s_{\rm NN}} = 5.02$ *TeV*", Phys. Lett. B **793**, 212 (2019).

[134] S. K. Das *et al.*, "*Propagation of heavy baryons in heavy-ion collisions*", Phys. Rev. D **94**, 114039 (2016).

[135] H.-h. Li, F.-l. Shao, J. Song, and R.-q. Wang, "*Production of single-charm hadrons by the quark-combination mechanism in p-Pb collisions at* $\sqrt{s_{NN}} = 5.02$ *TeV*", Phys. Rev. C **97**, 064915 (2018).

[136] J. Song, H.-h. Li, and F.-l. Shao, "*New feature of low* p_T *charm quark hadronization in pp collisions at* $\sqrt{s} = 7$ *TeV*", Eur. Phys. J. C **78**, 344 (2018).

[137] ALICE Collaboration, "*Measurement of* D^0*,* D^+*,* D^{*+} *and* D_s^+ *production in Pb-Pb collisions at* $\sqrt{s_{NN}} = 5.02$ *TeV*", J. High Energy Phys. **2018**, 174 (2018).

[138] ALICE Collaboration, "*Transverse momentum spectra and nuclear modification factors of charged particles in pp, p-Pb and Pb-Pb collisions at the LHC*", J. High Energy Phys. **2018**, 13 (2018).

[139] The LHCb Collaboration, "*Precision luminosity measurements at LHCb*", J. Inst. **9**, P12005 (2014).

[140] E. Maurice on behalf of the LHCb collaboration, "*New high resolution measurements of open and hidden charm production in proton-nucleus collisions at* $\sqrt{s}$ *= 110 GeV with LHCb*", Presentation: QUARK MATTER XXIV (2017).

[141] L. Musa, "*Conceptual Design Report for the Upgrade of the ALICE ITS*", CERN-LHCC-2012-005. LHCC-G-159 (2012).

[142] PHENIX Collaboration, A. Adare *et al.*, "*An Upgrade Proposal from the PHENIX Collaboration*", (2015), arXiv:1501.06197[nucl-ex].

[143] W. Fischer, "*Run overview of the Relativistic Heavy Ion Collider*", `http://www.agsrhichome.bnl.gov/RHIC/Runs/` (cited on February 15, 2021).

[144] M. Harrison, T. Ludlam, and S. Ozaki, "*RHIC project overview*", Nucl. Inst. Meth. A **499**, 235 (2003).

[145] H. Hahn *et al.*, "*The RHIC design overview*", Nucl. Inst. Meth. A **499**, 245 (2003).

[146] K. C. Meehan, "*Fixed Target Collisions at STAR*", Nucl. Phys. A **956**, 878 (2016), Quark Matter XXV.

[147] I. Alekseev *et al.*, "*Polarized proton collider at RHIC*", Nucl. Inst. Meth. A **499**, 392 (2003).

[148] J. G. Alessi *et al.*, "*The Brookhaven National Laboratory electron beam ion source for RHIC*", Rev. Sci. Instrum. **81**, 02A509 (2010).

[149] "*RHIC official web site*", `https://www.bnl.gov/rhic/` (cited on October 16, 2018).

[150] N. Tsoupas *et al.*, "*BNL alternating gradient synchrotron with four helical magnets to minimize the losses of the polarized proton beam*", Phys. Rev. ST Accel. Beams **16**, 043501 (2013).

[151] W. MacKay, L. Ahrens, M. Bennan, and K. Brown, "*AGS to RHIC transfer line: Design and commissioning*", Upton, New York (1996).

[152] STAR Collaboration, K. H. Ackermann *et al.*, "*STAR detector overview*", Nucl. Inst. Meth. A **499**, 624 (2003).

[153] M. Anderson *et al.*, "*The STAR time projection chamber: a unique tool for studying high multiplicity events at RHIC*", Nucl. Inst. Meth. A **499**, 659 (2003).

[154] J. Abele *et al.*, "*The laser system for the STAR time projection chamber*", Nucl. Inst. Meth. A **499**, 692 (2003).

[155] STAR Collaboration, L. Adamczyk *et al.*, "*A Proposal for STAR Inner TPC Sector Upgrade (iTPC)*", (2015), `https://drupal.star.bnl.gov/STAR/system/files/STAR_iTPC_proposal_06_09_2015.pdf`.

[156] The STAR TOF Collaboration, B. Bonner *et al.*, "*Proposal for a Large Area Time of Flight System for STAR*", (2004).

[157] E. C. Zeballos *et al.*, "*A new type of resistive plate chamber: The multigap RPC*", Nucl. Inst. Meth. A **374**, 132 (1996).

[158] D. Hu *et al.*, "*MRPC3b mass production for CBM-TOF and eTOF at STAR*", arXiv:1807.02452 [physics.ins-det] (2018).

[159] J. M. Heuser, "*The Compressed Baryonic Matter Experiment at FAIR: Progress with feasibility studies and detector developments*", Nucl. Phys. A **830**, 563c (2009), Quark Matter XXI.

[160] STAR and CBM Collaborations, "*eTOF Letter of Interest*", `https://drupal.star.bnl.gov/STAR/files/CBM_STAR_LOI_September_30_2015_0.pdf` (cited on June 12, 2019).

[161] W. Snoeys, "*CMOS monolithic active pixel sensors for high energy physics*", Nucl. Inst. Meth. A **765**, 167 (2014), HSTD-9 2013 - Proceedings of the 9th International "Hiroshima" Symposium on Development and Application of Semiconductor Tracking Detectors.

[162] A. Besson, "*A MAPS digitiser, Building a digitiser algorithm for CMOS/MAPS sensors with analog or digital output*", `http://phys.kent.edu/~smargeti/STAR/HFT/Simulators/digmaps_note_auguste_besson.pdf` (cited on June 16, 2019).

[163] L. Landau, "*On the energy loss of fast particles by ionization*", J. Phys.(USSR) **8**, 201 (1944).

[164] Y.-F. Xu *et al.*, "*Physics performance of the STAR zero degree calorimeter at relativistic heavy ion collider*", Nucl. Sci. Tech. **27**, 126 (2016).

[165] Y. Zhu, "*ZDC Testing, Electronics Layout and Result Analysis*", `https://drupal.star.bnl.gov/STAR/system/files/ZDC_Document_20101005.pdf` (cited on February 7, 2017).

[166] M. Simko, L. Kramarik, J. Vanek, L. C. Bland, and Z. Xu, "*Test of ZDC PMTs and possible spares from Brahms*", `https://docs.google.com/spreadsheets/d/1E0_PEfIwpkxFE8akk1zveQZgpWWD2qElOYhLvDSjPkg/edit?usp=sharing` (cited on June 11, 2019).

[167] W. Llope *et al.*, "*The STAR Vertex Position Detector*", Nucl. Inst. Meth. A **759**, 23 (2014).

[168] STAR Collaboration, "*The STAR Forward Calorimeter System and Forward Tracking System*", Proposal (2017), `https://drupal.star.bnl.gov/STAR/starnotes/public/sn0648` (cited on February 15, 2021).

[169] Y. Shi, C. Yang, and Q. Yang, "*The sTGC prototyping and performance test for the STAR forward upgrade*", J. Inst. **15**, C09021 (2020).

[170] A. Abusleme *et al.*, "*Performance of a Full-Size Small-Strip Thin Gap Chamber Prototype for the ATLAS New Small Wheel Muon Upgrade*", Nucl. Instrum. Meth. A **817**, 85 (2016).

[171] L. Aphecetche *et al.*, "*PHENIX calorimeter*", Nucl. Inst. Meth. A **499**, 521 (2003), The Relativistic Heavy Ion Collider Project: RHIC and its Detectors.

[172] STAR Collaboration, C. Adler *et al.*, "*Centrality Dependence of High-p_T Hadron Suppression in* Au + Au *Collisions at* $\sqrt{s_{NN}} = 130\,\mathrm{GeV}$", Phys. Rev. Lett. **89**, 202301 (2002).

[173] H. Masui, "*Glauber Monte Carlo simulation in heavy ion collisions*", `https://drupal.star.bnl.gov/STAR/system/files/masui_glaubermc_Jun16_2008.pdf` (cited on July 6, 2019).

[174] A. Hoecker *et al.*, "*TMVA: Toolkit for Multivariate Data Analysis*", PoS **ACAT**, 040 (2007).

[175] M. Gyulassy and X.-N. Wang, "*HIJING 1.0: A Monte Carlo program for parton and particle production in high energy hadronic and nuclear collisions*", Comput. Phys. Commun. **83**, 307 (1994).

[176] A. Ryd *et al.*, "*EvtGen – A Monte Carlo Generator for B-Physics*", `https://evtgen.hepforge.org/doc/EvtGenGuide.pdf` (cited on May 16, 2019).

[177] T. Sjöstrand *et al.*, "*An introduction to PYTHIA 8.2*", Comput. Phys. Commun. **191**, 159 (2015).

[178] V. Greco, C. Ko, and R. Rapp, "*Quark coalescence for charmed mesons in ultrarelativistic heavy-ion collisions*", Phys. Lett. B **595**, 202 (2004).

[179] R. Aaij *et al.*, "*Study of the production of and hadrons in pp collisions and first measurement of the branching fraction*", Chin. Phys. C **40**, 011001 (2016).

[180] S. Wheaton, J. Cleymans, and M. Hauer, "*THERMUS—A thermal model package for ROOT*", Comput. Phys. Commun. **180**, 84 (2009).

[181] STAR Collaboration, B. I. Abelev *et al.*, "*Identified Baryon and Meson Distributions at Large Transverse Momenta from* Au + Au *Collisions at* $\sqrt{s_{NN}} = 200\,\text{GeV}$", Phys. Rev. Lett. **97**, 152301 (2006).

[182] P. Skands, S. Carrazza, and J. Rojo, "*Tuning PYTHIA 8.1: the Monash 2013 tune*", Eur. Phys. J. C **74**, 3024 (2014).

[183] S. Cho, K.-J. Sun, C. M. Ko, S. H. Lee, and Y. Oh, "*Charmed hadron production in an improved quark coalescence model*", Phys. Rev. C **101**, 024909 (2020).

[184] S. Plumari, V. Minissale, S. K. Das, G. Coci, and V. Greco, "*Charmed hadrons from coalescence plus fragmentation in relativistic nucleus–nucleus collisions at RHIC and LHC*", Eur. Phys. J. C **78**, 348.

[185] Y. Ji for the sPHENIX collaboration, "*sPHENIX capabilities for measuring* Λ_c *production in Au+Au collisions*", Hard Probes 2020 (2020).

[186] M. C. Llatas *et al.*, "*A Monolithic-Active-Pixel-Sensor-based Vertex Detector (MVTX) for the sPHENIX Experiment at RHIC*", A proposal submitted to the DOE Office of Science , available at `https://indico.bnl.gov/event/4072/attachments/11335/13816/sPH-HF-2018-001-final.pdf` (cited on February 15, 2021).

[187] M. Simko for the STAR Collaboration, "*Measurements of open charm hadrons at the STAR experiment*", J. Phys. Conf. **832**, 012028 (2017).

[188] M. Simko for the STAR Collaboration, "*Measurements of open charm hadrons in Au+Au collisions at the STAR experiment*", PoS **EPS-HEP2017**, 194 (2017).

Appendices

Appendix A

Papers, proceedings, and posters

The following pages contain full texts of published proceedings and posters presented during the period of my Ph.D. studies.

1. M. Simko for the STAR collaboration, *"Simulations for Heavy Flavor Tracker–Pixel Detector"*, Poster at Vertex2014 (2014).

2. M. Simko for the STAR collaboration, *"Λ_c baryon production in Au+Au collisions at $\sqrt{s_{NN}} = 200\ GeV$"*, Poster at Quark Matter 2015 (2015).

3. M. Simko for the STAR collaboration, *"Λ_c baryon production in Au+Au collisions at $\sqrt{s_{NN}} = 200\ GeV$"*, Poster at European School of High-Energy Physics 2016 (2016).

4. M. Simko for the STAR Collaboration, "Measurements of open charm hadrons at the STAR experiment", Journal of Physics: Conference Series **832**, 012028 (2017), [187].

5. M. Simko for the STAR Collaboration, *"Measurements of open charm hadrons in Au+Au collisions at the STAR experiment"*, PoS **EPS-HEP2017**, 194 (2017), [188].

6. M. Simko for the STAR collaboration, *"Measurement of $\overline{\Lambda_c}^- / \Lambda_c^+$ ratio in Au+Au collisions at $\sqrt{s_{NN}} = 200\ GeV$ with the STAR experiment"*, Poster at Quark Matter 2018 (2018).

7. STAR Collaboration, J. Adam et al., *"First Measurement of* Λ_c *Baryon Production in Au+Au Collisions at* $\sqrt{s_{NN}} = 200\ GeV$*"*, Phys. Rev. Lett. **124**, 172301 (2020), [9].

Simulations for Heavy Flavor Tracker–Pixel Detector

Miroslav Simko for the STAR collaboration

Faculty of Nuclear Sciences and Physical Engineering
Czech Technical University in Prague

Abstract

The Heavy Flavor Tracker (HFT) is a new state-of-the-art detector installed at the STAR experiment in January 2014. It consists of four layers of silicon detectors divided into three subsystems: A double sided strip detector SSD (Silicon Strip Detector), a silicon pad detector, called IST (Intermediate Silicon Tracker), and finally two layers of pixel detectors, based on the state-of-the-art MAPS (Monolithic Active Pixel Sensors) technology.

The HFT provides excellent primary and secondary vertex position measurement capability (pointing resolution of ~30 μm) which allows for measurements of hadrons containing heavy flavor, such as D^0 and Λ_c. Moreover, the combined analysis of the identified charm hadrons and the non-photonic electrons will allow the measurement of bottom production and azimuthal anisotropy at RHIC top energy.

A new tool DIGMAPS [4] has been developed for the simulation of the response of the pixel sensors. Results from tuning of DIGMAPS as well as comparison between simulation and recently taken data by the STAR experiment is being presented.

HFT physics

The high energy collisions at RHIC allow us to study nuclear matter at extremely high temperatures. In these conditions a new state of matter, called quark-gluon plasma (QGP), is created.

Heavy flavored quarks are produced during the initial phase of the collision, therefore they are an important tool for study of QGP. However they are also hard to analyze owing to the large combinatorial background.

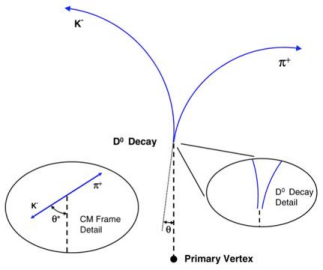

Figure 1: D^0 production and subsequent decay into K^- and π^+.

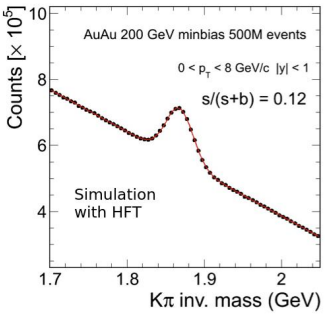

Figure 2: Simulated D^0 peak with HFT used.

HFT can detect heavy flavor particles through precise measurements of displaced vertices. This greatly reduces the combinatorial background. The pointing resolution has to be approximately 30 μm.

Examples of displaced decay vertices
- $D^0 \rightarrow K^-\pi^+$ BR = 3.83 % $c\tau \sim 120\ \mu$m
- $\Lambda_c^+ \rightarrow p\ K^-\pi^+$ BR = 5.0 % $c\tau \sim 60\ \mu$m
- B mesons $\rightarrow J/\psi$ + X or e + X $c\tau \sim 500\ \mu$m

Technical Design

The HFT consists of three subsystems [1]:

- **Silicon Strip Detector (SSD):** One layer of double sided silicon strip detector located 22 cm from the beam axis. This existing detector was refurbished and equipped with new readout electronics.
- **Intermediate Silicon Tracker (IST):** A new single layer silicon pad detector, placed at 14 cm radius. The purpose of the IST and SSD is to guide the particle tracks from the Time Projection Chamber to the PXL layers.

Figure 3: Photograph of the Silicon Pixel Detector.

- **Silicon Pixel Detector (PXL):** The two innermost layers at 8 and 2.8 cm consist of silicon pixel detectors. They are based on the state-of-the-art MAPS technology and have pixel size of 20.7 μm × 20.7 μm.

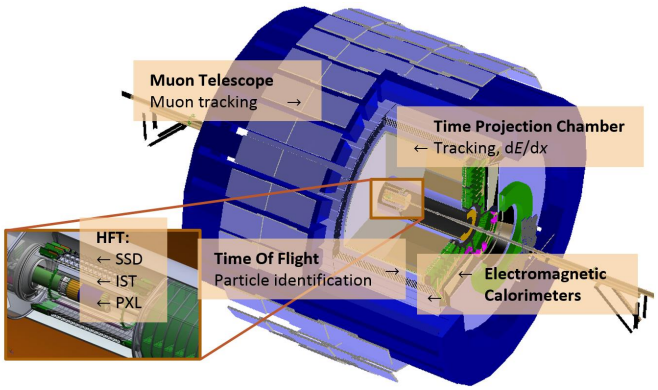

Figure 4: HFT inside the STAR detector; (right) four layers of silicon detectors of the HFT.

In addition, the PXL features a very fast and precise insertion mechanism which allows to quickly access the whole system. Insertion was done in less than 24 hours.

Slow simulator

A part of every analysis is efficiency study. For this purpose a slow simulator is needed. Simulation tool DIGMAPS was developed for the PXL at IPHC – CNRS of Université de Strasbourg [4].

The sensitive area of the pixel sensor is called epitaxial layer (see Fig. 5). As a particle passes through this layer, it creates a cloud of electrons which is then collected by the N-wells. The clouds usually cause that the particles fire more than one pixels and leave a trace in the form of a cluster of pixels.

Simulation consists of the following steps:

- **Energy deposition and creation of electron/hole pairs:** The energy deposition in the epitaxial layer can be translated directly into created electron/hole pairs (3.6 e^-/eV) and is currently implemented as Landau law with MPV of approximately 80 e^-/μm.

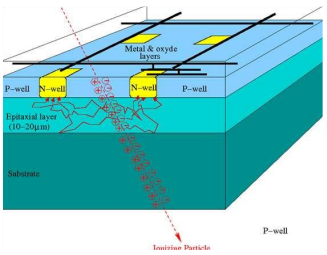

Figure 5: Illustration of a particle, traversing a MAPS sensor.

- **Charge transport:** Ionization electrons transport to and collection by N-wells is emulated by probability distribution functions for charge collection by the nearest and next-to-nearest neighbors N-wells. Studies at IPHC showed that a distribution of a guassian + lorentzian describe the beam test data very well.
- **Digitization:** In the end, noise is added to each channel and an ADC threshold is applied.

Comparison between data and simulations

To evaluate and tune the simulation tool, a comparison between the STAR data and the simulation had to be undertaken. Because the traversing particle usually fires more than one pixel, the best way of comparing the simulation to the measured data is to study the pixel clusters.

The parameters for the charge deposition and collection model were tuned to beam test data at IPHC [4]. At STAR we have to tune the ADC threshold because every pixel column has a different discriminator and therefore a different ADC threshold value.

An analysis of zero field cosmic data was done. In order to reduce the noise in PXL, following steps were taken:
- Only tracks going through all the PXL and IST layers were included (see Fig. 6).
- Hits had to be within 3 mm radius from the track.
- No more than one hit had to be within the radius
- At least one hit with cluster size > 1 was required

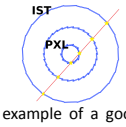

Figure 6: An example of a good zero field cosmic track

Slices for different incident angles were compared to the simulations with different ADC thresholds. The threshold for the simulation was optimized by a Chi^2/NDF comparison.

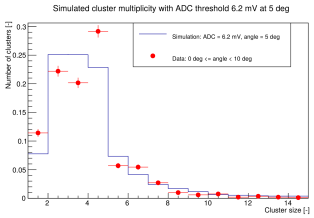

Figure 7: Cluster multiplicity from simulation (blue line) and zero field cosmic data (red dots).

Conclusion and outlook

- The HFT has been successfully installed and is taking data during RHIC 2014 run.
- Accurate simulation is imperative for detector efficiency corrections.
- PXL sensors simulator (DIGMAPS) has been tuned to cosmics data.
- A more thorough comparison to the Au+Au data is currently being carried out.

References

[1] STAR Heavy Flavor Tracker Technical Design Report, https://drupal.star.bnl.gov/STAR/starnotes/public/sn0600.
[2] J. Kapitan, Eur. Phys. J. C 62, 217 (2009).
[3] J. Bouchet, Nucl. Phys. A 830, 636c (2009).
[4] A. Besson, DIGMAPS Documentation: A standalone software tool to study digitization with MAPS sensors (2011), http://www.iphc.cnrs.fr/IMG/pdf/DIGMAPS_doc.pdf

Acknowledgement: This work was supported by Lawrence Berkeley National Laboratory, the grant of the Grant Agency of Czech Republic n. 1 3-20841 S and by the Grant Agency of the Czech Technical University in Prague, grant No. SGS1 3/21 SOHK4/3T/1 4.

Presented at VERTEX 2014, Doksy Czech Republic, 15–19 September 2014

Λ_c baryon production in Au+Au collisions at $\sqrt{s_{NN}}$ = 200 GeV

Miroslav Simko, *for the STAR Collaboration*

Nuclear Physics Institute of the Czech Academy of Sciences,

Faculty of Nuclear Sciences and Physical Engineering of Czech Technical University in Prague

2015 KOBE JAPAN

Baryon-to-meson yield ratios (p/π, Λ/K^0_s) are observed to be significantly enhanced in central heavy-ion collisions than those in peripheral heavy-ion collisions and p+p collisions at RHIC and LHC. This effect can be explained by taking into account coalescence hadronization that recombine thermalized light and strange quarks in heavy-ion collisions as opposed to fragmentation hadronization in elementary nucleon-nucleon collisions. Several model calculations suggest that coalescence hadronization between charm quarks and light quarks will lead to an enhancement in the Λ_c/D^0 ratio. The possible Λ_c/D^0 enhancement in heavy-ion collisions will introduce additional suppression for charm decay electrons due to smaller semi-leptonic decay branching ratios of Λ_c, which could lead to a different interpretation of the heavy flavor decay electron results.

Λ_c baryons have an extremely small lifetime ($c\tau \sim 60\ \mu$m) and have not been measured in heavy-ion collisions yet. The newly installed STAR Heavy Flavor Tracker (HFT) has shown high efficiency and excellent pointing resolution that can facilitate Λ_c reconstruction in heavy-ion collisions. We report studies of reconstruction of Λ_c baryons via three body hadronic decays into p K and π, using year 2014 Au+Au data at $\sqrt{s_{NN}}$ = 200 GeV .

Λ_c baryon

- Ratios of baryons/mesons (such as p/π, Λ/K^0) in heavy-ion colliusions significantly enhanced compared to p+p collisions – due to quark coalescence.
- Similar enhancement expected in the ratio of Λ_c/D^0.
- This would bring insight into coalescence hadronization of charm quarks.
- The enhancement of Λ_c/D^0 is one of the signatures of the formation of the strongly coupled Quark-Gluon Plasma.
- Challenging to measure, $c\tau \sim 60\ \mu$m.
- Λ_c have never been observed in high energy heavy-ion collisions.

Λ_c branching ratios for three body decay:

• $\Lambda_c^+ \to$ p $K^-\pi^+$	(5.0±1.3)%
• $\Lambda_c^+ \to$ pK*	(1.6±0.5)%
• $\Lambda_c^+ \to \Lambda(1520)\,\pi^+$	(1.8±0.6)%
• $\Lambda_c^+ \to K^-\Delta^{++}$	(0.86±0.3)%
• Nonresonant	(2.6±0.8)%

[Particle Data Group, Chin. Phys. C38 (2014) 090001]

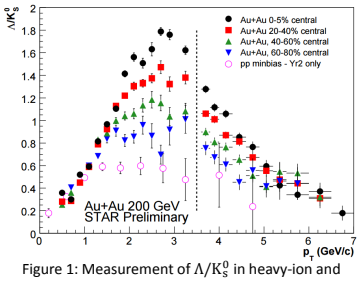

Figure 1: Measurement of Λ/K^0_s in heavy-ion and p+p collisions. Strong enhancement is observed in intermediate p_T [J.Phys.Conf.Ser. 50 (2006) 192].

Detector layout

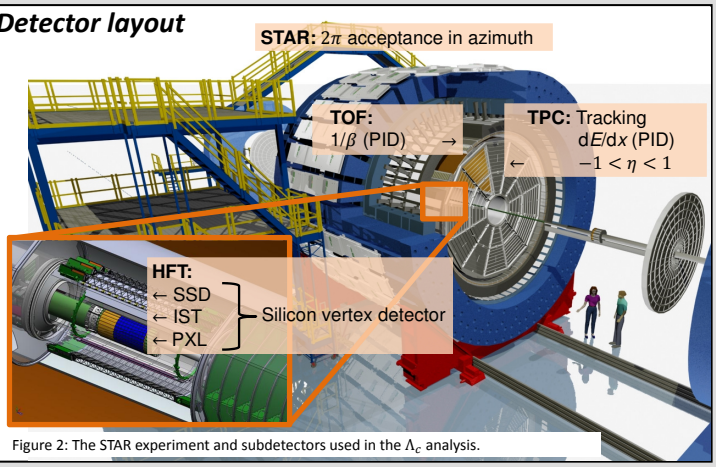

Figure 2: The STAR experiment and subdetectors used in the Λ_c analysis.

Kinematic and topological variables for Λ_c analysis

- **Decay length:** distance of secondary vertex to the primary vertex
- **θ:** angle between Λ_c momentum and position relative to primary vertex
- **Daughter pair DCA:** distance of closest approach (DCA) between the daughter pairs
- **Distance between vertices of daughter pairs**
- **Daughter p_T**

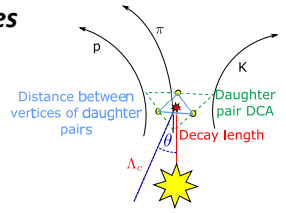

Figure 3: Variables used in topological cuts

Λ_c signal simulation

- Data driven Monte Carlo simulation was used:
  - Λ_c decayed in Pythia.
  - p_T and positions of the daughter particles were smeared, according to resolution observed in data.:
  - Λ_c were generated with flat rapidity distribution within $|y| < 1$.
  - The p_T distribution was obtained from the D^0 minimum bias spectrum from 0–80% centrality Au+Au collisions [Phys. Rev. Lett. **113** (2014) 142301].

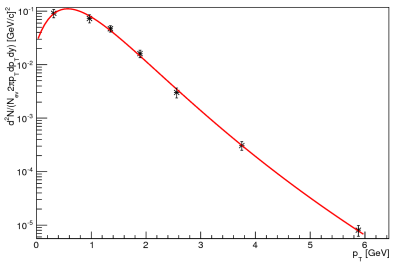

Figure 4: D0 spectrum fitted by Levy function (used as p_T distribution for Λ_c)

- Fragmentation ratio 0.275 between $\Lambda_c$and D^0 was taken from ZEUS data [Eur. Phys. J. C44 (2005) 351].
- Scaling of Λ_c production with the number of binary collisions was used.

Comparison: Simulation and Background from data

- p K π channel – triplets of Λ_c candidates.
- Simulated Λ_c compared to background from 200 GeV Au+Au data.
- Background was selected from p K π triplets with wrong sign combinations of the daughters.
- The same cuts were applied on background and Λ_c from simulation.

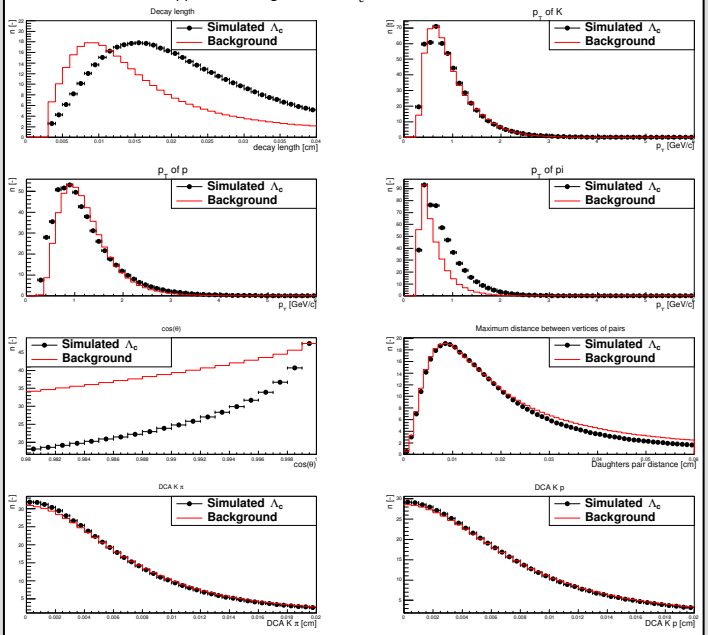

Figure 5: Distribution of variables: Decay length, daughters p_T, cos(θ), distance of pairs vertices, and daughters DCA for signal simulation and background from data. The background is scaled to show the difference in shape.

Run 2016 and future upgrades

- STAR has recorded 1.2 B minimum bias events in Au+Au collisions at $\sqrt{s_{NN}}$ = 200 GeV in the year 2014 and plans to take 2 B more in 2016.
- The inner HFT pixel layer will have reduced material budget thanks to changed cable material of the sensors from copper to aluminum.
- The HFT will have higher efficiency because of replacing non-working sensors.
- This increases the pointing and p_T resolution of STAR and increases the efficiency of tracking with HFT.

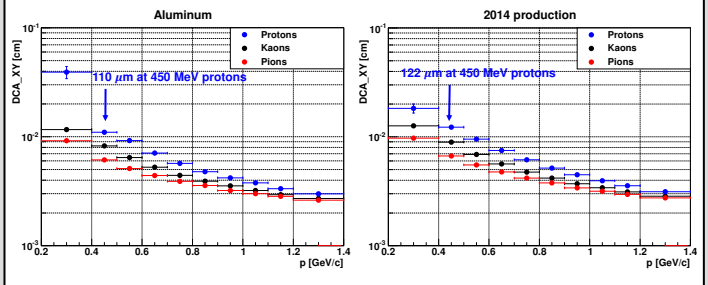

Figure 6: Comparison of the DCA resolution in XY plane with aluminum (left) and copper cables (right).

Conclusion and outlook

- Λ_c measurements are ongoing with the new Heavy Flavor Tracker at STAR.
- Λ_c reconstruction efficiency will increase in run 2016 thanks to reduced mass of the HFT infrastructure and reduced number of dead sensors.
- With the statistics of the future runs, STAR could measure Λ_c baryons for the first time thanks to excellent pointing resolution of the HFT.

Acknowledgement: This work was supported by Grant Agency of the Czech Technical University in Prague, grant No. SGS13/215/OHK4/35/14 and by Grant Agency of the Czech Republic, grant No. 13-20841S.

Office of Science U.S. DEPARTMENT OF ENERGY

The STAR Collaboration: http://drupal.star.bnl.gov/STAR/presentations

Λ_c baryon production in Au+Au collisions at $\sqrt{s_{NN}}$ = 200 GeV

Miroslav Simko, *for the STAR Collaboration*

Nuclear Physics Institute of the Czech Academy of Sciences,

Faculty of Nuclear Sciences and Physical Engineering of Czech Technical University in Prague

Λ_c baryon

- Ratios of baryons/mesons (such as p/π, Λ/K^0) in heavy-ion colliusions significantly enhanced compared to p+p collisions – due to quark coalescence.
- Similar enhancement expected in the ratio of Λ_c/D^0.
- This would bring insight into coalescence hadronization of charm quarks.
- The enhancement of Λ_c/D^0 is one of the signatures of the formation of the strongly coupled Quark-Gluon Plasma.

- Challenging to measure, $c\tau \sim 60\ \mu m$.
- Λ_c have never been observed in high energy heavy-ion collisions.

Λ_c branching ratios for three body decay:

- $\Lambda_c^+ \to p\ K^-\pi^+$ (5.0±1.3)%
  - $\Lambda_c^+ \to pK^*$ (1.6±0.5)%
  - $\Lambda_c^+ \to \Lambda(1520)\ \pi^+$ (1.8±0.6)%
  - $\Lambda_c^+ \to K^-\Delta^{++}$ (0.86±0.3)%
  - Nonresonant (2.6±0.8)%

[Particle Data Group, Chin. Phys. C38 (2014) 090001]

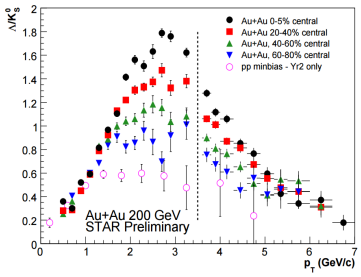

Figure 1: Measurement of Λ/K_s^0 in heavy-ion and p+p collisions. Strong enhancement is observed in intermediate p_T [J.Phys.Conf.Ser. 50 (2006) 192].

Detector layout

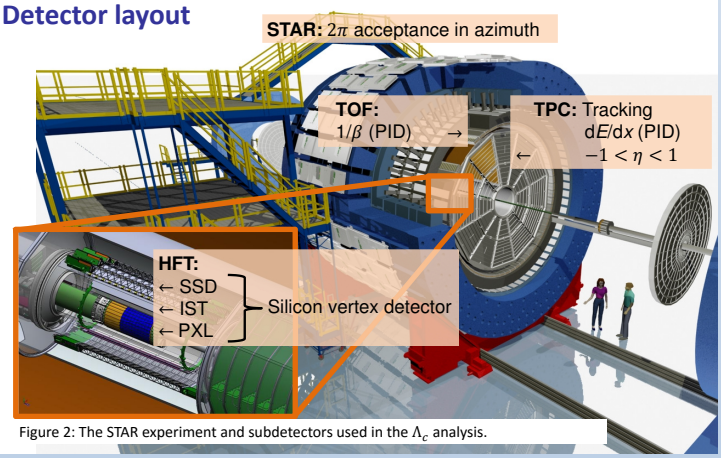

Figure 2: The STAR experiment and subdetectors used in the Λ_c analysis.

Kinematic and topological variables for Λ_c analysis

- **Decay length:** distance of secondary vertex to the primary vertex
- **θ:** angle between Λ_c momentum and position relative to primary vertex
- **Daughter pair DCA:** distance of closest approach (DCA) between the daughter pairs
- **Distance between vertices of daughter pairs:** the maximum distance was used
- **Daughter p_T**

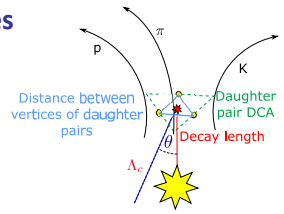

Figure 3: Variables used in topological cuts

Λ_c signal simulation

- Data driven Monte Carlo simulation was used:
  - Λ_c decayed in Pythia.
  - Positions of the daughter particles were smeared, according to resolution observed in data and p_T was smeared according to simulations
  - Λ_c were generated with flat rapidity distribution within $|y| < 1$.
  - The p_T distribution was obtained from the D^0 minimum bias spectrum from 0–80% centrality Au+Au collisions.
- Fragmentation ratio 0.275 between $\Lambda_c$and D^0 was taken from ZEUS data [Eur. Phys. J. C44 (2005) 351].
- Scaling of Λ_c production with the number of binary collisions was used.

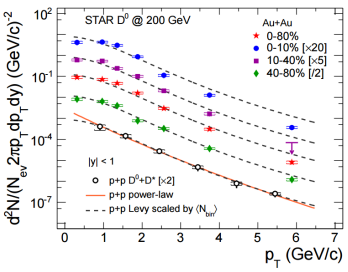

Figure 3: D^0 spectra used for the p_T distribution [Phys. Rev. Lett. **113** (2014) 142301].

Comparison: Simulation and Background from data

- p K π channel – triplets of Λ_c candidates.
- Simulated Λ_c compared to background from 200 GeV Au+Au data.
- Background was selected from p K π triplets with wrong sign combinations of the daughters. Very open cuts were applied.
- The same cuts were applied on background and Λ_c from simulation.

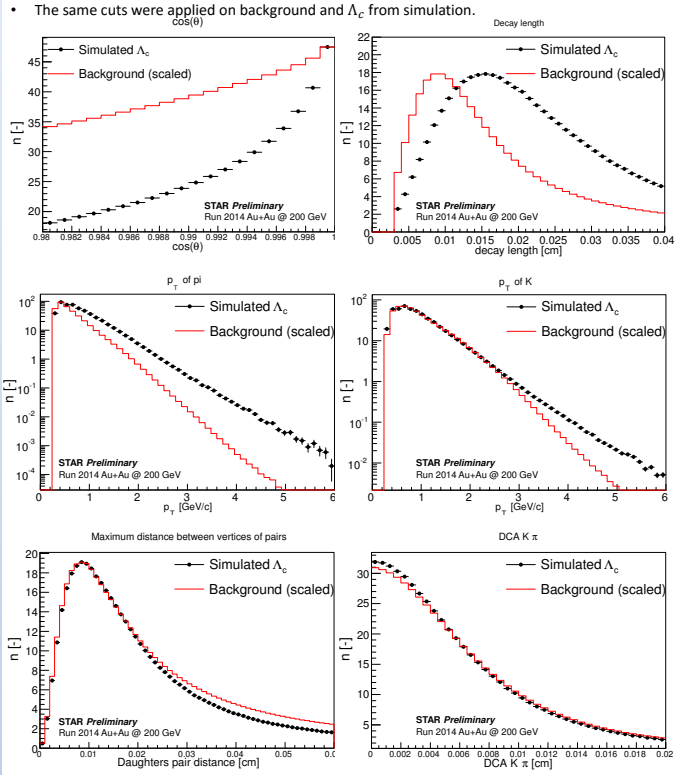

Figure 4: Distribution of variables: Decay length, daughters p_T, cos(θ), distance of pairs vertices, and daughters DCA for signal simulation and background from data. The background is scaled to show the difference in shape.

Multivariate Analysis for Cuts Optimization

- Toolkit for MultiVariate Data Analysis (TMVA)

[PoS ACAT 040 (2007), arXiv:physics/0703039]

  - Rectangular cuts, Neural networks, Boosted decision trees,…
  - Ongoing work

- Preselection for TMVA – Iterative method equivalent to rectangular cuts:
  - *N*-dim array of cuts for *N* variables with small increments
  - Maximizing significance for the set of cuts: $s = \frac{N_{sig}}{\sqrt{N_{sig}+N_{bg}}}$
  - Select Signal and Background
  - Next iteration with an *N*-dim array of cuts with 2× smaller increments around the best cuts

Conclusion and outlook

- Λ_c baryons present an important probe for coalescence of c-quarks
- STAR may be able to measure Λ_c baryons for the first time in heavy-ion collisions thanks to excellent pointing resolution of the HFT
- Cuts optimization was performed using data driven simulation
- 2016: More statistics with better HFT

Acknowledgement: This work was supported by Grant Agency of the Czech Technical University in Prague, grant No. SGS13/215/OHK4/35/14 and by Grant Agency of the Czech Republic, grant No. 13-20841S.

Measurements of open charm hadrons at the STAR experiment

2017 J. Phys.: Conf. Ser. 832 012028

(http://iopscience.iop.org/1742-6596/832/1/012028)

IOP Conf. Series: Journal of Physics: Conf. Series **832** (2017) 012028 doi:10.1088/1742-6596/832/1/012028

Measurements of open charm hadrons at the STAR experiment

M Simko[1,2] for the STAR Collaboration

[1] Nuclear Physics Institute of the Czech Academy of Sciences, Na Truhlarce 39/64, 18086 Praha, Czech Republic;
[2] Faculty of Nuclear Sciences and Physical Engineering, Czech Technical University in Prague, Brehova 7, 11519 Praha, Czech Republic.

E-mail: simko@ujf.cas.cz

Abstract. Because of their large masses, charm quarks are predominantly produced in the early stages of the heavy-ion collisions via hard scatterings. Therefore, they experience the entire evolution of the Quark-Gluon Plasma created in such collisions. Compared to light quarks, charm quarks thermalize more slowly. Therefore, the open charm hadrons present a unique probe to the properties of the hot and dense nuclear matter by measuring their energy loss and degree of thermalization in the medium. Furthermore, with the combined measurements of D^0 and D_s mesons, we can study multiple modes of coalescence of charm quarks with light quarks in heavy-ion collisions. Heavy Flavor Tracker at the STAR experiment enables full topological reconstruction of open charm hadrons which greatly improves measurements of D^0 mesons and opens the door to reconstructing the D_s mesons for the first time at RHIC. In this paper, we present the nuclear modification factor and azimuthal anisotropy for the D^0 and D_s mesons as well as the ratio of D_s/D^0 in Au+Au collisions at the center-of-mass energy $\sqrt{s_{NN}} = 200$ GeV.

1. Introduction

Charm quarks are considered to be an excellent probe to study the strongly coupled quark-gluon plasma (sQGP) as they are produced predominantly in hard scatterings during the early stages of heavy-ion collisions due to their large masses which are mostly unaffected by the medium. Thus, they experience the full evolution of the system. Analogous to the Brownian motion, charm quarks are sensitive to the transport properties of the sQGP, e.g. $2\pi TD_s$, where T is the temperature of the system and D_s the spatial diffusion coefficient for the c-quark [1].

The inclusive production of the c-quark has been measured at STAR [2] and exhibits scaling with the number of binary nucleon–nucleon collisions (N_{coll}) in Au+Au collisions. The D^0 meson, being the lightest hadron that contains a charm quark, provides, therefore, an excellent calibrated probe to the behavior of the medium. Recent measurements of the D^0 meson at Relativistic Heavy-Ion Collider (RHIC) and the Large Hadron Collider (LHC) [3–5] show suppression of yields at high transverse momenta (p_{T}) and suggest a non-zero v_2 at intermediate to high p_{T}. Measurements of better precision are, however, needed to provide more stringent constraints on model calculations.

The D_s meson, which contains a strange quark, provides an additional handle on the hadronization process of charm quarks. Recent calculations [6] suggest an enhancement of the D_s meson yield compared to the D^0 meson because of the process of quark coalescence.

2. The STAR experiment and open charm hadron reconstruction

The Solenoidal Tracker at RHIC (STAR) is a large-acceptance multi-purpose detector that covers the full azimuth and pseudorapidity range of $|\eta| < 1$ [7]. The main tracking detector of STAR is the Time Projection Chamber, which also provides the $\mathrm{d}E/\mathrm{d}x$ information for particle identification (PID). The Time-Of-Flight detector is also used to improve the PID capabilities.

Since the beginning of 2014, a new detector, Heavy Flavor Tracker (HFT), has been installed at STAR. The HFT consists of 4 layers of silicon detectors: one layer of double strip, one layer of silicon pad, and finally two layers of PiXeL (PXL) detectors using the state-of-the-art slimmed-down Monolithic Active Pixel Sensor technology for the first time in a collider experiment. It provides excellent distance of closest approach resolution down to $\sim 30\,\mu\mathrm{m}$ at high-p_{T} while maintaining a very small material budget as the first layer of PXL has a radiation length of $\sim 0.4\,\% X_0$.

The excellent track pointing resolution provided by the HFT allows for a direct topological reconstruction of the secondary vertices of open charm meson decays via hadronic channels, i.e. $\mathrm{D}^0 \to \pi^{\pm} + \mathrm{K}^{\mp}$, $\mathrm{D}_{\mathrm{s}}^{\pm} \to \pi^{\pm} + \phi(1020) \to \pi^{\pm} + \mathrm{K}^{\pm} + \mathrm{K}^{\mp}$. This greatly reduces the combinatorial background for these measurements. In the case of the D_{s} meson, the decay channel via $\phi(1220)$ is used to place an additional constraint on the $\mathrm{K}^{\pm}+\mathrm{K}^{\mp}$ invariant mass and, therefore, to reduce the background even further. STAR has recorded $\sim 3.2\,\mathrm{B}$ minimum-bias events in Au+Au collisions at $\sqrt{s_{\mathrm{NN}}} = 200\,\mathrm{GeV}$ in the years 2014 and 2016. Results from $\sim 780\,\mathrm{M}$ of these events are shown in this paper.

3. Results

3.1. D^0 measurements

Although the inclusive charm quark production scales with N_{coll} [2], the D^0 spectrum shape is significantly modified in Au+Au collisions. Fig. 1a shows the D^0 nuclear modification factor R_{AA} as a function of p_{T} in the most central (0–10 %) collisions, where R_{AA} is the ratio between the yield in Au+Au collisions and that in p+p collisions scaled by N_{coll}. The new results (black full circles) obtained with the HFT are consistent with the published R_{AA} from 1.1 B minimum-bias events taken in the years 2010 and 2011 without the HFT (red empty circles) [3]. For the new results, a much better precision is achieved despite the less statistics used. The D^0 production is significantly suppressed at high-p_{T} which indicates strong interactions between charm quarks and the medium in this kinematic region. In the intermediate p_{T} range (~ 0.7–$2\,\mathrm{GeV}/c$), data show an enhancement which can be described by models including coalescence of charm quarks.

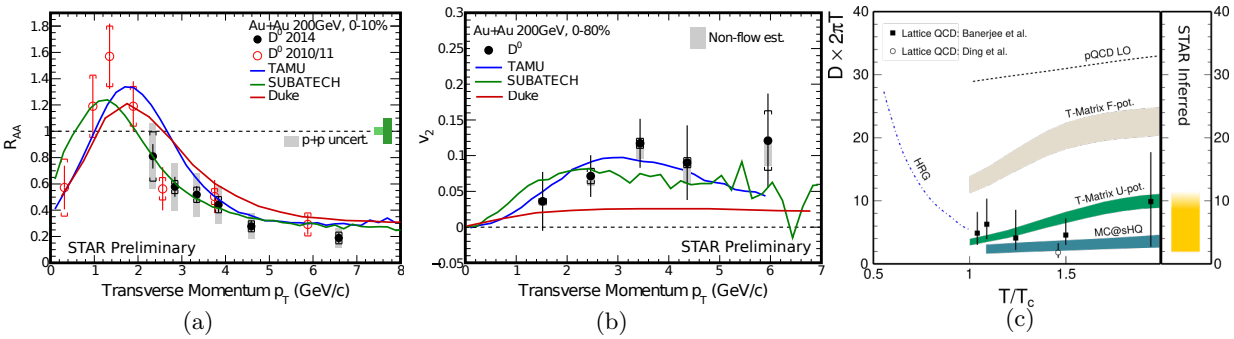

Figure 1. **(a)** D^0 R_{AA} as a function of p_{T} for 0–10 % central Au+Au collisions. The gray bands are systematic uncertainties from the p+p baseline and the light and dark green vertical bands around unity are uncertainties related to the N_{coll} in Au+Au collisions and the global normalization in the p+p collisions, respectively; **(b)** D^0 v_2 as a function of p_{T} for Au+Au collisions at $\sqrt{s_{\mathrm{NN}}} = 200\,\mathrm{GeV}$; **(c)** Charm-quark diffusion coefficient used in various models compared to that inferred from the STAR data.

The HFT also enables the measurement of the D^0 v_2 for the first time at RHIC, as shown in Fig. 1b. The vertical bars (brackets) indicate the statistical (systematic) uncertainties while the gray bands represent the estimated non-flow contribution inferred from D meson–hadron correlations in p+p collisions. The data show that the v_2 is significantly larger than 0 above 2 GeV/c.

Several models, which use different approaches to determine the charm quark diffusion coefficient, are compared to the measurements of $R_{\rm AA}$ and v_2. The group from TAMU [8] (blue) employs a non-perturbative T-matrix approach with the assumption that two body interactions can be described by a potential, which is a function of the transferred 4-momentum. This model predicts the charm quark diffusion coefficient multiplied by temperature as $3 \leq 2\pi TD_s \lesssim 11$. The SUBATECH group [9] (green) uses a pQCD approach with the Hard Thermal Loop approximation for soft collisions. In this approach, the diffusion coefficient is within $2 \leq 2\pi TD_s \leq 4$. The model by the Duke university group [11] uses $2\pi TD_s$ as a free parameter. The red curves shown in Figs. 1a and 1b use the value $2\pi TD_s = 7$ which is fixed to match the D^0 $R_{\rm AA}$ measured at the LHC. The Duke model can describe the shape of $R_{\rm AA}$ well, however it systematically underestimates the v_2. The other two models are consistent with both $R_{\rm AA}$ and v_2 data. Fig. 1c shows the $2\pi TD_s$ values obtained from different models [8, 12–17] compared to the range inferred from the STAR data which is drawn as the yellow band. The STAR inferred range of $2 \leq 2\pi TD_s \lesssim 12$ is consistent with the lattice QCD calculations [16,17] shown as the black points.

3.2. D_s measurements

Thanks to the HFT, the D_s meson, consisting of a charm quark and a strange quark, is measured for the first time at RHIC. Such measurements are expected to shed more light on the mechanism of the charm quark coalescence.

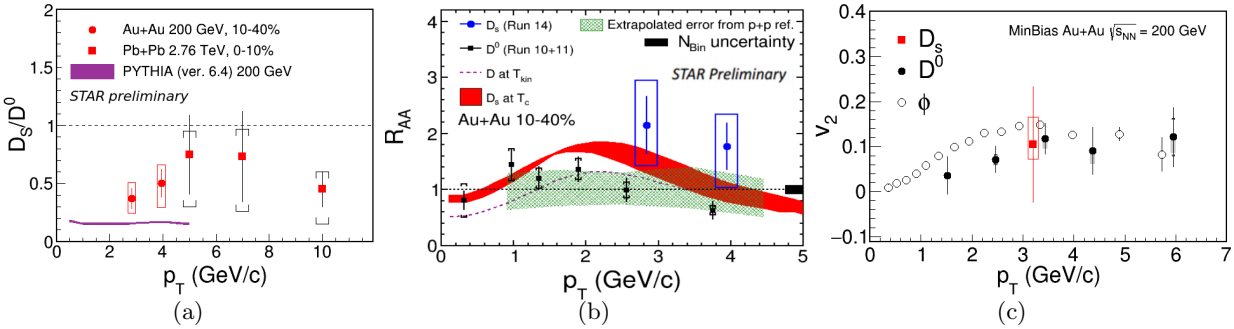

Figure 2. **(a)** The ratio between D_s and D^0 yield in Au+Au collisions at $\sqrt{s_{\rm NN}} = 200$ GeV for 10–40 % centrality; **(b)** D_s $R_{\rm AA}$ in the 10–40 % centrality class; **(c)** D_s v_2 in minimum-bias Au+Au collisions at $\sqrt{s_{\rm NN}} = 200$ GeV.

In Fig. 2a, the yield ratio of produced D_s to D^0 is shown as a function of $p_{\rm T}$ in 10–40 % central Au+Au collisions at $\sqrt{s_{\rm NN}} = 200$ GeV (red circles). The D^0 spectrum is obtained from the published STAR data [3]. The measured D_s/D^0 ratios are compared to similar measurements at the LHC for minimum-bias Pb+Pb collisions [18] (red squares). Both of the measurements are consistent with each other within uncertainties. To compare our measurement to the D_s/D^0 in p+p collisions, PYTHIA 6.4 [19] (purple curve) is used. The STAR measurement is slightly enhanced compared to the p+p ratio; however, the enhancement is statistically insignificant.

In Fig. 2b, the nuclear modification factor for D_s is shown as blue points. The p+p baseline is obtained from the measured total charm cross-section by STAR [2] multiplied by the $c \to D_s$ fragmentation factor obtained from the measurements at HERA [20,21]. The uncertainty of the baseline is indicated by the green hashed band and the uncertainty on $N_{\rm coll}$ is plotted as the

black rectangle. The D_s R_{AA} is compared to the calculation done by the TAMU group [6] and the published D^0 R_{AA} by STAR [3]. Again, we observe a hint of D_s enhancement compared to D^0, which can be described by the TAMU model within uncertainties; however, more data is needed to draw firmer conclusions.

Fig. 2c shows the first result of D_s v_2 at RHIC as the red filled square. The data slightly prefer a non-zero v_2, albeit not significantly. The D_s v_2 is compared to the v_2 of D^0 and ϕ meson [22] which, like the D_s, contains strange quarks. The D_s v_2 is consistent with both measurements within uncertainties.

4. Summary and outlook

We report the first measurements of the open charm hadrons using the state-of-the-art vertex detector HFT. D^0 v_2 is measured for the first time at RHIC. These data are significantly above zero and favor models with charm diffusion. Moreover, the D^0 R_{AA} is measured with a much improved precision, compared to the previous measurements without the HFT. Comparing both R_{AA} and v_2 measurements to different models, STAR is able to infer the value of the charm spatial diffusion coefficient D_s multiplied by the temperature T to be $2 \leq 2\pi T D_s \lesssim 12$, which is consistent with the lattice QCD calculations.

The first measurement of the D_s meson at RHIC is enabled by the HFT. The ratio of the production yield of D_s/D^0 is compatible with a simmilar LHC measurement and indicates an enhancement of the D_s mesons in Au+Au collisions compared to the p+p collisions. The R_{AA} of the D_s is measured and is consistent with model calculations. Moreover, the D_s v_2 is also measured for the first time at RHIC.

In the years 2014 and 2016, $\sim$ 4 times more minimum-bias Au+Au events were recorded compared to the shown results. All of these measurements will benefit greatly from the increased statistics. In addition, there have been significant improvements in terms of HFT performance in 2016 as well as offline software, which greatly enhance the tracking efficiency. In 2015, STAR took reference p+p and p+Au collisions at $\sqrt{s_{NN}} = 200\,\text{GeV}$, which will provide a baseline of better precision and help to quantify the cold nuclear matter effects.

This work has been supported by the grant LG15001 of the Ministry of Education of the Czech Republic.

References

[1] Abreu L M, Cabrera D, Llanes-Estrada F J and Torres-Rincon J M 2011 *Annals of Physics* **326** 2737–2772
[2] Adamczyk L *et al.* (STAR Collaboration) 2012 *Phys. Rev. D* **86** 072013
[3] Adamczyk L *et al.* (STAR Collaboration) 2014 *Phys. Rev. Lett.* **113** 142301
[4] Adam J *et al.* (ALICE Collaboration) 2016 *Journal of High Energy Physics* **2016** 1–43
[5] Abelev B *et al.* (ALICE Collaboration) 2013 *Phys. Rev. Lett.* **111** 102301
[6] He M, Fries R J and Rapp R 2013 *Phys. Rev. Lett.* **110** 112301
[7] Ackermann K H *et al.* (STAR Collaboration) 2003 *Nucl. Inst. Meth. A* **499** 624–632
[8] He M, Fries R J and Rapp R 2012 *Phys. Rev. C* **86** 014903
[9] Nahrgang M, Aichelin J, Bass S, Gossiaux P B and Werner K 2015 *Phys. Rev. C* **91** 014904
[10] Berrehrah H, Bratkovskaya E, Cassing W, Gossiaux P B and Aichelin J 2015 *Phys. Rev. C* **91** 054902
[11] Cao S, Qin G Y and Bass S A 2013 *Phys. Rev. C* **88** 044907
[12] Andronic A *et al.* 2016 *Eur. Phys. J. C* **76** 107
[13] Kaczmarek O 2014 *Nuclear Physics A* **931** 633–637
[14] Riek F and Rapp R 2010 *Phys. Rev. C* **82** 035201
[15] Svetitsky B 1988 *Phys. Rev. D* **37** 2484–2491
[16] Ding H T, Francis A, Kaczmarek O, Karsch F, Satz H and Soeldner W 2012 *Phys. Rev. D* **86** 014509
[17] Banerjee D, Datta S, Gavai R and Majumdar P 2012 *Phys. Rev. D* **85** 014510
[18] Adam J *et al.* (ALICE Collaboration) 2016 *Journal of High Energy Physics* **2016** 1–33
[19] Sjstrand T, Mrenna S and Skands P 2006 *Journal of High Energy Physics* **2006** 026
[20] The H1 Collaboration 2005 *Eur. Phys. J. C* **38** 447–459
[21] The ZEUS Collaboration 2005 *Eur. Phys. J. C* **44** 351–366
[22] Adamczyk L *et al.* (STAR Collaboration) 2016 *Phys. Rev. Lett.* **116** 062301

PROCEEDINGS OF SCIENCE

Measurements of open charm hadrons in Au+Au collisions at the STAR experiment

Miroslav Simko* [ab] **for the STAR Collaboration**

[a] *Nuclear Physics Institute of the Czech Academy of Sciences, Na Truhlarce 39/64, 18086 Praha, Czech Republic;*

[b] *Faculty of Nuclear Sciences and Physical Engineering, Czech Technical University in Prague, Brehova 7, 11519 Praha, Czech Republic.*

E-mail: simko@ujf.cas.cz

Charm quarks possess a large mass and thus they are expected to be primarily produced during the initial stages of heavy-ion collisions. Hot and dense nuclear matter, usually referred to as the Quark-Gluon Plasma (QGP), can also be created in these collisions. Therefore, the QGP can be studied using charm quarks as penetrating probes via measurements of the parton energy loss and collective behavior, which are directly related to the intrinsic properties of the medium. In particular, a mass ordering of the parton energy loss in the hot medium is predicted, i.e. heavy-flavor quarks are expected to lose less energy than light quarks. Moreover, STAR has measured several species of charm hadrons and, therefore, can probe several modes of charm quark hadronization in the medium. In these proceedings we report on the most recent measurements of the production of D^0 and $D^{\pm}$, as well as D_s, containing a strange quark, and the Λ_c baryon in Au+Au collisions at the center-of-mass energy per nucleon–nucleon pair of $\sqrt{s_{NN}} = 200$ GeV. These particles are reconstructed via their hadronic decay channels, where the daughter particles are tracked and identified with excellent precision.

The European Physical Society Conference on High Energy Physics
5-12 July, 2017
Venice

*Speaker.

In ultra-relativistic heavy-ion collisions, such as those carried out at Relativistic Heavy Ion Collider (RHIC), a new state of matter, the so-called strongly-coupled quark-gluon plasma (sQGP), is expected to be created [1]. Charm quarks are mainly produced in hard processes during the early stages of such collisions since the charm quark mass is much larger than the temperature of the sQGP which makes the thermal production improbable. Therefore, charm quarks experience the whole evolution of the medium and can be used to probe the properties of the hot and dense strongly-interacting matter [2]. Analogous to the Brownian motion, charm quarks are sensitive to the transport properties of the sQGP and can be used to extract $2\pi TD_s$, where T is the temperature of the system and D_s the spatial diffusion coefficient of the c-quark in the medium.

The D^0 and $\mathrm{D}^{\pm}$ mesons, the lightest hadrons containing a charm quark, provide excellent probes to the medium properties. Previous measurements of the D^0 meson production at RHIC [3] and the Large Hadron Collider (LHC) [4,5] show suppression of yields at high transverse momenta (p_{T}) and suggest a non-zero elliptic flow coefficient (v_2) at intermediate to high p_{T}. Measurements of better precision are, however, needed to provide more stringent constraints on model calculations.

The $\mathrm{D_s}$ meson and the charmed baryon Λ_c provide additional handles on understanding the hadronization process of charm quarks. Model calculations [6–10] suggest enhancements of the $\mathrm{D_s}/\mathrm{D}^0$ and $\Lambda_\mathrm{c}/\mathrm{D}^0$ yield ratios in Au+Au collisions, because of the presence of the quark coalescence mechanism in contrast to only quark fragmentation in p+p collisions.

1. The STAR experiment and open charm hadron reconstruction

The Solenoidal Tracker at RHIC (STAR) is a large multi-purpose detector that covers the full azimuthal angle and pseudorapidity range of $|\eta| < 1$ [11]. The main tracking detector of STAR is the Time Projection Chamber which also provides $\mathrm{d}E/\mathrm{d}x$ information for particle identification (PID). The Time-Of-Flight detector is also used to improve the PID capabilities, especially at low p_{T}.

In 2014–2016, a novel high-precision silicon vertex detector, the Heavy Flavor Tracker (HFT), was installed at STAR. The HFT provided excellent track pointing resolution and allowed for direct topological reconstruction of the secondary vertices of open charm hadron decays via hadronic channels, i.e. $\mathrm{D}^0 \to \pi^{\pm}\mathrm{K}^{\mp}$, $\mathrm{D}^{\pm} \to \pi^{\pm}\pi^{\pm}\mathrm{K}^{\mp}$, $\Lambda_\mathrm{c}^{\pm} \to \mathrm{p}^{\pm}\mathrm{K}^{\mp}\pi^{\pm}$, and $\mathrm{D_s^{\pm}} \to \pi^{\pm}\phi(1020) \to \pi^{\pm}\mathrm{K}^{\pm}\mathrm{K}^{\mp}$, which greatly reduced the combinatorial background. In the case of the $\mathrm{D_s}$ meson, the decay channel through $\phi(1220)$ is used to place an additional constraint on the $\mathrm{K}^{\pm} + \mathrm{K}^{\mp}$ invariant mass, reducing the background even further.

2. Results

2.1 D^0 and $\mathrm{D}^{\pm}$ nuclear modification factor R_{AA}

Figure 1 shows the D^0 and $\mathrm{D}^{\pm}$ nuclear modification factors (R_{AA}) as a function of p_{T} in the 0–10 % most central Au+Au collisions. R_{AA} is a ratio between the particle yield in Au+Au collisions and that in p+p collisions scaled by the number of binary collisions N_{coll}. The new results (black squares for D^0 and red circles for $\mathrm{D}^{\pm}$), which were obtained using the HFT, have a much better precision, compared to the published R_{AA} from 1.1 B minimum-bias events taken in 2010 and 2011 without the HFT (blue triangles) [3], despite the less statistics used. The D^0 and $\mathrm{D}^{\pm}$ yields are

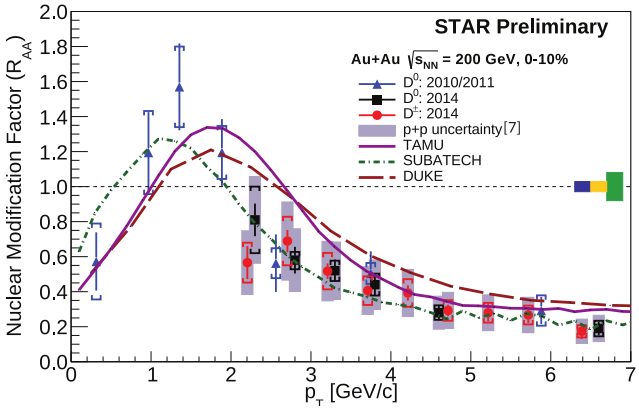

Figure 1: D^0 and $D^{\pm}$ meson R_{AA} as a function of p_T for 0–10 % central Au+Au collisions. The gray bands are systematic uncertainties from the p+p baseline and the blue, yellow, and green vertical bands around unity are uncertainties related to the N_{coll} in Au+Au collisions in 2010 and 2014, and the global normalization in p+p collisions, respectively.

consistent with each other after taking into account their different fragmentation ratios from charm quarks and are significantly suppressed at high-p_T, indicating strong interactions between charm quarks and the medium in this kinematic region.

Several theoretical calculations that use different approaches to describe charm quark transportation in the sQGP and correspond to different values of the diffusion coefficient can qualitatively describe the measured R_{AA}. The group from TAMU [12] predicts $3 \leq 2\pi TD_s \lesssim 11$ for $T_c < T < 2T_c$, where T_c is the QCD critical temperature, while in the SUBATECH calculation [13] the diffusion coefficient is within $2 \leq 2\pi TD_s \leq 4$. The model by the Duke university group [14] uses $2\pi TD_s$ as a free parameter which is fixed for the RHIC energies to be 7 by matching to the R_{AA} measured at the LHC.

2.2 D^0 elliptic and triangular anisotropies

The HFT has enabled the measurement of the D^0 elliptic (v_2) [15] as well as triangular (v_3) anisotropies for the first time at RHIC. STAR results on v_2 are shown in Figs. 2a–2c. The vertical bars (brackets) indicate the statistical (systematic) uncertainties while the gray bands represent an estimate of the non-flow contribution inferred from D^*–hadron correlations in p+p collisions. The data show that the v_2 is significantly larger than 0 above 1.5 GeV/c.

Figures 2a and 2b show the D^0 v_2 for 10–40 % central collisions, compared to those of light-flavor hadrons. In Fig. 2a a clear mass ordering is observed for $p_T < 2$ GeV/c. If divided by the number of constituent quarks n_q, as shown in Fig. 2b, and displayed as a function of $(m_T - m_0)/n_q$, where m_0 is the rest mass and $m_T = \sqrt{p_T^2 + m_0^2}$, the D^0 v_2 follows the same pattern as those of light-flavor hadrons. This observation points to strong collective behavior of the charm quarks.

Several model calculations are compared to the measured D^0 v_2 in Fig. 2c. A 3D viscous hydrodynamical calculation [17] is consistent with the data within the region of $p_T < 4$ GeV/c, suggesting thermalization of the c-quark. In addition to R_{AA}, the SUBATECH and TAMU models are consistent with the measured v_2 as well. The Duke model can describe the shape of the R_{AA}, however it systematically underestimates the v_2. The LBT [18] and PHSD [19] calculations, corresponding to $3 \leq 2\pi TD_s \leq 6$ and $5 \leq 2\pi TD_s \leq 12$, respectively, describe both the measured R_{AA}

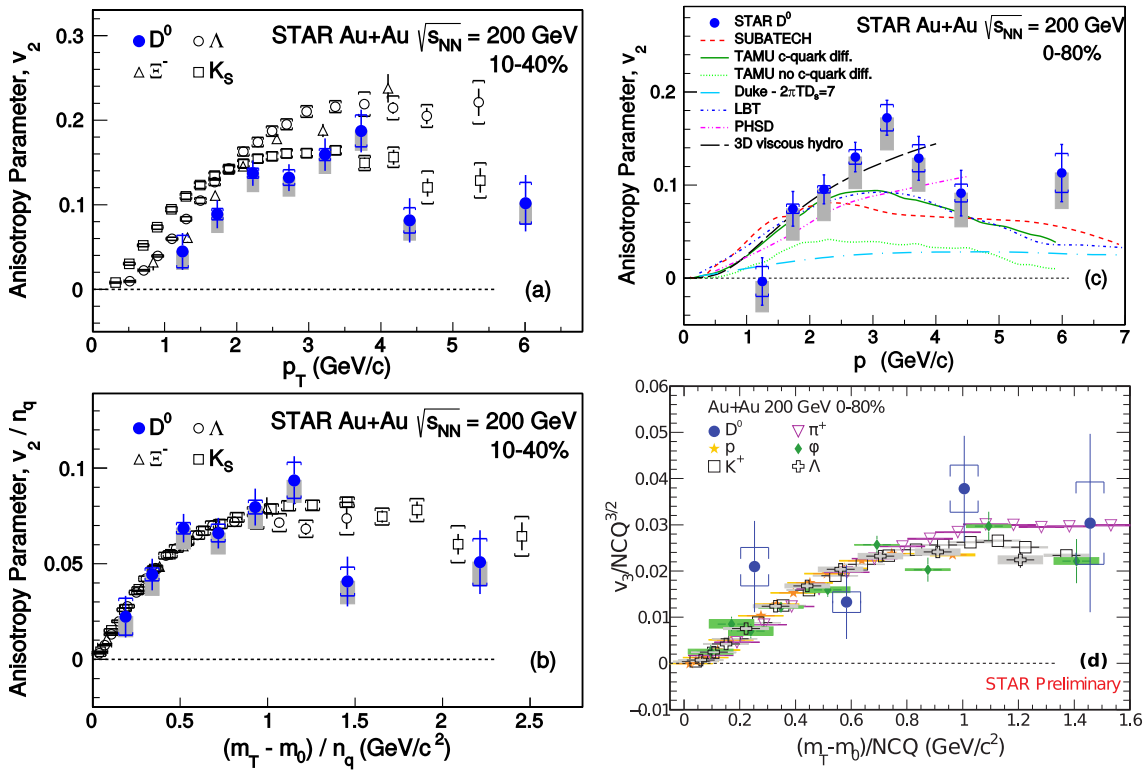

Figure 2: **(a)** D^0 v_2 as a function of p_T in 10–40 % central collisions [15], compared to light hadrons [16]; **(b)** v_2/n_q of D^0 and light hadrons as a function of $(m_T - m_0)/n_q$; **(c)** D^0 v_2 as a function of p_T in 0–80 % centrality bin; **(d)** $v_3/n_q^{3/2}$ of D^0 and light hadrons as a function of $(m_T - m_0)/n_q$ in 0–80 % centrality bin.

and v_2. From these models, the range of $2 \leq 2\pi T D_s \lesssim 12$ can be inferred for $T_c < T < 2T_c$. This range is consistent with lattice QCD calculations [20, 21].

Figure 2d shows the triangular anisotropy v_3 of the D^0 compared to that of light flavor hadrons. A strong indication of non-zero v_3 is observed. Similarly to the v_2 measurement, the D^0 v_3 is scaled by $n_q^{3/2}$ (indicated $NCQ^{3/2}$ in Fig. 2d) and plotted as a function $(m_T - m_o)/n_q$, which is seen to follow the same trend for the D^0 meson and light hadrons.

2.3 Strangeness and baryon enhancements in open-charm hadrons

Thanks to the HFT, the D_s meson is measured for the first time at RHIC and the Λ_c baryon is measured for the first time in heavy-ion collisions.

In Fig. 3a, the yield ratio of produced D_s to D^0 is shown as a function of p_T in 0–10 % and 10–40 % central Au+Au collisions at $\sqrt{s_{NN}} = 200$ GeV. The measured D_s/D^0 yield ratio in Au+Au collisions is compared to the PYTHIA [22] prediction for p+p collisions, as well as the average of the fragmentation ratio from the measurements in p+p, e+e, and e+p collisions [23]. The D_s/D^0 yield ratio in Au+Au collisions is significantly enhanced compared to that in elementary collisions. The calculation by the TAMU group [6], including charm quark coalescence, underpredicts the data in the corresponding centrality interval of 10–40 %. The Statistical Hadronization Model (SHM [24]) is consistent with the data.

Λ_c baryons are reconstructed in the p_T region of 3–6 GeV/c in the 10–60% centrality interval. Figure 3b shows the comparison of the measured yield ratio of Λ_c/D^0 to several theoretical

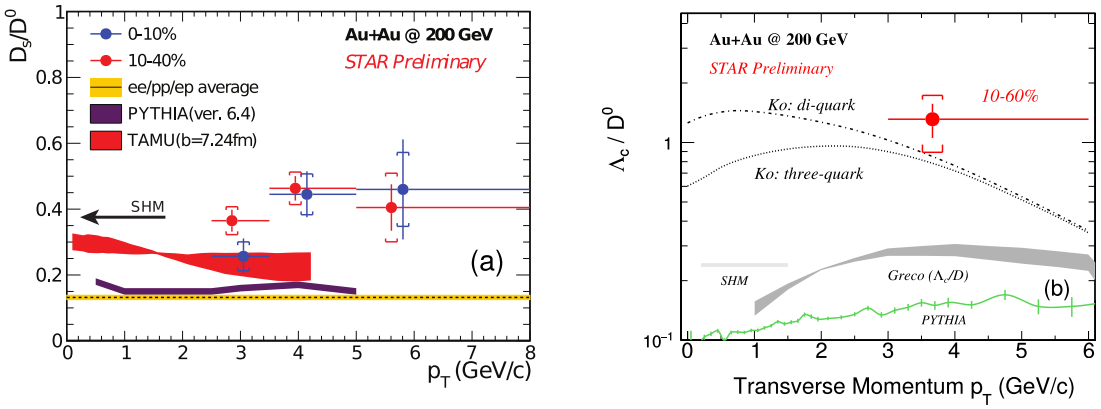

Figure 3: **(a)** Yield ratio of D_s/D^0 in 0–10 % and 10–40 % central Au+Au collisions at $\sqrt{s_{NN}} = 200$ GeV; **(b)** Yield ratio of Λ_c/D^0 in 10–60 % central Au+Au collisions at $\sqrt{s_{NN}} = 200$ GeV.

calculations. The calculation with no coalescence, obtained from PYTHIA, is significantly below the data. The SHM [10, 24] underpredicts the data as well. The Ko model [7] uses two coalescence calculations: one where the charm quark coalesces with a light di-quark structure and the other where three quarks coalesce. No rescattering in the hadron gas is considered in these two scenarios. The data are consistent with both the di-quark and three-quark coalescence scenarios. The Greco model [8, 9] employs the three-quark coalescence mechanism, and calculates the diffusions of Λ_c and D^0 in the hadron gas. Note that the denominator for this calculation is the sum of all D meson species rather than only D^0, and one expects it to increase if only the D^0 meson is considered.

3. Summary and outlook

STAR has made a comprehensive study of the behavior of the charm quarks in the sQGP. We report measurements of the open charm hadrons using the state-of-the-art vertex detector HFT. The D^0 v_2 and v_3 are measured for the first time at RHIC and are significantly above zero, favoring models with charm diffusion. Moreover, the D^0 and $D^{\pm}$ R_{AA} are measured with much improved precision, compared to the previous measurements without the HFT. Comparing both the R_{AA} and v_2 results to different models, the value of the charm quark spatial diffusion coefficient is inferred to be $2 \leq 2\pi T D_s \lesssim 12$ in the range of $T_c < T < 2T_c$, which is consistent with lattice QCD calculations.

The yield ratios of D_s/D^0 and Λ_c/D^0 are measured for the first time at RHIC. Compared to the fragmentation-only scenario, both ratios are strongly enhanced, suggesting that charm quarks also participate in the coalescence hadronization.

In addition to the data taken in 2014, on which the reported results are based, twice more minimum-bias Au+Au events were recorded at STAR with the HFT in 2016. All the measurements in these proceedings will benefit greatly from the increased statistics.

This work has been supported by the Czech Technical University in Prague grant no. SGS16/238/OHK4/3T/14 and by the grant LG15001 of the Ministry of Education of the Czech Republic.

References

[1] M. Gyulassy in *Structure and dynamics of elementary matter. Proceedings, NATO Advanced Study Institute, Camyuva-Kemer, Turkey, September 22-October 2, 2003*, pp. 159–182, 2004, nucl-th/0403032.

[2] A. Andronic et al.*Eur. Phys. J. C* **76** (2016) 107.

[3] STAR collaboration, L. Adamczyk et al.*Phys. Rev. Lett.* **113** (Sep, 2014) 142301.

[4] ALICE collaboration, J. Adam et al.*Journal of High Energy Physics* **2016** (2016) 1–43.

[5] ALICE collaboration, B. Abelev et al.*Phys. Rev. Lett.* **111** (Sep, 2013) 102301.

[6] M. He, R. J. Fries and R. Rapp*Phys. Rev. Lett.* **110** (Mar, 2013) 112301.

[7] Y. Oh, C. M. Ko, S. H. Lee and S. Yasui*Phys. Rev. C* **79** (Apr, 2009) 044905.

[8] V. Greco, C. Ko and R. Rapp*Physics Letters B* **595** (2004) 202 – 208.

[9] H. van Hees, M. Mannarelli, V. Greco and R. Rapp*Phys. Rev. Lett.* **100** (May, 2008) 192301.

[10] S. H. Lee, K. Ohnishi, S. Yasui, I.-K. Yoo and C. M. Ko*Phys. Rev. Lett.* **100** (Jun, 2008) 222301.

[11] STAR collaboration, K. H. Ackermann et al.*Nucl. Inst. Meth. A* **499** (2003) 624–632.

[12] M. He, R. J. Fries and R. Rapp*Phys. Rev. C* **86** (Jul, 2012) 014903.

[13] M. Nahrgang, J. Aichelin, S. Bass, P. B. Gossiaux and K. Werner*Phys. Rev. C* **91** (Jan, 2015) 014904.

[14] S. Cao, G.-Y. Qin and S. A. Bass*Phys. Rev. C* **88** (Oct, 2013) 044907.

[15] STAR collaboration, L. Adamczyk et al.*Phys. Rev. Lett.* **118** (May, 2017) 212301.

[16] STAR collaboration, B. I. Abelev et al.*Phys. Rev. C* **77** (May, 2008) 054901.

[17] L.-G. Pang, Y. Hatta, X.-N. Wang and B.-W. Xiao*Phys. Rev. D* **91** (Apr, 2015) 074027.

[18] S. Cao, T. Luo, G.-Y. Qin and X.-N. Wang*Phys. Rev. C* **94** (Jul, 2016) 014909.

[19] T. Song, H. Berrehrah, D. Cabrera, J. M. Torres-Rincon, L. Tolos, W. Cassing et al.*Phys. Rev. C* **92** (Jul, 2015) 014910.

[20] H.-T. Ding, A. Francis, O. Kaczmarek, F. Karsch, H. Satz and W. Soeldner*Phys. Rev. D* **86** (Jul, 2012) 014509.

[21] D. Banerjee, S. Datta, R. Gavai and P. Majumdar*Phys. Rev. D* **85** (Jan, 2012) 014510.

[22] T. Sjöstrand, S. Mrenna and P. Skands*Journal of High Energy Physics* **2006** (2006) 026.

[23] M. Lisovyi, A. Verbytskyi and O. Zenaiev*Eur. Phys. J. C* **76** (Jul, 2016) 397.

[24] I. Kuznetsova and J. Rafelski*Eur. Phys. J. C* **51** (Jun, 2007) 113–133.

Measurement of $\overline{\Lambda_c}^-/\Lambda_c^+$ ratio in Au+Au collisions at $\sqrt{s_{NN}}$ = 200 GeV with the STAR experiment

Miroslav Simko *for the STAR Collaboration*

Nuclear Physics Institute of the Czech Academy of Sciences

Faculty of Nuclear Sciences and Physical Engineering, Czech Technical University in Prague

Venezia 2018 Quark Matter

Abstract

The yield ratios of strange anti-baryons to baryons have been measured in heavy-ion collisions and exhibit a trend that is getting closer to unity with increasing number of valence strange quarks. This ratio has, however, never been measured for charm baryons, and it is important to establish if they exhibit a similar amount of baryon-to-anti-baryon enhancement as strange baryons. Λ_c is the lightest baryon containing a charm quark and, as such, presents a unique probe to study the hadronization of charm quarks in the hot and dense QCD medium created in ultra-relativistic heavy-ion collisions. Λ_c has, however, an extremely short lifetime ($c\tau \sim 60$ μm) which makes the reconstruction experimentally challenging. The Heavy Flavor Tracker, installed at the STAR experiment between the years 2014 – 2016, has shown a high efficiency and an unparalleled track-pointing resolution that can facilitate the Λ_c reconstruction in heavy-ion collisions. In this poster, we present the reconstruction of Λ_c baryons via hadronic decays and the studies on the measurement of the yield ratio of $\overline{\Lambda_c}^-/\Lambda_c^+$ utilizing the high-statistics data samples of Au+Au collisions at $\sqrt{s_{NN}}$ = 200 GeV, recorded with the STAR experiment in 2014 and 2016.

Motivation

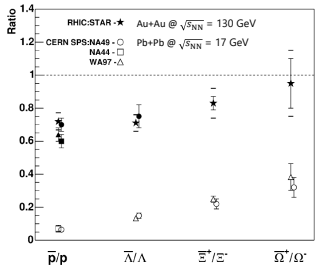

Figure 1: Ratios of anti-baryons to baryons [1].

- Ratios of strange anti-baryons to baryons grow towards unity with increasing number of strange valence quarks in the baryon.
- This ratio has never been measured for charm baryons and anti-baryons in heavy-ion collisions.
- $\overline{\Lambda_c}^-/\Lambda_c^+$ can bring important insights into the hadronization of charm quarks.

$\overline{\Lambda_c}^-/\Lambda_c^+$ statistical uncertainty projection

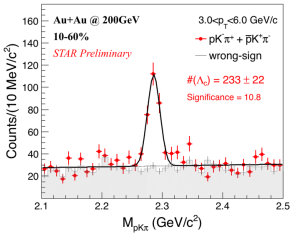

Figure 5: Λ_c invariant mass spectrum from 2014 and 2016 data. Red points are right-sign and blue points wrong-sign pKπ triplets.

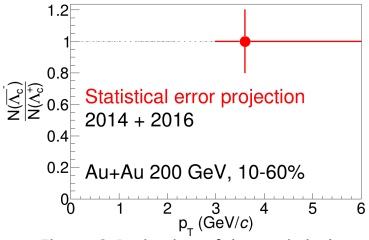

Figure 6: Projection of the statistical uncertainty of the $\overline{\Lambda_c}^-/\Lambda_c^+$ ratio using 2014 and 2016 Au+Au data.

Solenoidal Tracker at RHIC: 2π acceptance in azimuth

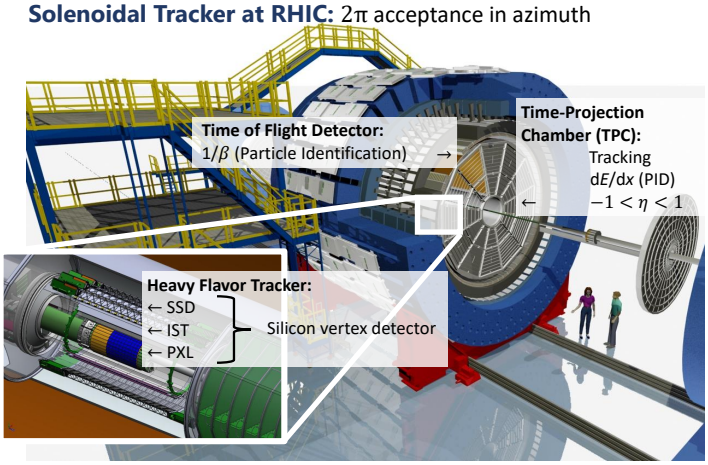

Figure 2: The STAR experiment and the main subdetectors used in the Λ_c analysis.

Charge dependent reconstruction efficiency

- There is an observable charge dependence of detector efficiencies.

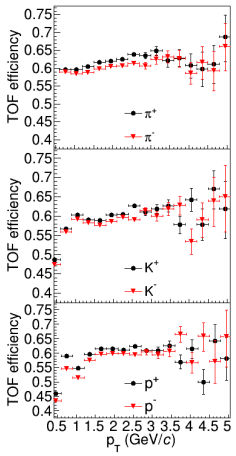

Figure 7: Difference in the TOF-matching efficiency.

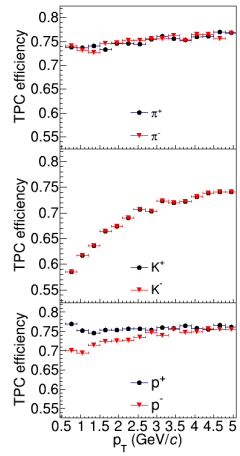

Figure 8: Difference in the TPC efficiency.

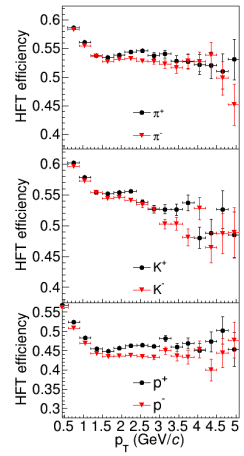

Figure 9: Difference in the HFT-matching efficiency.

Data-driven fast simulation:

- The Λ_c were decayed, using the EvtGen simulator [4].
- HFT- and TOF-matching efficiencies were obtained from data.
- TPC efficiency was obtained from embedding of simulated tracks in real data.
- The positions of the daughter particles are smeared according to the DCA resolution extracted from data.
- Momenta are smeared according to detector simulation.

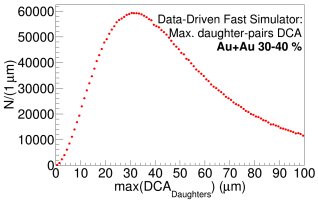

Figure 10: Maximum daughter pair DCA from the data-driven fast simulation.

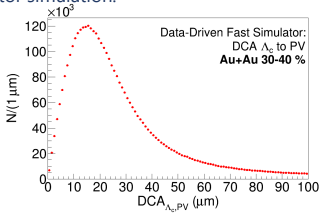

Figure 11: DCA between Λ_c and the primary vertex from the data-driven fast simulation.

Outlook: Efficiencies will be applied separately for Λ_c^+ and $\overline{\Lambda_c}^-$ to obtain the final $\overline{\Lambda_c}^-/\Lambda_c^+$ ratio.

Λ_c reconstruction

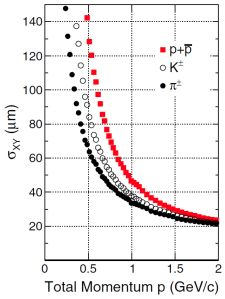

Figure 3: DCA resolution in the transverse plane of identified tracks with the HFT [2].

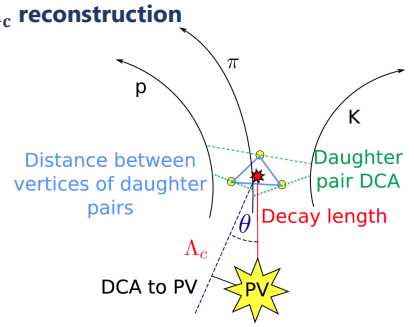

Figure 4: Topological reconstruction of the Λ_c secondary vertex.

- Short life time of $c\tau = 60$ μm.
- Three-body decay channel $\Lambda_c^\pm \to \pi^\pm K^\mp p^\pm$ used.
- Topological reconstruction thanks to the excellent tracking resolution of the HFT.
- Cuts on topological variables optimized via the Toolkit for Multi-Variate Analysis (TMVA – [3]) package, using the Boosted-Decision Trees method.

Acknowledgement

This work was also supported by the grants LG15001, LM2015054 and CZ.02.1.01/0.0/0.0/16_013/0001569 (Brookhaven National Laboratory - participation of the Czech Republic) of Ministry of Education, Youth and Sports of the Czech Republic.

References

[1] J. Adams et al. (STAR), Phys. Lett. B **567** (2003) 167 – 174.
[2] L. Adamczyk et al. (STAR), Phys. Rev. Lett. **118** (2017) 212301.
[3] L. Hoecker et al., arXiv:physics/0703039.
[4] D.J. Lange, Nucl. Instrum. Meth. A**462** (2001) 152-155.

EUROPEAN UNION
European Structural and Investment Funds
Operational Programme Research, Development and Education

MINISTRY OF EDUCATION, YOUTH AND SPORTS

The STAR Collaboration
drupal.star.bnl.gov/STAR/presentations

FACULTY OF NUCLEAR SCIENCES AND PHYSICAL ENGINEERING CTU IN PRAGUE

First Measurement of Λ_c Baryon Production in Au + Au Collisions at $\sqrt{s_{NN}} = 200$ GeV

J. Adam,[6] L. Adamczyk,[2] J. R. Adams,[39] J. K. Adkins,[30] G. Agakishiev,[28] M. M. Aggarwal,[40] Z. Ahammed,[59] I. Alekseev,[3,35] D. M. Anderson,[53] A. Aparin,[28] E. C. Aschenauer,[6] M. U. Ashraf,[11] F. G. Atetalla,[29] A. Attri,[40] G. S. Averichev,[28] V. Bairathi,[22] K. Barish,[10] A. Behera,[51] R. Bellwied,[20] A. Bhasin,[27] J. Bielcik,[14] J. Bielcikova,[38] L. C. Bland,[6] I. G. Bordyuzhin,[3] J. D. Brandenburg,[48,6] A. V. Brandin,[35] J. Butterworth,[44] H. Caines,[62] M. Calderón de la Barca Sánchez,[8] D. Cebra,[8] I. Chakaberia,[29,6] P. Chaloupka,[14] B. K. Chan,[9] F-H. Chang,[37] Z. Chang,[6] N. Chankova-Bunzarova,[28] A. Chatterjee,[11] D. Chen,[10] J. H. Chen,[18] X. Chen,[47] Z. Chen,[48] J. Cheng,[55] M. Cherney,[13] M. Chevalier,[10] S. Choudhury,[18] W. Christie,[6] H. J. Crawford,[7] M. Csanád,[16] M. Daugherity,[1] T. G. Dedovich,[28] I. M. Deppner,[19] A. A. Derevschikov,[42] L. Didenko,[6] X. Dong,[31] J. L. Drachenberg,[1] J. C. Dunlop,[6] T. Edmonds,[43] N. Elsey,[61] J. Engelage,[7] G. Eppley,[44] R. Esha,[51] S. Esumi,[56] O. Evdokimov,[12] J. Ewigleben,[32] O. Eyser,[6] R. Fatemi,[30] S. Fazio,[6] P. Federic,[38] J. Fedorisin,[28] C. J. Feng,[37] Y. Feng,[43] P. Filip,[28] E. Finch,[50] Y. Fisyak,[6] A. Francisco,[62] L. Fulek,[2] C. A. Gagliardi,[53] T. Galatyuk,[15] F. Geurts,[44] A. Gibson,[58] K. Gopal,[23] D. Grosnick,[58] W. Guryn,[6] A. I. Hamad,[29] A. Hamed,[5] J. W. Harris,[62] W. He,[18] X. He,[26] S. Heppelmann,[8] S. Heppelmann,[41] N. Herrmann,[19] E. Hoffman,[20] L. Holub,[14] Y. Hong,[31] S. Horvat,[62] Y. Hu,[18] H. Z. Huang,[9] S. L. Huang,[51] T. Huang,[37] X. Huang,[55] T. J. Humanic,[39] P. Huo,[51] G. Igo,[9] D. Isenhower,[1] W. W. Jacobs,[25] C. Jena,[23] A. Jentsch,[6] Y. JI,[47] J. Jia,[6,51] K. Jiang,[47] S. Jowzaee,[61] X. Ju,[47] E. G. Judd,[7] S. Kabana,[29] M. L. Kabir,[10] S. Kagamaster,[32] D. Kalinkin,[25] K. Kang,[55] D. Kapukchyan,[10] K. Kauder,[6] H. W. Ke,[6] D. Keane,[29] A. Kechechyan,[28] M. Kelsey,[31] Y. V. Khyzhniak,[35] D. P. Kikoła,[60] C. Kim,[10] B. Kimelman,[8] D. Kincses,[16] T. A. Kinghorn,[8] I. Kisel,[17] A. Kiselev,[6] A. Kisiel,[60] M. Kocan,[14] L. Kochenda,[35] L. K. Kosarzewski,[14] L. Kramarik,[14] P. Kravtsov,[35] K. Krueger,[4] N. Kulathunga Mudiyanselage,[20] L. Kumar,[40] R. Kunnawalkam Elayavalli,[61] J. H. Kwasizur,[25] R. Lacey,[51] S. Lan,[11] J. M. Landgraf,[6] J. Lauret,[6] A. Lebedev,[6] R. Lednicky,[28] J. H. Lee,[6] Y. H. Leung,[31] C. Li,[47] W. Li,[49] W. Li,[44] X. Li,[47] Y. Li,[55] Y. Liang,[29] R. Licenik,[38] T. Lin,[53] Y. Lin,[11] M. A. Lisa,[39] F. Liu,[11] H. Liu,[25] P. Liu,[51] P. Liu,[49] T. Liu,[62] X. Liu,[39] Y. Liu,[53] Z. Liu,[47] T. Ljubicic,[6] W. J. Llope,[61] R. S. Longacre,[6] N. S. Lukow,[52] S. Luo,[12] X. Luo,[11] G. L. Ma,[49] L. Ma,[18] R. Ma,[6] Y. G. Ma,[49] N. Magdy,[12] R. Majka,[62] D. Mallick,[36] S. Margetis,[29] C. Markert,[54] H. S. Matis,[31] J. A. Mazer,[45] N. G. Minaev,[42] S. Mioduszewski,[53] B. Mohanty,[36] I. Mooney,[61] Z. Moravcova,[14] D. A. Morozov,[42] M. Nagy,[16] J. D. Nam,[52] Md. Nasim,[22] K. Nayak,[11] D. Neff,[9] J. M. Nelson,[7] D. B. Nemes,[62] M. Nie,[48] G. Nigmatkulov,[35] T. Niida,[56] L. V. Nogach,[42] T. Nonaka,[11] G. Odyniec,[31] A. Ogawa,[6] S. Oh,[62] V. A. Okorokov,[35] B. S. Page,[6] R. Pak,[6] A. Pandav,[36] Y. Panebratsev,[28] B. Pawlik,[2] D. Pawlowska,[60] H. Pei,[11] C. Perkins,[7] L. Pinsky,[20] R. L. Pintér,[16] J. Pluta,[60] J. Porter,[31] M. Posik,[52] N. K. Pruthi,[40] M. Przybycien,[2] J. Putschke,[61] H. Qiu,[26] A. Quintero,[52] S. K. Radhakrishnan,[29] S. Ramachandran,[30] R. L. Ray,[54] R. Reed,[32] H. G. Ritter,[31] J. B. Roberts,[44] O. V. Rogachevskiy,[28] J. L. Romero,[8] L. Ruan,[6] J. Rusnak,[38] N. R. Sahoo,[48] H. Sako,[56] S. Salur,[45] J. Sandweiss,[62] S. Sato,[56] W. B. Schmidke,[6] N. Schmitz,[33] B. R. Schweid,[51] F. Seck,[15] J. Seger,[13] M. Sergeeva,[9] R. Seto,[10] P. Seyboth,[33] N. Shah,[24] E. Shahaliev,[28] P. V. Shanmuganathan,[6] M. Shao,[47] F. Shen,[48] W. Q. Shen,[49] S. S. Shi,[11] Q. Y. Shou,[49] E. P. Sichtermann,[31] R. Sikora,[2] M. Simko,[38] J. Singh,[40] S. Singha,[26] N. Smirnov,[62] W. Solyst,[25] P. Sorensen,[6] H. M. Spinka,[4] B. Srivastava,[43] T. D. S. Stanislaus,[58] M. Stefaniak,[60] D. J. Stewart,[62] M. Strikhanov,[35] B. Stringfellow,[43] A. A. P. Suaide,[46] M. Sumbera,[38] B. Summa,[41] X. M. Sun,[11] Y. Sun,[47] Y. Sun,[21] B. Surrow,[52] D. N. Svirida,[3] P. Szymanski,[60] A. H. Tang,[6] Z. Tang,[47] A. Taranenko,[35] T. Tarnowsky,[34] J. H. Thomas,[31] A. R. Timmins,[20] D. Tlusty,[13] M. Tokarev,[28] C. A. Tomkiel,[32] S. Trentalange,[9] R. E. Tribble,[53] P. Tribedy,[6] S. K. Tripathy,[16] O. D. Tsai,[9] Z. Tu,[6] T. Ullrich,[6] D. G. Underwood,[4] I. Upsal,[48,6] G. Van Buren,[6] J. Vanek,[38] A. N. Vasiliev,[42] I. Vassiliev,[17] F. Videbæk,[6] S. Vokal,[28] S. A. Voloshin,[61] F. Wang,[43] G. Wang,[9] J. S. Wang,[21] P. Wang,[47] Y. Wang,[11] Y. Wang,[55] Z. Wang,[48] J. C. Webb,[6] P. C. Weidenkaff,[19] L. Wen,[9] G. D. Westfall,[34] H. Wieman,[31] S. W. Wissink,[25] R. Witt,[57] Y. Wu,[10] Z. G. Xiao,[55] G. Xie,[31] W. Xie,[43] H. Xu,[21] N. Xu,[31] Q. H. Xu,[48] Y. F. Xu,[49] Y. Xu,[48] Z. Xu,[6] Z. Xu,[9] C. Yang,[48] Q. Yang,[48] S. Yang,[6] Y. Yang,[37] Z. Yang,[11] Z. Ye,[44] Z. Ye,[12] L. Yi,[48] K. Yip,[6] H. Zbroszczyk,[60] W. Zha,[47] D. Zhang,[11] S. Zhang,[47] S. Zhang,[49] X. P. Zhang,[55] Y. Zhang,[47] Z. J. Zhang,[37] Z. Zhang,[6] J. Zhao,[43] C. Zhong,[49] C. Zhou,[49] X. Zhu,[55] Z. Zhu,[48] M. Zurek,[31] and M. Zyzak[17]

(STAR Collaboration)

[1]*Abilene Christian University, Abilene, Texas 79699*
[2]*AGH University of Science and Technology, FPACS, Cracow 30-059, Poland*
[3]*Alikhanov Institute for Theoretical and Experimental Physics NRC "Kurchatov Institute," Moscow 117218, Russia*

[4]Argonne National Laboratory, Argonne, Illinois 60439
[5]American University of Cairo, New Cairo 11835, Egypt
[6]Brookhaven National Laboratory, Upton, New York 11973
[7]University of California, Berkeley, California 94720
[8]University of California, Davis, California 95616
[9]University of California, Los Angeles, California 90095
[10]University of California, Riverside, California 92521
[11]Central China Normal University, Wuhan, Hubei 430079
[12]University of Illinois at Chicago, Chicago, Illinois 60607
[13]Creighton University, Omaha, Nebraska 68178
[14]Czech Technical University in Prague, FNSPE, Prague 115 19, Czech Republic
[15]Technische Universität Darmstadt, Darmstadt 64289, Germany
[16]ELTE Eötvös Loránd University, Budapest, Hungary H-1117
[17]Frankfurt Institute for Advanced Studies FIAS, Frankfurt 60438, Germany
[18]Fudan University, Shanghai, 200433
[19]University of Heidelberg, Heidelberg 69120, Germany
[20]University of Houston, Houston, Texas 77204
[21]Huzhou University, Huzhou, Zhejiang 313000
[22]Indian Institute of Science Education and Research (IISER), Berhampur 760010, India
[23]Indian Institute of Science Education and Research (IISER) Tirupati, Tirupati 517507, India
[24]Indian Institute Technology, Patna, Bihar 801106, India
[25]Indiana University, Bloomington, Indiana 47408
[26]Institute of Modern Physics, Chinese Academy of Sciences, Lanzhou, Gansu 730000
[27]University of Jammu, Jammu 180001, India
[28]Joint Institute for Nuclear Research, Dubna 141 980, Russia
[29]Kent State University, Kent, Ohio 44242
[30]University of Kentucky, Lexington, Kentucky 40506-0055
[31]Lawrence Berkeley National Laboratory, Berkeley, California 94720
[32]Lehigh University, Bethlehem, Pennsylvania 18015
[33]Max-Planck-Institut für Physik, Munich 80805, Germany
[34]Michigan State University, East Lansing, Michigan 48824
[35]National Research Nuclear University MEPhI, Moscow 115409, Russia
[36]National Institute of Science Education and Research, HBNI, Jatni 752050, India
[37]National Cheng Kung University, Tainan 70101
[38]Nuclear Physics Institute of the CAS, Rez 250 68, Czech Republic
[39]Ohio State University, Columbus, Ohio 43210
[40]Panjab University, Chandigarh 160014, India
[41]Pennsylvania State University, University Park, Pennsylvania 16802
[42]NRC "Kurchatov Institute," Institute of High Energy Physics, Protvino 142281, Russia
[43]Purdue University, West Lafayette, Indiana 47907
[44]Rice University, Houston, Texas 77251
[45]Rutgers University, Piscataway, New Jersey 08854
[46]Universidade de São Paulo, São Paulo, Brazil 05314-970
[47]University of Science and Technology of China, Hefei, Anhui 230026
[48]Shandong University, Qingdao, Shandong 266237
[49]Shanghai Institute of Applied Physics, Chinese Academy of Sciences, Shanghai 201800
[50]Southern Connecticut State University, New Haven, Connecticut 06515
[51]State University of New York, Stony Brook, New York 11794
[52]Temple University, Philadelphia, Pennsylvania 19122
[53]Texas A&M University, College Station, Texas 77843
[54]University of Texas, Austin, Texas 78712
[55]Tsinghua University, Beijing 100084
[56]University of Tsukuba, Tsukuba, Ibaraki 305-8571, Japan
[57]United States Naval Academy, Annapolis, Maryland 21402
[58]Valparaiso University, Valparaiso, Indiana 46383
[59]Variable Energy Cyclotron Centre, Kolkata 700064, India

[60]Warsaw University of Technology, Warsaw 00-661, Poland
[61]Wayne State University, Detroit, Michigan 48201
[62]Yale University, New Haven, Connecticut 06520

(Received 1 November 2019; revised manuscript received 24 February 2020; accepted 27 March 2020; published 1 May 2020)

We report on the first measurement of the charmed baryon $\Lambda_c^{\pm}$ production at midrapidity ($|y| < 1$) in Au + Au collisions at $\sqrt{s_{\rm NN}} = 200$ GeV collected by the STAR experiment at the Relativistic Heavy Ion Collider. The Λ_c/D^0 [denoting $(\Lambda_c^+ + \Lambda_c^-)/(D^0 + \bar{D}^0)$] yield ratio is measured to be 1.08 ± 0.16 (stat) $\pm$ 0.26 (sys) in the 0%–20% most central Au + Au collisions for the transverse momentum (p_T) range $3 < p_T < 6$ GeV/c. This is significantly larger than the PYTHIA model calculations for $p + p$ collisions. The measured Λ_c/D^0 ratio, as a function of p_T and collision centrality, is comparable to the baryon-to-meson ratios for light and strange hadrons in Au + Au collisions. Model calculations including coalescence hadronization for charmed baryon and meson formation reproduce the features of our measured Λ_c/D^0 ratio.

DOI: 10.1103/PhysRevLett.124.172301

Heavy-ion collisions offer a unique opportunity to study quantum chromodynamics (QCD), the theory describing strong interactions between quarks and gluons through color charges. Data collected from the Relativistic Heavy Ion Collider (RHIC) and the Large Hadron Collider (LHC) demonstrate that novel QCD matter, quark-gluon plasma (QGP), in which quarks and gluons are deconfined, is created in high-energy nucleus-nucleus collisions [1,2]. QCD hadronization is a nonperturbative process and remains a challenging process to model. Fragmentation fractions measured in high-energy ee, ep, and pp collisions have been used to successfully describe hadron production at high transverse momentum (p_T) and are deployed in Monte Carlo event generators like PYTHIA [3] using a string fragmentation hadronization scheme. Recently, different schemes, such as color reconnection (CR) in PYTHIA, where strings from different multiparton interactions are allowed to recombine, have been developed to reproduce the low-p_T hadron data, including an enhanced production of baryons, in pp collisions [4]. In central heavy-ion collisions, baryon-to-meson ratios for light and strange hadrons in $2 < p_T < 6$ GeV/c show an enhancement compared to pp collisions [5–7]. A coalescence hadronization mechanism, in which hadrons can be formed via recombination of close-by partons in phase space in the deconfined QGP, has been utilized to describe the enhancement in heavy-ion collisions [8,9]. Alternatively to these microscopic schemes, a statistical hadronization scheme, which determines hadron yields statistically by their quantum numbers and thermal properties of the system, is used to fit successfully various light and strange hadron integrated yields in ee, pp, and heavy-ion collisions [10].

Because of their large masses, heavy quarks (c and b) are predominately created from initial hard scatterings in heavy-ion collisions. The relative yields of heavy-flavor hadrons can serve as a tag to study their hadronization process. The c quark fragmentation fraction ratio $(c \to \Lambda_c^+)/(c \to D^0)$ was measured to be around 0.10–0.15 in ee and ep collisions [11–13]. Recently, ALICE and LHCb measured [14,15] the Λ_c/D^0 ratio in $p + p$ and $p + \mathrm{Pb}$ collisions at the LHC to be 0.4–0.5 at $2 < p_T < 8$ GeV/c, larger than the PYTHIA model calculation based on string fragmentation. The PYTHIA model with color reconnection yields a larger Λ_c/D^0 ratio that is close to the data [14].

In heavy-ion collisions, models including coalescence hadronization of charm quarks predict a large Λ_c/D^0 ratio of ~1, in the low to intermediate p_T regions ($< \sim 8$ GeV/c) [16–18]. The ALICE Collaboration reported the Λ_c/D^0 ratio to be ~1 at $6 < p_T < 12$ GeV/c in Pb + Pb collisions at $\sqrt{s_{\rm NN}} = 5.02$ TeV, consistent with a contribution of coalescence hadronization for charm quarks [19]. Measurement of $\Lambda_c^{\pm}$ production in heavy-ion collisions over a broad momentum region, particularly at lower p_T, will offer significant insights into the hadronization mechanism of charm quarks in the presence of a QGP. Furthermore, understanding the hadronization mechanism of charm quarks in heavy-ion collisions is crucial to the study of charm-quark energy loss in the QGP using the measurements of nuclear modification factors ($R_{\rm AA}$) of D mesons [20–22] in heavy-ion collisions. Since the charm quarks are dominantly produced through initial hard scatterings, a large baryon-to-meson ratio directly impacts the charm meson $R_{\rm AA}$.

In this Letter, we report on the first measurement of $\Lambda_c^{\pm}$ production in Au + Au collisions at $\sqrt{s_{\rm NN}} = 200$ GeV. The analysis is carried out at midrapidity ($|y| < 1$) and utilized a total of 2.3 billion minimum bias (MB) triggered events collected by the STAR experiment during 2014 and 2016 runs at RHIC. The heavy flavor tracker (HFT) [23], a four-layer high-resolution silicon detector, was used for excellent vertex resolution that improves significantly the signal-to-background ratio for charmed hadron reconstruction. The MB events are selected by requiring a coincidence between the east and west vertex position detectors [24]. The events are required to have the reconstructed primary vertex (PV) position along the beam direction within 6 cm from the detector center, to ensure

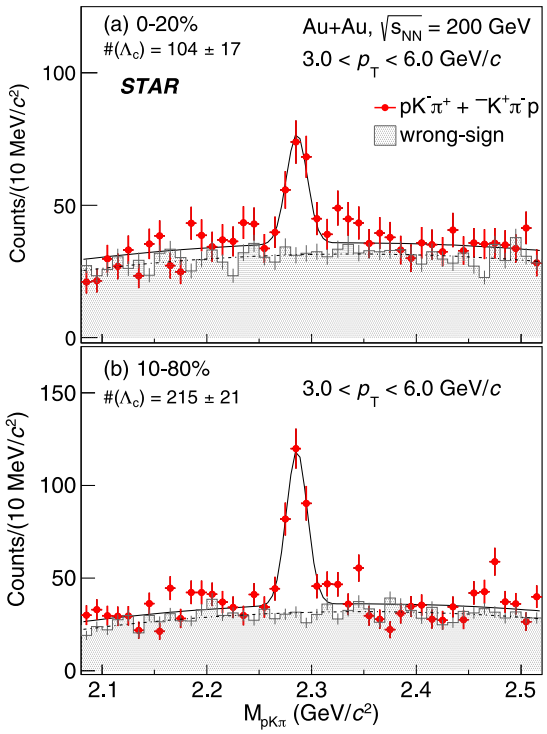

FIG. 1. The $pK\pi$ invariant mass distributions for right-sign (solid red points) and wrong-sign (shaded histograms) combinations in Au + Au collisions at $\sqrt{s_{\mathrm{NN}}} = 200$ GeV for 0%–20% (top) and 10%–80% (bottom) centrality classes. The wrong-sign distributions are scaled by $1/3$, the ratio of the number of right-sign to wrong-sign combinations for the $pK\pi$ triplet. The error bars shown are statistical uncertainties. The solid line depicts a fit with a Gaussian function, for a $\Lambda_c^{\pm}$ signal, and a second-order polynomial function, the shape of which is fixed by fit to the wrong-sign distribution (dashed line), for the background.

good HFT acceptance. The collision centrality, a measure of the geometric overlap between the two colliding nuclei, is defined using the measured charged track multiplicity at midrapidity, as compared to a Monte Carlo Glauber simulation [25].

The $\Lambda_c^{\pm}$ baryons are reconstructed via the hadronic decay channel $\Lambda_c^+ \to K^-\pi^+p$ and its charge conjugate. Charged particle tracks are reconstructed from hits in the STAR time projection chamber (TPC) [26] and HFT detectors, in a 0.5 T magnetic field. Tracks are required to have a minimum of 20 TPC hits (out of a maximum of 45) and at least three hits in the HFT subdetectors. The tracks are also required to be within pseudorapidity $|\eta| < 1$ with $p_T > 0.5$ GeV/c. Particle identification (PID) is achieved by a combination of the ionization energy loss dE/dx, measured by the TPC, and the timing, measured by the time of flight detector [27].

The $\Lambda_c^{\pm}$ decay vertex is reconstructed as the midpoint of the distance of closest approach (DCA) between the three daughter tracks. To improve separation of the signal from combinatorial background of tracks originating from the primary vertex, we utilized a supervised machine learning algorithm, the boosted decision trees (BDTs), implemented in the TMVA package [28]. The BDTs are trained with a signal sample of $\Lambda_c^{\pm} \to K\pi p$ decays simulated using the EvtGen generator [29] with detector effects taken into account and a background sample of wrong-sign $K\pi p$ combinations from data. The variables characterizing the decay topology, viz. the decay length, DCA of daughter tracks to the PV, and the DCA of the reconstructed Λ_c candidate to the PV are used as input variables in the training. The cut on BDT response is optimized for maximum $\Lambda_c^{\pm}$ signal significance using the estimated number of signal and background $\Lambda_c^{\pm}$ candidates in the data. Figure 1 shows examples of invariant mass distributions with the BDT selection, of $K\pi p$ triplets with the right and wrong sign (scaled by $1/3$) combinations. The distributions in the 0%–20% most central collisions (top) and the 10%–80% central collisions (bottom), the centrality range used for p_T-dependent measurement, are shown. The right-sign distributions are fit to a Gaussian for the signal plus a second-order polynomial for the background, with the shape of the polynomial function fixed from fitting to the wrong-sign distribution. The raw signal yields are obtained as the counts of the right-sign triplets within a mass window of three standard deviations of the Gaussian fit with background counts, evaluated using the polynomial component of the fit in the same mass window, subtracted.

The $\Lambda_c^{\pm}$ reconstruction efficiency is evaluated using a hybrid method, similarly to the D^0 spectra measurement with the STAR HFT [20]. The TPC tracking efficiency is obtained using the standard embedding technique used in many other STAR analyses [30]. The PID efficiencies are evaluated using pure π, K, and p samples from the data. The HFT tracking and the BDT selection efficiency are calculated using a data-driven simulation framework with the input distributions taken from the real data. The input distributions include the TPC-to-HFT matching efficiency (the fraction of good TPC tracks matched to hits in HFT) and the DCA distributions of tracks with respect to the reconstructed collision vertex. Protons reconstructed in the real data have a sizable secondary contribution from other hyperon decays, which impacts the TPC-to-HFT matching ratio and DCA distributions. A correction factor to the efficiency calculated using the data-driven simulation is evaluated using Au + Au events from HIJING [31] propagated through the STAR GEANT detector geometry [32] and digital signals embedded into those from zero-bias data (denoted HIJING + ZB). Zero-bias data consist of events taken with no collision requirement and capture the background conditions in the detectors during the run. The p_T distributions of protons and hyperons from HIJING are reweighted to match the data [5,30]. The events are then reconstructed with the same algorithm as the real data. The correction is calculated as a ratio of the efficiency from the data-driven simulation, using the input distributions for

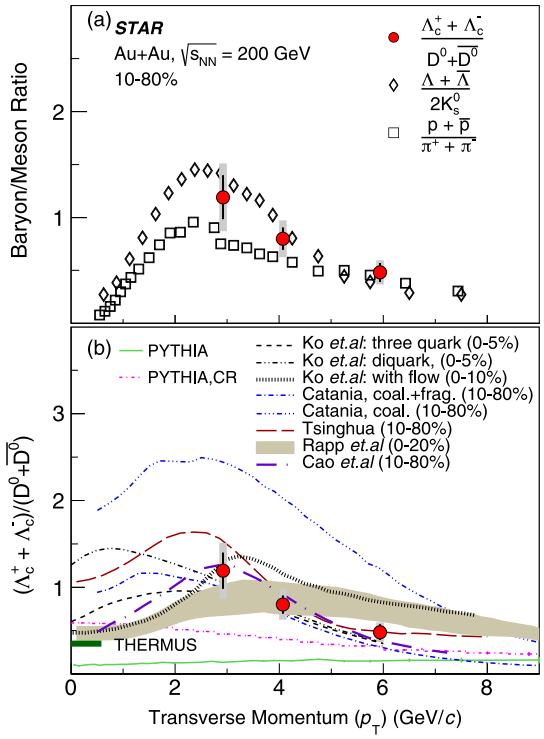

FIG. 2. The measured Λ_c/D^0 ratio at midrapidity ($|y| < 1$) as a function of p_T for Au + Au collisions at $\sqrt{s_{\rm NN}} = 200$ GeV in 10%–80% centrality, compared to the baryon-to-meson ratios for light and strange hadrons (top) and various model calculations (bottom). The vertical lines and shaded boxes on the Λ_c/D^0 data points indicate statistical and systematic uncertainties, respectively. The p_T integrated Λ_c/D^0 ratio from the THERMUS [10] model calculation with a freeze-out temperature of $T_{\rm ch} = 160$ MeV is shown as a horizontal bar on the left axis of the plot.

inclusive tracks from the reconstructed HIJING + ZB data, to the one using inputs from primary tracks from the same data. The correction factor is found to be about 30% with very weak p_T and centrality dependences. The impact of the finite primary vertex resolution on the reconstruction efficiency obtained by this method is also evaluated using the HIJING + ZB events with procedures similar to those described in Ref. [20]. It is found to be within 10% for the 50%–80% centrality class and negligible for more central events. The yields are finally corrected for the $\Lambda_c^\pm \to K\pi p$ branching ratio (BR) of $6.28 \pm 0.32\%$ [33].

The systematic uncertainties to the measurement include the uncertainties in raw yield extraction and various efficiency correction factors. The former is evaluated by varying the background estimation method (varying the fit range and choice of background function and leaving the background shape unconstrained) and is between 6% and 14% in the measured p_T region. The contribution to the yield under the mass peak from incorrectly assigned PID for daughter tracks is less than 1%. The TPC efficiency uncertainty is evaluated to be ~15%, and PID efficiency uncertainties to be ~6%, for three daughter tracks combined. The uncertainty in the HFT tracking and topological cut efficiency is estimated by changing the BDT response cuts so that the reconstruction efficiency varies by 50% above and below relative to the nominal one. The resulting nonstatistical variations to final results are included in the systematic uncertainties and range from 10% to 15%. For the correction factor due to secondary protons, the uncertainties from the measured proton and Λ spectra [5,30], as well as those on other hadrons that decay to protons, are propagated. This uncertainty is estimated to be about 4%. We also include a 10% uncertainty from a closure test for the data-driven simulation method, evaluated by comparing the efficiencies calculated using a data-driven simulation with input distributions from reconstructed HIJING + ZB events, to the efficiencies evaluated directly from the reconstructed HIJING + ZB events. The feed-down contribution from bottom hadrons to the measurements is found to be small and less than 4% in the measured p_T range. Finally, the uncertainty in the decay BR from the latest PDG [33] value is added as a global normalization uncertainty in the $\Lambda_c^\pm$ yield.

The $\Lambda_c^\pm$ invariant yields in the 10%–80% centrality class for the different p_T bins are shown in Table I, along with the statistical and systematic uncertainties. The 10%–80% centrality class is chosen for p_T-dependent measurement, as it had the best Λ_c signal significance in the measured regions. The ratio of the invariant yield of $\Lambda_c^\pm$ to that of D^0 is shown as a function of p_T in Fig. 2 for the 10%–80% centrality class. The correlated systematic uncertainties from efficiency correction that go into both $\Lambda_c^\pm$ and D^0 measurements cancel. Figure 2(a) compares the Λ_c/D^0 ratio to the baryon-to-meson ratios from light and strange-flavor hadrons [5,30]. The Λ_c/D^0 ratio is comparable in magnitude to the Λ/K_s^0 and p/π ratios and shows a similar p_T dependence in the measured region.

The measured values are compared to different model calculations in Fig. 2(b). The values show a significant enhancement compared to the calculations from the latest PYTHIA 8.24 release (Monash tune [34]) without CR [4]. The implementation with CR (mode2 in Ref. [4]) enhances the baryon production with respect to mesons and gives a Λ_c/D^0 yield ratio consistent with those measured in $p + p$ and $p +$ Pb collisions at the LHC [14,15]. However, both calculations fail to fully describe the Au + Au data and their p_T dependence. The mode without CR is ruled out at a p value of 1×10^{-4} ($\chi^2/\mathrm{NDF} = 20.7/3$), while the CR mode gives a p value of 0.04 ($\chi^2/\mathrm{NDF} = 8.2/3$) using a reduced χ^2 test.

Figure 2(b) shows the comparison to calculations from various models that include coalescence hadronization of charm quarks (labeled Ko *et al.* with three quarks and diquarks [16], Ko *et al.* with flow [35], Catania [36], Tsinghua [37], Rapp *et al.* [38], and Cao *et al.* [39]). The models differ among themselves in the choice of hadron

TABLE I. The $\Lambda_c^{\pm}$ invariant yields measured in the 10%–80% centrality class for the different p_T bins, in Au + Au collisions at $\sqrt{s_{\rm NN}} = 200$ GeV.

p_T (GeV/c)	$1/(2\pi p_T N_{\rm evt}) d^2N/dp_T dy$ (GeV/c)$^{-2}$
2.5–3.5	$8.2 \times 10^{-4} \pm 1.4 \times 10^{-4}$ (stat) $\pm 2.4 \times 10^{-4}$ (sys)
3.5–5.0	$6.0 \times 10^{-5} \pm 7.7 \times 10^{-6}$ (stat) $\pm 1.5 \times 10^{-5}$ (sys)
5.0–8.0	$2.1 \times 10^{-6} \pm 3.8 \times 10^{-7}$ (stat) $\pm 5.5 \times 10^{-7}$ (sys)

wave functions, light- and charm-quark spectra in the QGP, and also treatment of space-time correlations during coalescence and excited states that decay into Λ_c and D^0 that are considered. Most of the models are able to give enhanced Λ_c/D^0 yield ratios and describe the measured p_T dependence of the ratio. A reduced χ^2 test is carried out, taking into account the finite p_T bin width in the measurement. The Catania model calculations of the Λ_c/D^0 ratio from hadrons formed only through coalescence hadronization overpredict the measurement at all p_T (reduced $\chi^2 = 26.1$). The calculations from Ko *et al.* with flow give a reduced χ^2 value of 4.8, mainly from the overprediction of the ratio in the highest two p_T bins. The other coalescence model calculations are consistent with the data within uncertainties over the measured p_T range. It should be noted that the calculations from Rapp *et al.* and Ko *et al.* have different centrality ranges than in the measurement, which may impact the χ^2 values quoted. In the models discussed above, charm-quark radial flow is implicitly included mainly through the charm-quark diffusion in the medium. However, it was found that a purely radial flow effect without coalescence hadronization, evaluated using a blast-wave model with freeze-out parameters from D^0 measurement [20], causes the Λ_c/D^0 ratio to rise strongly with increasing p_T in the measured p_T region. This is similar to the behavior observed for light hadrons [6] and opposite to the trend measured in the data. The comparisons favor coalescence hadronization as having an important role in charm-quark hadronization in the presence of QGP. The data offer constraints to the model parameters and to the coalescence probabilities of charm quarks in the medium.

The p_T-integrated Λ_c/D^0 ratio is calculated to be 0.80 ± 0.12 (stat) ± 0.22 (sys, data) ± 0.41 (sys, model). The coalescence model curves shown in Fig. 2(b) were used to extrapolate to $p_T = 0$ GeV/c, with the mean of the extrapolated values from different models taken as the central value and the maximum difference between them included in the systematic uncertainty. The ratio is consistent, including extrapolation uncertainties, with the value (0.35) from the thermal model calculation using THERMUS [10] with a freeze-out temperature $T_{\rm ch} = 160$ MeV. This suggests $\Lambda_c^{\pm}$ contribute sizably to the total charm yield in heavy-ion collisions.

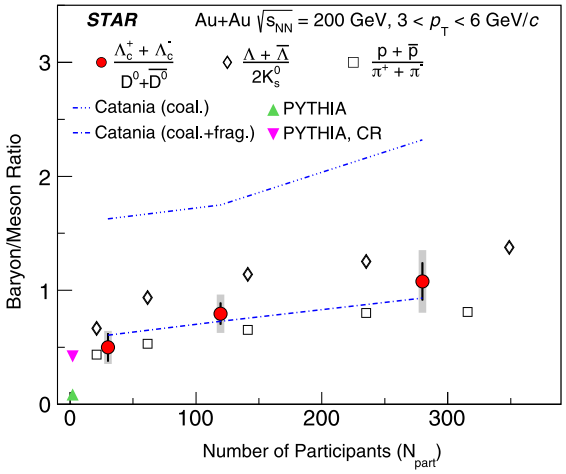

FIG. 3. The measured Λ_c/D^0 yield ratio in $3 < p_T < 6$ GeV/c (solid circles) as a function of collision centrality (expressed in $N_{\rm part}$) for Au + Au collisions at $\sqrt{s_{\rm NN}} = 200$ GeV. The open diamonds and squares show the baryon-to-meson ratio measured for strange and light-flavor hadrons, respectively. The vertical lines and the shaded boxes on the Λ_c/D^0 data points indicate statistical and systematic uncertainties, respectively. The dashed curves indicate the Λ_c/D^0 ratio calculated from a model with charm-quark coalescence, and the up and down triangles indicate the ratios from the PYTHIA model for $p + p$ collisions without and with CR respectively, for the same p_T region.

The centrality dependence of the Λ_c/D^0 ratio, plotted as a function of the number of participant nucleons $N_{\rm part}$, for $3 < p_T < 6$ GeV/c is shown in Fig. 3. The measurements correspond to the centrality ranges 50%–80%, 20%–50%, and 0%–20%. The Λ_c/D^0 ratio shows an increase toward more central collisions. The increasing trend is qualitatively similar to that seen for the baryon-to-meson ratio for light and strange-flavor hadrons and to that predicted by coalescence model calculations. The measured Λ_c/D^0 ratio in 0%–20% central collisions of 1.08 ± 0.16 (stat) $\pm$ 0.26 (sys) is larger than the values from PYTHIA 8.2 without CR (at 3.1σ significance) and with CR (at 2.1σ significance).

In summary, STAR reports on the first measurement of $\Lambda_c^{\pm}$ baryon production in Au + Au collisions at $\sqrt{s_{\rm NN}} =$ 200 GeV utilizing its high-resolution silicon detector. The measured Λ_c/D^0 yield ratio at midrapidity ($|y| < 1$) is found to be comparable to the baryon-to-meson ratios for light and strange-flavor hadrons in the same kinematic regions. The large Λ_c/D^0 ratio also suggests that charmed baryons contribute significantly to the total charm cross section at midrapidity in heavy-ion collisions at RHIC. The Λ_c/D^0 ratio in Au + Au collisions is considerably larger than the PYTHIA expectation at the same energy. Several model calculations that include coalescence hadronization for charm hadron formation can reproduce the features of our data. Our data are expected to offer significant constraints toward the understanding of QCD hadronization in

the finite temperature region and to the charm-quark transport and energy loss in the QGP.

We thank the RHIC Operations Group and RCF at BNL, the NERSC Center at LBNL, and the Open Science Grid consortium for providing resources and support. This work was supported in part by the Office of Nuclear Physics within the U.S. DOE Office of Science, the U.S. National Science Foundation, the Ministry of Education and Science of the Russian Federation, National Natural Science Foundation of China, Chinese Academy of Science, the Ministry of Science and Technology of China and the Chinese Ministry of Education, the National Research Foundation of Korea, Czech Science Foundation and Ministry of Education, Youth and Sports of the Czech Republic, Hungarian National Research, Development and Innovation Office, New National Excellency Programme of the Hungarian Ministry of Human Capacities, Department of Atomic Energy and Department of Science and Technology of the Government of India, the National Science Centre of Poland, the Ministry of Science, Education and Sports of the Republic of Croatia, RosAtom of Russia and German Bundesministerium fur Bildung, Wissenschaft, Forschung and Technologie (BMBF), and the Helmholtz Association.

[1] Y. Akiba *et al.*, arXiv:1502.02730.
[2] J. Adams *et al.* (STAR Collaboration), Nucl. Phys. **A757**, 102 (2005); K. Adcox *et al.* (PHENIX Collaboration), Nucl. Phys. **A757**, 184 (2005); B. B. Back *et al.*, Nucl. Phys. **A757**, 28 (2005); I. Arsene *et al.* (BRAHMS Collaboration), Nucl. Phys. **A757**, 1 (2005).
[3] T. Sjostrand, S. Mrenna, and P. Z. Skands, J. High Energy Phys. 05 (2006) 026.
[4] C. Bierlich and J. R. Christiansen, Phys. Rev. D **92**, 094010 (2015).
[5] B. I. Abelev *et al.* (STAR Collaboration), Phys. Rev. Lett. **97**, 152301 (2006).
[6] B. B. Abelev *et al.* (ALICE Collaboration), Phys. Rev. Lett. **111**, 222301 (2013).
[7] B. I. Abelev *et al.* (STAR Collaboration), Phys. Lett. B **655**, 104 (2007).
[8] Z. W. Lin and D. Molnar, Phys. Rev. C **68**, 044901 (2003).
[9] R. J. Fries, V. Greco, and P. Sorensen, Annu. Rev. Nucl. Part. Sci. **58**, 177 (2008).
[10] S. Wheaton, J. Cleymans, and M. Hauer, Comput. Phys. Commun. **180**, 84 (2009).
[11] R. Barate *et al.* (ALEPH Collaboration), Eur. Phys. J. C **16**, 597 (2000).
[12] H. Abramowicz *et al.* (ZEUS Collaboration), J. High Energy Phys. 09 (2013) 058.
[13] M. Lisovyi, A. Verbytskyi, and O. Zenaiev, EPJ Web Conf. **120**, 03002 (2016).
[14] S. Acharya *et al.* (ALICE Collaboration), J. High Energy Phys. 04 (2018) 108.
[15] R. Aaij *et al.* (LHCb Collaboration), J. High Energy Phys. 02 (2019) 102.
[16] Y. Oh, C. M. Ko, S. H. Lee, and S. Yasui, Phys. Rev. C **79**, 044905 (2009).
[17] V. Greco, C. M. Ko, and R. Rapp, Phys. Lett. B **595**, 202 (2004).
[18] S. H. Lee, K. Ohnishi, S. Yasui, I.-K. Yoo, and C.-M. Ko, Phys. Rev. Lett. **100**, 222301 (2008).
[19] S. Acharya *et al.* (ALICE Collaboration), Phys. Lett. B **793**, 212 (2019).
[20] J. Adam *et al.* (STAR Collaboration), Phys. Rev. C **99**, 034908 (2019).
[21] A. M. Sirunyan *et al.* (CMS Collaboration), Phys. Lett. B **782**, 474 (2018).
[22] J. Adam *et al.* (ALICE Collaboration), J. High Energy Phys. 03 (2016) 081.
[23] G. Contin *et al.*, Nucl. Instrum. Methods Phys. Res., Sect. A **907**, 60 (2018).
[24] W. J. Llope *et al.*, Nucl. Instrum. Methods Phys. Res., Sect. A **522**, 252 (2004).
[25] B. I. Abelev *et al.* (STAR Collaboration), Phys. Rev. C **79**, 034909 (2009).
[26] M. Anderson *et al.*, Nucl. Instrum. Methods Phys. Res., Sect. A **499**, 659 (2003).
[27] W. J. Llope (STAR Collaboration), Nucl. Instrum. Methods Phys. Res., Sect. A **661**, S110 (2012).
[28] A. Hoecker *et al.*, arXiv:physics/0703039.
[29] D. J. Lange, Nucl. Instrum. Methods Phys. Res., Sect. A **462**, 152 (2001).
[30] G. Agakishiev *et al.* (STAR Collaboration), Phys. Rev. Lett. **108**, 072301 (2012).
[31] M. Gyulassy and X.-N. Wang, Comput. Phys. Commun. **83**, 307 (1994).
[32] S. Agostinelli *et al.* (GEANT4 Collaboration), Nucl. Instrum. Methods Phys. Res., Sect. A **506**, 250 (2003).
[33] M. Tanabashi *et al.* (Particle Data Group), Phys. Rev. D **98**, 030001 (2018).
[34] P. Skands, S. Carrazza, and J. Rojo, Eur. Phys. J. C **74**, 3024 (2014).
[35] S. Cho, K.-J. Sun, C. M. Ko, S. H. Lee, and Y. Oh, Phys. Rev. C **101**, 024909 (2020).
[36] S. Plumari, V. Minissale, S. K. Das, G. Coci, and V. Greco, Eur. Phys. J. C **78**, 348 (2018).
[37] J. Zhao, S. Shi, N. Xu, and P. Zhuang, arXiv:1805.10858.
[38] M. He and R. Rapp, Phys. Rev. Lett. **124**, 042301 (2020).
[39] S. Cao, K.-J. Sun, S. Y. F. Liu, W.-J. Xing, G.-Y. Qin, and C.-M. Ko, arXiv:1911.00456.